Complementary strategies to promote the regeneration of bone-ligament transitions using graded electrospun scaffolds

Satyavrata Samavedi

Dissertation submitted to the faculty of the Virginia Polytechnic Institute and State University in partial fulfillment of the requirements for the degree of

Doctor of Philosophy
In
Chemical Engineering

Abby R. Whittington, Co-Chair
Aaron S. Goldstein, Co-Chair
Linda A. Dahlgren
Richey M. Davis
Joseph W. Freeman

3rd April 2013
Blacksburg, VA

Keywords: bone-ligament transition, graded scaffold, electrospinning, hydroxyapatite, contact guidance, growth factor, gelatin microsphere, bone marrow stromal cell

Complementary strategies to promote the regeneration of bone-ligament transitions using graded electrospun scaffolds

Satyavrata Samavedi

ABSTRACT

Grafts currently used for the repair of anterior cruciate ligament (ACL) ruptures integrate poorly with bone due to a significant mismatch in properties between graft and bone. Specifically, conventional grafts (e.g., hamstring tendon) are unable to recapitulate intricate gradients in mechano-chemical properties and extracellular matrix (ECM) architecture found at natural bone-ligament (B-L) transitions, and thus result in stress-concentrations at the graft-bone interface leading to graft failure. In contrast, tissue-engineered scaffolds possessing gradients in properties can potentially guide the establishment of phenotypic gradients in bone marrow stromal cells (BMSCs), and thus aid the regeneration of B-L transitions in the long-term. Towards the eventual goal of regenerating complex tissue transitions, this project employs three complementary strategies to fabricate graded scaffolds. The three strategies involve the presentation of gradients in 1) mineral content, 2) scaffold architecture and 3) growth factor (GF) concentration within scaffolds to control BMSC morphology and phenotype.

The first strategy involved co-electrospinning two polymers (one doped with hydroxyapatite) from offset spinnerets onto a rotating drum to produce scaffolds possessing a gradient in mineral content. Post-electrospinning, these graded scaffolds were treated with a simulated body fluid to further enhance the gradient. Analysis of mRNA expression of osteoblastic makers by BMSCs and the deposition of bone-specific ECM proteins indicated that the scaffolds could guide the formation of an osteoblastic phenotypic gradient. The second strategy involved electrospinning two polymer solutions onto a custom-designed dual-drum collector to fabricate scaffolds possessing region-wise differences in fiber alignment, diameter and chemistry. Specifically, electrospinning onto the dual-drum collector resulted in the deposition of aligned fibers from one polymer solution in the gap region between the drums,

randomly oriented fibers from the other polymer solution on one of the drums and a mixture of fibers from both polymer solutions in the overlap region in between. The topographical cues within these scaffolds were shown to result in region-dependent BMSC morphology and orientation. Although the long-term goal of the third strategy was to create a co-electrospun scaffold possessing a gradient in GF concentration, a new technique to protect GF activity within electrospun scaffolds via the use of gelatin microspheres was first validated. Preliminary results from these studies indicate that microspheres can protect and deliver a model protein (lysozyme) in active conformation from electrospun scaffolds. These results further suggest that gradients of GF concentration can be achieved in the long-term by protecting GFs within microspheres and co-electrospinning as described in the first strategy.

In conclusion, the results from this project suggest that graded scaffolds can help guide the formation of gradients in cell morphology, orientation and phenotype, and thus potentially promote the regeneration of B-L transitions in the long-term. The three strategies described in this project can be employed in concert to create scaffolds intended for the regeneration of complex tissue transitions.

Author's acknowledgements

At the outset, I wish to place on record my heart-felt thanks to my advisors Dr. Abby Whittington and Dr. Aaron Goldstein. Dr. Whittington has been very supportive of my research efforts and has been a kind and patient advisor. I am especially thankful to her for motivating me, and for the many opportunities she has provided to aid my professional development. I am greatly indebted to Dr. Goldstein for welcoming me into his lab at a very crucial juncture in my career, and for the time and effort he has invested towards molding me into a researcher. I've valued his scientific inputs far beyond words can describe, and I am very grateful for the care and interest he has shown in mentoring me. I also want to thank Dr. Linda Dahlgren, Dr. Joseph Freeman and Dr. Richey Davis for serving on my thesis committee, for their valuable inputs and for allowing me the use of lab supplies/equipment frequently. I sincerely thank Dr. John Walz for providing students with a very cohesive atmosphere within the chemical engineering department.

Next, I want to thank Riley Chan for designing several pieces of equipment and Michael Vaught for patiently building the same. Without Riley's and Mike's timely help, much of my work would have been impossible to complete. I'd also like to sincerely acknowledge Dr. Chris Bashur for teaching me electrospinning and cell culture, Dr. Robyn Cardwell for very patiently taking the time to answer my questions and for introducing me to several topics in molecular biology, Sarah Lapp for help and moral support within and outside the lab, Tyler Horseman for being a friend-philosopher, and Patrick Thayer and Prasad Vaidya for being helpful lab-mates. My thanks to the students in the Goldstein, Whittington, Dahlgren, Freeman, Rajagopalan, Lee and Rylander labs for their friendship, help and advice over the last few years. I also want to thank the Institute of Critical Technologies and Applied Sciences, the National Science Foundation and the Francis scholarship fund for financial support.

Over the years, I have had the opportunity to work with several talented undergraduate students and research scholars: C Olsen Horton, Samuel Inkrote, Cullen Fleming, Prudhvidhar Gaddam, Megan Cox, Alexander DiSavino and Lauren Poindexter; my heart-felt thanks to these wonderful people for helping me immensely with my research. I am also very grateful to several staff at Virginia Tech: Stephen McCartney for training me on the use of SEM, EDS and micro-

tensile tester, Rick Caudill for helping me with obtaining XRD spectra, Diane Cannaday for being a very helpful student coordinator, Nora Bentley, Tina Russell and Pamela Stiff for promptly following up on processing/purchasing requisitions, and James Lane and Jason Schroedl for their help during technological glitches. I also want to express my deep gratitude to all my friends, both in the U.S. and India, for providing me emotional support all along.

I can't thank enough my undergraduate research mentor Dr. Mukesh Doble (Professor, IIT Madras, India), who first taught me the ropes of conducting research and gave me ample opportunities for scientific and professional development. I am also extremely grateful to HH Paramarthananda for strengthening my faith in the Almighty, despite the growing importance of science in my life. He has also been instrumental in making me a more balanced and mature person than I was prior to meeting him. At this juncture, I also want to thank Mr. Prabhakar Reddy and Ms. Santhi Sathiapalan, my high-school teachers, for instilling in me a passion to pursue a career in biotechnology.

My family has been extremely supportive of all my endeavors. I am especially thankful to my uncle VK Rajagopal for consistently believing in my abilities even during times when I've severely doubted them, my aunt Vasanta Rajagopal for being almost a second mother to me, my sister Dr. Lata Kumar and her husband Kumar Ramanathan for their encouragement and support, and Siddharth Gopal for sticking by my side as a close friend through the thick and thin. Finally, I'm ever indebted to my parents who have sacrificed much for my sake. They have wanted to see me earn a Ph.D. more than even I have, and I know that I couldn't have come this far without their love, support and blessings. I'm particularly thankful to them for gifting me with a heritage that I will cherish forever.

I am eternally grateful to God for His benevolence. His unconditional grace, in spite of all my shortcomings, has been a source of immense mental strength.

Satyavrata Samavedi
Blacksburg, VA

Dedication

To all my teachers

I have been blessed with the best of teachers all through my life, and to this day I am in awe of their erudition, discipline and selfless attitude. I owe the little that I know to their patient guidance and meticulous instruction.

"Lead me from falsehood to reality
Lead me from darkness to light
Lead me from death to immortality"

Brhadaranyaka Upanishad 1.3.28

Table of Contents

Chapter 5: Fabrication of electrospun meshes possessing region-wise differences in fiber orientation, diameter and chemistry

Chapter 6: Development of microspheres for protecting protein activity during electrospinning

Appendix C: Synthetic biomaterials for regenerative medicine applications

List of Figures

List of tables

Chapter 1

Introduction

1.1. Clinical significance and motivation

The anterior cruciate ligament (ACL) is a vital connective tissue in the knee that is prone to injury [1]. In particular, more than 200,000 disruptions to the ACL are diagnosed each year in the U.S., and over 100,000 reconstruction surgeries performed to repair tears and ruptures [2, 3]. Current surgical options to treat ruptured ACLs include autologous grafts (patellar or hamstring tendon) and allogeneic grafts. These grafts primarily serve as replacements for the injured ACL, and result in varying levels of success with regard to post-operative knee function. However, each graft option has limitations. While autografts result in reduced mechanical properties at the donor site, allografts may risk disease transmission and are also limited in supply [4]. Synthetic polymer-based grafts are also potential repair options, but they are prone to failure from excessive creep and fatigue [5]. Consequently, they are not FDA-approved as a primary treatment option for ACL ruptures, although they have been conditionally approved for testing.

A serious concern with autografts and allografts for ligament reconstruction is poor integration with bone [6, 7]. Since the native insertion site – where ligaments anchor to bone – is marked by distinct gradients in mechanical and biochemical properties [8], the repair of ligament ruptures with soft tissue (e.g., hamstring tendon graft) introduces a mismatch of properties between graft and bone [9, 10]. As a result, stress-concentrations develop at the graft-bone interface, eventually resulting in graft failure. Although bone-patellar tendon-bone (B-PT-B) autografts preserve bone-ligament (B-L) transitions, excessive tibial rotation has been shown to persist two years after ACL reconstruction with B-PT-B autografts [11].

The limitations with autografts and allografts have motivated research towards the development of tissue-engineered ACL grafts. Generally, a tissue engineering strategy involves the use of a polymeric scaffold impregnated with stem cells, and the presentation of mechano-chemical cues within the scaffold to direct the differentiation of cells. The graft is expected to stimulate the formation of neo-tissue *in vivo* as the scaffold degrades [12]. However, engineered

tissue would need to possess bony insertion regions and robust B-L transition zones (similar to B-PT-B autografts) to integrate with bone successfully post-implantation.

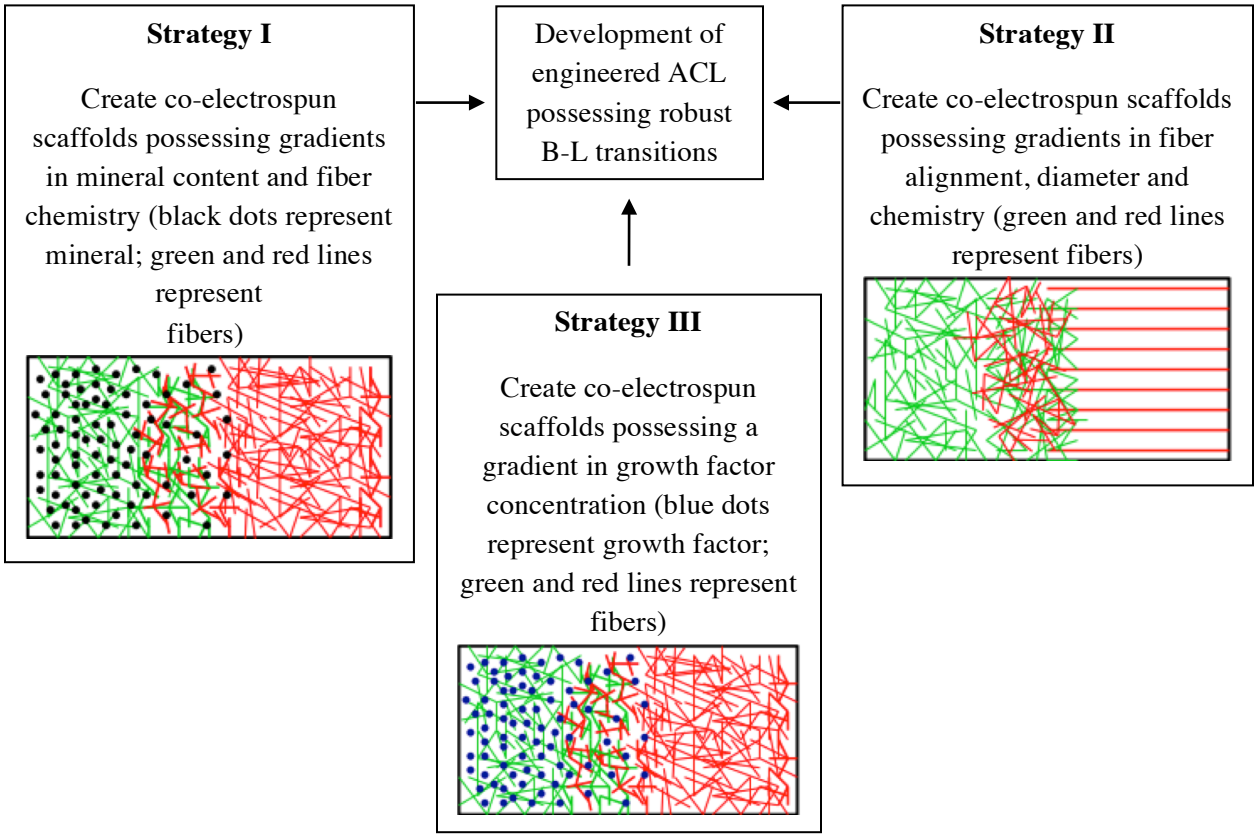

Figure 1.1: Scheme depicting three independent but complementary strategies for developing graded scaffolds to promote the regeneration of ACLs possessing robust B-L transitions.

1.2. Approach

The overall goal of this project is to build graded scaffolds that have the potential to regenerate B-L transitions *in vivo* in the long-term. As a step towards this larger goal, model scaffolds possessing gradients in architecture and mechano-chemical properties are created to independently control cell fates within spatially distinct zones. Herein, three complementary strategies are undertaken to fabricate scaffolds possessing gradients in 1) mineral content, 2) fiber orientation and 3) growth factor (GF) concentration (**Figure 1.1**). All three strategies involve electrospinning because this technique has the potential to create fairly complex scaffolds for engineering composite tissues [13-15].

1.3. Strategy I: Scaffolds possessing gradients in mineral content

The first strategy involves the incorporation of mineral gradient cues within co-electrospun scaffolds to guide the development of a gradient of an osteoblastic phenotype. Previous studies have demonstrated that a mineral phase (e.g., hydroxyapatite, tricalcium phosphate) not only supports the adhesion and proliferation of bone-like cells (osteoconduction), but also aids the differentiation of mesenchymal stem cells (MSCs) towards the osteoblastic lineage (osteoinduction) [16, 17]. Moreover, a gradient of mineral content exists at natural B-L transitions *in vivo*. Therefore, in Strategy I, scaffolds possessing gradients in mineral concentration are fabricated by co-electrospinning two polymers (one doped with a mineral phase) from offset spinnerets and subsequently treating these scaffolds with a simulated body fluid solution to enhance the gradient. These graded scaffolds are characterized thereafter, and evaluated for their ability to guide osteoblastic differentiation of MSCs in a spatially dependent manner.

1.4. Strategy II: Scaffolds possessing region-wise differences in fiber orientation

The second strategy involves the incorporation of topographical gradient cues within co-electrospun scaffolds to spatially guide cell morphology and alignment. Gradients in architecture exist at native B-L transitions: collagen fibers in soft tissues (e.g., ligament, tendon) are highly aligned, while those in bone are comparatively less ordered in their organization [18, 19]. Moreover, certain cell types – particularly those found in oriented tissues such as ligament – have been shown to align in response to aligned topographies [20-22] and also deposit oriented extra cellular matrix (ECM) through the phenomenon of contact guidance [23]. Furthermore, cells also respond to differences in fiber diameter [24]. Thus, in Strategy II, scaffolds possessing spatially distinct regions of aligned, randomly oriented and mixed fibers are fabricated by co-electrospinning two polymers from offset spinnerets onto a novel dual-drum collector. Here, the use of two polymers allows for the creation of region-wise differences in fiber chemistry and mechanical properties, in addition to differences in fiber alignment and diameter. Scaffolds thus fabricated are subsequently evaluated for their ability to influence the shape and alignment of MSCs, based on underlying fiber orientation and diameter.

1.5. Strategy III: Scaffolds possessing a gradient in GF concentration

The third strategy involves the incorporation of a GF gradient cue within co-electrospun scaffolds to result in a gradient of cell phenotype. GFs (e.g., bone morphogenic protein 2, fibroblastic growth factor-2) – incorporated and subsequently released from scaffolds – have been shown to stimulate the differentiation of MSCs towards specific phenotypes [25-27]. However, the delivery of GFs from electrospun scaffolds poses a challenge due to the harsh nature of processing conditions used in electrospinning [28-30]. In particular, the organic solvents and high voltage used for electrospinning can interfere with protein structure and consequently diminish GF activity. Therefore, in Strategy III, gelatin microspheres are used to protect and deliver GFs in active conformation from electrospun scaffolds. While the eventual goal of this strategy is to create scaffolds possessing a gradient in GF concentration, the immediate goal is to validate the delivery system using a model protein.

1.6. Dissertation layout

This dissertation comprises six chapters and three appendices. Chapter 2 is a review of the literature related to tissue engineering and the regeneration of tissue interfaces. Chapters 3 and 4 focus on Strategy I, and describe the fabrication of and *in vitro* response to co-electrospun scaffolds possessing gradients in mineral content. Chapter 5 addresses Strategy II and describes the development of co-electrospun scaffolds possessing gradients in fiber alignment, diameter and chemistry. Chapter 6 concerns Strategy III and describes a strategy to protect and deliver a model protein in active conformation from electrospun scaffolds. Chapter 7 summarizes the major findings from this project and also provides directions for future work with regard to developing graded scaffolds for engineering complex tissue transitions. Thereafter, three appendices are included. Appendix A is a review of the influence of the physical and chemical properties of calcium phosphate ceramics on cell adhesion and differentiation, appendix B is a study describing the fabrication of a mineral scaffold using an indirect fabrication technique for application in bone tissue engineering, and appendix C is a book chapter titled "Synthetic Biomaterials for Regenerative Medicine Applications" (to appear in "Solid Organ Transplantation in the Regenerative Medicine Era").

Chapter 2

A review of the literature

2.1. Biology of ligaments and their bony insertions

2.1.1. Ligament composition and organization

Ligaments are dense fibrous tissues whose primary roles are to provide mechanical stability to joints and prevent excessive stretching or torsion [31]. In general, ligaments exhibit strong structure-function relationships, which arise as a result of their hierarchical organization. Ligaments are composed of fibroblasts embedded within a dense extracellular matrix (ECM), consisting of proteins, cells and proteoglycans [32]. Fibroblasts, which make up roughly 20% of tissue volume, are responsible for the synthesis of ECM components and the maintenance of ligament function. These cells are spindle-shaped and aligned in the direction of ECM architecture. The ECM, composed of collagens, elastin, proteoglycans and glycoproteins, provides structural stability as well as functionality.

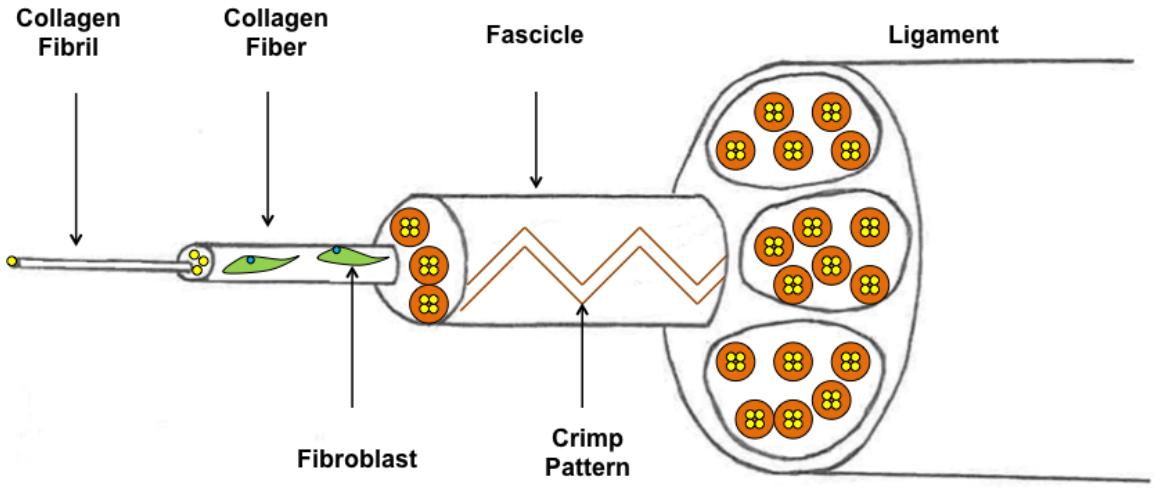

Figure 2.1: Cartoon of the hierarchical structure of ligaments (adapted from [33]).

The hierarchical structure of ligaments (**Figure 2.1**) arises from the organization of type I collagen fibers within the ECM [34]. The process of collagen fiber formation (fibrilogenesis)

begins with individual collagen molecules aggregating to form fibrils. Several fibrils bundle together to form collagen fibers. Groups of fibers are packed into large tube-like structures called fascicles, and two to three fascicles combine to make a ligament.

Other proteins in the ligament include type III collagen, type XII collagen and small quantities of elastin. (Non-fibrillar collagens such as types IV and VII are not found in ligaments.) Type III collagen is thought to control fibril diameter, while type XII collagen aids fibrilogenesis by providing temporary cross-links. The ratio of the amount of type I collagen to type III collagen in ligaments is typically around 8:1, in contrast to a ratio of more than 19:1 in tendons [12]. In addition, the ligament contains a variety of proteoglycans such as decorin and biglycan, which are thought to be important mediators of fibrillogenesis and fiber organization. Glycoproteins such as tenascin-C also regulate the formation and organization of fibers, contribute to the elasticity of ligaments and provide sites for binding of matrix proteins.

2.1.2. Ligament insertion into bone

At their origin and insertion, ligaments insert into bones via a fibrocartilage (FC) transition zone (**Figure 2.2**). This zone allows for a smooth transition in properties from ligament to bone [9]. The following sub-sections provide a brief overview of the chemical, biological and mechanical properties of the transition zone as well as bone.

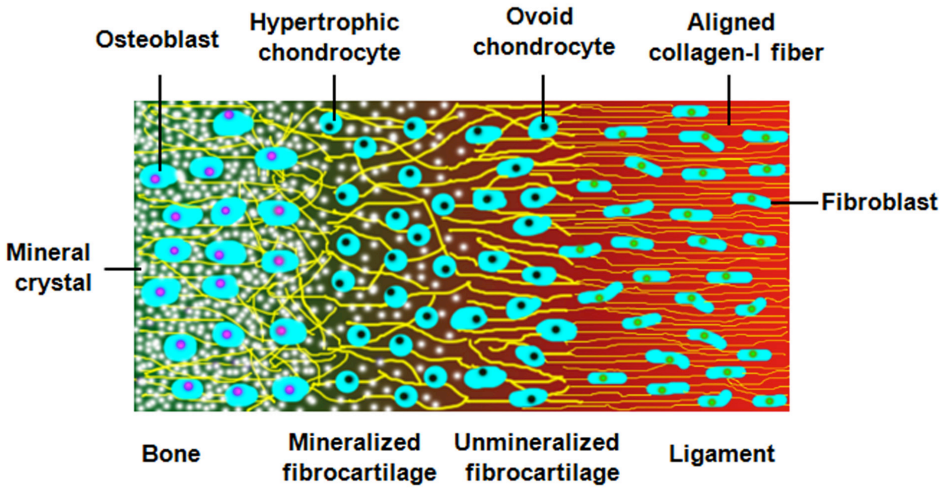

Figure 2.2: Cartoon of the bone-ligament transition depicting transitions in properties from soft tissue to stiff tissue via a fibrocartilage intermediate [35] (included with permission).

The FC zone appears to facilitate effective transfer of loads between the ligament and bone [9]. It is marked by a smooth transition in mechanical properties to minimize stress-concentrations at the interface between the soft (i.e., ligament) and hard (i.e., bone) tissues. The FC zone is further divided into the unmineralized and mineralized FC regions. The unmineralized region is vascularized, consists of ovoid-shaped chondrocyte cells, a mixture of type I and type II collagen fibers, and a variety of proteoglycans including aggrecan. The collagen fibers in this region are not necessarily aligned and are larger in diameter than those found in the ligament. The unmineralized FC region smoothly transitions into the mineralized FC region, which is characterized by the presence of circular and hypertrophic chondrocytes, type X collagen and mineral deposits [36]. Furthermore, the interface between mineralized FC and bone possesses several deep interdigitations [9], that are thought to increase resistance to shear and tensile forces, and provide a smooth mechanical transition.

Bone is a calcified tissue with a high degree of vascularity [37]. It is comprised of channels called osteons that house osteocytes within pockets known as lacunae. The anatomical structure of bone may be divided into two phases, namely cortical (compact), and trabecular (cancellous). Cortical bone forms the outer layers of bones and typically possesses low porosity (~5-10%) and superior mechanical properties (~1-4 GPa in tension) compared to trabecular bone (~75% porosity and ~0.4-1 GPa in tension) [37, 38].

The biochemical composition of calcified bone tissue can be subdivided into an inorganic and an organic matrix. The inorganic matrix is composed of a calcium phosphate mineral, frequently referred to as bone mineral, while the organic matrix consists of a wide array of proteins embedded in a dense ECM. Bone mineral is thought to consist of several different phases of calcium phosphates [39]. In relatively new bone (woven bone), the predominant phases are amorphous dicalcium phosphate dihydrate and amorphous calcium phosphate, while in mature bone (lamellar bone), the primary phase is a form of hydroxyapatite. The inorganic matrix is a major contributor towards the very high rigidity and strength of bone.

The organic matrix of bone is comprised of four different types of cells, namely osteoblasts, osteocytes, bone lining cells and osteoclasts [40]. Osteoblasts are bone-forming cells, which secrete several proteins that are embedded in the ECM and help in matrix

mineralization during the late stages of differentiation. Osteocytes are fully differentiated osteoblasts that are embedded in the mature mineralized matrix. Bone-lining cells – which line the surface of forming bone tissue – are thought to be osteoprogenitor cells, as well as being involved in regulating the activity of osteoclasts. Lastly, osteoclasts are multinucleated cells derived from the hematopoietic niche that are primarily involved in bone resorption. These four different cell types interact constantly to regulate bone homeostasis: the synchronized process of bone formation and resorption [41]. In addition to cells, the organic matrix consists of glycosylated ECM proteins, proteoglycans and a host of growth factors. The most abundantly found protein is type I collagen, which is present in the form of fibers. The mineralized collagen fibers confer strength in tension to bone. In addition to type I collagen, several other non-collagenous proteins such as osteocalcin, bone sialoprotein and osteopontin are also found in the ECM; these proteins are thought to be involved in regulating the nucleation, growth, size and orientation of mineral crystallites [42].

2.1.3. Anterior cruciate ligament (ACL)

The ACL is one of four major ligaments in the knee that connects the femur and the tibia (**Figure 2.3**). It stabilizes the knee by preventing the anterior translation of the tibia as well as excessive tibial rotation [2, 12]. The human ACL averages between 27 and 32 mm in length, 7 and 12 mm in width, and 45 and 57 mm^2 in cross-sectional area [43-45]. It originates from the posterior part of the medial surface of the lateral femoral condyle and inserts on the tibia in front of, and lateral to the anterior spine. The ACL consists of two distinct bundles: antereomedial and postereolateral [46]. Both bundles have distinct attachment points on the femur and tibia, and play important synergetic roles in permitting normal mechanical motion of the knee [47]. In addition, the two bundles are twisted around one another ~180° between the femoral and tibial attachment sites [48] to reduce compression and tension of the ACL during normal articulation of the knee.

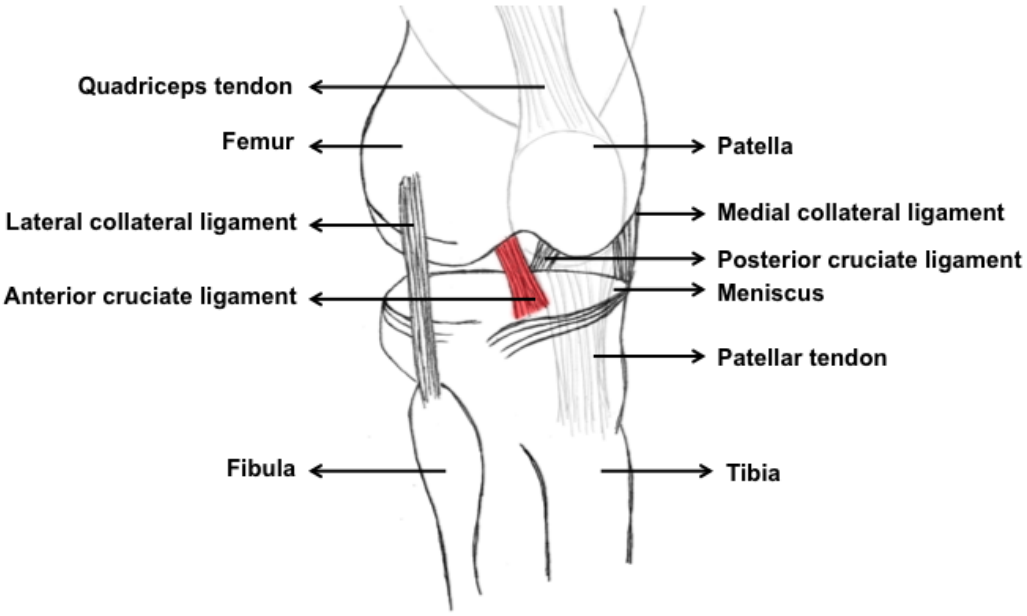

Figure 2.3: Anatomy of the human knee showing the four ligaments. Translucent overlay depicts the quadriceps tendon and the patellar tendon attached to the patella (knee cap). The overlay is moved away from its actual anatomical location to expose the ligaments.

The ACL is bathed in synovial fluid that in turn is housed in a synovial membrane within the knee joint [49]. The synovial fluid provides lubrication to the joint. Due to its location within an intra-articular environment, the ACL is neither extensively vascularized nor highly innervated. The proximal part of the ACL receives its blood supply from the middle genicular artery, while the distal portion receives its blood supply from branches of the lateral and medial inferior geniculate artery [50]. The primary innervation to the ACL arises from the tibial nerve.

A typical stress-strain curve for an ACL under tensile strain is marked by three regions [48] (**Figure 2.4**). Loading begins with a toe-in region, which corresponds to uncrimping of crimp patterns (zig-zag repeating patterns in collagen fibrils that allow ligaments to increase in length under low strains without stretching the collagen molecules) and the expulsion of water. This region, typically between 1 and 3% strain, is followed by a linear region (typically between ~3% and ~7% strain), which corresponds to stretching of the collagen fibers. Upon further loading, the linear region is followed by a yield region (between ~8% and ~16%), where permanent deformation and rupture (defibrillation) of collagen fibers occurs, after which the ligament fails.

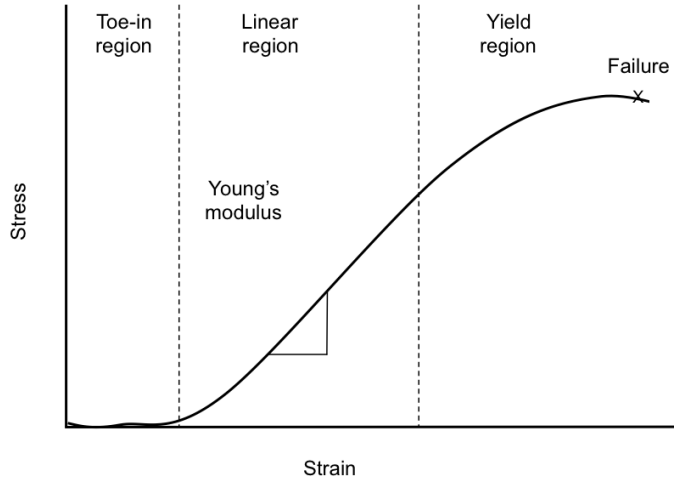

Figure 2.4: Representative stress-strain curve for a ligament.

The hierarchy in the ECM organization (in particular, the parallel bundles of collagen) as well as the covalent cross-links between collagen fibers are chiefly responsible for the mechanical properties of ligament. More specifically, the ACL possesses a Young's modulus of around 111 MPa [51, 52]. While the ultimate tensile strength of ACL in healthy adults is 2000 N, the peak tensile force that the ACL experiences during routine activities is much lower, typically between 100 and 400 N [53]. Such activities also result in a peak strain of around 4%, whereas the ligament can withstand strains upto 18% before complete failure [53, 54].

2.2. ACL ruptures and current treatment options

2.2.1. Clinical problem

The ACL is very often injured during torsion, hyperextension or distortion of the knee during routine movement or while playing a sport [2, 12, 55, 56]. Moreover, patients sustaining ACL ruptures suffer a 78% risk of radiographic osteoarthritis within 14 years of injury [57]. Due to its location within the intra-articular space in the synovial fluid as well as limited blood supply and low cellularity, injuries to the ACL do not heal readily (unlike injuries to the medial collateral ligament) [4, 58, 59]. While the fibroblasts in the ACL have been observed to proliferate and produce collagen following a rupture, the collagen fascicles do not spontaneously reconnect. Further, non-surgical treatments for ACL ruptures are largely unsuccessful in

restoring full functionality [60]. Therefore, surgical intervention is strongly recommended to restore knee stability following ACL rupture [5].

2.2.2. Current surgical options for the treatment of ACL ruptures

Surgical replacement of ruptured ACLs with grafts is generally performed via arthroscopy using a three-stage process [4, 61, 62]. In the first stage, the torn ligament is excised and damage to the menisci, cartilage and other ligaments is evaluated. In the second stage, a tunnel is drilled into the tibia, followed by another tunnel within the femur. In the third stage, an ACL graft is passed through the bone tunnels and anchored firmly first within the femoral tunnel, and then within the tibial tunnel using interference screws. Post-surgery, the early stages of host response within the bone tunnels includes the formation of a hematoma, activation of inflammatory cells, migration of mesenchymal stem cells, adhesion of osteoblast to the graft surface and the deposition of non-collagenous proteins [63]. Thereafter, osteoblasts secrete a collagenous matrix following which the matrix is mineralized. Osteogenesis is accompanied by vascularization and woven bone is slowly replaced by lamellar bone over time. Osseointegration of grafts within bone tunnels can occur over several months.

Current grafting options to replace ruptured ACLs include autografts, allografts and synthetic grafts [3, 5]. Each of these grafts has unique merits and limitations, which are discussed further.

Autografts – typically the hamstring or patellar tendon – are considered the current gold standard for ACL reconstruction. While they possess the appropriate mechanical properties for ACL repair and present little to no risk of immune rejection, they compromise the mechanical properties at the donor site and risk morbidity [3, 31]. Patients who undergo a patellar tendon-based ACL reconstruction experience discomfort as well as an inability to kneel and/or knee-walk [64]. Further, significant clinical, radiographic and histological abnormalities persist at the donor site post-surgery. Moreover, the hamstring tendon may result in greater bone tunnel expansion than the patellar tendon [65], while the bone-patellar tendon-bone (B-PT-B) autograft has been shown to result in excessive tibial rotation two years post-surgery [11].

Allografts – derived from cadavers (or from a younger patient to be used in an older patient) – overcome the limitations of autografts in that they do not risk donor site morbidity or compromise mechanical properties [12]. However, allografts suffer from an increased risk of host rejection and disease transmission. Moreover, sterilization and storage procedures can affect graft properties and their applicability. For example, ethylene oxide sterilization of grafts can potentially cause intra-articular reactions after implantation, while gamma irradiation and freeze-drying can negatively affect the mechanical and biochemical properties of the grafts [66, 67].

Synthetic materials for ACL replacement overcome the limitations presented by autografts and allografts [5]. Early synthetic replacements such as Leeds-Keio (poly (ethylene terephthalate)-based), Gore-Tex (poly (tetrafluoroethylene)-based) and Stryker (poly (ethylene terephthalate)-poly (propylene)-based) were stiff and provided sufficient structural support during the initial stages following ACL reconstruction [58]. Subsequently, second-generation synthetic replacements such as the Kennedy Ligament Augmentation Device were designed to improve graft integration with host tissue. Although such synthetic replacements have generally resulted in positive outcomes in the short-term, many of them suffer from immunological response, recurrent knee instability and failure from excessive creep in the long-term [68]. Thus, these materials are currently not FDA-approved for primary ACL reconstruction, although some of them are conditionally approved for testing purposes. More recently, poly (ethylene terephthalate)-based replacements, called the Ligament Advanced Reinforcement System have been shown to allow tissue in-growth and function similar to traditional autografts in the long-term [69].

2.2.3. Engineered grafts

While current grafting options for the repair of ACL ruptures suffer from several limitations, an engineered graft that promotes the regeneration of tissue presents an attractive alternative [58]. Engineered grafts can potentially overcome limitations such as donor site morbidity and risk of disease transmission commonly found in autografts and allografts respectively. For ligament regeneration, such grafts must possess certain important properties. They must be biocompatible, biodegradable and possess mechanical properties similar to native

ACL [2]. Further, they must allow for cell infiltration and tissue remodeling during degradation, without resulting in a significant loss of mechanical strength. The following section describes strategies for creating engineered grafts, with a special focus on ligament tissue engineering.

2.3. Tissue Engineering

2.3.1. General strategy

A tissue engineering strategy typically involves four components: biomaterial scaffolds, cells, biochemical cues and bioreactors. The general tissue engineering paradigm is that a functional tissue can be formed by combining a biomaterial scaffold incorporating biochemical factors with stem cells, and conditioning these constructs within a bioreactor to mechanically stimulate cells and induce the secretion of tissue-specific ECM [70] (**Figure 2.5**). Within this framework, biomaterial scaffolds play a vital role in providing a conducive and instructive microenvironment for tissue regeneration. Over the years, scaffolds have evolved from being simple supporting constructs (first generation) to constructs that present biological cues to promote cell adhesion and proliferation (second generation) to constructs that actively present/deliver biochemical signals (e.g., growth actors (GFs)) that promote cell differentiation and tissue morphogenesis (third generation) [12]. Tissue-engineered grafts may also be conditioned in bioreactors prior to implantation to further promote stem cell commitment and aid the organization of cell-secreted ECM. In the following subsections, three critical components of the tissue engineering paradigm viz., biomaterial scaffolds, cells and GFs are discussed in detail.

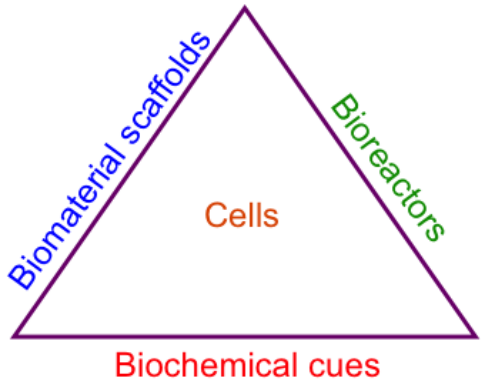

Figure 2.5: Tissue engineering paradigm.

2.3.2. Biomaterials for ligament regeneration

Biocompatible materials can broadly be classified into two categories: natural and synthetic. Natural materials are bio-inspired and possess a number of advantages including biocompatibility, biological activity and enzymatic degradability [71]. However, they are not amenable to certain processing conditions (e.g., harsh solvents or high temperatures) as they can be easily denatured. In contrast, synthetic materials can be processed into a wide variety of 3-dimensional scaffolds. In addition, their properties can be tailored for the materials to degrade over time. (A detailed description of the properties of synthetic biomaterials used for tissue engineering can be found in appendix C of this dissertation.)

Several types of materials, both natural and synthetic, have been investigated for the regeneration of ligament tissue. Natural materials such as collagen, silk, alginate and hyaluronan have been successfully processed into scaffolds and tested for their potential in ligament/tendon tissue engineering [72-75]. Among these materials, collagen and silk degrade enzymatically albeit slowly [76]. Slow degradation can potentially interfere with *in vivo* regenerative mechanisms, although the rate of degradation can be increased by reducing the molecular weight of the polymer as well as its cross-linking. Furthermore, these materials – though possessing high strengths – are limited by their elasticity for use in ACL regeneration.

Synthetic materials such as poly-caprolactone (PCL), poly-lactide-co-glycolide (PLGA), Teflon and Dacron have also been investigated for ACL regeneration [5, 71, 77]. While these polymers exhibit high strengths and moduli, they possess poor elastic properties and can easily deform plastically. In contrast, elastic materials may be more suitable for the regeneration of the ACL. In this regard, several types of polyurethanes (PUs) have been explored as potential materials for the regeneration of ligaments [78]. Segmented PUs are synthesized using a soft segment (e.g., PCL or PLGA) and a hard segment (e.g., putrescine, PDAB). PUs can deform elastically to large strains and also undergo repeated cycles of strain with little to no creep. These properties make PUs suitable materials for ligament tissue engineering. However, one shortcoming with processed PUs scaffolds is their low modulus, compared to the human ACL [51, 79].

2.3.3. Biomaterial scaffolds

Biomaterials scaffolds for ligament tissue engineering must possess certain key properties [73]. Firstly, they must support cell adhesion and tissue growth. Secondly, they must be biocompatible and not elicit an adverse immune response when implanted. Thirdly, they must be porous to permit cell infiltration [73]. Fourthly, they must have sufficient mechanical strength to withstand physiological forces *in vivo* as neo-tissue forms [5]. Lastly, the scaffold must degrade (hydrolytically or enzymatically) over time to the permit regeneration of functional ligament [2, 73].

2.3.3.1. Classic fibrous scaffolds

Fibrous scaffolds are ideally suited for ligament tissue engineering as they mimic the ECM organization of connective tissues and are also strong in tension [13]. Several studies have reported the fabrication of yarns, braids and woven scaffolds for ligament tissue engineering. For example, Altman et al described a wire-rope (twisted yarn) scaffold design for the fabrication of silk-fiber matrices [74]. These scaffolds were designed to mimic the complex hierarchy of ACLs and were shown to possess stress-strain behavior and mechanical properties similar to those of native human ACLs. Cooper et al reported the fabrication of 3-dimensional braided scaffolds, composed of fibers, which were arranged into bundles and wound throughout the thickness of the scaffold [3]. Ge et al created knitted scaffolds fabricated from poly (L-lactide) (PLLA) and showed that they possess properties suitable for ACL reconstruction [80]. Although such scaffolds have been shown to be useful in ligament tissue engineering, potential limitations with knitted and braided scaffolds are poor cell retention upon seeding (often requiring the use of a gel-based system) and low porosity (that prevents cell infiltration) respectively [81, 82]. Moreover, the creation of complex architectures and scaffold functionalization are difficult to achieve with classic techniques such as knitting and braiding.

2.3.3.2. Electrospun scaffolds

Electrospinning has been widely used in tissue engineering because of its ability to create complex non-woven scaffolds [13, 83]. Moreover, electrospinning is cost-effective, easy to set up and offers flexibility in tuning scaffold properties both *in situ* and post-fabrication [13].

Generally, electrospinning involves the ejection of one or more streams from a viscous polymeric solution by means of an electric potential. A combination of high solvent volatility and electrostatic repulsion causes the stream to condense and be drawn into a fiber (typically 100 nm - 5 μm in diameter) (**Figure 2.6**). The fibers are collected on a rounded target in the form of non-woven fused structures, commonly referred to as meshes. Several process parameters such as solution concentration, flow rate, potential, throw distance (distance from the tip of the nozzle to the collector) and ambient conditions have been shown to affect the properties of fibers [13, 83, 84]. In addition, the lower end of the size range for electrospun fibers is of the same order of dimension as collagen fibers (150 nm) found in the ACL [73], and may thus provide topographical features that cells can recognize. In particular, aligned fibers can help guide alignment in adherent cells via contact guidance [24].

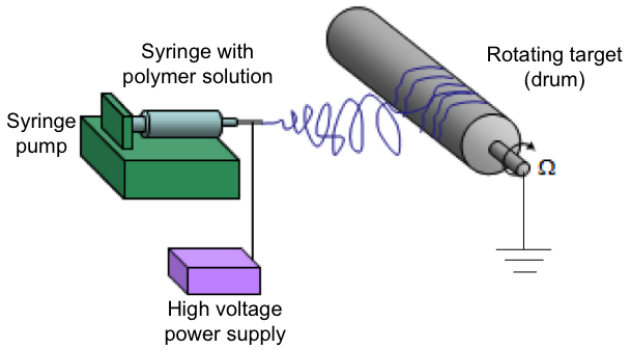

Figure 2.6: A typical electrospinning apparatus.

Electrospun meshes can be fabricated from a wide variety of synthetic and natural polymers. Synthetic polymers are potentially more amenable to processing via electrospinning because the rigid molecular chains in natural polymers such as alginate prevent effective chain entanglements in solution [85]. PCL [86], PLLA [87, 88] and PLGA [89] and various PUs [24] have all been electrospun and tested in various tissue engineering applications. In contrast, naturally derived polymers such as collagen [90, 91], elastin [92], gelatin [93, 94], silk [95, 96], alginate [97, 98] and chitosan [99] are usually blended with synthetic polymers (e.g., PCL [100], poly (ethylene oxide) (PEO) [101]) prior to electrospinning.

In recent years, the electrospinning technique has been modified considerably to meet the demand for fabricating scaffolds possessing complex architectures. Three of these modifications include a) new nozzle configurations, b) novel collector geometries and c) the introduction of multiple spinnerets.

a) Nozzle configuration: In its simplest configuration, electrospinning involves a single nozzle that delivers a polymer to form a nano-fibrous network [90, 102]. A more complicated set-up involves the use of two nozzles present side-by-side that deliver two polymer solutions simultaneously, resulting in dissimilar fibers wrapped around each other [103]. Alternatively, co-axial electrospinning employs a nozzle-within-a-nozzle configuration to deliver fibers possessing a core-sheath structure (**Figure 2.7**). This technique has been used to encapsulate proteins within electrospun scaffolds for controlled release applications [104, 105]. However, co-axial electrospinning requires the use of an expensive and elaborate apparatus [28].

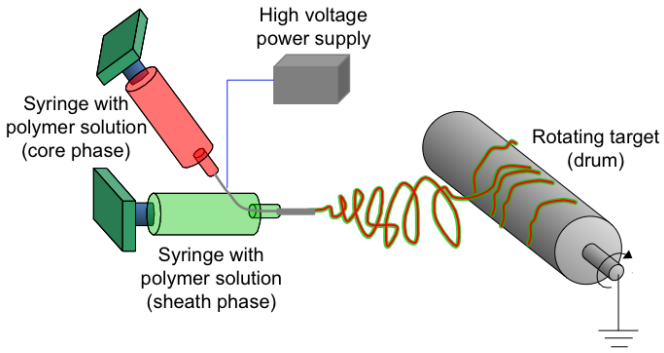

Figure 2.7: Co-axial electrospinning set-up depicting the nozzle-within-nozzle configuration, resulting in fibers that possess a core-sheath structure.

b) Collector geometry: In addition to the use of modified nozzle configurations, electrospinning has also been performed on a number of collectors possessing a wide range of geometries. The use of novel collector geometries permits the creation of meshes possessing architectures that can mimic the ECM organization of a range of tissue types. For example, scaffolds have been fabricated on a flat plate collector [106], a rotating drum [24] and between two rods [107]. Meshes created on fast-rotating collectors have been shown to consist of highly aligned fibers, ideally suited for the regeneration of an anisotropic soft tissues such as ligament [108]. Meshes possessing highly aligned fibers can also be fabricated by electrospinning

between two grounded rods [107]. (A schematic of obtaining aligned fibers by electrospinning between two flat plate collectors is presented in **Figure 2.8**.)

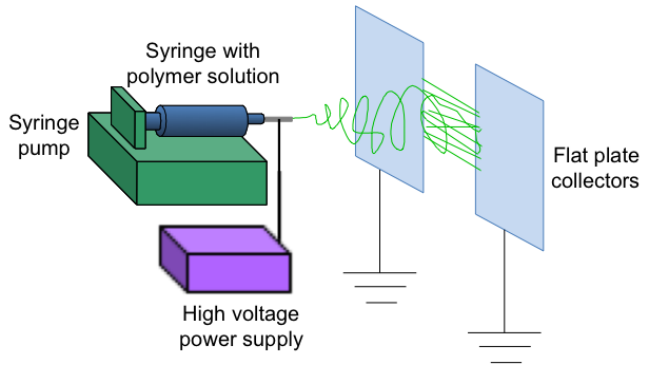

Figure 2.8: Electrospinning between two flat plates yields a region of highly aligned fibers in the gap region between the plates.

c) Multiple spinnerets: In recent years, simultaneous electrospinning from two or more spinnerets (known as co-electrospinning) has been studied due to the increased level of flexibility it offers in creating scaffolds possessing hybrid properties. For example, Baker et al. created a porosity gradient by co-electrospinning PCL and PEO from offset spinnerets and subsequently leaching out the water-soluble PEO nano-fibers [15]. In another study, Li et al. created blends of natural and synthetic polymeric scaffolds by co-electrospinning solutions of gelatin, elastin and PLGA in two different ratios from separate spinnerets [109]. Co-electrospinning can also be used to fabricate graded scaffolds for the regeneration of orthopedic interfaces, as demonstrated in a recent study by Ladd et al [14]. Here the authors co-electrospun PCL-collagen and PLLA-collagen from offset spinnerets onto a grounded rotating collector to result in scaffolds possessing gradients in fiber chemistry and mechanical properties for engineering muscle-tendon junctions.

2.3.4. Cells: the central component of the tissue engineering paradigm

Within the general tissue engineering paradigm (**Figure 2.5**), the purpose of cells is to jump-start healing *in vivo* by forming tissue-like surfaces within and around the biomaterial scaffold. To be suitable for ligament tissue engineering, cells must have sufficient capacity for proliferation, develop into a ligamentous tissue phenotype in response to external stimuli, be able to deposit ligament-specific ECM (e.g., type I collagen, type III collagen, tenascin-C and

biglycan [12]) and not induce an adverse immune response *in vivo*. Two classes of cells have clinical potential for achieving a functional engineered ligament: terminally differentiated primary cells and adult stem cells.

Terminally differentiated primary cells derived from a variety of sources (e.g., ACL, patellar tendon, MCL) are potential candidates for ligament tissue engineering [58]. Primary fibroblasts have been shown to function well because they produce ligament-specific ECM [110]. However, they proliferate slowly in culture and may thus not be amenable to sufficient expansion in culture [32]. Moreover, they appear to exhibit differences in their proliferative and differentiation capacities based on source [58].

Adult stem cells are also promising candidates for use in tissue engineering [111, 112]. They are highly proliferative (which means that a only a small biopsy explant is required), and they have the capacity to differentiate into a large number of phenotypes. Commonly used types of adult stem cells include bone marrow stromal cells (BMSCs) and adipose derived stem cells. Specifically, BMSCs have been reported to have the potential for regenerating several tissue types because of their ability to differentiate into a variety of lineages, including bone, cartilage, ligament, fat and muscle [112, 113]. However, this property may in itself be disadvantageous to ligament tissue engineering, as precise control of differentiation is a challenge.

Based on previous reports in the literature, BMSCs appear to outperform fibroblasts for potential application in ligament tissue engineering. For example, in a study that compared goat BMSCs, ACL fibroblasts and skin fibroblasts, BMSCs exhibited the highest DNA content and collagen production, although all cell types synthesized ECM rich in type I collagen [114]. In another study that compared rabbit BMSCs to ACL fibroblasts seeded on silk scaffolds, BMSCs were found to proliferate faster than fibroblasts [115]. Furthermore, the expression of type I collagen, type III collagen and tenasicn-C mRNA by BMSCs was elevated after two weeks of culture, while mRNA expression by fibroblasts remained the same. In summary, adult stem cells (and BMSCs in particular) have great potential for ligament tissue engineering applications.

2.3.5. Growth factors (GFs)

In the tissue engineering paradigm (**Figure 2.5**), biochemical cues are incorporated within scaffolds to direct cell fate and guide tissue formation. In this regard, GFs are attractive biochemical cues for stimulating cell proliferation and differentiation. They are cytokines that get sequestered in the ECM and interact with adhesive molecules and proteoglycans to trigger a wide variety of signaling pathways [116]. Once secreted by cells, GFs influence cell behavior by binding to specific trans-membrane receptors on the target cells.

Several biochemical events such as protein phosphorylation, changes in ion fluxes and metabolism and gene expression occur as a result of GF binding [117]. Consequently, GFs affect a variety of cell functions such as protein expression, ECM synthesis, cell proliferation and differentiation [116, 118]. Due to their specific ability to induce differentiation in undifferentiated or progenitor cells, GFs have been extensively used in tissue engineering applications [116]. For ligament tissue engineering in particular, insulin-like growth factor-1 (IGF-1), transforming growth factor-β1 (TGF-β1), vascular endothelial growth factor, platelet-derived growth factor (PDGF), fibroblastic growth factor-2, growth and differentiation factor-5, epidermal growth factor and insulin-like growth factor-2 (IGF-2) have all been used for directing BMSCs to differentiate towards the ligament lineage and secrete ligament-like ECM [118-121].

2.4. Interfacial tissue engineering

While the previous section described the general tissue engineering paradigm, more specific strategies are required to engineer complex tissues such as those found at transitions between two or more tissues. Interfacial tissue engineering (ITE) aims to regenerate tissue transitions using composite scaffolds and multiple cell types [122]. In particular, ITE involves the use of graded scaffolds that recapitulate gradients in mechanical and biochemical properties found at natural tissue transitions. Such graded scaffolds, in conjunction with one or more cell types, can potentially guide the formation of mechanically robust spatial gradients of cell phenotype and ECM composition [6, 9].

2.4.1. Medical need for a transition tissue

A serious concern with current ACL grafts is laxity failure arising from poor graft integration with host bone at the femoral and tibial fixation sites [6, 10]. As described in **Section 2.1.2**, the natural ligament insertion into bone is marked by an FC transition zone that efficiently transfers loads without the development of stress concentrations. However, the absence of this transition zone can result in a mismatch of properties between graft and host bone, leading to stress-concentrations at the graft-bone interface and eventual graft failure [123]. In this regard, engineered grafts modeled after B-PT-B grafts (which preserve bone-ligament (B-L) transitions) may help in ligament regeneration as well as osseointegration.

2.4.2. Current strategies to regenerate orthopedic tissue transitions

Current strategies to regenerate orthopedic tissue transitions (e.g., B-L, muscle-tendon, osteo-chondral) aim at guiding the formation of phenotypic gradients in stem cells. The establishment of gradients in cell phenotype, and consequently ECM composition and architecture, can potentially promote the regeneration of tissue transitions in the long-term. Towards this end, several studies have described the fabrication of scaffolds possessing gradient properties that broadly fall under three categories: a) mineral gradients, b) architecture gradients and c) GF gradients. Each of these categories is discussed further.

2.4.2.1. Mineral gradients

Since natural bone tissue is composed of a form of apatite (a type of calcium phosphate) [124], the incorporation of a calcium phosphate mineral phase within scaffolds can provide an osteoconductive micro-environment that cells may recognize [125]. Moreover, mineral has been shown to support the attachment and growth of bone cells, as well as potentially guide cell differentiation towards the osteoblastic lineage [16, 126-128]. (An exhaustive analysis of the osteoconductive/osteoinductive properties of different types of calcium phosphate ceramics is provided in appendix A of this dissertation.) Consequently, it is anticipated that a mineral gradient can promote the formation of a gradient in cell phenotype intended for regenerating orthopaedic interfaces. A few studies have recently investigated the fabrication of scaffolds possessing mineral gradients by incorporating mineral either during or after the scaffold

fabrication step. For example, Erisken et al and Ozkan et al used a twin-screw extrusion device to deliver different amounts of polymer and hydroxyapatite to result in a gradient of mineral content within the scaffold [129, 130], while Singh et al introduced $CaCO_3/TiO_2$ nano-particles into 3-dimensional PLGA microsphere scaffolds in a graded manner [131]. Li et al formed mineral gradients by exposing various sections of a scaffold to a 5× simulated body fluid solution for different time-periods [132]. Though not directly involving the use of a calcium phosphate mineral, Spalazzi et al fabricated tri-phasic scaffolds using PLGA and bioactive glass for the regeneration of B-L transitions [133, 134]. In summary, these studies suggest that the incorporation of mineral gradients within scaffolds may help engineer orthopedic tissue transitions.

2.4.2.2. Architecture gradients

Gradients in ECM architecture exist at natural B-L and tendon-bone transitions. The collagen fibers found in anisotropic tissues such as ligament and tendons are highly aligned, compared to the fibers found in bone [18]. Scaffolds that possess gradients in fiber orientation can mimic *in vivo* gradients in fiber architecture and thus guide the formation of gradients in cell shape, orientation and potentially phenotype. In this regard, Cooper et al reported the fabrication of braided scaffolds possessing regions with different fiber orientations [3]. These scaffolds comprised bony attachment ends possessing fibers at high braiding angles and an intra-articular zone possessing fibers at low braiding angles. Differences in fiber orientation were also shown to change pore size between the intra-articular zone and the bony attachment ends. Recently, Thomopolous et al have reported the fabrication of graded scaffolds by electrospinning between two metal frames [19]. This process was shown to result in the electrospun fibers aligning between the two frames, while simultaneously depositing randomly on the frames. Finally, Xie et al have reported the fabrication of graded scaffolds using a two-step electrospinning process [135]. Highly aligned fibers were obtained by electrospinning onto an air-gap collector in the first step, followed by electrospinning a layer of randomly oriented fibers atop the aligned fibers (in a spatially controlled manner) in the second step. In the studies by Thomopoulos et al and Xie et al, cells were found to respond positively to the differences in the orientation of underlying electrospun fibers, suggesting that scaffolds possessing gradients in fiber orientation can be used to spatially control cell shape and potentially cell phenotype in the long-term.

2.4.2.3. Growth factor gradients

Although GFs have been widely used for promoting cell differentiation, only a few studies have reported the fabrication of scaffolds possessing GF gradients for the regeneration of orthopedic tissue transitions. Recently, Dormer et al reported the use of bone morphogenic protein-2 (BMP-2)- and TGF-β1-loaded PLGA microspheres to result in scaffolds possessing opposing gradients of GF signals [26]. In follow-up studies, they demonstrated that these graded scaffolds had the potential to aid the regeneration of an osteochondral interface in an *in vivo* model [136, 137]. Similarly, Wang et al have also used dual gradients of BMP-2 and IGF-1 within silk microsphere-based scaffolds to engineer the osteochondral interface [138]. Though not directly involving a GF gradient, Phillips et al demonstrated zonal organization of osteoblastic and fibroblastic phenotypes by seeding fibroblasts onto scaffolds containing a spatial distribution of a retrovirus encoding the osteogenic transcription factor Runx2/Cbfa1 [139]. In summary, the results from these studies suggest that the incorporation of GF gradients into scaffolds may be a beneficial strategy to engineer tissue transitions.

2.5. Conclusion

Towards the long-term goal of regenerating B-L transitions and improving the osseointegration of ACL grafts, this project aims to create scaffolds possessing gradients in mechanical and biochemical properties. The fabrication of scaffolds possessing gradients in mineral content is described in chapter 3, while cell response to these gradient cues is described in chapter 4. Chapter 5 describes the development of scaffolds possessing region-wise differences in fiber alignment, while chapter 6 describes a novel technique to protect and deliver GFs in an active form from electrospun scaffolds. The technique developed in chapter 6 will be used in future studies to create scaffolds possessing gradients in GF concentration.

Reprinted from S Samavedi et al, Acta Biomaterialia, 7(2011), pp. 4131-4138: included with permission from Elsevier Science

Chapter 3

Fabrication of a model continuously graded co-electrospun mesh for regeneration of the ligament-bone interface

Satyavrata Samavedi[a], C. Olsen Horton[a], Scott A. Guelcher[b], Aaron S. Goldstein[a,c], Abby R. Whittington[a,d*]

[a] Department of Chemical Engineering, Virginia Polytechnic Institute and State University, Blacksburg, VA 24061, USA

[b] Department of Chemical and Biomolecular Engineering, Vanderbilt University, Nashville, TN 37235, USA

[c] School of Biomedical Engineering and Sciences, Virginia Polytechnic Institute and State University, Blacksburg, VA 24061, USA

[d] Department of Materials Science and Engineering, Virginia Polytechnic Institute and State University, Blacksburg, VA 24061, USA

3.1. Abstract

Current scaffolds for the regeneration of anterior cruciate ligament injuries are unable to capture intricate mechanical and chemical gradients present in the natural ligament-bone interface. As a result, stress concentrations can develop at the scaffold-bone interface, leading to poor osseointegration. Hence, scaffolds that possess appropriate mechano-chemical gradients would help establish normal loading properties at the interface, while promoting scaffold integration with bone. With the long-term goal of investigating regeneration of the ligament-bone interface, this feasibility study aimed to fabricate a continuously graded mesh. Specifically, graded meshes were fabricated by co-electrospinning nano-hydroxyapatite/polycaprolactone (nHAP-PCL) and poly-(ester urethane) urea elastomer solutions from offset spinnerets. Next, mineral crystallites were selectively deposited on the nHAP-PCL fibers by treatment with a

5×simulated body fluid (5×SBF). X-ray diffraction and energy dispersive spectroscopy indicated calcium deficient hydroxyapatite-like mineral crystallites with an average Ca/P ratio of 1.48. Tensile testing demonstrated the presence of a mechanical gradient, which became more pronounced upon treatment with 5×SBF. Finally, biocompatibility of the graded meshes was verified using an MC3T3-E1 osteoprogenitor cell line. The study demonstrates that graded meshes, for potential application in interfacial tissue engineering, can be fabricated by co-electrospinning.

Keywords: ligament-bone interface, graded mesh, electrospinning, simulated body fluid, mineralization

3.2. Introduction

Despite significant advances in tissue engineering for the repair of anterior cruciate ligament (ACL) tears and ruptures [2, 31], a concern with current regeneration strategies is poor integration of the engineered ligament with bone [6, 7]. Weak osseointegration of scaffolds stems from the presence of sharp gradients in mechanical, chemical and biological properties at the natural ligament-bone interface [9, 10]. Homogenous scaffolds do not capture the intricate gradients from soft unmineralized tissue to hard mineralized tissue found at bony insertion sites and rely on post-operative healing to generate these gradients. Therefore, a scaffold that possesses gradients in mechanical properties and chemical composition is anticipated to integrate better with bone and help regenerate the interfacial tissue.

Graded scaffolds that mimic the ligament to bone transition have been the subject of recent efforts. Cooper et al. [3] designed a 3-D fiber-based woven scaffold consisting of a femoral attachment region, a ligament region and a tibial attachment region. The scaffold possessed gradients in porosity, pore size and fiber orientation along its length to promote good integration with the femoral and tibial tunnels. Spalazzi et al. fabricated triphasic scaffolds using poly (lactide-co-glycolide) (PLGA) and bioactive glass for the regeneration of the ligament to bone transition [133, 134]. The biodegradable polymer component was employed to help support cell attachment and proliferation, while the bioactive glass was used for its

osteoinductive property. While these and previous efforts have produced graded scaffolds by combining multiple phases into a composite, the fabrication of continuously graded scaffolds with appropriate geometry and chemistry has not been achieved. The choice of scaffolding technique in particular will play an important role in determining scaffold geometry and morphology, which in turn may have a significant impact on tissue regeneration.

Among the various scaffolding techniques available, electrospinning has been widely used chiefly because of its ability to create fairly complex non-woven meshes [13, 83]. Specifically, it has great potential for developing engineered ligament tissue, as aligned fibers in the meshes can provide appropriate cues to cells through contact guidance [24]. Electrospinning from two or more spinnerets, known as co-electrospinning, has been studied in recent years due to the increased level of flexibility it offers in creating meshes with complex geometries and hybrid properties. For example, Baker et al. created a porosity gradient by co-electrospinning poly (ε-caprolactone) (PCL) and poly (ethylene oxide) (PEO) from offset spinnerets and subsequently leaching out the water-soluble PEO nano-fibers [15]. In another study, Li et al. created blends of natural and synthetic polymeric scaffolds by co-electrospinning solutions of gelatin, elastin and PLGA in two different ratios from separate spinnerets [109]. Co-electrospinning can also be used to fabricate continuously graded scaffolds for the regeneration of orthopaedic interfaces. In a recent study, Ladd et al. co-electrospun polymers from offset spinnerets to create a mechanical gradient for engineering the muscle-tendon junction [14]. This approach has the advantage of controlling scaffold chemistry by using polymers with different chemical properties to create spatial gradients in chemistry. Further, the selective incorporation of mineral into one set of fibers to create a mineral gradient may aid the regeneration of the ligament-bone interface.

A few strategies have been employed for the fabrication of mineral gradients towards regeneration of orthopaedic interfaces. Such methods have involved the use of a twin-screw extrusion device to deliver different amounts of polymer and hydroxyapatite [129, 130] and the inclusion of $CaCO_3/TiO_2$ nano-particles into 3-D PLGA microsphere scaffolds [131]. Another approach for incorporating a mineral gradient is the immersion of scaffolds in a simulated body fluid (SBF) [132]. SBF is a supersaturated solution that deposits hydroxyapatite-like mineral on various surfaces [140]. Studies in the literature have reported that the use of higher

concentrations such as 5×SBF and 10×SBF increases the rates of mineralization [141-144]. Higher concentrations also result in the incorporation of impurities in the mineral due to cationic substitutions for calcium. However, the presence of minor amounts of impurity may improve solubility and bioactivity of the mineral in the context of bone tissue formation. Previously, a mineral gradient has been formed by exposing various sections of a scaffold to a 5×SBF solution for different time-periods [132]. However, an approach that exploits the surface chemistry of different polymers to nucleate and grow different amounts of mineral from SBF solutions is intrinsically simpler and may result in better reproducibility.

The aim of this study was to fabricate meshes possessing model mechanical and mineral gradients that could be used to study regeneration of the ligament-bone interface. PCL and a custom-made poly-(ester urethane) urea elastomer (PEUUR2000) were employed to create meshes that could potentially help in the integration of the scaffold with bone and ligament tissues, respectively. PCL was doped with nano-hydroxyapatite particles (nHAP) and co-electrospun with PEUUR2000 from offset spinnerets to form graded meshes. To create mineral gradients, meshes were treated with a 5×SBF solution that selectively deposited crystallites of hydroxyapatite-like mineral on nHAP-PCL fibers. Mineral composition, water contact angles and mechanical properties of different regions of the meshes were measured to characterize the gradient properties and mammalian cell culture was performed to confirm cell metabolic activity.

3.3. Materials and methods

3.3.1. Materials

All chemicals and laboratory supplies were purchased from Fisher Scientific (Pittsburgh, PA) and biological supplies from Invitrogen (Gaithersburg, MD), unless otherwise noted. PCL (inherent viscosity: 1.15 dL/g) was purchased from LACTEL biodegradable polymers (Birmingham, AL) and 2,2,2- trifluoroethanol was purchased from Acros Organics (Morris Plains, NJ). 1,1,1,3,3,3- hexafluoro-2 propanol and nHAP particles (<200 nm) were purchased from Sigma-Aldrich (St. Louis, MO).

3.3.2. Polyurethane synthesis

A linear segmented degradable poly (ester urethane) urea elastomer (PEUUR2000) was synthesized using a standard two-step technique. Briefly, a 2000 Da PCL diol was end-capped with 1,6 diisocyanatohexane and then chain extended with 1,3 propanediol bis(4-aminobenzoate). The detailed procedure for this synthesis is described elsewhere [24].

3.3.3. Electrospinning of graded meshes

PCL was dissolved in 2,2,2-trifluoroethanol at 12% (w/v) and nHAP particles were added to the solution at 3% (w/v). Fluorescent dye 1,1'-dilinoleyl-3,3,3',3'-tetramethylindocarbocyanine perchlorate (DiI, Invitrogen) was added to the solution at a concentration of 5 μg/mL and the solution/suspension stirred vigorously for two days to dissolve the PCL and disperse the nHAP particles. PEUUR2000 was dissolved in 1,1,1,3,3,3-hexafluoro-2-propanol at 14% (w/w) and doped with fluorescent dye 3,3'-dilinoleyloxacarbocyanine perchlorate (DiO, Invitrogen) at a concentration of 8 μg /mL and the solution was stirred for two days.

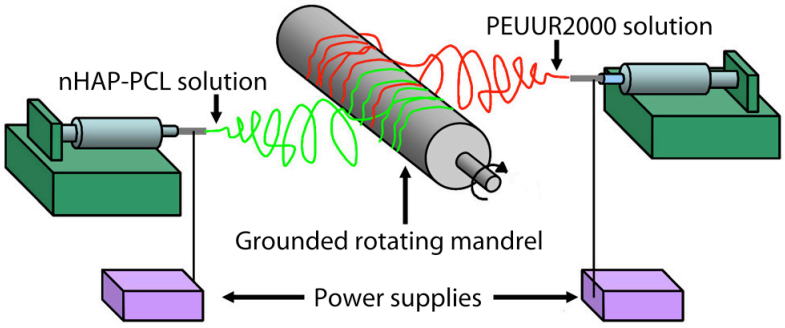

Figure 3.1: Diagram of electrospinning apparatus depicting offset spinnerets.

Prior to electrospinning, a mandrel was wrapped in aluminum foil and three 25 mm circular glass cover slips (sonicated in acetone and air-dried) were attached with double-sided tape to the foil along its length. Solutions of nHAP-PCL and PEUUR2000 were loaded into two 10 mL plastic syringes, capped with 22 gauge Teflon tipped needles and placed on opposite ends of the mandrel. The grounded mandrel was rotated at 1.2 m/s and nHAP-PCL was electrospun using a +20 kV potential, a throw distance of 20 cm and a flow rate of 2 mL/h while

PEUUR2000 was electrospun using a +15 kV potential, a throw distance of 15 cm and a flow rate of 3 mL/h. Subsequently, the syringes were offset 7 cm along the length of the mandrel (**Figure 3.1**) to achieve a gradient in fiber deposition. After a few minutes of electrospinning, the cover slips were detached from the mandrel and imaged under an Olympus IX50 inverted microscope (Opelco, Sterling, VA), equipped with a digital camera (Model C4742-95, Hamamatsu, Bridgewater, NJ). Electrospinning was continued for over an hour to obtain a graded mesh. In order to achieve uniform thickness along the length of the mesh, electrospinning was performed roughly twice as long on the pure nHAP-PCL and PEUUR ends as compared to the transition region in the middle. For ease of processing, the graded mesh was divided into three regions: a region consisting only of nHAP doped PCL fibers (nHAP-PCL(u)); another consisting solely of PEUUR2000 fibers (PEUUR2000(u)) and a transition consisting roughly of a 50:50 mix of both types of fibers (GRAD(u)). The samples were stored in a desiccator until further use.

In a modification to the electrospinning described previously, a 14% (w/v) PCL solution (loaded with 3.5% (w/v) nHAP) and a 12% (w/v) PEUUR2000 solution were co-electrospun as described previously. These new solution concentrations were selected to obtain comparable diameters for nHAP-PCL(u) and PEUUR(u) fibers. The resulting meshes were used for contact angle measurements, mechanical testing and cell culture. Here, comparable fiber diameters for the different sections sought to minimize the influence of differences in fiber diameters on the results of characterization.

Thicknesses of all three sections of the meshes were determined using digital calipers. Briefly, 12 meshes from each section were stacked between two glass cover-slips and the thickness of the stack was measured. The thickness of individual meshes was determined from the average of 12 meshes and measurements were performed in triplicate.

3.3.4. Treatment with 5×simulated body fluid

A 5×SBF solution (ion composition listed in **Table 3.1**) was prepared following a standard recipe adapted from the literature [141]. Briefly, 800 mL of a stock solution, consisting of appropriate amounts of NaCl, KCl, $CaCl_2.2H_2O$, $MgCl_2.6H_2O$, NaH_2PO_4 and Na_2SO_4, was

prepared. A 200 mL solution of $NaHCO_3$ was made separately. Electrospun meshes from the three regions designated nHAP-PCL(u), GRAD(u) and PEUUR2000(u) were cut into smaller samples, and taped down to the bottom of 150 mm Petri dishes. Just prior to use, the stock and $NaHCO_3$ solutions were mixed under vigorous stirring to result in a clear 5×SBF solution with a pH of 6.2. Approximately 40 mL of this solution was added to each of the meshes to cover the entire surface. Petri dishes were placed on an orbital shaker table (rotated at 60 rpm) at 37 °C to ensure even distribution of 5×SBF solution across the surface of the meshes. After 2 h, the solution was removed and meshes rinsed gently with deionized water. Meshes were removed from the Petri dishes while wet and dried in a desiccator for two days before further use. The resultant mineralized samples were designated nHAP-PCL(m), GRAD(m) and PEUUR2000(m).

Ion	**Blood plasma (mM)**	**5×SBF (mM)**
Na^+	142.0	710.0
K^+	5.0	25.0
Mg^{2+}	1.5	7.5
Ca^{2+}	2.5	12.5
Cl^-	103.0	760.0
HCO_3^-	27.0	5.0
$H_2PO_4^-$	1.0	5.0
SO_4^{2-}	0.5	2.5
pH	7.2-7.4	6.2

Table 3.1: Ion concentration (mM) of the 5×SBF used in this study. The composition of human blood plasma is listed for comparison [141].

3.3.5. Field emission scanning electron microscopy (FESEM) of graded meshes

As-spun and 5×SBF treated meshes were imaged using FESEM. Briefly, meshes were mounted onto studs and sputter-coated with a 10 nm layer of palladium-gold (Model 208 HR, Cressington Scientific Instruments, Cranberry, PA). Surfaces were then imaged using an FESEM instrument (LEO1550, Oxford Instruments, Oxfordshire, UK) fitted with an in-lens secondary electron detector, operating at 5 kV and a working distance of 7 mm. Images were imported into ImagePro Plus software (ICube, Crofton, MD) and fiber diameters measured.

3.3.6. Evaluation of mineral composition

Mineral composition was determined using X-ray diffraction (XRD) and energy dispersive spectroscopy (EDS). XRD spectra of nHAP powder, electrospun PCL, nHAP-PCL(u) and nHAP-PCL(m) meshes were obtained using an X-ray diffractometer (D8 Discover, Bruker AXS Inc., Madison, WI) with a CuKα radiation source, operating at 40 kV and 40 mA. Spectra were obtained in the 2θ range 20° to 40° at a scan speed of 2.4 °/min. EDS was performed using an INCAx-act EDS instrument (Carl Zeiss SMT, Thornwood, NY) fitted with a silicon drift detector, connected to and viewed using FESEM, at an accelerating voltage of 10 kV.

3.3.7. Contact angle measurements

Dynamic water contact angles of nHAP-PCL(u) and PEUUR2000(u) electrospun samples were measured using a contact angle goniometer (FTA125, First Ten angstroms, Portsmouth, VA). Briefly, 10 μL of deionized water was gently placed on electrospun meshes spun on 25 mm glass cover slips, and the volume increased until the drop began to advance. For the receding angle, fluid was withdrawn until the drop began to recede. Images were captured by a video camera attached to the goniometer and the advancing and receding contact angles were determined using an image analysis software (FTA32, First Ten angstroms).

3.3.8. Tensile testing of graded meshes

Tensile moduli of the three regions of the mesh were determined using an Instron 5869 (Norwood, MA), equipped with a BioPuls temperature-controlled bath, submersible pneumatic grips and a 10 N load cell. All specimens were tested wet in phosphate buffered saline (PBS) at 37 °C. Briefly, specimens measuring 30 mm × 10 mm with a 0.1 N pre-load were pulled monotonically at 10% strain/min until failure. Modulus, ultimate tensile strength (UTS) and strain at failure (SaF) were determined from the load-displacement curves. In particular, modulus was calculated from the first linear region (that corresponded to 1 - 4 % strain for nHAP-PCL, 4 - 20 % strain for GRAD and 10 - 20 % strain for PEUUR) of the load-displacement curve.

3.3.9. Cell metabolic activity on graded meshes

Cell metabolic activity on the graded meshes was investigated using MC3T3-E1 osteoprogenitor cells (ATCC, Manassas, VA) and a 3-(4,5-dimethylthiazolyl-2)-2,5-diphenyl tetrazolium bromide (MTT) colorimetric assay. Briefly, cells were maintained in growth medium, consisting of minimal essential medium α modification (Invitrogen) supplemented with 10% fetal bovine serum (Gemini, Calabasas, CA) and 1% antibiotic/antimycotic (Invitrogen). Cells were expanded in a 37°C, 5% CO_2 incubator, lifted every 3 days with trypsin/EDTA (Sigma Aldrich) and re-plated at a density of 10^5cells per 100 mm Petri dish.

Graded meshes were affixed to the bottom of 24 well plates using a small amount of medical adhesive silicone (Factor II, Lakeside, AZ) and sterilized using a Co-60 gamma irradiator (Model 484R, JL Shepherd and Associates, San Fernando, CA). . Prior to seeding, all meshes were incubated with 1 mL of 10 μg/mL human fibronectin (Sigma Aldrich) for 1 h. Subsequently, cells were seeded onto as-spun and 5×SBF treated graded meshes at a density of 5,000 cells/cm^2. Cells seeded on the bottom of tissue culture polystyrene (TCPS) plates acted as controls. Cells were maintained in 1 mL of growth medium and were allowed to grow for 7 days, with medium replaced every 3 days. After 7 days of culture, growth media were aspirated and all meshes were washed twice with sterile PBS and incubated with 0.5 mL of MTT working solution (0.5 mg/mL MTT reagent in phenol-red free Eagle's-MEM, MP Biomedicals, Solon, OH) for 2 h. Following incubation, the solution was aspirated and meshes further treated with 0.5 mL of dimethyl sulfoxide (DMSO) for 15 min on a rotary shaker (60 rpm). Absorbance of DMSO was measured at 570 nm using a uv-vis spectrophotometer (Genesys 5 Spectronic spectrophotometer, Spectral Analysis Instruments, Leeds UK).

3.3.10. Statistical analysis

JMP 8.0 (SAS Institute Inc., Cary, NC) was used to determine statistical significance using a one-way ANOVA and a Tukey-Kramer *post-hoc* test. A p-value of less than 0.05 was considered statistically significant. Results are reported as mean ± standard deviation for $n \geq 200$ fibers collected from at least 8 different spots on every group for fiber diameter, n = 3 groups of 12 samples each for mesh thickness, n = 3 samples for each group for contact angle

measurements, n = 10 spots for EDS analysis, n = 3 meshes for tensile testing and n = 3 meshes for cell metabolic activity.

3.4. Results

3.4.1. Fabrication and characterization of co-electrospun meshes

Co-electrospinning yielded fibrous meshes with varying polymer composition along the length of the meshes. In the first set of studies, the diameters of nHAP-PCL and PEUUR were specifically made different in order to distinguish the two types of fibers. Fluorescence microscopy **(Figure 3.2)** revealed the presence of only DiI-stained nHAP-PCL(u) fibers (shown in green) at one end of the mesh, only DiO-stained PEUUR2000(u) fibers (shown in red) at the other end, and a mixture of the two fibers in the transition region.

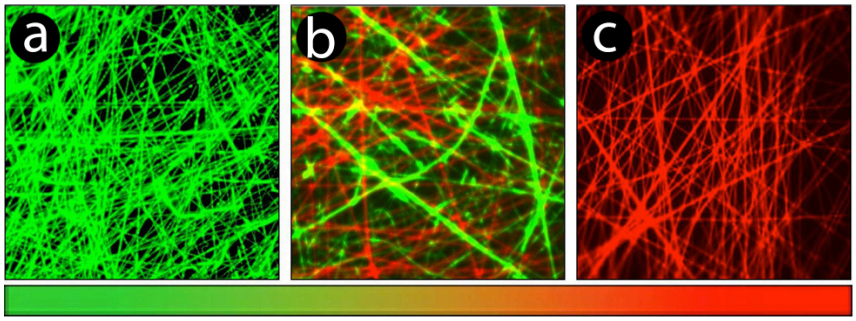

Figure 3.2: Fluorescent images from three spots along the length of the graded mesh showing (a) nHAP-PCL fibers (green), (b) transition region in-between and (c) PEUUR2000 fibers (red).

FESEM of graded meshes revealed the presence of a gradient in fiber composition. nHAP-PCL(u) samples **(Figure 3.3a)** showed the presence of nano-fibers with a bimodal diameter distribution (consistent with a splaying phenomenon), and average diameters of 0.47±0.07 μm and 1.06±0.16 μm. The fibers appeared rough, consistent with the presence of nano-hydroxyapatite particles on the surface of the fibers. In contrast, PEUUR2000(u) fibers **(Figure 3.3c)** were larger, smoother and unimodal with an average diameter of 1.92±0.28 μm. GRAD(u) samples **(Figure 3.3b)** exhibited a mixture of smaller, rougher nHAP-PCL(u) fibers and larger, smoother PEUUR2000(u) fibers. In the second set of studies, meshes with comparable diameters of nHAP-PCL and PEUUR2000 fibers, were fabricated for contact angle measurements, mechanical testing and cell culture. The fiber diameters for these samples were

0.55±0.07 μm and 1.65±0.22 μm for nHAP-PCL(u) and 1.65±0.38 μm for PEUUR2000(u). Thicknesses of the electrospun nHAP-PCL, GRAD and PEUUR2000 sections were 0.051 ± 0.004, 0.052 ± 0.002 and 0.045 ± 0.007 mm, respectively.

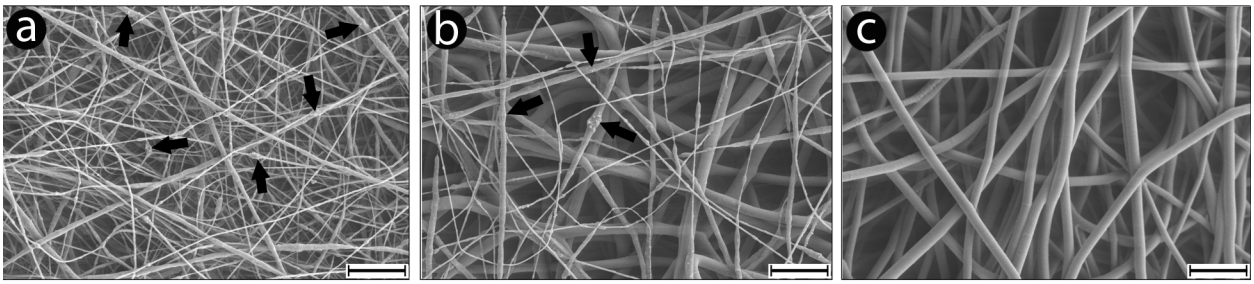

Figure 3.3: SEM micrograph of unmineralized gradient: (a) nHAP-PCL(u), (b) GRAD(u) and (c) PEUUR2000(u) fibers**.** Scale bar on all three sections is 10 μm. Arrows indicate nHAP particles in the nHAP-PCL fibers.

3.4.2. Characterization of mineral gradient

FESEM imaging was performed on 5×SBF treated meshes to verify the presence of the mineral gradient. Imaging revealed the presence of tiny mineral crystallites on the nHAP-PCL(m) fibers **(Figure 3.4a)** while the PEUUR2000(m) fibers **(Figure 3.4c)** showed very little mineral. In the GRAD(m) samples **(Figure 3.4b)** where both fibers were present, the smaller nHAP-PCL fibers were completely covered with mineral while the larger PEUUR2000 fibers showed very little mineral.

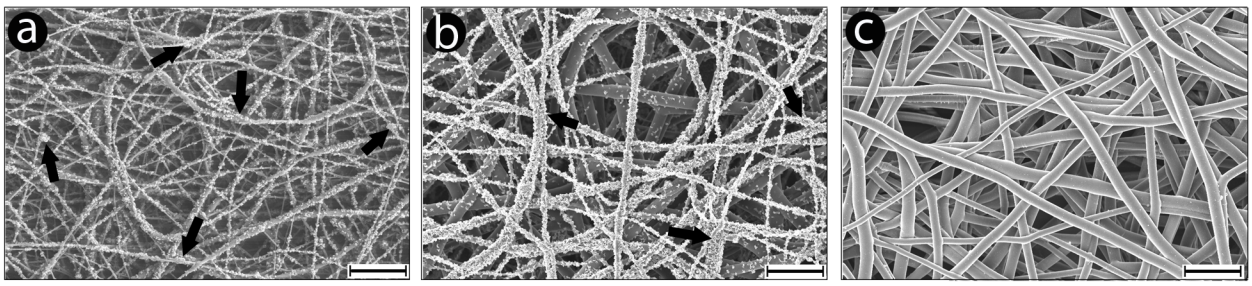

Figure 3.4: SEM micrograph of 5×SBF treated mineral gradient (a) nHAP-PCL(m), (b) GRAD(m) and (c) PEUUR2000(m) fibers. Scale bar on all three sections is 10 μm. Arrows indicate mineral deposits after treatment with 5×SBF.

XRD and EDS were performed to determine the composition of mineral crystallites. XRD analysis of nHAP powder (**Figure 3.5a**) revealed peaks at 25.8°, 28.1°, 28.9°, 31.8°, 32.2°,

32.9° and 34.1°, which are characteristic of hydroxyapatite. The XRD spectrum of electrospun PCL (**Figure 3.5b**) showed peaks at 21.4° and 23.7°, while that of nHAP-PCL(u) mesh (**Figure 3.5c**) had peaks for both hydroxyapatite and PCL. The spectrum for nHAP-PCL(m) samples (**Figure 3.5d)** showed the same peaks for hydroxyapatite that appeared in the spectrum for nHAP-PCL(u) samples. EDS data of mineral present on nHAP-PCL(m) samples indicated the presence of calcium and phosphorous in the ratio of 1.48±0.07. In addition, EDS revealed the presence of magnesium, potassium, sodium and chlorine.

3.4.3 Water contact angle on electrospun meshes

Water contact angle measurements were performed to determine relative hydrophobicity of nHAP-PCL(u) and PEUUR(u), in order to relate their wettability to their mineral nucleating ability from SBF. The measurements revealed that PEUUR2000(u) samples had a significantly higher advancing contact angle ($p<0.001$) than nHAP-PCL samples: 116.1 ± 0.9°, as compared to 93.6 ± 0.3°. Likewise, the receding angle for PEUUR(u) samples was significantly higher ($p<0.001$) than that for nHAP-PCL(u): 85.1 ± 1.8°, as compared to 54.1 ± 2.8°.

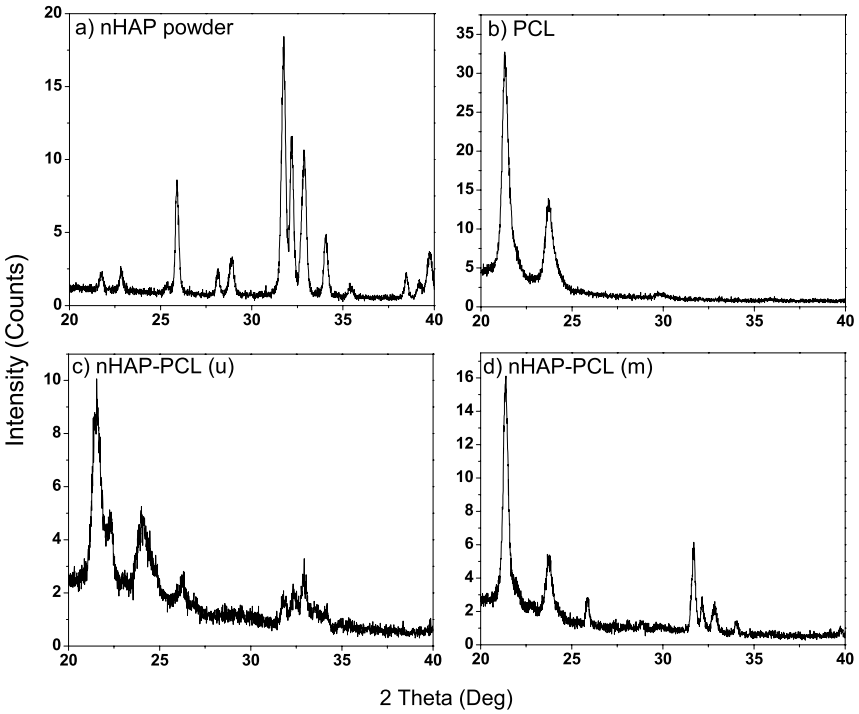

Figure 3.5: XRD spectra of (a) nHAP powder, (b) PCL, (c) nHAP-PCL(u) and (d) nHAP-PCL(m) samples.

3.4.4. Mechanical properties of graded meshes

Tensile testing was performed on unmineralized and mineralized meshes to determine differences in mechanical properties along the length of the gradient. Representative stress-strain curves for unmineralized and mineralized meshes are shown in **Figure 3.6a** and **Figure 3.6b** respectively. Steeper curves for nHAP-PCL indicate that it is stiffer than the GRAD and PEUUR2000 sections of the mesh. The stress-strain curves for the GRAD samples were in between those for nHAP-PCL and PEUUR2000. The curve for nHAP-PCL became steeper upon treatment with 5×SBF. The tensile moduli of nHAP-PCL(u), GRAD(u) and PEUUR2000(u) were 0.64±0.04 MPa, 0.58±0.09 MPa and 0.22±0.03 MPa respectively, while those for nHAP-PCL(m), GRAD(m) and PEUUR2000(m) were 2.4±0.23 MPa, 0.55±0.01 MPa and 0.23±0.04 MPa respectively (**Figure 3.7a**). Post mineralization, nHAP-PCL samples showed a significant increase in tensile modulus, compared to their unmineralized counterparts ($p=0.002$). nHAP-PCL and PEUUR2000 samples possessed significantly different tensile moduli irrespective of 5×SBF treatment ($p=0.046$ before and $p<0.001$ after treatment with 5×SBF).

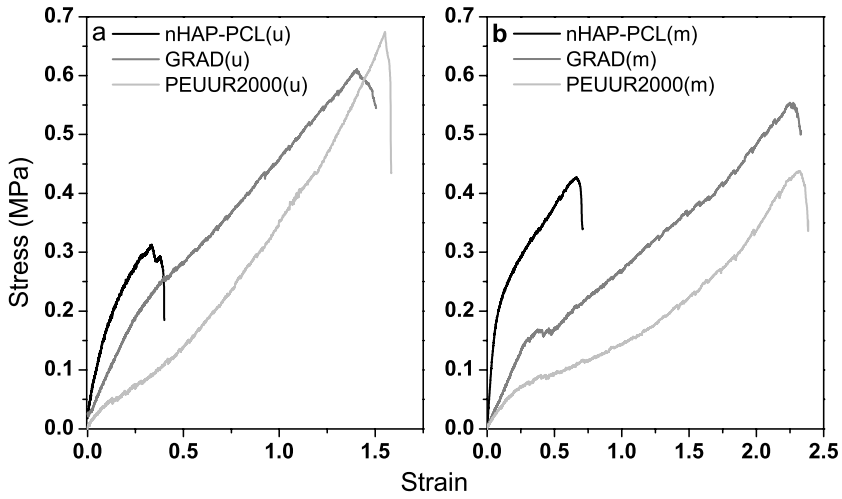

Figure 3.6: Representative stress-strain plot of nHAP-PCL, GRAD and PEUUR2000 regions of (a) unmineralized mesh and (b) mineralized mesh.

UTS values of PEUUR2000(u) samples were higher than nHAP-PCL(u) samples ($p=0.049$) (**Figure 3.7b**). Moreover, nHAP-PCL(m) ($p=0.017$) showed a significantly greater UTS compared than its unmineralized counterpart. Similarly, SaF values of PEUUR2000 samples were higher than their respective nHAP-PCL samples, both without ($p=0.001$) and with

(p=0.012) 5×SBF treatment (**Figure 3.7c**). Both nHAP-PCL(m) (p=0.015) and PEUUR2000(m) (p=0.007) samples showed a significant increase in SaF values, compared to their unmineralized counterparts.

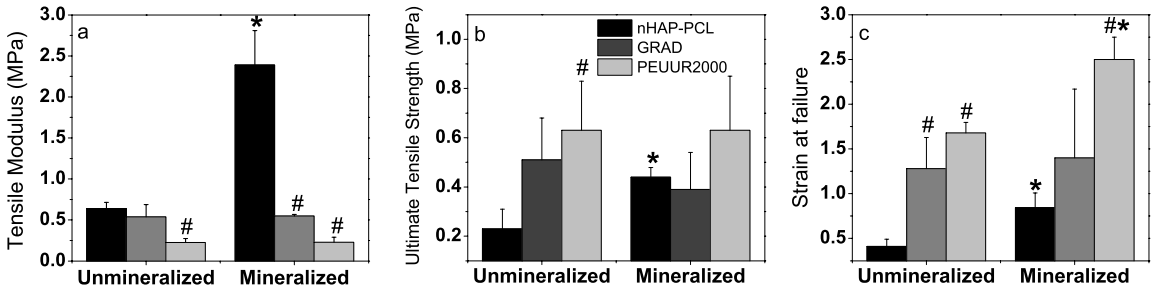

Figure 3.7: a) Tensile moduli, b) ultimate tensile strength and c) strain at failure of the three regions of unmineralized and mineralized meshes. Bars correspond to mean ± std. deviation for n=3 samples. A pound symbol indicates statistical significance compared to respective nHAP-PCL section, while an asterisk indicates statistical significance compared to respective unmineralized counterpart.

3.4.5. Cell metabolic activity on graded meshes

Mammalian cell culture was performed to confirm biocompatibility of meshes. Measurement of extracted MTT dye for all samples after 7 days of culture (**Figure 3.8**) indicated that the absorbances for nHAP-PCL(u) (p=0.041), nHAP-PCL(m) (p=0.019) and GRAD(m) (p=0.017) were significantly lower than the TCPS control. PEUUR2000 samples showed the highest absorbance, regardless of treatment with 5×SBF.

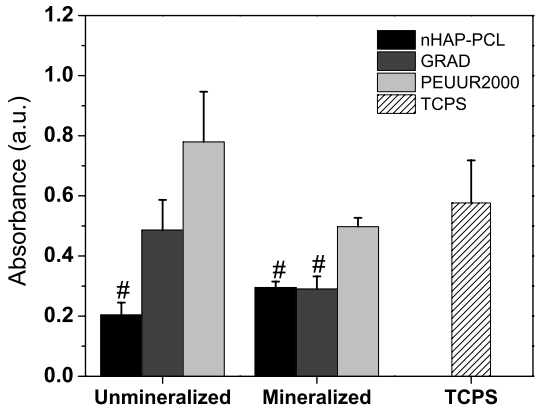

Figure 3.8: Absorbance values indicating cell metabolic activity on unmineralized and mineralized meshes. Bars correspond to mean ± std. deviation for n=3 samples. A pound symbol indicates statistical significance compared to TCPS control.

3.5. Discussion

The present study constitutes a preliminary effort towards the fabrication of model graded meshes to study the regeneration of the ligament-bone interface. To this end, PCL doped with nHAP particles and PEUUR2000 were co-electrospun from offset spinnerets. A physically large gradient zone (>2 cm) was intentionally constructed to permit reliable characterization of the GRAD section of the graded meshes (However, a smaller and physiologically more relevant gradient region can be fabricated by using shields at appropriate positions during the electrospinning process [14]). Next, a 5×SBF solution was used to superimpose a mineral gradient along the length of the meshes. XRD revealed the presence of hydroxyapatite-like mineral on the surface of the meshes. Tensile testing of graded meshes confirmed the presence of a gradient of tensile modulus along the length of the meshes, with the gradient becoming more pronounced upon treatment with 5×SBF. Finally, *in vitro* cell culture demonstrated that MC3T3-E1 osteoprogenitor cells were metabolically active on all regions of the meshes.

The polymers in the study were chosen based on their favorable properties for regeneration of the ligament-bone interface. PCL was chosen because of its wide-spread use for bone tissue engineering applications due to its biocompatibility, processability, and degradability [126, 127, 145]. A poly (ester urethane) urea elastomer was chosen primarily for its biocompatibility, degradability and elastic properties to support regeneration of ligament tissue [24, 146]. Since PEUUR2000 contains PCL segments, electrospun PEUUR2000 fibers may bond well with the nHAP-PCL fibers and also have similar degradation rates.

To improve the osteoconductivity of scaffolds for bone tissue engineering, a mineral phase (e.g., hydroxyapatite, amorphous calcium phosphate) is frequently incorporated [126-128, 147]. In this study, a hydroxyapatite-like mineral phase was deposited on the fibers from a 5×SBF solution, using a modification of the process described by Jayasuriya et al [141]. The use of SBF solutions to deposit minerals like hydroxyapatite on a variety of surfaces has been well reported in the literature [140, 148]. One of the goals of using a 5×SBF solution in this study was to selectively mineralize nHAP-PCL fibers in order to create a mineral gradient. XRD spectra confirmed the presence of predominantly hydroyapatite-like mineral on the surface of nHAP-PCL(m) fibers (**Figure 3.5d**), the results of which are consistent with previous reports in

the literature [142, 149]. The Ca/P ratio of 1.48 measured by EDS was lower than the ratio of 1.67 for hydroxyapatite [142] and likely resulted from the substitution of magnesium and potassium cations.

Mineral nucleation from SBF solutions may involve a variety of factors and multiple mechanistic routes. In this study, nHAP-PCL fibers showed presence of significantly more mineral within two hours than PEUUR2000 fibers (**Figure 3.4**). This could have resulted from the presence of hydroxyapatite particles on the surface of PCL fibers, which would have provided nucleation sites for ions to precipitate from the 5×SBF solution [150]. Also, the presence of bulky non-polar hydrophobic benzyl rings in PEUUR2000 could have slowed the deposition of ions from solution due to a combination of hydrophobic and steric effects [151].

Tensile testing of various parts of the mesh (**Figs. 3.6a** and **3.6b**) revealed that while nHAP-PCL displayed elastic behavior at low strain, PEUUR2000 demonstrated predominantly elastic behavior with a large strain to failure (The incorporation of hydroxyapatite in the nHAP-PCL samples could have contributed to brittleness of the fibers). Independent studies by Baker et al. [15] and Ladd et al. [14] have reported that samples consisting of two types of electrospun fibers will display properties of both types. In agreement with their findings, the stress-strain curve of the GRAD samples was found to lie between nHAP-PCL and PEUUR2000 samples. In addition, GRAD samples possessed a slight kink at around 40% strain and a larger slope preceding the kink, which suggests that under uniaxial strain, the stiffer nHAP-PCL fibers fail first followed by the deformation and failure of the PEUUR2000 fibers. A gradient in tensile modulus from 0.23 to 2.4 MPa (**Figure 3.7a**) was present along the length of the meshes. This range of moduli is two to three orders of magnitude lower than human ACL (111-144 MPa [43]), human tibial (100-300 MPa [152]) and femoral (400-1500 MPa [38]) trabecular bone. However, the bulk moduli of PEUUR2000 (18MPa (unpublished data)) and PCL (400 MPa [153]) are comparable to the moduli of the target tissues. This suggests that while the materials used in this study are not directly suitable for use in a clinical application, their mechanical properties should support *in vitro* development of ligament and bone. Future studies will involve culturing mesenchymal stem cells (MSCs) on the graded meshes to investigate *in vitro* formation of ligament and bone tissues.

Treatment with a 5×SBF solution resulted in a significantly greater modulus for nHAP-PCL(m) as compared to its unmineralized counterpart, due to the presence of mineral on the fibers (**Figure 3.7.a**). The GRAD(m) samples were expected to show an increase in modulus due to positive contribution from the mineralized nHAP-PCL fibers in the elastic region. However, in this study, the GRAD(m) samples showed no significant increase in tensile modulus compared to the GRAD(u) samples. Micro-tensile testing with simultaneous imaging will help examine the contribution of the different materials towards the overall mechanical properties and also elucidate the exact mechanism of failure. SaF values of all sections of the mineralized meshes were higher than their unmineralized counterparts (**Figure 3.7c**). This could be a consequence of the 2 hr treatment with 5×SBF, which may have allowed additional water and ions to penetrate the polymeric fibers (and act as plasticizers [154]), as compared to the unmineralized meshes that received no such treatment.

Cell culture studies demonstrated that all sections of the graded meshes supported adhesion of MC3T3-E1 cells (**Fig 3.8**). However, metabolic activity (an indirect measure of cell viability) on the mineralized meshes was lower compared to the TCPS control, which could be attributed to the decreased ability of the cells to form attachment points on the fibers with mineral. A similar result was obtained in a previous study that showed higher proliferation rate of MC3T3-E1 cells after 5 days on surfaces without mineral than on surfaces with β–tricalcium phosphate [129]. In the present study, increased metabolic activity on the PEUUR2000 samples could also have resulted from the presence of larger fiber diameters for these samples, as MC3T3-E1 cells have been shown to attach and spread better on fibers with larger diameters [106]. In contrast, nHAP-PCL fibers had a mixture of both smaller and larger fiber diameters. Despite these differences, the cell study demonstrated biocompatibility of graded meshes. Future studies will investigate proliferation and differentiation of MSCs on the graded mesh. Specifically, these studies will test for osteogenic differentiation of MSCs in response to mechanical and mineral gradients. Moreover, the approach used in this study can be extended to include bio-active factors in the electrospun fibers to aid differentiation of MSCs towards bone and ligament like phenotypes on the graded meshes.

3.6. Conclusions

This study describes the fabrication of a model continuously graded co-electrospun mesh, with a long-term goal of regenerating the ligament-bone interface. Specifically, nano-hydroxyapatite doped polycaprolactone and poly-(ester urethane) urea elastomer solutions were co-electrospun from offset spinnerets. Differences in surface properties were exploited to create a mineral gradient. The resultant mineral phase was found to consist of a hydroxyapatite-like mineral. Tensile testing of graded meshes revealed the presence of a mechanical gradient with differences in tensile moduli along the length of the mesh. Preliminary cell studies revealed that MC3T3-E1 osteoprogenitor cells were metabolically active on the graded meshes. The study demonstrates that graded scaffolds for interfacial tissue engineering can be fabricated by co-electrospinning.

3.7. Acknowledgements

The authors thank the Institute for Critical Technologies and Applied Sciences at Virginia Tech for funding, Dr. Garth Wilkes (Department of Chemical Engineering, Virginia Tech) for the use of the electrospinning apparatus, Dr. Joseph Freeman (School of Biomedical Engineering and Sciences, Virginia Tech) for the use of the tensile testing machine, Dr. William Ducker (Department of Chemical Engineering, Virginia Tech) for the use of the contact angle goniometer and Stephen McCartney (Nano-characterization and Fabrication Laboratory, Virginia Tech) and Rick Caudill (Department of Wood Sciences, Virginia Tech) for help with characterization.

Reprinted from S Samavedi et al, Biomaterials, 33(2012), pp. 7727-7735: included with permission from Elsevier Science

Chapter 4

Response of bone marrow stromal cells to graded co-electrospun scaffolds and its implications for engineering the ligament-bone interface

Satyavrata Samavedi[a], Scott A. Guelcher[b], Aaron S. Goldstein[a,c], Abby R. Whittington[a,c,d]

[a] Department of Chemical Engineering, Virginia Polytechnic Institute and State University, Blacksburg, VA, USA

[b] Department of Chemical and Biomolecular Engineering, Vanderbilt University, Nashville, TN, USA

[c] School of Biomedical Engineering and Sciences, Virginia Polytechnic Institute and State University, Blacksburg, VA, USA

[d] Department of Materials Science and Engineering, Virginia Polytechnic Institute and State University, Blacksburg, VA, USA

4.1. Abstract

Biomaterial scaffolds with gradients in architecture, mechanical and chemical properties have the potential to improve the osseointegration of ligament grafts by recapitulating phenotypic gradients that exist at the natural ligament-bone (L-B) interface. Towards the larger goal of regenerating the L-B interface, this *in vitro* study was performed to investigate the potential of two scaffolds with mineral gradients in promoting a spatial gradient of osteoblastic differentiation. Specifically, the first graded scaffold was fabricated by co-electrospinning two polymer solutions (one doped with nano-hydroxyapatite particles) from offset spinnerets, while the second was created by immersing the first scaffold in a 5× simulated body fluid. Rat bone marrow stromal cells, cultured in the presence of osteogenic supplements, were found to be metabolically active on all regions of both scaffolds after 1 and 7 days of culture. Gene expression of bone morphogenic protein-2 and osteopontin was elevated on mineral-containing

regions as compared to regions without mineral, while the expression of alkaline phosphatase mRNA revealed the opposite trend. Finally, the presence of osteopontin and bone sialoprotein confirmed osteoblastic phenotypic maturation by day 28. This study indicates that co-electrospun scaffolds with gradients in mineral content can guide the formation of phenotypic gradients and may thus promote the regeneration of the L-B interface.

NB: The unmineralized (u) and mineralized graded scaffolds (m) described in chapter 3 are referred to as electrospun (ES) and simulated body fluid (SBF) graded scaffolds in this chapter.

Keywords: ligament-bone interface, graded scaffold, electrospinning, hydroxyapatite, bone marrow stromal cells, osteoblastic differentiation

4.2. Introduction

Interfacial tissue engineering is a rapidly growing field that aims to regenerate tissue interfaces through the use of graded scaffolds that recapitulate *in vivo* transitions between tissues [122]. In recent years, regeneration of the ligament-bone (L-B) interface has received significant attention due to its potential for improving the osseointegration of ligament grafts [9]. The L-B interface consists of complex gradients that transition over four different regions: ligament, unmineralized fibrocartilage, mineralized fibrocartilage and bone [8]. Since this interface consists of gradients in architecture, mechanical properties, chemical properties and cell phenotypes (**Figure 4.1**), scaffolds possessing structural, mechanical and biochemical gradients have the potential to facilitate the regeneration of this interface [10]. Specifically, gradient cues in such scaffolds can help guide the formation of tissues with phenotypic gradients, which in turn may aid the osseointegration of ligament grafts [9, 10]. With the long-term goal of regenerating the L-B interface, this *in vitro* study evaluates the potential for graded scaffolds to guide the establishment of an osteoblastic gradient.

Continuously graded scaffolds for regenerating interfacial tissues can be fabricated by the process of electrospinning [122]. This approach offers the ability to create nano-fibrous scaffolds and tune their mechanical and chemical properties via simple *in situ* alterations such as

the use of multiple spinnerets [15]. Furthermore, electrospun scaffolds can be modified post-fabrication, by performing appropriate chemical treatments to change their surface chemistry [155]. In particular, electrospun scaffolds with mineral gradients have been investigated for establishing gradients of cell response towards potentially engineering the L-B interface [129, 132]. Recently, Samavedi et al created graded co-electrospun scaffolds with a spatial gradient in nano-hydroxyapatite (nHAP) content and subsequently immersed these scaffolds into a simulated body fluid to develop a second mineral gradient [156]. Both scaffolds possessed continuous gradients in mechanical properties, chemical properties and mineral content, and were found to support the growth of MC3T3-E1 osteoprogenitor cells. However, the effect of mineral on cell attachment and osteoblastic differentiation was not tested in this study.

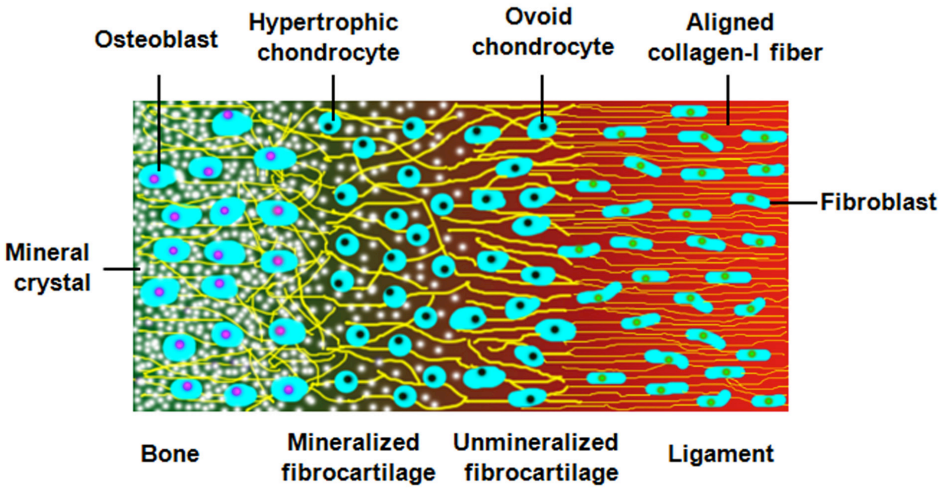

Figure 4.1: Diagram of the L-B interface depicting gradients of mineral content, collagen fiber diameter/alignment and cell phenotype. The interface consists of complex gradients in mechanical and biochemical properties that smoothly transition over four regions: ligament, unmineralized fibrocartilage, mineralized fibrocartilage and bone.

Incorporation of a mineral phase (e.g., HAP, tricalcium phosphate) into/onto scaffolds has been shown to influence mesenchymal stem cell behavior including attachment, osteoblastic differentiation and phenotypic maturation [157-160]. Osteoblastic differentiation is marked by the induction of proteins such as alkaline phosphatase (ALP), whose expression is elevated during early stages of differentiation, and growth factors such as bone morphogenetic protein-2 (BMP-2), whose early expression may initiate autocrine signaling pathways that result in

maturation [161, 162]. Osteoblastic phenotypic maturation is characterized by deposition of extracellular matrix (ECM) proteins like osteopontin (OPN) and bone sialoprotein (BSP).

The goal of this study was to characterize the role of scaffolds possessing mineral gradients in influencing osteoblastic differentiation and maturation of bone marrow derived stromal cells (BMSCs). Towards this end, scaffolds with two different mineral gradients were fabricated. The first scaffold was created by co-electrospinning nHAP-doped poly(caprolactone) (nHAP-PCL) and poly(ester urethane urea) (PUR) solutions from offset spinnerets to result in gradients of fiber chemistry and mineral content. The second scaffold was prepared by treating the co-electrospun graded scaffold with a 5× simulated body fluid (5×SBF). Here, nHAP particles were chosen for their stability and superior osteoconductive properties, compared to other types of ceramics [124, 163]. Moreover, their inclusion into electrospun PCL fibers was intended to promote selective nucleation of mineral crystallites when treated with the 5×SBF solution. Thereafter, rat BMSCs were cultured on scaffolds in the presence of osteogenic supplements. Subsequently, cell metabolic activity, morphology, density, mRNA expression for BMP-2, ALP, OPN and BSP, and deposition of OPN and BSP were investigated.

4.3. Materials and methods

4.3.1. Materials

Chemicals and laboratory supplies were purchased from Fisher Scientific (Pittsburgh, PA), while biological supplies were purchased from Life Technologies (Gaithersburg, MD), unless otherwise noted. PCL (inherent viscosity: 1.15 dL/g in chloroform) was purchased from LACTEL biodegradable polymers (Birmingham, AL), while a linear segmented degradable PUR was synthesized from 2 kDa PCL diol as described previously [24]. Sodium sulfate salt and 2,2,2- trifluoroethanol (TFE) were purchased from Acros Organics (Morris Plains, NJ). Alizarin red S dye, nHAP particles (< 200 nm), 1,1,1,3,3,3-hexafluoro-2-propanol (HFIP), trypsin/sodium salt of ethylenediamine tetraacetic acid (trypsin/EDTA), dexamethasone, disodium salt of glycerol-2-phosphate, ascorbic acid, Triton X-100, rhodamine-phalloidin, 4',6-diamidino-2-phenylindole (DAPI) and bovine serum albumin (BSA) were purchased from Sigma-Aldrich (St. Louis, MO). Fetal bovine serum (FBS) was purchased from Gemini Bio-Products (Calabasas,

CA), while phenol red-free Eagle's-MEM and 3-(4,5-dimethylthiazolyl-2)-2,5-diphenyl tetrazolium bromide (MTT) were purchased from MP Biomedicals (Solon, OH). RNeasy Mini kit, DNase I and QIAshredder columns were purchased from Qiagen (Valencia, CA), methanol-free formaldehyde from Polysciences Inc (Warrington, PA) and primers from Integrated DNA Technologies (Coralville, IA). Primary antibodies against OPN and BSP, and fluorescein thioisocyanate (FITC)-conjugated secondary antibody were purchased from Abcam Inc. (Cambridge, MA). Vectamount AQ was purchased from Vector labs (Burlingame, CA).

4.3.2. Fabrication of graded scaffolds

Scaffolds with gradients in chemistry and mineral content were fabricated by co-electrospinning two polymer solutions from offset spinnerets, as described previously [156]. Briefly, a 14% (w/v) PCL solution containing 3.5% (w/v) nHAP particles was prepared in TFE, while PUR was dissolved in HFIP at 12% (w/w). These concentrations were selected because they resulted in similar fiber diameters: ~ 0.55 μm and ~ 1.65 μm for the PCL region (bimodal diameter distribution), and ~ 1.65 μm for the PUR region [9]. These two solutions were loaded into separate 10 mL plastic syringes and initially co-electrospun onto a single region of a grounded rotating mandrel wrapped in aluminum foil. Subsequently, the syringes were offset ~7 cm along the length of the mandrel to achieve a gradient in fiber deposition and mineral content. Electrospinning was performed for over an hour and the resultant graded scaffold, denoted ES scaffold (for electrospun scaffold), was stained with Alizarin Red S dye to demonstrate the gradient. Briefly, the scaffold was immersed in a 40 mM solution of dye in de-ionized water for 2.5 h, followed by thorough washing in de-ionized water. Images of the scaffold were captured after air drying.

After electrospinning, scaffold ES was divided into three regions for ease of processing and characterization: a region consisting only of nHAP doped PCL fibers (nHAP-PCL(ES)), a region consisting solely of PUR fibers (PUR(ES)) and a transition region consisting of a mixture of both types of fibers (GRAD(ES)). Subsequently, samples from various regions of graded scaffold ESwere treated with approximately 40 mL of a 5×SBF solution, prepared using a previously reported formulation [156]. Samples were treated for 2 h at 37 °C with gentle agitation to coat the surface of the fibers with a calcium phosphate mineral layer (CaP). Previous

analysis of a mineral layer produced in this manner suggested that it consists of calcium-deficient hydroxyapatite crystallites [156]. After treatment, the 5×SBF solution was discarded and the samples were rinsed gently with de-ionized water and dried in a dessicator before further use. The resulting 5×SBF-treated scaffold was designated SBF scaffold and its various regions were denoted nHAP-PCL(SBF), GRAD(SBF) and PUR(SBF), corresponding to similar regions in scaffold ES.

4.3.3. Scanning electron microscopy (SEM)

nHAP particles and regions from both types of graded scaffolds were examined using SEM to visually estimate size range and surface coverage of mineral respectively. Briefly, samples were mounted onto SEM studs and sputter-coated with a 10 nm layer of palladium-gold (Model 208 HR, Cressington Scientific Instruments, Cranberry, PA). Sputter-coated surfaces were imaged using an SEM instrument (LEO1550, Oxford Instruments, Oxfordshire, UK) operating at 5 kV and fitted with in-lens secondary electron and backscatter detectors.

4.3.4. Rat bone marrow harvest and cell culture

BMSCs were harvested from femurs and tibias of juvenile male Sprague-Dawley rats weighing 125-150 g (Harlan, Dublin, VA), in accordance with the Institutional Animal Care and Use Committee at Virginia Tech, as described previously [164]. Briefly, bone marrow extracts were thoroughly dispersed and plated on two 100 mm tissue culture polystyrene Petri dishes. Cells containing a population of BMSCs were maintained in growth medium (minimal essential medium-alpha modification, supplemented with 10% FBS and 1% antibiotic/antimycotic) for 10 days and expanded in a 37 °C, 5% CO_2 incubator. Cells were lifted every 3 or 4 days with trypsin/EDTA and re-plated at a density of 10^5 cells per 100 mm Petri dish.

Samples from all three regions of scaffolds ESand SBF were cut using a circular biopsy punch (ID ~ 1.15 cm) and secured to the bottom of 48 well plates (well area ~ 0.95 cSBF) using cloning cylinder rings (ID ~ 0.8 cm). Samples were subsequently sterilized by exposure to ultraviolet radiation for 48 h. Prior to cell seeding, all samples were incubated with 1 mL of growth medium for 24 h at 37 °C and 5% CO_2. Thereafter, BMSCs (between passage 3 and 5) were seeded onto samples at a density of ~2.5×10^4 cells/well, which corresponded to a

theoretical seeding density of ~5.0×10^4 cells/cm^2. To allow for an initial phase of cell proliferation, cells were cultured in growth medium for 5 days before switching to differentiation medium (growth medium supplemented with 10 nM dexamethasone, 2 mM disodium salt of glycerol-2-phosphate and 0.13 mM ascorbic acid). Cells were cultured for a total of 28 days, with medium changed every 3 or 4 days.

4.3.5. Cell metabolic activity on graded scaffolds

Cell metabolic activity on various regions of the graded scaffolds was investigated using an MTT colorimetric assay. After 1 and 7 days of culture, growth medium was aspirated and all scaffolds were washed twice with phosphate buffered saline (PBS) before being incubated with 0.25 mL of MTT working solution (0.5 mg/mL MTT reagent in phenol red-free Eagle's-MEM) for 4 h. Following incubation, the solution was aspirated and scaffolds were further treated with 0.25 mL of dimethyl sulfoxide for 15 min on a rotary shaker (60 rpm). Finally, absorbance of 0.2 mL of each sample was measured in a 96 well plate at 570 nm using a SpectraMax SBFe multi-mode micro-plate reader (Molecular Devices, Sunnyvale, CA).

4.3.6. Cytoskeletal organization and cell density on graded scaffolds

Cytoskeletal organization and cell density on various regions of the graded scaffolds were assessed at day 28 by fluorescence staining of F-actin and counter-staining of nuclei. Briefly, cells on various regions of the graded scaffolds were washed twice with PBS and subsequently fixed with 4% methanol-free formaldehyde. Cells were then permeabilized with 0.5% Triton X-100 solution in PBS. Next, samples were treated with a solution of rhodamine-phalloidin in PBS (1:40 dilution) for 20 min, followed by DAPI counter-stain (300 nM in PBS) for 5 min. Samples were finally rinsed with PBS before mounting on glass slides with Vectamount AQ. Images were obtained at 20× magnification with wide green and ultraviolet filters using an Olympus IX50 fluorescence microscope (Opelco, Sterling,VA) equipped with a cooled CCD camera (Hamamatsu C4742-98-12NRB).

4.3.7. mRNA expression on graded scaffolds

Reverse transcription quantitative polymerase chain reaction (RT-qPCR) was used to determine mRNA expression of osteoblastic differentiation markers BMP-2 and ALP at day 14 and phenotypic maturation markers OPN and BSP at day 21, as reported previously [161]. Briefly, total RNA was isolated from cells on days 14 and 21 using the RNeasy Mini Kit according to the manufacturer's instructions. Isolated total RNA was quantified using Quant-It RiboGreen kit according to the manufacturer's instructions. Thereafter, approximately 50 ng of total RNA was reverse-transcribed to cDNA with the SuperScript® First-Strand Synthesis kit using random hexamers as primers according to the manufacturer's protocol. Finally, RT-qPCR was performed in a ABI 7300 Real Time PCR System (Life Technologies, Foster City, CA) using appropriate forward/reverse primers (**Table 4.1)** and a Power Sybr®Green Master Mix. Specific forward and reverse primer sequences for BMP-2, ALP, OPN, BSP and β-actin (reference gene) were designed using Primer Express software (Life Technologies). Quantification of target gene expression was performed using the comparative threshold cycle ($\Delta\Delta$Ct) method, with minor modifications [165]. Relative gene expression was reported as $2^{-\Delta\Delta Ct}$, normalized to PUR(ES) samples.

Protein	Forward Primer	Reverse Primer	Product size (bps)	Accession number
β-actin	CGTGAAAAGATGACCCAGATCA	CACAGCCTGGATGGCTACGT	71	NM_031144
BMP-2	GGAAAACTTCCCGACGCTTCT	CCTGCATTTGTTCCCGAAAA	99	NM_017178
ALP	GTGGAAGGAGGCAGGATTGA	GTGTCTTTCTGGGAAGTCATGGT	122	NM_013059
OPN	TGAGACTGGCAGTGGTTTGC	CCACTTTCACCGGGAGACA	62	M14656
BSP	TACAACACTGCGTATGAAACCTATGAC	TGGTAGTAATAATCCTGACCCTCGTA	136	AB001383

Table 4.1: RT-qPCR primer sequences for rat.

4.3.8. Immunofluorescent staining for ECM proteins

The presence of ECM proteins OPN and BSP was detected using a standard immunofluorescent staining protocol. After 28 days of culture, medium was aspirated and samples were rinsed twice with PBS. Thereafter cells were fixed by treatment with 4% methanol-free formaldehyde for 20 min, washed thrice with PBS and permeabilized with 0.5% Triton X-100 solution in PBS for 15 min. Samples were again rinsed thrice in PBS and blocked in a 1% BSA solution in PBS for 1 h at room temperature. Next, samples were treated with either a rabbit polyclonal anti-OPN primary antibody (1:100 dilution) or a rabbit polyclonal anti-BSP primary antibody (1:100 dilution) for ~ 15 h in a humid chamber at 4 °C. After washing three times with PBS, samples were treated with a FITC-conjugated goat polyclonal secondary antibody to rabbit IgG (1:1000 dilution) for 1 h at room temperature. Samples were washed twice with PBS and counterstained with a DAPI solution (300 nM in PBS) for 5 min at room temperature. Finally, samples were washed twice with PBS before mounting on glass slides with Vectamount AQ. Images were obtained at 20× magnification with wide blue and ultraviolet filters using an Olympus IX50 fluorescence microscope equipped with a cooled CCD camera.

4.3.9. Statistical analyses

JMP 9.0 (SAS Institute Inc., Cary, NC) was used to determine statistical significance using a one-way ANOVA followed by a Tukey-Kramer *post-hoc* test, or a non-parametric Wilcoxon test. A p-value less than 0.05 was considered statistically significant. Results are reported as mean ± standard error of mean for n = 5 samples per group for cell viability and n = 8 samples per group for gene expression (except for GRAD(ES) at day 14: n = 7). RT-qPCR data were combined over two studies with n = 4 samples per study and statistical analyses were performed on $2^{-\Delta\Delta Ct}$ values for the combined data.

4.4. Results

4.4.1. Co-electrospun graded scaffold

Co-electrospinning resulted in the formation of ES scaffold with gradients in fiber chemistry and mineral content. A large GRAD region (~7 cm) was intentionally constructed to

allow for reliable characterization of the different regions of the scaffold. Alizarin red S staining was used to demonstrate the presence of a mineral gradient (**Figure 4.2**). Bright red staining in the nHAP-PCL region indicated the presence of calcium in the form of nHAP particles. The staining reduced in intensity in the GRAD region, indicating a lower mineral content than in the nHAP-PCL region. The PUR region, devoid of mineral content, showed negligible presence of bound dye and thus appeared yellow.

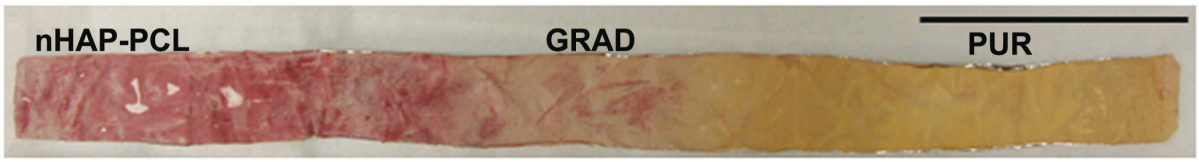

Figure 4.2: Photograph of Alizarin Red S-stained scaffold ESdemonstrating the presence of a mineral gradient from the nHAP-PCL transitioning through the GRAD to the PUR region. Scale bar corresponds to 5 cm.

4.4.2. nHAP particle size range and surface coverage of mineral on graded scaffolds

SEM imaging was performed to estimate nHAP particle size-range, as well as mineral distribution in ES and SBF scaffolds. While nHAP particles were found to possess diameters less than 200 nm, several large particles with diameters over 500 nm were also observed (**Figure 4.3a**). Within the ES scaffold, these nHAP particles were only partially exposed on the surface of the electrospun PCL fibers (**Figure 4.3b**). Upon treatment with 5×SBF, the nHAP-PCL(ES) fibers were found to be covered with CaP crystallites (**Figure 4.2c**). Moreover, the fibers in this nHAP-PCL(SBF) region (**Figure 4.3c**) were found to be coated with more crystallites than the fibers in the PUR(SBF) region (**Figure 4.3d**). Fiber diameters for the nHAP-PCL and PUR regions were made significantly different for imaging purposes only.

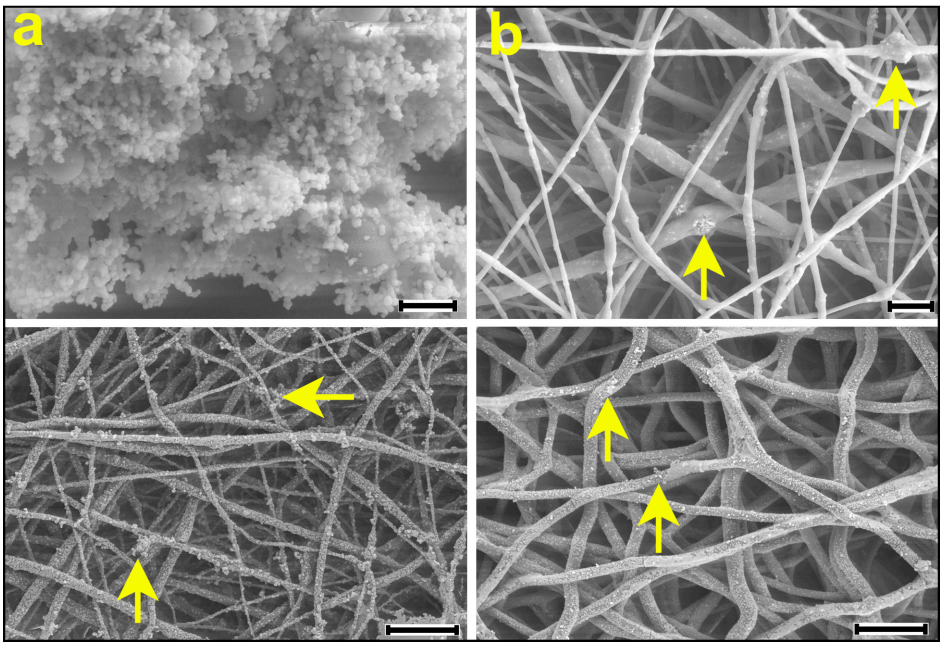

Figure 4.3: SEM micrographs of: (a) nHAP particles used to fabricate ES scaffold (scale bar: 600 nm), (b) nHAP-PCL(ES) region, with arrows showing incorporated nHAP partially exposed on the surface of fibers (scale bar: 2 μm), (c) nHAP-PCL(SBF) region, with arrows showing mineral crystallites (grown from 5×SBF) decorating fibers (scale bar: 10 μm) and (d) PUR(SBF) region, with arrows showing mineral crystallites (grown from 5×SBF) decorating fibers (scale bar: 10 μm). Fiber diameters for nHAP-PCL and PUR were designed to be significantly different for imaging purposes only.

4.4.3. Cell metabolic activity on graded scaffolds

To evaluate the effect of the two types of mineral gradients on cell behavior, rat BMSCs were cultured on various regions of ES and SBF scaffolds. Cells were found to be metabolically active on all regions of both scaffolds, and activity increased from day 1 to 7 **(Figure 4.4)**, indicating cell proliferation. Metabolic activity on all regions of the SBF scaffold was diminished compared to corresponding regions in the ES scaffold at both time points. Within each type of scaffold, activity was consistently lower on nHAP-PCL and GRAD regions as compared to PUR regions. These results suggest that nHAP particles and CaP crystallites may interfere with cell attachment and/or proliferation.

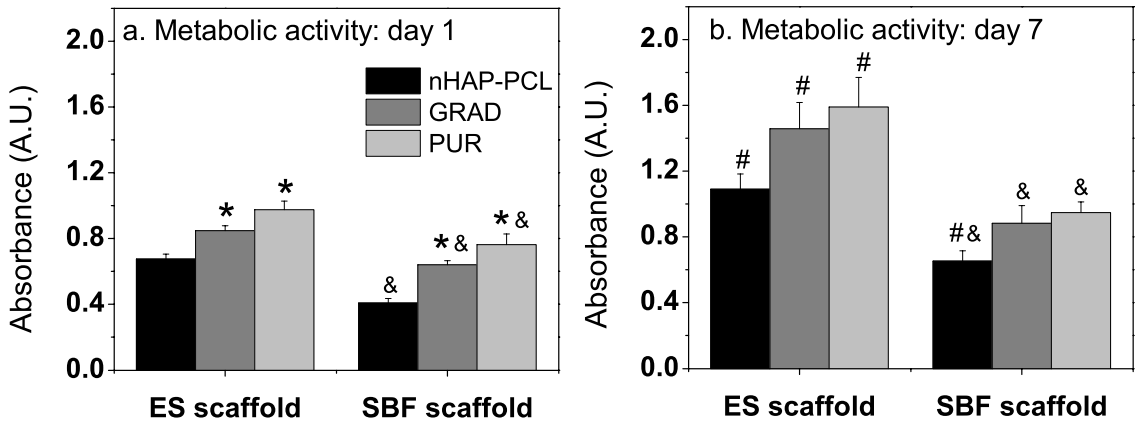

Figure 4.4: Cell metabolic activity on ES and SBF scaffolds, as determined by an MTT assay. Absorbance values correspond to mean ± standard error of mean for n =5 samples. An asterisk indicates statistical significance ($p < 0.05$) compared to the nHAP-PCL region within the same scaffold and time point. An ampersand indicates statistical significance ($p < 0.05$) compared to corresponding regions in the ES scaffold within the same time point. A pound symbol indicates statistical significance ($p < 0.05$) compared to activity on respective regions at day 1.

4.4.4. Cytoskeletal organization and cell density on graded scaffolds

Cells were stained for F-actin and nuclei at day 28 to determine the effect of different surface chemistries and topographies in influencing cell cytoskeletal organization and density (**Figure 4.5**). Among the regions of the ES scaffold, cells on nHAP-PCL(ES) appeared to possess well-developed aligned F-actin fibers (**Figure 4.5a**). In addition, this region was found to possess a high density of cells, although occasional regions of low cell density were also observed (**Figure 4.5d**). The cells on the PUR(ES) region exhibited fewer stress fibers (**Figure 4.5c**) and this region had a visually lower cell density (**Figure 4.5f**) than the nHAP-PCL(ES) region. Although occasional cell clusters were found on the PUR(ES) samples, these clusters were isolated. Cells on GRAD(ES) appeared the least-spread (**Figure 4.5b**) and this region had the lowest cell density (**Figure 4.5e**). Among the SBF scaffolds, cells on the PUR(SBF) region had a visually high density (**Figure 4.5l**), comparable to that of cells on the PUR(ES) region, and these cells possessed well-developed actin fibers (**Figure 4.5i**). Cells on the nHAP-PCL(SBF) region appeared less spread (**Figure 4.5g**) and this region had a lower cell density (**Figure 4.5j**) than the PUR(SBF) region. Moreover, cells in the nHAP-PCL(SBF) region appeared to possess a lower density than those in the nHAP-PCL(ES) region. Finally, cells in the GRAD(SBF)

region had the fewest actin stress fibers (**Figure 4.5h**) and lowest density (**Figure 4.5k**) among all regions from both types of scaffolds.

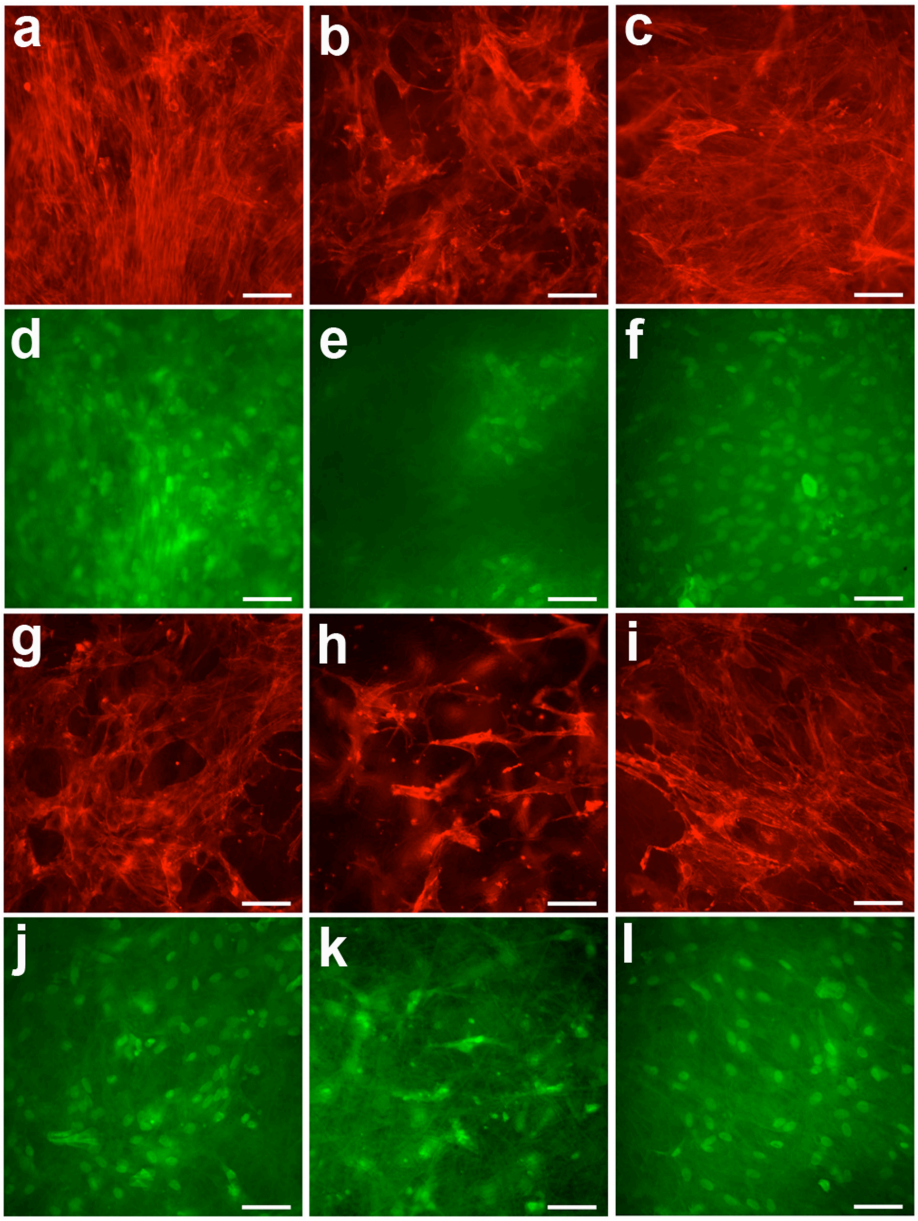

Figure 4.5: Cytoskeletal organization and cell density on ES and SBF scaffolds, as determined by staining for F-actin (rhodamine-phalloidin: red) and nuclei (DAPI: green) at day 28: (a,d) nHAP-PCL(ES), (b,e) GRAD(ES), (c,f) PUR(ES), (g,j) nHAP-PCL(SBF), (h,k) GRAD(SBF), (i,l) PUR(SBF). Scale bars correspond to 25 μm.

4.4.5. Osteoblastic differentiation on graded scaffolds

Expression of osteoblastic genes on various regions of the ES and SBF scaffolds was investigated to determine the potential of the scaffolds in guiding a gradient of osteoblastic phenotype in BMSCs. At day 14, BMP-2 expression by BMSCs was elevated on the nHAP-PCL(ES) and nHAP-PCL(SBF) regions compared to their respective PUR counterparts, although these results were not statistically significant (**Figure 4.6a**). ALP expression showed the opposite trend at day 14, with the cells on PUR(ES) and PUR(SBF) regions revealing increased expression compared to nHAP-PCL counterparts (**Figure 4.6b**).

At day 21, OPN expression was elevated on nHAP-PCL(ES) and nHAP-PCL(SBF) regions compared to their respective PUR regions (**Figure 4.7a**). BSP expression was higher on the GRAD(ES) regions compared to nHAP-PCL(ES) and PUR(ES), although these results were not statistically significant (**Figure 4.7b**). Moreover, BSP expression was similar on all regions of the SBF samples. Overall, BMP-2 and OPN mRNA were expressed in a graded fashion on the ES and SBF scaffolds, with the presence of nHAP particles and CaP crystallites enhancing their expression. In contrast, ALP mRNA expression was suppressed on the mineralized surfaces. BSP mRNA expression did not reveal a specific trend, given the large experimental variability.

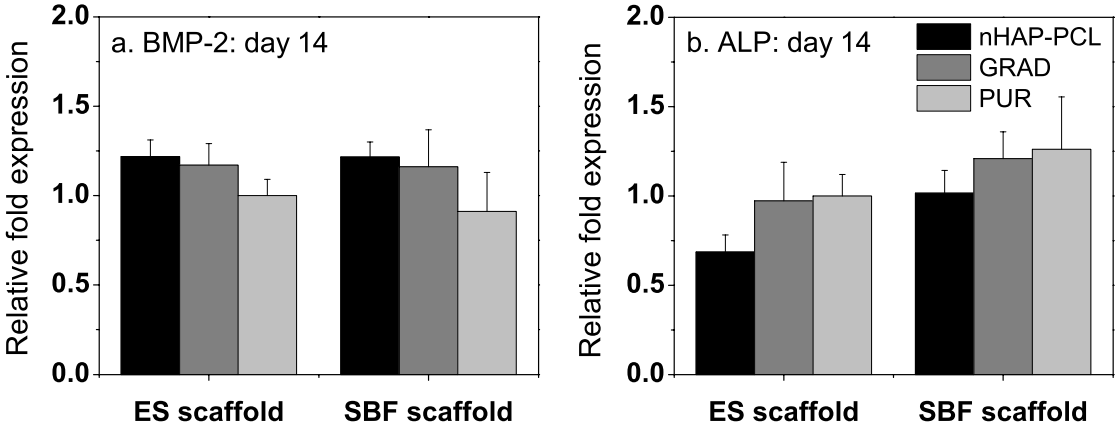

Figure 4.6: mRNA expression of markers of osteoblastic differentiation (a) BMP-2 and (b) ALP on graded scaffolds at day 14, as determined by RT-qPCR. Bars correspond to mean ± standard error of mean for n = 8 samples (n = 7 for GRAD(SBF)). β-actin was used as the reference gene and all data are normalized to PUR(ES). Data are not significantly different ($p \geq 0.05$).

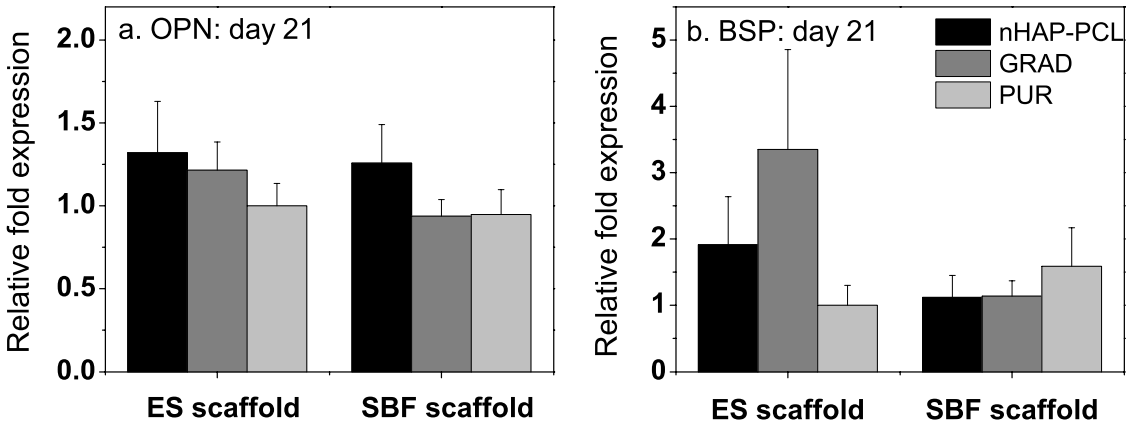

Figure 4.7: mRNA expression of markers of phenotypic maturation (a) OPN and (b) BSP on graded scaffolds at day 21, as determined by RT-qPCR. Bars correspond to mean ± standard error of mean for n = 8 samples. β-actin was used as the reference gene and all data are normalized to PUR(ES). Data are not significantly different ($p \geq 0.05$).

Immunofluorescent staining confirmed the presence of OPN and BSP in the nHAP-PCL(ES) and nHAP-PCL(SBF) regions (**Figure 4.8**). Moreover, these ECM proteins co-localized with clusters of cells.

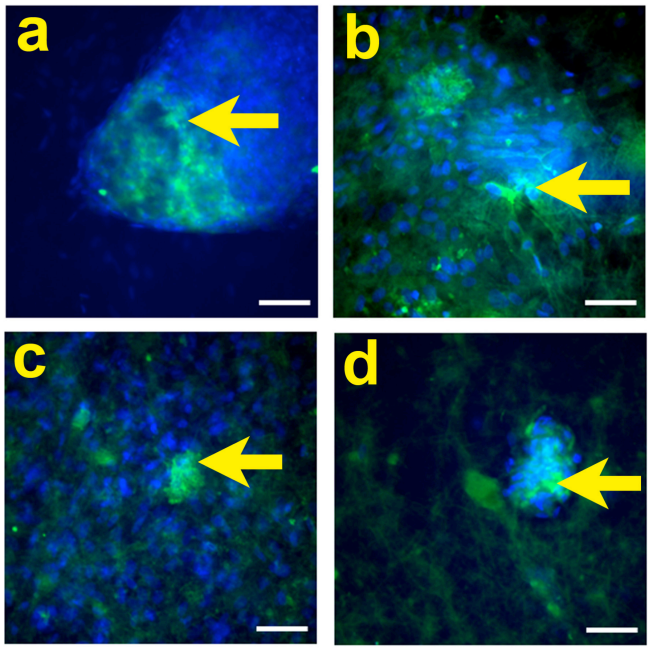

Fig 4.8: Immunofluorescent staining for ECM proteins: OPN on (a) nHAP-PCL(ES), (b) nHAP-PCL(SBF) and BSP on (c) nHAP-PCL(ES) and (d) nHAP-PCL(SBF). ECM proteins are shown in green (FITC) and cell nuclei in blue (DAPI). Arrows indicate ECM protein co-localizing with clusters of cells. Scale bars correspond to 25 μm.

4.5. Discussion

Towards achieving the long-term goal of regenerating the L-B interface, two graded scaffolds were tested for their ability to promote gradients of osteoblastic differentiation *in vitro*. Graded ES scaffolds were fabricated by co-electrospinning two polymers (one doped with nHAP particles) from offset spinnerets, while SBF scaffolds were created by immersing ES scaffolds in a 5×SBF solution. Here, the two-fold goal of introducing nHAP particles in the PCL fibers was to guide graded osteoblastic differentiation of BMSCs on the ES scaffolds and to promote selective nucleation of mineral crystallites when treated with the 5×SBF solution. PCL and PUR were chosen for the bone and ligament regions respectively due to their biocompatibility, degradability and attractive mechanical properties. To evaluate the biological effect of ES and SBF scaffolds, rat BMSCs were cultured on all regions of both scaffolds. Cells were found to be metabolically active on both scaffolds at days 1 and 7, although the presence of mineral (both nHAP particles and CaP crystallites) appeared to suppress metabolic activity. Cells were also found to be generally present in higher densities and better-spread on regions without mineral, consistent with the metabolic activity data. All regions of both graded scaffolds supported osteoblastic differentiation of BMSCs in the presence of osteogenic supplements. Gene expression of osteoblastic markers indicated that graded scaffolds have the potential to facilitate the formation of phenotypic gradients, while immunofluorescent staining confirmed phenotypic maturation.

Differences in surface topography and mineral distribution patterns between the two types of graded scaffolds were observed. On ES scaffolds, these particles were found to be only partially exposed on the surface of the fibers (**Figure 4.3b**), as has been reported previously for a similar system [147]. In addition, the nHAP particles appeared to aggregate mildly, conferring roughness on the PCL fibers, consistent with previous work [166, 167]. On SBF scaffolds, the fibers were covered with CaP crystallites whose shape and coverage were different from the nHAP particles incorporated into ES scaffolds. The mineral crystallites in the SBF scaffolds were previously determined by X-ray diffraction and energy dispersive spectroscopy to be a form of calcium-deficient hydroxyapatite [156]. Although the nHAP-PCL fibers nucleated and grew mineral from the 5×SBF solution (**Figure 4.3c**), the PUR fibers were also found to nucleate some CaP crystallites (**Figure 4.3d**), possibly due to hydrophilic urethane and urea groups in the

PUR and the random nature of the mineral precipitation process.

Cell adhesion may be affected by the nature and quantity of adsorbed proteins on regions with mineral, which may in turn be influenced by a number of factors including surface topography, surface chemistry and hydrophilicity [168]. In the present study, cell attachment and proliferation on graded ES and SBF scaffolds may be affected primarily by underlying differences in mineral distribution and surface roughness. Although the presence of nano-crystalline HAP has been shown to enhance adhesion and proliferation of BMSCs [169, 170], the results from the present study suggest that mineral (nHAP particles and/or CaP crystallites) may interfere with cell adhesion and proliferation, as indicated by the decreased cell metabolic activity on the nHAP-PCL(ES) and nHAP-PCL(SBF) regions compared to the PUR(ES) and PUR(SBF) regions respectively (**Figure 4.4**). In addition, lower cell density and fewer actin stress fibers for cells at day 28 on regions with either type of mineral as compared to cells on regions without mineral (**Figure 4.5**) indicate that inhibition of cell proliferation may have persisted throughout the course of the study. Also, the presence mineral appears to inhibit cell metabolic activity irrespective of cell type, as MC3T3-E1 osteo progenitor cells were found to be less metabolically active on mineral-containing nHAP-PCL and GRAD regions as compared to the PUR regions [9]. Moreover, this result is consistent with previous studies that have shown poor cell attachment, spreading and proliferation on rough calcium phosphate surfaces [171, 172], possibly due to an insufficient density of cell-adhesive features on rough and discontinuous surfaces. Finally, cells on the GRAD(ES) and GRAD(SBF) regions in the present study appeared to possess the lowest density and fewest actin stress fibers among all regions, suggesting that mixtures of different fiber chemistries may also affect cell adhesion and proliferation.

Conversely, osteoblastic differentiation may be enhanced by the presence of a mineral phase. BMP-2 mRNA expression by BMSCs was found to be elevated at day 14 on regions containing mineral (i.e. nHAP particles in nHAP-PCL(ES) and CaP crystallites in nHAP-PCL(SBF)), compared to regions with none to low amounts of mineral (PUR(ES) and PUR(SBF)) (**Figure 4.6a)**. This result is consistent with Kim et al. who showed elevated BMP-2 mRNA expression by BMSCs on HAP/poly(propylene fumarate) scaffolds as compared to BMSCs on scaffolds without HAP [173]. Similar to BMP-2 mRNA expression, OPN mRNA

was elevated on the mineral-containing surfaces, as compared to the PUR regions (**Figure 4.7a**). The enhanced expression of OPN mRNA by BMSCs in the presence of mineral and osteogenic supplements has been previously reported [170, 174, 175]. In addition to mRNA expression, the presence of OPN and BSP co-localizing with clusters of cells (**Figure 4.8**) indicated the formation of bone nodules, whose presence is consistent with matrix mineralization and phenotypic maturation in differentiating osteoblasts [162].

In contrast to BMP-2 and OPN, expression of ALP mRNA was lower for BMSCs on nHAP-PCL and GRAD regions than for BMSCs on PUR regions for both ES and SBF scaffolds (**Figure 4.6b**). Although the elevated expression of both ALP mRNA and enzyme by BMSCs has been shown previously in the presence of HAP [175], the results from the present study are consistent with Liu et al, who showed suppression of ALP mRNA by BMSCs grown on octacalcium phosphate as compared to cells cultured on tissue culture polystyrene [174]. ALP is an enzyme secreted by pre-osteoblasts during early stages of differentiation [161, 176], and its production by BMSCs is enhanced by the presence of dexamethasone. Moreover, its activity has been shown to diminish with phenotypic maturation of osteoblasts [177]. By day 14, expression of ALP mRNA may have been declining for BMSCs cultured on the nHAP-PCL and GRAD regions of the ES and SBF scaffolds. However, determination of such a time-dependent trend would require the simultaneous monitoring of ALP mRNA and enzyme expression over the course of the study.

In the present study, cell differentiation was likely affected by several factors, chief among them being the mineral phases. The osteogenic capacity of mineral stems primarily from its ability to release calcium and phosphate ions in aqueous environments. Jung et al have suggested that differentiation of MC3T3-E1 cells (in the presence of osteogenic supplements) proceeds via the activation of L-type and non-L-type calcium sensing receptors and the CaMK2α/CAM pathway in response to dissolved calcium ions from HAP surfaces [178]. Khoshniat et al have recently suggested that the differentiation of MC3T3-E1 cells proceeds via the activation of the ERK1/2 dependent pathway in response to elevated extracellular calcium and phosphate ion levels, although this study was not conducted on HAP surfaces [179]. While the exact mechanism of cell differentiation in the present study is not clear, the results confirm that HAP is osteoconductive (but possibly not osteoinductive) as suggested previously [180,

181]. Another factor that could have potentially affected cell differentiation in the present study is scaffold chemistry. Although the nHAP-PCL and PUR regions possessed different surface chemistries, a study by Kavlock et al has indicated that osteoblastic differentiation may not be significantly affected by such differences [19]. Specifically, the authors found no significant differences in osteocalcin mRNA and ALP expression by BMSCs cultured on segmented-PUR surfaces with different PCL weight fractions and a control poly(lactic-co-glycolic acid) surface. Yet another factor that may affect cell differentiation is fiber diameter. Although the fibers in the PCL region possessed bimodal diameter distribution, where some fibers were significantly different in diameter as compared to the PUR region, a study by Badami et al using MC3T3-E1 cells has suggested that differences in fiber diameter may not significantly affect osteoblastic differentiation [106].

Finally, both the ES and SBF scaffolds seemed to promote graded osteoblastic differentiation of BMSCs to similar extents, although the goal fabricating the SBF scaffold was to enhance cell differentiation relative to the ES scaffold. Moreover, mineral in the SBF scaffold appears to inhibit cell metabolic activity more than the mineral incorporated in the ES scaffolds. Therefore, the ES scaffolds may be a better choice for engineering the L-B interface in the long-term. In future studies, the crystalline HAP particles in these scaffolds may be substituted with a more soluble mineral phase such as a biphasic calcium phosphate in order to promote differentiation in the absence of supplements, as reported previously [182]. Future studies will also seek to fabricate scaffolds with gradients in architecture and biochemical properties to promote the *in vitro* formation of tissues with dual phenotypic gradients.

4.6. Conclusions

The goal of this study was to assess the ability of scaffolds with two types of mineral gradients to guide a spatial gradient of osteoblastic differentiation in BMSCs. Graded ES scaffold was fabricated by a process of co-electrospinning to incorporate a gradient in nHAP mineral content, while graded SBF scaffold was created by immersing the ES scaffold in a 5×SBF solution to deposit CaP mineral crystallites on the fibers. BMSCs were found to be metabolically active on all regions of the graded scaffolds. The presence of mineral in the ES and SBF scaffolds promoted the elevation of BMP-2 and OPN mRNA, while suppressing the

expression of ALP mRNA. Finally, immunofluorescent staining confirmed the presence of OPN and BSP, indicating osteoblastic maturation by day 28. In conclusion, this study indicates that scaffolds with mineral gradients can promote a spatial gradient of osteoblastic phenotype in BMSCs, which in turn may serve as a useful strategy for the regeneration of the L-B interface.

4.7. Acknowledgements

The authors thank the Institute for Critical Technologies and Applied Sciences at Virginia Tech for funding, Dr. Garth Wilkes (Department of Chemical Engineering, Virginia Tech) for the use of the electrospinning apparatus, Riley Chan and Michael Vaught (Department of Chemical Engineering, Virginia Tech) for help with designing the electrospinning mandrel, Stephen McCartney (Nano-characterization and Fabrication Laboratory, Virginia Tech) for help with SEM imaging and Dr. Robyn Cardwell (Genomic Health Incorporation, CA) for help with primer design.

Chapter 5

Fabrication of electrospun meshes possessing region-wise differences in fiber orientation, diameter and chemistry

Satyavrata Samavedi[a], Prudhvidhar Gaddam[a], Abby R. Whittington[a,b,c], Aaron S. Goldstein[a,c]

[a] Department of Chemical Engineering, Virginia Tech, Blacksburg, VA 24061, USA

[b] Department of Materials Science and Engineering, Virginia Tech, Blacksburg, VA 24061, USA

[c] School of Biomedical Engineering and Sciences, Virginia Tech, Blacksburg, VA 24061, USA

5.1. Abstract

Although bone-patellar tendon-bone (B-PT-B) autografts intended for the repair of ligament ruptures successfully integrate with host bone, these grafts still suffer from limitations such as donor site morbidity and limited supply. In contrast, engineered ligament tissue grafts modeled after B-PT-B grafts present an attractive alternative because they can recapitulate the properties of ligaments and their bony insertions. Specifically, scaffolds that mimic the extracellular matrix organization and mechano-chemical properties of ligaments and their bony insertions can potentially guide the formation of cell phenotypic gradients in the long-term by promoting the establishment of gradients in cell morphology and orientation in the short-term. Towards achieving the larger goal of creating graded scaffolds, the specific goal of this study was to fabricate electrospun meshes possessing region-wise differences in fiber orientation, diameter and chemistry using a novel dual-drum collector. Meshes were fabricated by electrospinning poly (caprolactone) and poly (lactide-co-glycolide) solutions alternately from offset spinnerets onto a slowly rotating dual-drum collector. This process resulted in the deposition of aligned PCL fibers in a gap region between the dual drums, randomly oriented

PLGA fibers on one of the drums, and a mixture of both fibers in the interfacial region in-between. Next, bone marrow stromal cells (BMSCs) cultured on these meshes were characterized to determine how fiber orientation and diameter affect cell morphology and orientation. On the random regions, BMSCs were randomly oriented and exhibited low aspect ratios, while on the aligned regions the cells were highly aligned and exhibited high aspect ratios. Fiber diameter was found to have an insignificant effect on cell shape and orientation. In conclusion, these results demonstrate that electrospun meshes possessing region-wise differences in fiber orientation, diameter and chemistry can be fabricated by using a dual-drum collector. The results further show that such meshes can promote differences in cell morphology and alignment within spatially distinct regions that mimic the cell morphology and orientation found within bone and ligament tissues. Future studies will seek to evaluate the potential of these meshes towards promoting BMSC differentiation into specific phenotypes.

Keywords: bone-ligament transition, electrospinning, dual-drum collector, fiber orientation, contact guidance

5.2. Introduction

Natural bone-ligament (B-L) transitions consist of gradients in collagen fiber orientation, as well as mechano-chemical properties that smoothly transition from bone to ligament through a fibrocartilage interface [8, 18]. While the collagen fibers found in the extracellular matrix (ECM) of anisotropic tissues such as ligaments and tendons are preferentially aligned in the direction of load, the fibers in bone are comparatively less ordered in their organization [18, 183]. Due to the differences in architecture and mechano-chemical properties, the use of soft tissues (e.g., hamstring tendon autografts) for the reconstruction of ligament ruptures results in a mismatch of properties between graft and bone. Consequently, stress-concentrations develop at the graft-bone interface, resulting in poor osseointegration [6, 123]. In contrast, a tissue engineering approach to create ligament grafts via the use of degradable scaffolds is an attractive alternative. Specifically, scaffolds that recapitulate the gradients in properties that exist at natural B-L transitions may have the potential to regenerate these tissue transitions via the

establishment of phenotypic gradients in bone marrow stromal cells (BMSCs). As a step towards achieving this larger goal, scaffolds that mimic the differences in ECM architecture across bone and ligament tissues within spatially distinct zones can provide spatial control over cell morphology and orientation [10, 19, 135].

Electrospinning is a versatile scaffold fabrication technique that allows for the creation of non-woven meshes possessing a wide variety of architectures. By using different collector geometries, the orientation of the fibers within the meshes can be precisely controlled. For example, electrospinning onto a flat plate collector results in randomly oriented fibers [106], while deposition onto a rotating drum [184], a drum comprised of parallel copper wires [185] or two grounded rods [107] results in highly aligned fibers. In addition, a central point electrode in combination with a peripheral ring electrode has been shown to align fibers radially [186], while dual collection rotatable rings have been shown to result in the formation of fiber arrays and multi-filament yarns [187]. Overall, these studies demonstrate that electrospinning onto appropriately designed collectors can result in meshes possessing complex architectures.

Electrospun meshes possessing gradients in fiber orientation have been the focus of recent efforts. More specifically, such graded meshes have been shown to possess architectures similar to the collagen fiber network found at B-L and bone-tendon transitions. For example, Thomopoulos et al fabricated gradients of fiber alignment by electrospinning a single polymer solution between two metal frames [19]. This process resulted in the formation of a mesh possessing aligned fibers between the frames and randomly oriented fibers on the frames. However, this study did not aim to create a transition zone from a region of highly aligned fibers to randomly oriented fibers. In another recent study, Xie et al used a two-step method to fabricate graded meshes [135]. Specifically, meshes were fabricated by initially depositing aligned fibers onto a grounded air-gap collector in the first step, followed by masking regions of this mesh spatio-temporally, and electrospinning layers of randomly oriented fibers atop in the second step. These meshes were shown to promote regional differences in the morphology and orientation of adipose derived stem cells. Thus, it appears that meshes possessing topographical gradients can help establish gradients of cell morphology and orientation.

Towards the long-term goal of achieving gradients of cell phenotype, the present study examined the influence of scaffolds possessing region-wise differences in topography in influencing bone marrow stromal cell (BMSC) morphology and orientation. Accordingly, a novel rotating dual-drum collector was designed to collect randomly oriented fibers on the rotating drums, and highly aligned fibers in the gap region between the drums simultaneously. Solutions of polycaprolactone (PCL) in 2,2,2 trifluoroethanol (TFE) and poly (lactide-co-glycolide) (PLGA) in 1,1,1,3,3,3 hexafluoro-2-propanol (HFIP) were electrospun onto the dual-drum collector to result in meshes possessing distinct regions of randomly oriented PLGA fibers and aligned PCL fibers. The diameter of the PCL fibers was varied by changing the concentration of the PCL solution to demonstrate that the properties in one region of the electropun meshes (i.e. PCL region) could be varied independent of the properties in another region (i.e. PLGA region). Fiber orientation and diameter were measured by analyzing micrographs of three different regions (i.e., a random, an interfacial and an aligned regions) of the electrospun meshes. To evaluate cell response, rat BMSCs were seeded on the electrospun meshes and stained for actin cytoskeleton and nuclei. Orientation, area and aspect ratios of BMSCs were determined by analyzing images of fixed cells on two different regions (i.e., random and aligned) within the same mesh.

5.3. Materials and methods

5.3.1. Materials

All chemicals, solvents and material supplies were purchased from Fisher Scientific (Pittsburgh, PA), and biological supplies from Life Technologies (Gaithersburg, MD), unless otherwise specified. 85:15 PLGA (inherent viscosity: 0.66 dL/g in chloroform) was purchased from DURECT Corporation (Birmingham, AL), while TFE was purchased from Acros Organics (Morris Plains, NJ). PCL (Mn = 70,000 – 90,000), HFIP, minimal essential medium-α modification (α-MEM), Dulbecco's modified eagle medium (DMEM), trypsin/sodium salt of ethylenediamine tetraacetic acid (trypsin/EDTA), bovine serum albumin (BSA) and Triton X-100 were purchased from Sigma Aldrich (St. Louis, MO). Fetal bovine serum (FBS) was obtained from Gemini Bio-Products (Calabasas, CA), while Vectamount AQ was purchased from Vector Labs (Burlingame, CA).

5.3.2. Design of a dual-drum collector

A dual-drum collector was constructed by connecting two 8.9 cm diameter hollow aluminum drums mechanically via a 1.5 cm diameter metal rod that spanned the central axes of both drums (**Figure 5.1**). The drums, each 8.9 cm in length, were separated by a gap distance that could be adjusted between 0 cm and a maximum of 7.6 cm. The entire dual-drum system was mounted on a fiberglass-epoxy stand and connected to a 300-to-1 geared 12 V DC motor and a controller that regulated the speed of rotation at a pre-determined rate. Both drums were designed to rotate synchronously in the same direction. The inner transverse regions of the drums and the entire metal rod were covered with Plexiglas to provide electrical insulation. The drums were electrically connected internally and the entire dual-drum system was grounded.

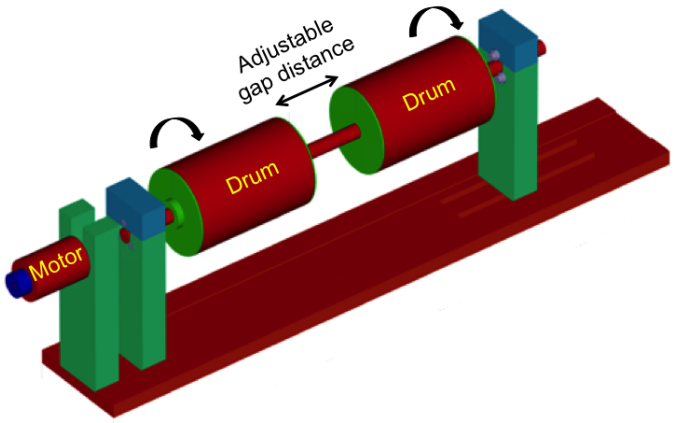

Figure 5.1: Cartoon of the dual-drum collector used in this study.

5.3.3. Electrospinning

PCL and PLGA solutions were electrospun onto the dual-drum collector to result in meshes possessing spatially distinct regions of different fiber orientations, diameters and chemistries simultaneously (**Figure 5.2**). Prior to electrospinning, the drums of the collector were wrapped in aluminum foil and the gap distance between the drums was set at 2.5 cm, which is close to the length scale of the human ACL [12]. (Moreover, a distance of 2.5 cm was determined to provide the greatest fiber alignment in pilot studies.) Cardboard shields were placed on either side of the drums to control the overlap of PCL and PLGA fibers along the length of the collector. (Representative blue shields are shown in **Figure 5.2**). Subsequently, a

13% (w/w) PLGA solution in HFIP was loaded into a 10 mL plastic syringe, and either a 7.5% (w/w) or a 10.5% (w/w) PCL solution in TFE was loaded into a separate 10 mL plastic syringe, and the PLGA and PCL solutions were dispensed from separate syringe pumps placed on opposite sides of the dual-drum collector. The syringes were oriented towards the collector such that the fibers from the PCL solution covered the gap region between the drums as well as an interfacial region on one of the drums, while the fibers from the PLGA solution covered the interfacial region plus an additional random region on one of the drums. PCL was initially electrospun for 2 min at a flow rate of 3 mL/h, throw distance of 12 cm and a voltage of 13 kV onto the dual-drum system rotating at a slow speed of ~20 rpm. Then, the power supply to the PCL solution was turned off and the PLGA solution was electrospun for 2 min at a flow rate of 3 mL/h, throw distance of 12 cm and a voltage of 13 kV. Subsequently, the solutions were spun alternately for 5 min each and thereafter for 10 min (PCL) and 6 min (PLGA). Electrospinning was performed in this manner for over an hour to result in an electrospun mesh consisting of three regions: an aligned region possessing PCL fibers in the gap distance (~ 2.5 cm wide), an interfacial region consisting of a mixture of randomly oriented PCL and PLGA fibers on the edge of one of the drums (~ 0.75 - 1.25 cm wide), and a random region comprising PLGA fibers on the same drum (~ 2 cm wide). Meshes fabricated using the 7.5% (w/w) PCL and 13% PLGA solutions were designated "PCL7.5-PLGA13", while meshes fabricated using the 10.5% (w/w) PCL and 13% (w/w) PLGA solutions were designated "PCL10.5-PLGA13". (Here, the diameter of the PLGA fibers was kept constant across the PCL7.5-PLGA13 and PCL10.5-PLGA13 meshes, while the diameter of the PCL fibers was varied.) Post-electrospinning, the meshes were allowed to dry in a fume hood overnight.

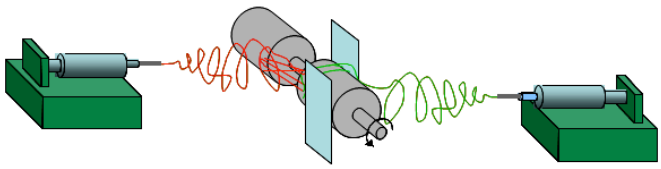

Figure 5.2: Cartoon of electrospinning set-up depicting offset spinnerets spinning onto the dual-drum collector. In this study, PCL (either a 7.5%(w/w) or a 10.5%(w/w) solution) was electrospun into the gap region between the drums (red fibers), while PLGA (a 13% (w/w) solution) was electrospun onto one of the rotating drums (green fibers).

5.3.4. Characterization of electrospun meshes

Fiber morphology, diameter and orientation were quantified from scanning electron micrographs. Briefly, samples from the aligned, interfacial and random regions of the electrospun meshes were mounted on scanning electron microscopy (SEM) stubs and sputter-coated with a layer of gold-palladium (Model 208 HR, Cressington Scientific Instruments, Cranberry, PA). Samples were subsequently imaged using an SEM instrument (LEO1550, Oxford Instruments, Oxfordshire, UK) at an operating voltage of 5 kV using a secondary electron detector. Images were exported to ImageJ software (National Institutes of Health, Bethesda, MD), and fiber orientation was quantified in terms of an angular standard deviation (ASD) for each region, as described previously [184]. Concurrently, fiber diameters were also determined.

5.3.5. BMSC harvest and cell culture

BMSCs were obtained from ~2 month old female Lewis rats in accordance with the Institute for Animal Care and Use Committee at Virginia Tech, using a procedure described previously [164]. Briefly, bone marrow was extracted from the femurs and tibia of the rats, and the plastic-adherent population of cells was isolated after 24 h of culture. Cells were maintained in α-MEM, supplemented with 10% FBS and 1% antibiotic/antimycotic in a 37 °C, 5% CO_2 incubator for 10 days, after which they were dissociated every 3 or 4 days with trypsin/EDTA and cryopreserved in liquid nitrogen vapor with the addition of 10% dimethylsulfoxide as a cryo-protectant. For the studies described further, cells were cultured in growth medium (DMEM supplemented with 10% FBS and 1% antibiotic/antimycotic).

For cell culture, electrospun meshes were carefully removed from the dual-drum, immobilized onto 7.6 cm × 2.5 cm glass slides using medical adhesive silicone (Factor II, Lakeside, AZ), and dried in a vacuum chamber overnight to remove residual solvent. Subsequently, the glass slides were transferred into the wells of custom designed polycarbonate dish inserts and sterilized by exposure to ultraviolet radiation overnight. The inserts were then transferred into sterile 150 mm Petri dishes, and the meshes were incubated in 8 mL of growth medium for 24 h at 37 °C and 5% CO_2 to promote the adsorption of serum proteins. Thereafter,

BMSCs (at passage 3) were seeded drop wise onto the aligned and random regions of the meshes at a density of ~5000 cells/ cm^2, which corresponded to a total of ~31,800 cells for the aligned region and ~25,400 cells for the random region. Cells were cultured on the meshes for a total of 3 days.

5.3.6. Cell morphology and orientation on electrospun meshes

Cell morphology and orientation on the electrospun meshes were determined from cell shape. Briefly, cells on the meshes were washed thrice with phosphate buffered saline (PBS) after 3 days of culture and fixed with a 4% methanol-free formaldehyde solution. Next, they were permeabilized with a 0.5% Triton X-100 solution (in PBS) and subsequently stained with a solution of rhodamine phalloidin (1:60 dilution in PBS) for 20 min. Finally, cells were counterstained with DAPI (1 μg/mL in PBS) for 5 min. (During this process, cells were washed thrice with PBS in between the staining steps.) Cells on the aligned and random regions of the meshes were imaged at 20 × magnification under a green (for rhodamine) and an ultraviolet filter (for DAPI) using a Leica DM IL microscope fitted with a DFC 420 color camera (Leica Microsystems Inc., Buffalo Grove, IL). Images were exported into ImageJ and outlines were drawn around cells to approximate cell shape to an ellipse. Thereafter, cell morphology was characterized in terms of area and aspect ratio, and cell orientation in terms of ASD. Cells in physical contact with each other were excluded from this analysis due to contact inhibition.

5.3.7. Statistical analysis

An unpaired one-tailed student's t-test was used to determine statistical significance, with a p-value < 0.05 considered significant. All results are reported as mean ± standard deviation. For fiber orientation and diameter, 100 fibers were analyzed, while for cell morphology, at least 125 cells per region over three different samples for each mesh group were analyzed.

5.4. Results

5.4.1. Fabrication and characterization of electrospun meshes

Co-electrospinning from offset spinnerets resulted in the formation of meshes with spatially distinct regions possessing different fiber orientations, diameters and chemistry. Differences in properties across three regions (i.e., random, interfacial and aligned) of the meshes were confirmed via SEM imaging (**Figure 5.3**). Specifically, in the PCL7.5-PLGA13 and PCL10.5-PLGA13 meshes, the PLGA fibers were randomly oriented, while the PCL fibers were aligned in the direction of the gradient. The interfacial region was comprised of randomly oriented PLGA (larger diameter) and randomly oriented PCL fibers (smaller diameter). In addition, the edges of the interfacial region consisted of perpendicularly oriented fibers (**Figure 5.4**). Due to the presence of this artifact, the interfacial region was not characterized further. ASD and diameters for fibers from the random and aligned regions of both meshes are presented in **Table 5.1**. Fibers in the aligned PCL region of both PCL7.5-PLGA13 and PCL10.5-PLGA13 meshes possessed ASD lower than fibers in the respective random PLGA regions. Moreover, the fiber diameter for the PCL region in the PCL7.5-PLGA13 mesh was smaller than the fiber diameter for the PCL region in the PCL10.5-PLGA13 mesh.

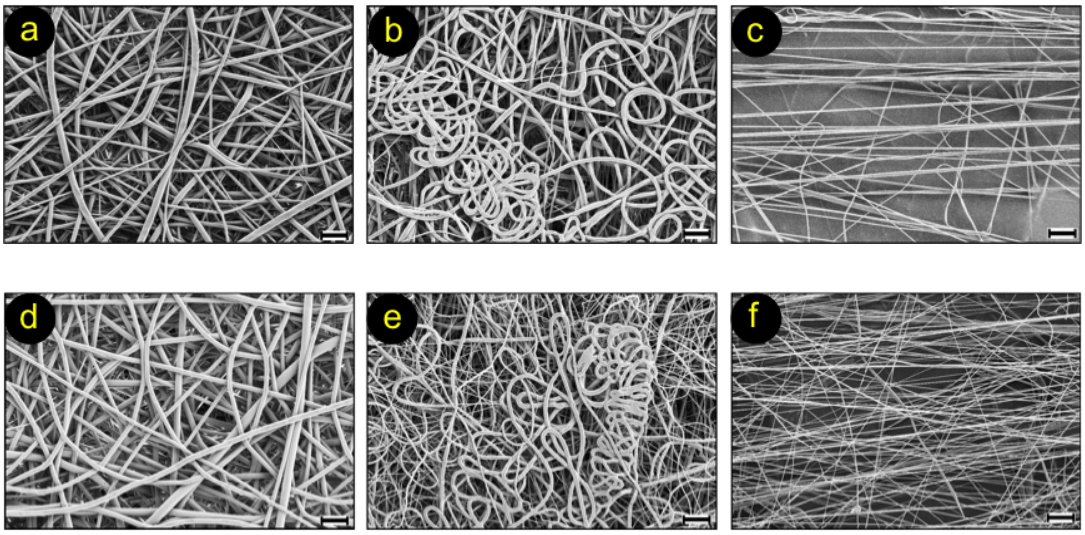

Figure 5.3: SEM micrographs (collected parallel to the direction of gradient) from the (a) random PLGA region, (b) interfacial PLGA/PCL region and (c) aligned PCL region of the PCL7.5-PLGA13 mesh, and (d) random PLGA region, (e) interfacial PLGA/PCL region and (f) aligned PCL region of the PCL10.5-PLGA13 mesh. Scale bars represent 10 μm.

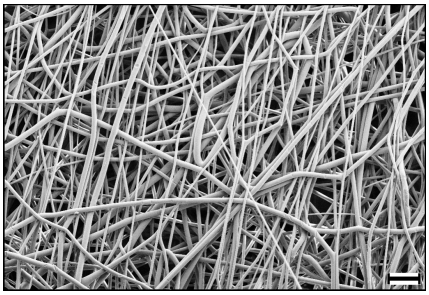

Figure 5.4: SEM micrograph of the edge of the interfacial region from PCL10.5-PLGA13 mesh showing perpendicularly oriented fibers. Scale bar represents 10 μm.

Graded mesh	Region	Fiber ASD (deg)	Fiber diameter (μm)
PCL7.5-PLGA13	Random	57.1	2.3 ± 0.69
	Aligned	20.3	0.36 ± 0.11
PCL10.5-PLGA13	Random	58.0	2.0 ± 0.51
	Aligned	24.8	0.74 ± 0.22

Table 5.1: ASD and diameters of fibers from the random and aligned regions of PCL7.5-PLGA13 and PCL10.5-PLGA13 meshes.

5.4.2. Cell morphology on electrospun meshes

BMSCs were cultured on electrospun meshes to evaluate the influence of fiber alignment, diameter and chemistry of two different regions (i.e., random and aligned) on cell response. Cells were randomly oriented and stretched in different directions on the random regions of both meshes, while they were aligned in the direction of the gradient on the aligned regions (**Figure 5.5**). Moreover, cells on the aligned regions were found to possess bundled actin cytoskeleton with distinct actin fibers, in contrast to the diffuse actin cytoskeleton found in cells on the random regions. In addition to the differences in cell shape, differences in the alignment of nuclei (dictated by the underlying fiber orientation) were also observed.

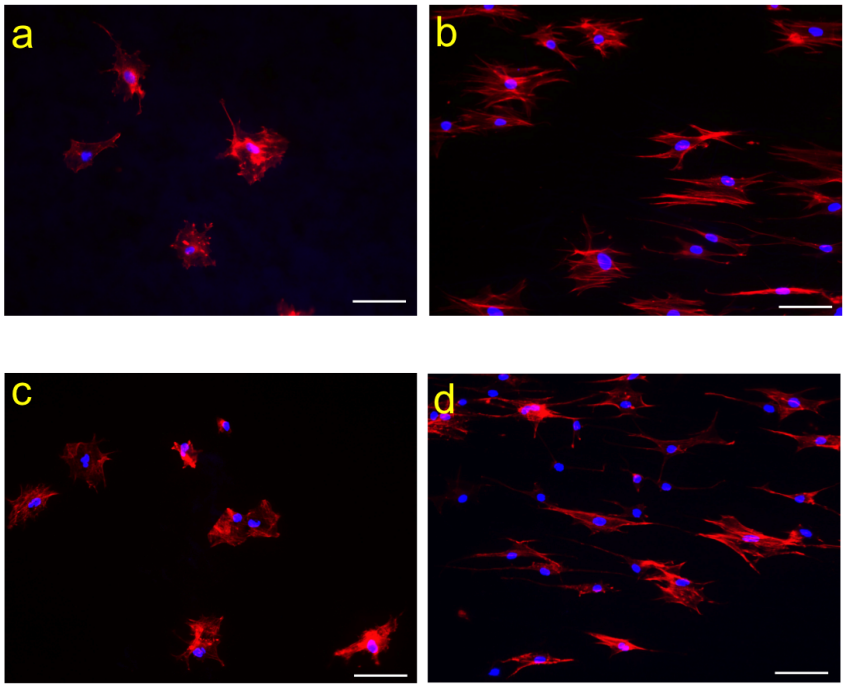

Figure 5.5: BMSC morphology on the (a) random and (b) aligned regions of the PCL7.5-PLGA13 mesh, and (c) random and (d) aligned regions of PCL10.5-PLGA13 mesh, stained for actin cytoskeleton (red) and nuclei (blue). Scale bars represent 100 μm.

Quantitative analysis of cell shape revealed differences in ASD and aspect ratios for cells on the random and aligned regions of both meshes (**Figure 5.6**). In general, cells on the random regions possessed ASD in excess of 50°, while cells on the aligned regions possessed ASD smaller than 20°. Although areas were not significantly different for cells on the random and aligned regions, the mean aspect ratio for cells was significantly different between the random and aligned regions. Specifically, cells on the random regions exhibited aspect ratios slightly lesser than 2, in contrast to cells on the aligned regions, which possessed aspect ratios in excess of 4. No differences in cell morphology and orientation were observed between the aligned PCL regions of the PCL7.5-PLGA13 mesh and the PCL10.5-PLGA13 mesh, indicating that fiber diameter had only a minor effect.

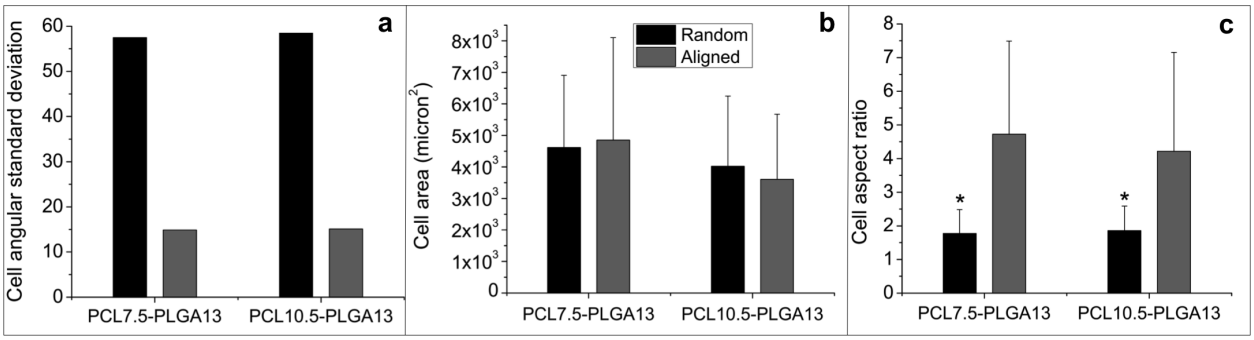

Figure 5.6: Cell shape on the random and aligned regions of the PCL7.5-PLGA13 mesh and the PCL10.5-PLGA13 mesh: a) ASD, b) area and c) aspect ratio. An asterisk indicates significantly different values compared to respective random regions ($p < 0.05$).

5.5. Discussion

The overall goal of this study was to construct and validate a dual-drum collector for the fabrication of meshes possessing simultaneous region-wise differences in fiber orientation, diameter and chemistry. Towards this end, meshes were fabricated by electrospinning either a 7.5% (w/w) or a 10.5 % (w/w) PCL solution in the gap region of a dual-drum collector and concurrently electrospinning a 13% (w/w) PLGA solution from an offset spinneret onto one of the drums of the same collector. This process resulted in the formation of meshes possessing a random PLGA region, an aligned PCL region and an interfacial region consisting of PLGA and PCL fibers. Analysis of SEM micrographs demonstrated differences in fiber ASD and fiber diameter in the random and aligned regions of both meshes. Finally, BMSCs were highly aligned in response to the fiber orientation in the aligned region as compared to the random region. Quantification of cell shape and morphology demonstrated distinct differences in cell ASD and aspect ratios between the random and aligned regions of both meshes.

Methods to align electrospun fibers have been widely reported in the literature. Although fast-rotating single drum collectors have been used for fabricating electrospun meshes possessing highly aligned fibers [90, 188], such collectors do not allow for the creation of meshes possessing gradients in fiber chemistry and alignment in the same direction. However, recent studies reporting the fabrication of meshes possessing gradients in fiber architecture also suffer from limitations. For example, Thomopulous et al – who reported the fabrication of scaffolds exhibiting an abrupt change from an aligned to a random section – did not aim to create an

interfacial zone [19]. Although Xie et al were able to overcome this limitation, they fabricated graded meshes by electrospinning an aligned region followed by a random region in two separate steps [135]. In contrast, the present study – using a novel dual-drum collector to create meshes possessing different properties across different regions – presents distinct improvements over previous studies. It allows not only for the creation of an interfacial region that integrates the random and aligned regions, but also permits the fabrication of scaffolds possessing region-wise differences in fiber orientation, diameter and chemistry in a single step (**Figure 5.3**). A minor caveat is the bridging of fibers between the shields and the drums, and the subsequent deposition of these perpendicularly aligned fibers at the edge of the interfacial region (**Figure 5.4**). A second caveat is the difference in thickness across the various regions of the scaffolds that arises from electrospinning two polymer solutions in the interfacial region as compared to one solution each in the aligned and random regions. Despite these limitations, the dual-drum system can be used to create scaffolds fully modeled after B-PT-B autografts by simultaneously electrospinning a third solution as randomly oriented fibers onto the second drum.

The properties of the meshes fabricated in this study were varied by changing polymer chemistry and solution concentration. First, the use of two different polymer solutions and the judicious placement of shields during electrospinning resulted in the selective deposition of PCL fibers in the aligned region and PLGA fibers in the random region. (The two polymers could not be electrospun simultaneously due to charge-charge repulsion in the interfacial region.) Second, the properties of the PCL region were varied independent of the properties of the PLGA region by changing the concentration of the PCL solution, while maintaining the PLGA solution concentration constant across the PCL7.5-PLGA13 and PCL10.5-PLGA13 meshes. This approach of changing polymer concentration to vary fiber diameter has been validated in previous studies [184, 189]. Smaller fiber diameters were chosen for the aligned region in comparison to the random region, because diameters in the sub-micron range can potentially enhance ligament differentiation of BMSCs compared to diameters larger than a micron [24].

In the present study, BMSCs responded to a variety of cues provided within the scaffolds, most significantly fiber alignment. BMSCs have been shown to respond to differences in underlying surface topography via the phenomenon of contact guidance. For example, Bashur et al showed that BMSCs aligned in the direction of fiber alignment [24]. Moreover, they reported

that cell ASD systematically decreased with an increase in fiber alignment, while cell aspect ratios showed the opposite trend. These results are consistent with the results from the present study that demonstrated significantly lower ASD and higher aspect ratios for cells on the aligned regions as compared to cells on the random regions of both the PCL7.5-PLGA13 and PCL10.5-PLGA13 meshes (**Figure 5.6**). Although cell area was not significantly different between the random and aligned regions, cells on the random region of the scaffolds were rhomboidally shaped, and possessed randomly oriented actin fibers, while cells on the aligned regions were elongated in the direction of fiber orientation and possessed aligned actin bundles (**Figure 5.5**). These results are consistent with the results reported by Li et al, who used a fast-rotating collector to systematically vary fiber orientation and subsequently studied the effect of fiber orientation on cell morphology and orientation [188].

In addition to differences in fiber alignment, BMSCs also responded to the differences in fiber chemistry and diameter across the random and aligned regions. Fiber chemistry possibly played only a minor role in influencing cell alignment because BMSCs have been shown in previous studies to align on oriented PLGA [190], PCL [191] and polyurethane [24] electrospun substrates. In contrast, fiber diameter was expected to have an impact on cell area and aspect ratios [24, 184, 189, 192], although no significant effects were noted in the present study. For example, Bashur et al, in two independent studies, reported significantly greater areas and aspect ratios for BMSCs [24] and fibroblasts [184] on large diameter fibers (> 2 μm) compared to small diameter fibers (< 0.25 μm). In the present study, the diameters for the fibers in the aligned PCL regions of the PCL7.5-PLGA13 and PCL10.5-PLGA13 meshes may not have been sufficiently different to result in significantly different cell areas and aspect ratios. Nevertheless, the ability to vary the properties in one region of the electrospun meshes independent of another can potentially be used to functionalize selected regions with therapeutics to control cell differentiation in future studies.

In summary, this study demonstrates for the first time that a dual-drum collector can be used for the fabrication of meshes possessing simultaneous differences in fiber orientation, diameter and chemistry across different regions within a single mesh. The results also demonstrate that these meshes can promote differences in cell morphology and orientation that recapitulate the differences in cell morphology found within natural bone and ligament tissues.

Future studies will seek to evaluate the effect of fiber alignment, diameter and chemistry on BMSC differentiation, as well as the orientation of collagen fibers in the ECM.

5.6. Acknowledgments

The authors thank Riley Chan, Michael Vaught and Kevin Holhouser from the Department of Chemical Engineering, Virginia Tech for their extensive help with the design and construction of the dual-drum collector as well as the P 150 dish inserts for cell culture. The authors are also grateful to Dr. Padma Rajagopalan (Chemical Engineering, Virginia Tech) for donating Lewis rats. This work was funded by a National Science Foundation grant (# 0854149).

Chapter 6

Development of microspheres for protecting protein activity during electrospinning

Satyavrata Samavedi[a*], Cullen J. Fleming[a*], Samuel D. Inkrote[a], Tyler M. Horseman[b], Aaron S. Goldstein[a,c], Abby R. Whittington[a,b,c]

[a] Department of Chemical Engineering, Virginia Tech, Blacksburg, VA 24061, USA

[b] Department of Materials Science and Engineering, Virginia Tech, Blacksburg, VA 24061, USA

[c] School of Biomedical Engineering and Sciences, Virginia Tech, Blacksburg, VA 24061, USA

* Both authors contributed equally to this chapter: S. Samavedi was responsible for generating ideas, designing experiments, conducting experiments, analyzing and interpreting results, and writing most of this chapter, while C.J. Fleming (S. Samavedi's undergraduate student mentee) was responsible for conducting a major portion of the experiments and assisting with writing sections in this chapter.

6.1. Abstract

Although electrospun scaffolds have been widely used for a variety of tissue engineering applications, they do not possess specific biological cues to precisely control the differentiation of stem cells. The incorporation of growth factors (GFs) into electrospun scaffolds, and the subsequent release of such factors in a controlled manner, can potentially provide tight control over cell differentiation. However, harsh processing conditions such as organic solvents and high voltages used during the electrospinning process can denature GFs and render them biologically inactive. Consequently, GFs must either be introduced into scaffolds post-fabrication, or incorporated into a carrier that can protect them during the electrospinning

process. The goal of this study was to protect GFs by encapsulating them within a microsphere (MS) carrier phase. Towards this end, four sets of experiments were conducted sequentially. The first set of experiments aimed to show that MSs could release a model protein in an active conformation. Accordingly, lysozyme was shown to be released in an active form from cross-linked gelatin MSs over a period of 3 weeks. Subsequently, the second set of experiments aimed to demonstrate that MSs could be incorporated into electrospun meshes. Here, MSs were shown to be successfully electrospun from a polymer solution to result in MS-mesh samples. Thereafter, the third set of experiments aimed to demonstrate that MSs could protect protein activity during electrospinning. Specifically, lysozyme – incorporated within MSs and electrospun – was found to be active, compared to lysozyme directly electrospun from a polymer solution. Finally, the fourth set of studies aimed to determine the effect of fibroblastic growth factor-2 (FGF-2) on the proliferation of bone marrow stromal cells. Here, FGF-2 was found to have a positive effect on cell metabolic activity after 3 and 7 days of culture, with a significant effect detectable only at a threshold concentration of 2.5 ng/mL FGF-2 at day 7. Overall, the results from these experiments indicate that gelatin MSs are a viable option to protect and deliver lysozyme in an active form from electrospun scaffolds.

Key words: electrospinning, growth factor activity, gelatin microsphere, lysozyme, fibroblastic growth factor-2

6.2. Introduction

Over the years, scaffolds possessing a variety of architectures, mechanical properties and chemistries have been investigated for their potential to regenerate tissues [193]. Among the various scaffolding techniques, electrospinning is widely popular for its ability to create scaffolds that can be used to engineer connective tissues such as the ligament [24, 189, 194, 195]. In particular, the fibrous architecture of electrospun scaffolds mimics the organization of collagen fibers found in the extracellular matrix of ligaments, and thus presents topographical features that cells can recognize. While electrospun scaffolds can affect cell morphology via the phenomenon of contact guidance [24], they lack sufficient biological cues to intrinsically guide

cell phenotypic fate [196]. Specifically, such scaffolds generally do not possess active binding sites for receptor-mediated cell adhesion, nor are they designed to deliver biochemical agents to guide cell differentiation and phenotypic maturation. Thus, the incorporation of therapeutics such as drugs or growth factors (GFs) into electrospun scaffolds offers great potential to precisely guide cell differentiation and maturation into specific tissue types.

GFs are a vital component of the tissue engineering paradigm because they help guide the differentiation of stem cells towards specific lineages. Typically, GFs play multiple roles in guiding tissue formation including influencing cell adhesion, proliferation, migration and differentiation [116, 118]. Several GFs such as fibroblastic growth factor-2 (FGF-2), epidermal growth factor, insulin-like growth factor II and transforming growth factor-β1 (TGF-β1) – both individually and in combination – have been shown to induce ligamentous differentiation of stem cells [120, 121]. FGF-2 in particular stimulates the proliferation of bone marrow stromal cells (BMSCs) and promotes their differentiation towards the fibroblastic lineage [197, 198]. Thus, the incorporation of FGF-2 within electrospun scaffolds can serve as a useful strategy for guiding the differentiation of BMSCs and promoting connective tissue formation in the long-term.

Although FGF-2 has been successfully incorporated within electrospun scaffolds by direct blending [27, 199], this approach suffers from two limitations [28, 29]. First, the use of harsh organic solvents to dissolve the carrier polymer can denature the GF and diminish its biological activity [30]. Second, intense processing conditions such as high voltage can also significantly reduce the biological activity of the GF. In contrast, the encapsulation of GFs within a protective hydrophilic carrier phase such as gelatin prior to incorporation within an electrospun scaffold can potentially protect GF activity. Here, the carrier phase may help prevent GF denaturation during electrospinning and also allow for the release of GF independent of the degradation kinetics of the electrospun polymer.

Towards the long-term goal of incorporating GFs within electrospun scaffolds for tissue engineering applications, a series of experiments were performed to determine the role of gelatin microspheres (MSs) in protecting the activity of sensitive proteins during electrospinning. First, MSs were fabricated and tested for their ability to release a model protein (lysozyme) in an

active form. Second, the feasibility of incorporating MSs within electrospun scaffolds was evaluated. Third, the role of MSs in protecting protein activity during electrospinning from an aqueous polymer solution was determined. Fourth, the biological effect of FGF-2 on BMSCs (in the absence of MSs) was investigated.

6.3. Materials and Methods

6.3.1. Materials

Polycaprolactone (PCL) (inherent viscosity: 1.21 dL/g) and 50:50 poly(lactic-co-glycolic acid) (PLGA) (inherent viscosity: 0.66 dL/g) were purchased from DURECT Corporation, Birmingham, AL, while 2,2,2 trifluoroethanol (TFE) was purchased from Acros Organics (Morris Plains, NJ). Pure-grade olive oil – imported from Italy – was purchased from The Kroger Co. (Blacksburg, VA). Gelatin type B powder (~ 225 g Bloom from bovine skin), glutaraldehyde solution, glycine, sodium azide, lysozyme powder (from chicken egg white), poly (ethylene oxide) (PEO), bovine serum albumin- fraction V (BSA), minimal essential medium-α modification (α-MEM) and Dulbecco's modified eagle medium (DMEM) were purchased from Sigma Aldrich (St. Louis, MO), while fetal bovine serum (FBS) was purchased from Gemini Bio-products (Calabasas, CA). Fluorescein isothiocyanate conjugated BSA (FITC-BSA), collagenase (type IV, prepared from Clostridium Histolyticum), Enzcheck® lysozyme assay kit, FGF-2 and alamar blue reagent were purchased from Life Technologies (Grand Island, NY). All other laboratory supplies, chemicals and solvents were purchased from Fisher Scientific (Pittsburgh, PA).

6.3.2. Gelatin MSs: fabrication, cross-linking and lysozyme release

6.3.2.1. Fabrication of gelatin MSs

Gelatin MSs were fabricated using a single emulsion method, as described previously [200, 201]. Briefly, a 10% (w/v) solution of gelatin B at 60 °C was dispensed drop-wise via a 30-G needle into olive oil stirring at 60 °C. Thereafter, the emulsion was allowed to cool and was subsequently treated with chilled acetone for 1 h to allow for dehydration of MSs. Next, MSs were separated via centrifugation at 4000 rpm and 4 °C for 5 min. They were then washed

thrice in chilled acetone to remove residual oil, and collected by centrifugation. Thereafter, they were separated into various size fractions by sieving. MSs in the size range 25-53 μm were dried at 4 °C and used for the remainder of the studies. (MSs larger than 53 μm were not used because electrospinning them from a polymer solution can result in clumping and needle-clogging.)

6.3.2.2. Cross-linking of MSs

Gelatin MSs were cross-linked via a previously established protocol [200, 201]. Briefly, MSs in the 25-53 μm range were cross-linked for 15 h in a chilled 40 mM glutaraldehyde solution containing 0.1% Tween-80. After cross-linking, they were separated via centrifugation at 4000 rpm and 4 °C for 5 min. Thereafter, they were treated with a 100 mM glycine solution containing 0.5% Tween-80 for 1 h at 37 °C to remove unreacted residual glutaraldehyde. Subsequently, they were separated via centrifugation at 4000 rpm and room temperature for 5 min, and washed thrice in deionized water. Cross-linked MSs were frozen overnight at -80 °C, and subsequently lyophilized in a FreeZone 6-liter console freeze dry system (Labconco Inc., Kansas City, MO). Post-drying, cross-linked MSs were stored dry at 4 °C and were subsequently imaged under a scanning electron microscope (SEM) (LEO1550, Oxford Instruments, Oxfordshire, UK) at an operating voltage of 5 kV.

6.3.2.3. Swelling ratio of MSs

The maximum swelling volume of MSs was determined by soaking a known amount of cross-linked MSs in a 10 mM solution of phosphate buffered saline (PBS) for 24 h in a glass container at room temperature [201]. The weight of MSs was recorded after 24 h, and the MSs were subsequently freeze-dried. A fold-swelling ratio, S, was determined according to **Equation 1**, where $W_{s,v}$ is the weight of the hydrated MSs plus the container, $W_{d,v}$ is the weight of freeze-dried MSs plus the container and W_v is the weight of the container.

$$S = \frac{W_{s,v} - W_{d,v}}{W_{d,v} - W_v} \qquad \textbf{Equation 1}$$

6.3.2.4. Lysozyme release study

In vitro release kinetics of a model protein lysozyme from MSs was determined by performing a 3-week release study. Briefly, 50 mg of cross-linked MSs were hydrated in 350 μL of a lysozyme solution (14.3 μg/mL in a 0.1% BSA solution) at 4 °C for 15 h within 1.5 mL micro-centrifuge tubes to allow a theoretical loading of 5 μg lysozyme within the MSs. A loading volume of 7 μL per mg of MSs (which is less than the maximum swelling volume) was used to ensure complete absorption of the lysozyme solution [201]. Lysozyme-free MS controls were prepared similarly by absorption of 10 mM PBS solution. Post-absorption, 1.15 mL of release medium (a 10 mM PBS and 2 mM NaN_3 solution, with or without 1 μg/mL collagenase) was added to the MS samples and incubated at 37 °C on a rocker table. At pre-determined time points (12 h, 1 d, 2 d, 3 d, 5 d, 7 d, 10 d, 14 d, 19 d and 23 d), the MS samples were centrifuged at 4000 rpm for 90 s, and 1 mL of supernatant was collected and frozen at -20 °C. At each time point, 1 mL of release medium (with or without 1 μg/mL collagenase) was replenished and the release study was continued for a period of over 3 weeks.

At the end of the release study, the amount of active lysozyme released from the MSs was determined using an EnzChek® lysozyme assay kit, performed according to the manufacturer's instructions. Briefly, the lysozyme-containing supernatant was thawed and diluted in 1× reaction buffer (0.1 M Na_3PO_4, 0.1 M NaCl, 2 mM NaN_3: pH 7.5), and 50 μL of diluted supernatant was added to the wells of a 96-well black bottom plate. Thereafter, 50 μL of a diluted fluorescein-lysozyme substrate (containing a culture of *Micrococcus lysodeikticus*) was added, and the enzymatic reaction was allowed to proceed in the dark for 30 min at 37 °C. After 30 min, fluorescence of the samples was measured at excitation and emission wavelengths of 494 nm and 518 nm respectively, using a SpectraMax SBFe multi-model micro-plate reader (Molecular Devices, Sunnyvale, CA). The fluorescence values were converted to a concentration of active lysozyme by constructing a standard curve from running this assay on known amounts of serially diluted lysozyme. Curves for the cumulative release of lysozyme from MSs were constructed based on the weights of active lysozyme obtained from the assay.

6.3.3. Fabrication of MS-mesh samples

6.3.3.1. Electrospinning MSs from a polymer solution

A 14% (w/v) PCL solution was prepared in TFE and stirred overnight. Immediately prior to electrospinning, dry cross-linked MSs were added to the PCL solution at final concentrations of 10, 30, and 50 mg MSs/mL of PCL solution. The MSs were subsequently sonicated in the PCL solution in a 10 mL plastic syringe (fitted with an 18-G blunt-tipped stainless steel needle) for a minute. The suspension was electrospun onto a slowly rotating grounded aluminum collector using a flow rate of 2.5 mL/h, throw distance of 15 cm, a potential of -15 kV and at ambient temperature and humidity. During the electrospinning process, MS-mesh samples (collected on glass coverslips) were periodically removed from the rotating collector, and imaged using a Leica DM IL microscope fitted with a DFC 420 color camera (Leica Microsystems Inc., Buffalo Grove, IL).

In a modification to this experiment, 315 μg lysozyme was loaded within 90 mg of cross-linked MSs by hydrating the MSs in a solution of lysozyme overnight at 4 °C. Subsequently, MSs were loaded into 3 mL of a 20% (w/v) PLGA solution in TFE, sonicated and electrospun at a flow rate of 3 mL/h, voltage of 15 kV and throw distance of 15 cm. Thereafter, MS-mesh samples were imaged by SEM to characterize scaffold morphology.

6.3.3.2. Protein retention within MS-mesh samples

Cross-linked MSs were hydrated with FITC-BSA overnight using the procedure described in **Section 6.3.2.4**. Hydrated MSs were added to a 20% (w/v) PLGA solution in TFE (at a concentration of 30 mg MSs/mL of polymer solution) within a 10 mL plastic syringe fitted with an 18-G blunt-tipped stainless steel needle, and the solution was sonicated to disperse the MSs. MS-containing PLGA solution was electrospun in the dark onto a grounded rotating aluminum collector decorated with 18 mm glass coverslips. During the electrospinning process, samples (on glass coverslips) were removed periodically from the collector and imaged using a Leica microscope under phase-contrast to observe the MS-mesh morphology, and a fluorescence field (using a blue excitation filter) to observe FITC-BSA.

6.3.4. Protection of lysozyme activity: electrospinning MSs from PEO

To determine if the MSs could protect protein activity during electrospinning, lysozyme was incorporated into MSs and electrospun from an aqueous PEO solution. (Here, a PEO solution avoided the use of organic solvents typically employed for electrospinning PCL and PLGA). Briefly, cross-linked MSs were loaded with 100 μg of lysozyme and dispersed in a 4% (w/v) solution of PEO in α-MEM. After sonication, the mixture was electrospun onto a slowly rotating grounded collector at a flow rate of 0.3 mL/h, a throw distance of 18 cm and a potential of 18 kV. The MS-mesh sample was allowed to dry for 12 h at 4 °C. Subsequently, it was treated with an aqueous 0.034 M collagenase solution, allowing for the dissolution of the PEO phase and the degradation of MSs. After 8 h of treatment, the suspension was centrifuged and the supernatant containing lysozyme was analyzed using an EnzChek® lysozyme assay kit as described in **Section 6.3.2.4**. Lysozyme directly electrospun from a PEO solution served as a negative control, while non-electrospun lysozyme served as a positive control.

6.3.5. Effect of FGF-2 on BMSC metabolic activity

As an initial step towards evaluating the biological effect of FGF-2 released from MS-mesh samples, a pilot study was performed to test the effect of 1, 2.5 and 5 ng/mL FGF-2 on BMSC proliferation. Briefly, BMSCs were harvested from adult female Lewis rats weighing 170-200 g (Harlan, Dublin, VA) according to a previously published protocol [35], and frozen in liquid nitrogen after the second passage in α-MEM supplemented with 10% FBS, 1% antibiotic/antimycotic and 10% dimethylsulfoxide. Subsequently, cells at passage 2 were seeded at 10,000 cells/well of two 24-well plates in growth medium (DMEM supplemented with 10% FBS and 1% antibiotic/antimycotic). Immediately thereafter, cells were supplemented with 1, 2.5 or 5 ng/mL of FGF-2 in triplicate, by the direct addition of FGF-2 diluted in a 0.1% BSA solution. An FGF-2 control (0 ng/mL) received an equivalent volume of 0.1% BSA solution. Cells were allowed to grow in a total of 1 mL growth medium within a 37 °C, 5 % CO_2 incubator for either 3 or 7 days, with the day 7 samples receiving medium change and FGF-2 replenishment at day 3. At days 3 and 7, cell metabolic activity was assessed by the addition of 100 μL of alamar blue reagent to each well, followed by incubation for 4 h within a 37 °C, 5 % CO_2 incubator. Thereafter, the fluorescence of 200 μL of medium from each well was read at

excitation and emission wavelengths of 550 nm and 590 nm respectively using a multi-mode micro-plate reader.

6.3.6. Statistical analysis

Results are reported as mean ± standard deviation for n = 3 samples for both the lysozyme release study and the FGF-2 supplementation study. A one-tailed unpaired student's t-test was used to determine statistical significance, with a p-value less than 0.05 considered significant.

6.4. Results

6.4.1. MS fabrication and lysozyme release

Gelatin MSs were successfully fabricated by a single emulsion method. SEM imaging of dry cross-linked MSs (**Figure 6.1**) revealed a porous structure and a distribution of MS sizes in the range 25-53 μm. These MSs were found to have a fold swelling volume (S value) of 8.3 ± 3.4. In addition, the maximum volume of PBS absorbed for equilibrium swelling was 9.5 ± 1.2 μL per mg of MSs.

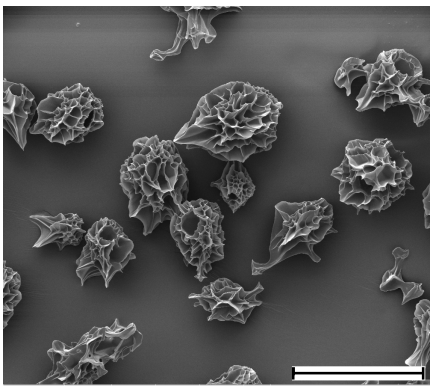

Figure 6.1: SEM image of dry cross-linked gelatin MSs in the 25-53 μm size range. Scale bar represents 100 μm.

Lysozyme, a model protein, was encapsulated and released from the cross-linked MSs in the presence and absence of a gelatin-degrading enzyme collagenase (**Figure 6.2**). Cumulative release curves indicated an initial burst, followed by sustained release over a 3-week period. The

presence of collagenase increased the rate of release (red curve), resulting in greater cumulative release of lysozyme compared to the no-collagenase samples (black curve). Over the course of 3 weeks, the MSs in the collagenase-treated samples appeared to have degraded more than the MSs in the no-collagenase samples. However, a 3-week period was found to be insufficient to degrade the MSs completely, even in the presence of 1 µg/mL collagenase.

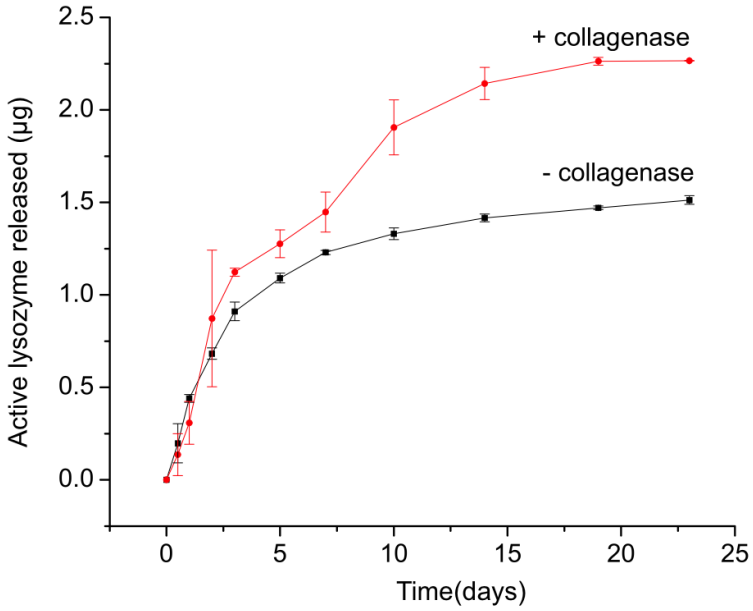

Figure 6.2: Cumulative release of lysozyme from cross-linked MSs in the presence and absence of collagenase (n = 3 per time point). Y-axis represents total active lysozyme released over a 3-week period. Initial lysozyme loading per group was 5 µg (theoretical).

6.4.2. MS-mesh samples

MS-mesh samples were fabricated by electrospinning a suspension of dry MSs from a PCL solution (**Figure 6.3**). The MSs did not clump within the mesh at any of the loading concentrations and were encapsulated within the polymeric fibers. In contrast, lysozyme-loaded pre-hydrated MSs incorporated within a PLGA mesh appeared clumped and sparsely dispersed, while also being fully encapsulated within the fibers (**Figure 6.4**).

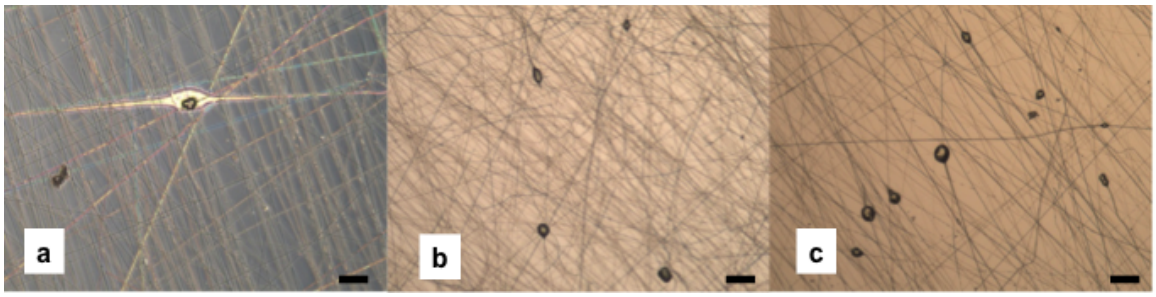

Figure 6.3: Phase-contrast microscopy images of MS-mesh samples showing gelatin MSs within a PCL fibrous mesh. Loading concentration of MSs in the polymer solution was increased from a) 10 mg/mL to b) 30 mg/mL to c) 50 mg/mL. Scale bars represent 25 μm.

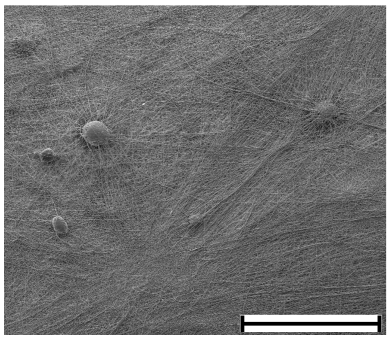

Figure 6.4: SEM image of lysozyme-loaded pre-hydrated gelatin MSs incorporated within a PLGA mesh. Scale bar represents 300 μm.

FITC-BSA-loaded MSs were also found to be encapsulated as clumps within large PLGA beads (~ 250 μm diameter) (**Figure 6.5**). Moreover, the fluorescence from the FITC-BSA was not detected in the PLGA phase, suggesting that protein was retained to a large extent within the MS phase.

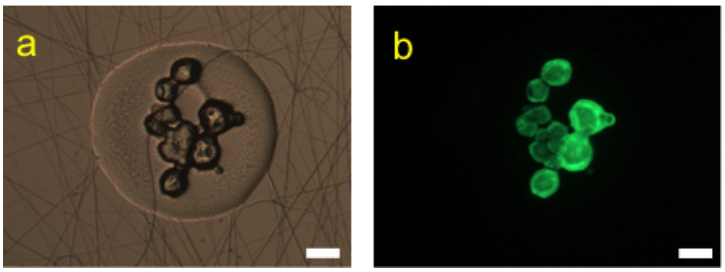

Figure 6.5: a) Phase-contrast and b) fluorescence images of FITC-BSA-loaded MSs incorporated within a large PLGA bead (droplet). Scale bars represent 50 μm.

6.4.3. Protection of lysozyme activity by MSs incorporated within electrospun meshes

To evaluate the protection of enzymatic activity conferred by gelatin MSs, lysozyme-loaded MSs were electrospun from a PEO solution, and the resultant MS-mesh sample was dissociated in a collagenase solution. After 8 h of degrading the MSs in collagenase, a lysozyme assay was performed to determine the amount of active lysozyme. The assay showed that 18.2 μg of enzyme was active when lysozyme was loaded into MSs and electrospun (theoretical loading: 100 μg), compared to the 107 μg of active lysozyme in the non-electrospun positive control (**Figure 6.6**). No active lysozyme was detected in the directly electrospun negative control (without MS protection).

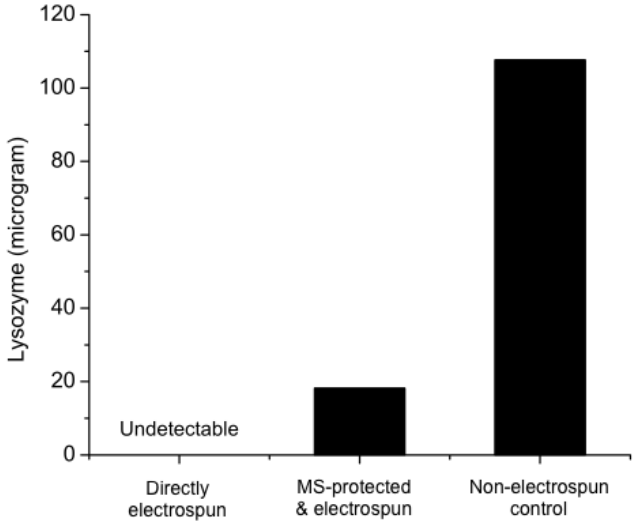

Figure 6.6: Amount of active lysozyme obtained from direct electrospinning (negative control), MS-protected electrospinning and non-electrospun sample (positive control). Each experimental group represents one sample.

6.4.4. Effect of FGF-2 supplementation on BMSCs

FGF-2 was directly supplemented in culture medium to evaluate its effect on cell metabolic activity (**Figure 6.7**). Metabolic activity was higher for the FGF-2-supplemented samples at day 3, although the 1 ng/mL and 5 ng/mL FGF-2 samples were not significantly different from the 0 ng/mL FGF-2 control samples. At day 7, cell metabolic activity was higher in all the samples, consistent with cell proliferation over the four-day period. Furthermore, the metabolic activity of the 2.5 ng/mL and 5 ng/mL FGF-2-supplemented samples was significantly

higher than the 0 ng/mL FGF-2 control samples. Overall, FGF-2 produced a positive effect on cell metabolic activity, with a significant effect detectable only at a threshold concentration of 2.5 ng/mL FGF-2 after 7 days of culture.

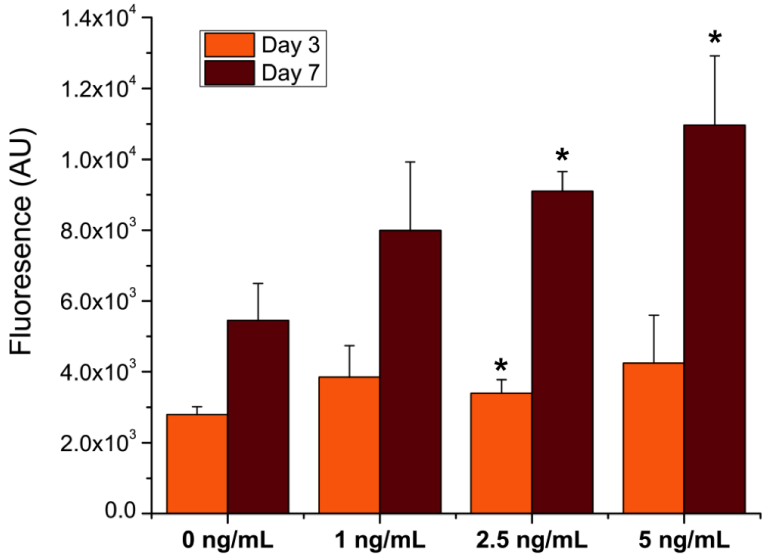

Figure 6.7: Fluorescence values obtained from an alamar blue assay indicating BMSC metabolic activity at days 3 and 7 in response to FGF-2 supplementation (n = 3 per time point per experimental group). An asterisk indicates significantly different values compared to the no-FGF-2 control (0 ng/mL) at respective time points ($p < 0.05$).

6.5. Discussion

In this feasibility study, four sets of experiments were performed to evaluate the potential of gelatin MSs to protect the activity of proteins during electrospinning. Towards this end, gelatin MSs were fabricated via a single emulsion method and cross-linked using glutaraldehyde. Lysozyme incorporated within the MSs was shown to release with an initial burst, which stabilized and plateaued at the end of 3 weeks. Furthermore, the presence of collagenase in the release medium was found to increase the release kinetics of lysozyme. Following this set of experiments, MSs were dispersed in a polymer solution and electrospun to result in MS-mesh samples. FITC-BSA – loaded within the MSs – was not observed outside the MS phase post-electrospinning. Next, lysozyme was found to retain some of its activity when incorporated within MSs and electrospun from a PEO solution as compared to a directly electrospun negative control; however, the activity of MS-protected lysozyme was approximately 16% of the activity

of the non-electrospun positive control. Finally, FGF-2 was found to have a positive effect on the metabolic activity of BMSCs, and the effect was significantly different compared to a 0 ng/mL FGF-2 control at a threshold concentration of 2.5 ng/mL after 7 days of culture.

The MSs prepared in this study degraded in an aqueous medium and thus allowed for the sustained release of a model protein. A fold swelling ratio (S value) of 8.3 obtained in this study is similar to the ratio of 10.5 reported in a previous study [201]. Throughout the present study, proteins were loaded into the MSs using a loading volume of 7 μL/mg of MSs (which is below the equilibrium swelling volume) to allow for the complete absorption of proteins within the MSs. In the first set of experiments, lysozyme was used a model protein because retention of enzyme activity following electrospinning can be readily determined [202]. Furthermore, lysozyme (isoelectric point ~ 11) was anticipated to complex ionically with gelatin B (isoelectric point ~ 5.0) and thus remain bound, if only weakly, to the MSs [203]. In the *in vitro* release study that was subsequently performed, lysozyme was found to exhibit an initial burst, followed by sustained release over a period of 3 weeks (**Figure 6.2**). Here, ~ 30% active lysozyme was released over 3 weeks, which increased to 45% in the presence of collagenase. These results are different from the results reported in a study by Hiwale et al, who showed that ~ 80% lysozyme was released from gelatin MSs within a period of 400 min (although the MS in this study were cross-linked only for 45 min) [203]. However, Holland et al reported an initial burst for TGF-β1 (isoelectric point ~ 9) from gelatin MSs (cross-linked overnight), followed by sustained release over a period of 4 weeks (~ 70% cumulative release) [201]. The differences in the release profiles reported across these studies may be related to the differences in the cross-linking parameters. In support of this theory, Dinarvand et al have shown that the release profiles of drugs from gelatin MSs depend on MS cross-linking parameters such as glutaraldehyde concentration and cross-linking duration [204]. Nevertheless, the results from the present study indicate that lysozyme can be encapsulated and released in an active form from MSs, and that the rate of release can be expedited by the addition of collagenase to the release medium. Collagenase-mediated degradation of MSs provides an indication of how cell-secreted matrix metalloproteinases might degrade the gelatin MSs in future cell studies. A minor caveat with the present study is that the lysozyme assay detects the presence of active lysozyme. Therefore, loss

of activity during the protein loading step and/or the release study could have reduced the apparent release rate.

GFs have been incorporated within electrospun scaffolds using a variety of techniques [29], including physical adsorption or covalent immobilization post-electrospinning [205], direct blending within polymer solutions prior to electrospinning [206] (also known as emulsion electrospinning) and co-axial electrospinning [207]. Each of these approaches presents a unique set of merits and limitations. For example, blend electrospinning is the easiest method to load GFs into electrospun scaffolds; however, the direct contact of GFs with the organic solvents used for electrospinning can potentially diminish or eliminate GF activity [30]. Moreover, scaffolds fabricated via blend electrospinning have been shown to release GFs over short time periods [199], raising the concern that the GF may not be released over a sufficiently long period to have a sustained effect on cell differentiation and phenotypic maturation. In contrast, co-axial electrospinning – which uses an aqueous polymer solution to encapsulate GFs within a core phase – overcomes some of the disadvantages seen with traditional methods of encapsulation. However, in this configuration, the rate of GF release can be very slow, depending on the rate of its diffusion through the polymeric sheath phase, as well as on the rate of polymer degradation [208]. In order to overcome the limitations with current strategies, the present study proposed to protect GFs by encapsulation within a MS carrier phase prior to electrospinning. Here, the MSs offer control over GF release kinetics independent of the degradation rate of the fibrous phase. Preliminary experiments indicated that dry MSs (**Figure 6.3**) were well dispersed within fibers, while pre-hydrated MSs appeared to clump within electrospun meshes (**Figures 6.4, 6.5**), consistent with the theory that large pre-hydrated MSs clump more than smaller dry MSs. In homogeneous dispersion of MSs within the electrospun mesh can inadvertently result in local micro-gradients of GF concentration. (However, the addition of a surfactant to the polymer solution prior to the addition of pre-hydrated MSs can potentially mitigate MS clumping and in homogeneous dispersion.) Moreover, the MSs were completely encapsulated within the polymeric fibers (**Figures 6.3, 6.4**), consistent with the results reported by Ionescu et al who electrospun polystyrene MSs from a PCL solution [209]. The encapsulation of MSs within fibers can potentially retard the release of GFs.

Although previous studies have reported the encapsulation of sensitive proteins within MSs prior to incorporation into electrospun fibers, those studies have shown either the encapsulation of such GFs without the investigation of release kinetics [210], or the release of molecules such as BSA and chondroitin sulfate (which do not possess a specific biological/enzymatic activity) post-electrospinning [209]. Therefore, the present study aimed to test the effect of electrospinning on protein activity using a model enzyme, lysozyme. MSs were found to protect lysozyme activity to some extent (**Figure 6.6**), compared to a directly-electrospun negative control, although lysozyme activity was much lower than a non-electrospun positive control. The collagenase used to degrade the MSs might have degraded the lysozyme to a certain extent and may have thus undermined enzyme activity. Moreover, the high voltage used during the electrospinning process might have also reduced lysozyme activity. Therefore, a technique that can incorporate the MSs within the mesh without the use of organic solvents and high voltages can possibly protect enzyme activity to a larger extent than the direct incorporation of MSs within electrospinning solutions.

In summary, the results from these studies demonstrate that the activity of lysozyme is significantly reduced during direct electrospinning, but that it can be partially protected by loading the enzyme within gelatin MSs prior to electrospinning. Future studies will seek to use a different technique (e.g., airbrushing) to incorporate gelatin MSs within the mesh and subsequently evaluate the protection effect of lysozyme activity.

6.6. Acknowledgments

S. Samavedi is grateful to Alexander DiSavino (Chemical Engineering, Virginia Tech) for his assistance in conducting experiments described in this chapter.

Chapter 7

Summary and future recommendations

7.1. Summary

The overall goal of this project was to develop and evaluate graded scaffolds, as a step towards regenerating bone-ligament (B-L) transitions in the long-term. Towards this end, scaffolds possessing gradients in architecture, mechanical and biochemical properties were fabricated using three complementary strategies. These scaffolds were tested for their potential to guide the establishment of cell alignment and phenotypic gradients in bone marrow stromal cells (BMSCs).

Strategy I (chapters 3 and 4) involved co-electrospinning polycaprolactone (PCL) (loaded with nano-hydroxyapatite (nHAP)) and a poly (ester urethane urea) elastomer (PUR) from offset spinnerets to create scaffolds possessing gradients in mineral content and fiber chemistry. These co-electrospun scaffolds were then immersed in a simulated body fluid (SBF) solution to produce a second and more pronounced mineral gradient. The mineral formed via SBF treatment was determined to be a calcium deficient apatite. Both the co-electrospun and SBF-treated scaffolds were shown to possess gradients in chemistry, tensile modulus, ultimate tensile strength and strain at failure, with the regions containing mineral being stronger and stiffer in comparison to the viscoelastic PUR regions. Furthermore, both scaffolds guided the establishment of a phenotypic gradient in BMSCs, as revealed by the gene expression of osteoblastic markers. Finally, BMSCs were found to mature into an osteoblastic phenotype as demonstrated by staining for bone-specific extracellular matrix (ECM) proteins. While these studies indicate that scaffolds possessing gradients in mineral content can help guide the formation of phenotypic gradients in BMSCs *in vitro,* gene expression was not significantly different between the different regions of the scaffolds. Two potential explanations for these results are that: a) these studies were performed in the presence of osteogenic supplements, which could have marginalized the contribution of the mineral phase, and b) HAP – although used extensively in bone regeneration – is thought to possess minimal osteoinductive properties [161]. Therefore, a strong need exists for the development of scaffolds possessing intrinsic

osteoinductive capabilities. Specifically, the substitution of nHAP in these scaffolds with a more osteoinductive phase can potentially enhance the gradients in gene expression, even in the absence of ostoegenic supplements.

Strategy II (chapter 5) involved co-electrospinning two polymer solutions – PCL and poly (lactide-co-glycolide) (PLGA) – onto a custom-designed dual-drum collector such that the PCL fibers aligned in the gap region between the drums, the PLGA fibers deposited randomly onto one of the drums and an overlap region possessing both PCL and PLGA fibers formed at the interface. The properties of the aligned region were varied independent of the properties of the random region to result in two sets of meshes possessing different fiber diameters in the aligned PCL region. Investigation of mesh properties demonstrated that the meshes possessed gradients in scaffold architecture, fiber diameter and fiber chemistry. Although the interfacial region was found to consist of artifacts from the electrospinning process, the presence of both fiber types in this region indicated robust integration of the polymers. (An interfacial region is critical towards the long-term stability of scaffolds when used in an *in vivo* application.) Finally, the meshes helped establish differences in cell morphology and alignment within spatially distinct zones. The presence of rhomboidally shaped cells with low aspect ratios on the random region and spindle-shaped cells with high aspect ratios on the aligned region suggested that these cells have the potential to become fibroblastic-like and osteoblast-like respectively. In summary, these results indicate that meshes possessing region-wise differences in fiber alignment, diameter and chemistry can guide the establishment of differences in cell shape within spatially distinct zones. Studies are currently underway to determine the effect of mesh properties such as fiber alignment, diameter and chemistry on BMSC differentiation.

Strategy III (chapter 6) was pursued to achieve the long-term goal of creating co-electrospun scaffolds possessing a gradient in growth factor (GF) concentration. Central to this strategy was the development of a technique to protect GFs within a microsphere (MS) carrier phase, and subsequently deliver GFs in active conformation from MS-mesh samples. Towards achieving this short-term goal, several sets of experiments were conducted sequentially. In the first set of experiments, active lysozyme (model protein) was shown to be released in a controlled manner over three weeks from cross-linked gelatin MSs. Subsequently, the second set of experiments demonstrated that MSs could be electrospun from polymer solutions to result in

MS-mesh samples. Further, fluorescently tagged bovine serum albumin – loaded within MSs – was found to remain localized within the MSs following electrospinning from a polymer solution, suggesting that the protein did not rapidly diffuse into the organic polymeric phase. In the third set of experiments – performed to demonstrate the role of MSs in protecting protein activity – cross-linked lysozyme-loaded MSs were electrospun from a poly (ethylene oxide) (PEO) solution (in cell culture medium). Post-electrospinning, the PEO phase was dissolved and the MSs degraded to test for lysozyme activity. The MS-protected sample showed higher lysozyme activity compared to lysozyme electrospun directly from a polymer solution. However, the activity from the MS-protected sample was much lower than a non-electrospun control. In the final set of experiments, the supplementation of fibroblastic growth factor-2 (FGF-2) was found to have a positive effect on BMSC proliferation, with the effect detectable only at a threshold concentration of 2.5 ng/mL FGF-2 at 7 days. While preliminary results from these studies indicate that the MSs can protect and deliver a model protein in an active form from electrospun scaffolds, further improvements in the scaffold fabrication process can result in greater protection of GF activity.

7.2. Future recommendations

The results from this project indicate that graded scaffolds have the potential to promote the regeneration of B-L transitions by guiding the formation of phenotypic gradients in BMSCs. Future efforts will be performed in the following research areas:

7.2.1. Developing electrospun scaffolds possessing intrinsic osteoinductive properties

In Strategy I, the use of HAP as a mineral gradient cue was found to be insufficient in inducing a strong gradient of osteoblastic gene expression. Therefore, the first area of future research aims to develop scaffolds possessing improved ability to induce osteoblastic differentiation. In this regard, biphasic calcium phosphates (BCPs) – possessing a mixture of HAP and tricalcium phosphate (TCP) – have been shown to promote osteoblastic differentiation even in the absence of osteogenic supplements [211]. Moreover, BCPs possessing high microporosities can potentially enhance cell differentiation via the adsorption of cell-adhesive proteins and osteogenic growth factors [212, 213]. *In vivo*, BCPs have recently been shown to

home BMSCs to ectopic sites to induce bone formation [214]. Thus, it is expected that electrospun scaffolds possessing gradients in BCP content can potentially guide the establishment of an osteoblastic phenotypic gradient in BMSCs even in the absence of osteogenic supplements.

The experiments to test this hypothesis can be performed by using the approaches described in chapters 3 and 4. Briefly, nano BCP particles – possessing high microporosities – can be loaded into PCL solutions and co-electrospun against PUR solutions from offset spinnerets onto a rotating drum. After 1 and 7 days of BMSC culture on the graded scaffolds, cell number can be determined to evaluate the effect of BCP loading on cell attachment and proliferation. After 10 and 20 days of cell culture (in the absence of osteogenic supplements), gene expression of early (e.g., alkaline phosphatase, bone morphogenic protein-2 (BMP-2)) and late (osteocalcin, bone sialoprotein) osteoblastic markers can be determined on the various regions of the graded scaffolds to evaluate the effect of both BCP presence and BCP concentration on BMSC differentiation. Concurrently, the deposition of bone-specific ECM proteins (e.g., osteocalcin) and the presence of cell clusters can be determined after 28 days of culture to confirm phenotypic maturation. Throughout these studies, graded scaffolds without mineral can function as a control group, in addition to the internal control of the PUR regions without mineral. These studies are expected to show that the inclusion of BCP in a gradient manner within co-electrospun scaffolds can guide the establishment of a phenotypic gradient in BMSCs in the absence of osteogenic supplements. Further, increasing the concentration of BCP within scaffolds – while still maintaining the gradient of BCP content – is expected to result in a systematic increase in osteoblastic gene expression by BMSCs on the mineral-containing regions as compared to regions without mineral.

7.2.2. Developing electrospun scaffolds possessing gradients in GF concentration

Although the ultimate goal of Strategy III was to fabricate electrospun scaffolds possessing a gradient in growth factor concentration, harsh processing conditions used for electrospinning necessitated the development of a delivery system that could protect GF activity during the scaffold fabrication step. While gelatin MSs were found to protect protein activity to a certain extent, the high voltage used during electrospinning was also possibly responsible for

denaturing the model protein (lysozyme). Therefore, another technique – that avoids both the use of organic solvents as well as high voltages – to incorporate MSs within electrospun scaffolds is expected to protect protein activity better than direct electrospinning of GF-loaded MSs. Further, the simultaneous incorporation of two types of MSs (loaded with bone-driving (e.g., BMP-2) and ligament-driving GFs (e.g., FGF-2)) will result in scaffolds possessing dual gradients of GF concentration that can help guide the formation of bone-like and ligament-like tissues within spatially distinct zones.

To test the hypothesis that an alternative technique to incorporate MSs within electrospun scaffolds can protect GF activity better than the technique proposed in chapter 6, the following experiments can be performed. Briefly, a PCL solution can be electrospun onto a rotating drum, while a spray gun or an airbrush (one such airbrush has been recently used for preparing nanofibrous scaffolds [215]) can be used to spray a suspension of lysozyme-loaded MSs from a PEO solution simultaneously. This process will allow for the successful incorporation of lysozyme-loaded MSs within the PCL scaffold. Since the MSs are sprayed using a PEO solution, the PEO phase will dissolve away upon exposure to water, leaving the MSs trapped within the fibrous network. Concurrently, lysozyme electrospun from a PCL solution directly, and lysozyme-loaded MSs electrospun from a PCL solution will serve as two negative controls. Post-fabrication, the PEO phase can be dissolved and the MSs degraded by treatment with a highly concentrated solution of collagenase, and the suspension centrifuged thereafter. The resulting supernatant can be assayed for lysozyme activity, which can be compared to a non-electrospun/non-sprayed lysozyme group (positive control). These studies are expected to show that spraying the MSs from a PEO solution protects lysozyme activity better than the direct inclusion of MSs within a polymer solution prior to electrospinning. Further, lysozyme activity obtained from the new protection technique is expected to be comparable to the positive control. Moreover, this technique of encapsulation is expected to possess the added advantage of entrapping the MSs outside the fibers [209], which can allow for the release of GFs independent of fiber degradation. Once validated, the technique can be used for the creation of co-electrospun scaffolds possessing simultaneous gradients in two GF concentrations, which can potentially be used in concert with a mineral gradient for establishing phenotypic gradients in BMSCs. Specifically, PCL and PUR can be co-electrospun from offset spinnerets onto a rotating

drum, while two air brushes can simultaneously deliver MSs (loaded with two different GFs) into spatially distinct zones, resulting in the formation of GF gradients (**Figure 7.1**). These scaffolds can subsequently be seeded with BMSCs and tested for their potential to induce osteoblastic and ligamentous differentiation in a spatially graded manner.

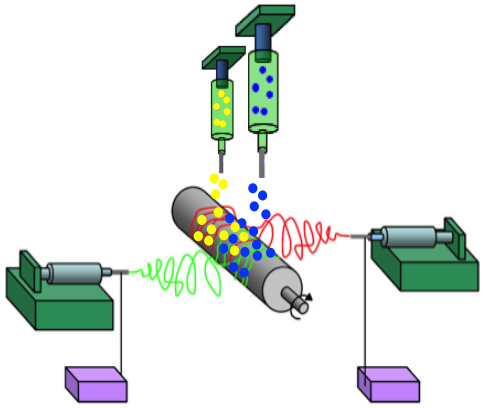

Figure 7.1: Electrospinning set-up depicting off-set spinnerets and two spray nozzles that deliver MSs containing different GFs.

7.2.3. Evaluating the potential of graded scaffolds in homing and differentiating BMSCs *in vivo*

Although the graded scaffolds in this project were shown to induce the formation of gradients in cell response *in vitro*, the potential of these gradient cues towards establishing gradients in cell response *in vivo* needs to be evaluated. While none of the graded scaffolds possess a structure suitable for implantation within the knee joint of an animal (to test for tissue regeneration), the scaffolds can be implanted subcutaneously in rats to a) evaluate the effect of biochemical cues in the scaffolds to home BMSCs *in vivo* and b) determine the response of such homed cells to the gradient cues incorporated within the scaffolds. It is expected that biochemical cues (e.g, BCP particles and FGF-2-loaded MSs) within scaffolds can home BMSCs and further promote their differentiation towards specific lineages across the scaffolds. A pilot study conducted to test this hypothesis will serve as a stepping-stone towards evaluating the role of acellular graded scaffolds in regenerating B-L transitions in the long-term.

Two types of graded scaffolds – incorporating two distinct biochemical cues – can be evaluated for their homing and differentiation potential. Specifically, scaffolds possessing a

gradient in BCP concentration (as described in section **7.3.1**), and scaffolds possessing a single gradient in GF concentration (FGF-2) can be created. Thereafter, acellular graded scaffolds can be implanted subcutaneously in Sprague-Dawley rats. One and two weeks following implantation, scaffolds can be harvested and stained with H&E to quantify cell number and ECM deposition. At these time points, major signs of acute immune response, if present, can also be evaluated. Following three and four weeks of implantation, scaffolds can be harvested and divided into two groups: one group will be used for evaluating gene expression of phenotypic markers and the other group will be used for immunohistochemistry to determine the deposition of phenotype-specific ECM and neo-vascularization. Throughout the study, co-electrospun scaffolds incorporating no biochemical cues (i.e., BCP and FGF-2) can be used as negative controls. The results from these studies are expected to show that both biochemical cues (i.e., BCP and FGF-2-loaded MS) can independently home BMSCs into scaffolds and thereafter promote their differentiation toward specific lineages. Testing a combination of gradient cues within the same scaffold for their homing and differentiation potential will be the next step.

7.3. Concluding remarks

The focus of this project was to develop complementary strategies for the fabrication and evaluation of graded scaffolds, as a step towards regenerating B-L transitions. Towards this end, novel methods for the fabrication of scaffolds possessing gradients in mineral content and scaffold architecture were developed. Moreover, a technique to protect and deliver GFs from electrospun scaffolds was also proposed. In conclusion, the results from this project demonstrate that graded scaffolds can be fabricated by electrospinning. The results further indicate that these scaffolds can potentially promote the regeneration of B-L transitions by guiding the formation of gradients in cell shape and phenotype in BMSCs. Future efforts will focus on developing electrospun scaffolds possessing intrinsic osteoinductive properties, creating electrospun scaffolds possessing gradients in GF concentration and evaluating the potential of graded scaffolds in homing and differentiating BMSCs *in vivo*.

References

[1] Soderman K, Pietila T, Alfredson H, Werner S. Anterior cruciate ligament injuries in young females playing soccer at senior levels. Scand J Med Sci Spor. 2002;12:65-8.
[2] Laurencin CT, Freeman JW. Ligament tissue engineering: an evolutionary materials science approach. Biomaterials. 2005;26:7530-6.
[3] Cooper JA, Lu HH, Ko FK, Freeman JW, Laurencin CT. Fiber-based tissue-engineered scaffold for ligament replacement: design considerations and in vitro evaluation. Biomaterials. 2005;26:1523-32.
[4] Murray MM. Current Status and Potential of Primary ACL Repair. Clin Sport Med. 2009;28:51-61.
[5] Mascarenhas R, MacDonald PB. Anterior cruciate ligament reconstruction: a look at prosthetics--past, present and possible future. Mcgill J Med. 2008;11:29-37.
[6] Yang PJ, Temenoff JS. Engineering orthopedic tissue interfaces. Tissue Eng Part B Rev. 2009;15:127-41.
[7] Robertson DB, Daniel DM, Biden E. Soft tissue fixation to bone. The American journal of sports medicine. 1986;14:398-403.
[8] Moffat KL, Sun WH, Pena PE, Chahine NO, Doty SB, Ateshian GA, et al. Characterization of the structure-function relationship at the ligament-to-bone interface. Proc Natl Acad Sci U S A. 2008;105:7947-52.
[9] Lu HH, Jiang J. Interface tissue engineering and the formulation of multiple-tissue systems. Adv Biochem Eng Biotechnol. 2006;102:91-111.
[10] Moffat KL, Wang IN, Rodeo SA, Lu HH. Orthopedic interface tissue engineering for the biological fixation of soft tissue grafts. Clin Sports Med. 2009;28:157-76.
[11] Ristanis S, Stergiou N, Patras K, Tsepis E, Moraiti C, Georgoulis AD. Follow-up evaluation 2 years after ACL reconstruction with bone-patellar tendon-bone graft shows that excessive tibial rotation persists. Clin J Sport Med. 2006;16:111-6.
[12] Vunjak-Novakovic G, Altman G, Horan R, Kaplan DL. Tissue engineering of ligaments. Annu Rev Biomed Eng. 2004;6:131-56.
[13] Pham QP, Sharma U, Mikos AG. Electrospinning of polymeric nanofibers for tissue engineering applications: A review. Tissue Eng 2006;12:1197-211.
[14] Ladd MR, Lee SJ, Stitzel JD, Atala A, Yoo JJ. Co-electrospun dual scaffolding system with potential for muscle-tendon junction tissue engineering. Biomaterials. 2011;32:1549-59.
[15] Baker BM, Gee AO, Metter RB, Nathan AS, Marklein RA, Burdick JA, et al. The potential to improve cell infiltration in composite fiber-aligned electrospun scaffolds by the selective removal of sacrificial fibers. Biomaterials. 2008;29:2348-58.
[16] Yang F, Both SK, Yang X, Walboomers XF, Jansen JA. Development of an electrospun nano-apatite/PCL composite membrane for GTR/GBR application. Acta Biomater. 2009;5:3295-304.
[17] Marino G, Rosso F, Cafiero G, Tortora C, Moraci M, Barbarisi M, et al. beta-Tricalcium phosphate 3D scaffold promote alone osteogenic differentiation of human adipose stem cells: in vitro study. J Mater Sci-Mater M. 2010;21:353-63.
[18] Thomopoulos S, Williams GR, Gimbel JA, Favata M, Soslowsky LJ. Variation of biomechanical, structural, and compositional properties along the tendon to bone insertion site. J Orthopaed Res. 2003;21:413-9.

[19] Thomopoulos S, Xie JW, Li XR, Lipner J, Manning CN, Schwartz AG, et al. "Aligned-to-random" nanofiber scaffolds for mimicking the structure of the tendon-to-bone insertion site. Nanoscale. 2010;2:923-6.
[20] Meyle J, Gultig K, Nisch W. Variation in contact guidance by human cells on a microstructured surface. J Biomed Mater Res. 1995;29:81-8.
[21] Dunn MG, Liesch JB, Tiku ML, Zawadsky JP. Development of fibroblast-seeded ligament analogs for ACL reconstruction. J Biomed Mater Res. 1995;29:1363-71.
[22] Curtis A, Wilkinson C. Topographical control of cells. Biomaterials. 1997;18:1573-83.
[23] Wang JHC, Jia FY, Gilbert TW, Woo SLY. Cell orientation determines the alignment of cell-produced collagenous matrix. Journal of Biomechanics. 2003;36:97-102.
[24] Bashur CA, Shaffer RD, Dahlgren LA, Guelcher SA, Goldstein AS. Effect of fiber diameter and alignment of electrospun polyurethane meshes on mesenchymal progenitor cells. Tissue Eng Pt A. 2009;15:2435-45.
[25] Meinel L, Hofmann S, Betz O, Fajardo R, Merkle HP, Langer R, et al. Osteogenesis by human mesenchymal stem cells cultured on silk biomaterials: comparison of adenovirus mediated gene transfer and protein delivery of BMP-2. Biomaterials. 2006;27:4993-5002.
[26] Dormer NH, Singh M, Wang L, Berkland CJ, Detamore MS. Osteochondral interface tissue engineering using macroscopic gradients of bioactive signals. Ann Biomed Eng. 2010;38:2167-82.
[27] Sahoo S, Ang LT, Goh JCH, Toh SL. Bioactive nanofibers for fibroblastic differentiation of mesenchymal precursor cells for ligament/tendon tissue engineering applications. Differentiation. 2010;79:102-10.
[28] Hu P, Qi HX, Xu J, Wang AJ. Encapsulation of drug reservoirs in fibers by emulsion electrospinning: Morphology characterization and preliminary release assessment. Biomacromolecules. 2006;7:2327-30.
[29] Jansen JA, Ji W, Sun Y, Yang F, van den Beucken JJJP, Fan MW, et al. Bioactive Electrospun Scaffolds Delivering Growth Factors and Genes for Tissue Engineering Applications. Pharm Res-Dordr. 2011;28:1259-72.
[30] Madurantakam PA, Rodriguez IA, Beckman MJ, Simpson DG, Bowlin GL. Evaluation of biological activity of bone morphogenetic proteins on exposure to commonly used electrospinning solvents. J Bioact Compat Pol. 2011;26:578-89.
[31] Laurencin CT, Ambrosio AM, Borden MD, Cooper JA, Jr. Tissue engineering: orthopedic applications. Annu Rev Biomed Eng. 1999;1:19-46.
[32] Doroski DM, Brink KS, Temenoff JS. Techniques for biological characterization of tissue-engineered tendon and ligament. Biomaterials. 2007;28:187-202.
[33] Kastelic J, Galeski A, Baer E. The multicomposite structure of tendon. Connective tissue research. 1978;6:11-23.
[34] Wang JH. Mechanobiology of tendon. J Biomech. 2006;39:1563-82.
[35] Samavedi S, Guelcher SA, Goldstein AS, Whittington AR. Response of bone marrow stromal cells to graded co-electrospun scaffolds and its implications for engineering the ligament-bone interface. Biomaterials. 2012;33:7727-35.
[36] Petersen W, Tillmann B. Structure and vascularization of the cruciate ligaments of the human knee joint. Anat Embryol. 1999;200:325-34.
[37] Urist MR. Fundamental and clinical bone physiology. Philadelphia ; Toronto: Lippincott; 1980.

[38] Pugh JW, Rose RM, Radin EL. Elastic and viscoelastic properties of trabecular bone: dependence on structure. J Biomech. 1973;6:475-85.
[39] Brown WE, Chow LC. Chemical Properties of Bone-Mineral. Annu Rev Mater Sci. 1976;6:213-36.
[40] Hadjidakis DJ, Androulakis, II. Bone remodeling. Ann N Y Acad Sci. 2006;1092:385-96.
[41] Robling AG, Castillo AB, Turner CH. Biomechanical and molecular regulation of bone remodeling. Annu Rev Biomed Eng. 2006;8:455-98.
[42] Roach HI. Why Does Bone-Matrix Contain Noncollagenous Proteins - the Possible Roles of Osteocalcin, Osteonectin, Osteopontin and Bone Sialoprotein in Bone Mineralization and Resorption. Cell Biol Int. 1994;18:617-28.
[43] Noyes FR, Grood ES. The strength of the anterior cruciate ligament in humans and Rhesus monkeys. J Bone Joint Surg Am. 1976;58:1074-82.
[44] Amis AA, Dawkins GP. Functional anatomy of the anterior cruciate ligament. Fibre bundle actions related to ligament replacements and injuries. The Journal of bone and joint surgery British volume. 1991;73:260-7.
[45] Odensten M, Gillquist J. Functional anatomy of the anterior cruciate ligament and a rationale for reconstruction. J Bone Joint Surg Am. 1985;67:257-62.
[46] Kato Y, Hoshino Y, Ingham SJ, Fu FH. Anatomic double-bundle anterior cruciate ligament reconstruction. J Orthop Sci. 2010;15:269-76.
[47] Edwards A, Bull AM, Amis AA. The attachments of the anteromedial and posterolateral fibre bundles of the anterior cruciate ligament: Part 1: tibial attachment. Knee surgery, sports traumatology, arthroscopy : official journal of the ESSKA. 2007;15:1414-21.
[48] Silver FH. Biomaterials, medical devices and tissue engineering : an integrated approach: Chapman and Hall; 1994.
[49] Dodds JA, Arnoczky SP. Anatomy of the anterior cruciate ligament: a blueprint for repair and reconstruction. Arthroscopy. 1994;10:132-9.
[50] Arnoczky SP. Anatomy of the anterior cruciate ligament. Clin Orthop Relat Res. 1983:19-25.
[51] Silver FH, Kato YP, Ohno M, Wasserman AJ. Analysis of Mammalian Connective-Tissue - Relationship between Hierarchical Structures and Mechanical-Properties. J Long-Term Eff Med. 1992;2:165-98.
[52] Beynnon BD, Fleming BC. Anterior cruciate ligament strain in-vivo: A review of previous work. Journal of Biomechanics. 1998;31:519-25.
[53] Escamilla RF, Macleod TD, Wilk KE, Paulos L, Andrews JR. Anterior cruciate ligament strain and tensile forces for weight-bearing and non-weight-bearing exercises: a guide to exercise selection. The Journal of orthopaedic and sports physical therapy. 2012;42:208-20.
[54] Levine JW, Kiapour AM, Quatman CE, Wordeman SC, Goel VK, Hewett TE, et al. Clinically Relevant Injury Patterns After an Anterior Cruciate Ligament Injury Provide Insight Into Injury Mechanisms. Am J Sport Med. 2013;41:385-95.
[55] Arendt EA, Agel J, Dick R. Anterior cruciate ligament injury patterns among collegiate men and women. J Athl Training. 1999;34:86-92.
[56] Kvist J. Rehabilitation following anterior cruciate ligament injury: current recommendations for sports participation. Sports Med. 2004;34:269-80.
[57] von Porat A, Roos EM, Roos H. High prevalence of osteoarthritis 14 years after an anterior cruciate ligament tear in male soccer players: a study of radiographic and patient relevant outcomes. Annals of the rheumatic diseases. 2004;63:269-73.

[58] Petrigliano FA, McAllister DR, Wu BM. Tissue engineering for anterior cruciate ligament reconstruction: A review of current strategies. Arthroscopy-the Journal of Arthroscopic and Related Surgery. 2006;22:441-51.
[59] Bray RC, Leonard CA, Salo PT. Correlation of healing capacity with vascular response in the anterior cruciate and medial collateral ligaments of the rabbit. Journal of orthopaedic research : official publication of the Orthopaedic Research Society. 2003;21:1118-23.
[60] Fu FH, Bennett CH, Ma CB, Menetrey J, Lattermann C. Current trends in anterior cruciate ligament reconstruction. Part II. Operative procedures and clinical correlations. The American journal of sports medicine. 2000;28:124-30.
[61] Brand J, Weiler A, Caborn DNM, Brown CH, Johnson DL. Graft fixation in cruciate ligament reconstruction. Am J Sport Med. 2000;28:761-74.
[62] Amis AA, Jakob RP. Anterior cruciate ligament graft positioning, tensioning and twisting. Knee surgery, sports traumatology, arthroscopy : official journal of the ESSKA. 1998;6 Suppl 1:S2-12.
[63] Dimitriou R, Babis GC. Biomaterial osseointegration enhancement with biophysical stimulation. Journal of musculoskeletal & neuronal interactions. 2007;7:253-65.
[64] Kartus J, Movin T, Karlsson J. Donor-site morbidity and anterior knee problems after anterior cruciate ligament reconstruction using autografts. Arthroscopy. 2001;17:971-80.
[65] L'Insalata JC, Klatt B, Fu FH, Harner CD. Tunnel expansion following anterior cruciate ligament reconstruction: a comparison of hamstring and patellar tendon autografts. Knee surgery, sports traumatology, arthroscopy : official journal of the ESSKA. 1997;5:234-8.
[66] Vangsness CT, Jr., Garcia IA, Mills CR, Kainer MA, Roberts MR, Moore TM. Allograft transplantation in the knee: tissue regulation, procurement, processing, and sterilization. The American journal of sports medicine. 2003;31:474-81.
[67] McAllister DR, Joyce MJ, Mann BJ, Vangsness CT, Jr. Allograft update: the current status of tissue regulation, procurement, processing, and sterilization. The American journal of sports medicine. 2007;35:2148-58.
[68] Legnani C, Ventura A, Terzaghi C, Borgo E, Albisetti W. Anterior cruciate ligament reconstruction with synthetic grafts. A review of literature. International orthopaedics. 2010;34:465-71.
[69] Nau T, Lavoie P, Duval N. A new generation of artificial ligaments in reconstruction of the anterior cruciate ligament. Two-year follow-up of a randomised trial. The Journal of bone and joint surgery British volume. 2002;84:356-60.
[70] Langer R, Vacanti JP. Tissue Engineering. Science. 1993;260:920-6.
[71] Laurencin CT, Nair LS. Biodegradable polymers as biomaterials. Prog Polym Sci. 2007;32:762-98.
[72] Majima T, Irie T, Sawaguchi N, Funakoshi T, Iwasaki N, Harada K, et al. Chitosan-based hyaluronan hybrid polymer fibre scaffold for ligament and tendon tissue engineering. Proc Inst Mech Eng H. 2007;221:537-46.
[73] Ge ZG, Yang F, Goh JCH, Ramakrishna S, Lee EH. Biomaterials and scaffolds for ligament tissue engineering. J Biomed Mater Res A. 2006;77A:639-52.
[74] Altman GH, Horan RL, Lu HH, Moreau J, I M, Richmond JC, et al. Silk matrix for tissue engineered anterior cruciate ligaments. Biomaterials. 2002;23:4131-41.
[75] Majima T, Funakosi T, Iwasaki N, Yamane ST, Harada K, Nonaka S, et al. Alginate and chitosan polyion complex hybrid fibers for scaffolds in ligament and tendon tissue engineering. J Orthop Sci. 2005;10:302-7.

[76] Horan RL, Antle K, Collette AL, Huang YZ, Huang J, Moreau JE, et al. In vitro degradation of silk fibroin. Biomaterials. 2005;26:3385-93.
[77] Trepte CT. [Animal experiment studies of the resistance to wear of a teflon ligament prosthesis]. Sportverletz Sportschaden. 1987;1:81-5.
[78] Guelcher SA. Biodegradable polyurethanes: Synthesis and applications in regenerative medicine. Tissue Eng Pt B-Rev. 2008;14:3-17.
[79] Stankus JJ, Guan J, Wagner WR. Fabrication of biodegradable elastomeric scaffolds with sub-micron morphologies. J Biomed Mater Res A. 2004;70:603-14.
[80] Ge Z, Goh JCH, Wang L, Tan EPS, Lee EH. Characterization of knitted polymeric scaffolds for potential use in ligament tissue engineering. J Biomat Sci-Polym E. 2005;16:1179-92.
[81] Vaquette C, Kahn C, Frochot C, Nouvel C, Six JL, De Isla N, et al. Aligned poly(L-lactic-co-e-caprolactone) electrospun microfibers and knitted structure: A novel composite scaffold for ligament tissue engineering. J Biomed Mater Res A. 2010;94A:1270-82.
[82] Sahoo S, Cho-Hong JG, Siew-Lok T. Development of hybrid polymer scaffolds for potential applications in ligament and tendon tissue engineering. Biomed Mater. 2007;2:169-73.
[83] Sill TJ, von Recum HA. Electro spinning: Applications in drug delivery and tissue engineering. Biomaterials. 2008;29:1989-2006.
[84] Subbiah T, Bhat GS, Tock RW, Pararneswaran S, Ramkumar SS. Electrospinning of nanofibers. J Appl Polym Sci. 2005;96:557-69.
[85] Nie HR, He AH, Zheng JF, Xu SS, Li JX, Han CC. Effects of chain conformation and entanglement on the electrospinning of pure alginate. Biomacromolecules. 2008;9:1362-5.
[86] Kim GH. Electrospun PCL nanofibers with anisotropic mechanical properties as a biomedical scaffold. Biomed Mater. 2008;3.
[87] Freeman JW, Andric T, Wright LD. Rapid Mineralization of Electrospun Scaffolds for Bone Tissue Engineering. J Biomat Sci-Polym E. 2011;22:1535-50.
[88] Freeman JW, McKeon-Fischer KD. Characterization of electrospun poly(L-lactide) and gold nanoparticle composite scaffolds for skeletal muscle tissue engineering. J Tissue Eng Regen M. 2011;5:560-8.
[89] Bini TB, Gao SJ, Tan TC, Wang S, Lim A, Hai LB, et al. Electrospun poly(L-lactide-co-glycolide) biodegradable polymer nanofibre tubes for peripheral nerve regeneration. Nanotechnology. 2004;15:1459-64.
[90] Lee CH, Shin HJ, Cho IH, Kang YM, Kim IA, Park KD, et al. Nanofiber alignment and direction of mechanical strain affect the ECM production of human ACL fibroblast. Biomaterials. 2005;26:1261-70.
[91] Rho KS, Jeong L, Lee G, Seo BM, Park YJ, Hong SD, et al. Electrospinning of collagen nanofibers: Effects on the behavior of normal human keratinocytes and early-stage wound healing. Biomaterials. 2006;27:1452-61.
[92] Li MY, Mondrinos MJ, Gandhi MR, Ko FK, Weiss AS, Lelkes PI. Electrospun protein fibers as matrices for tissue engineering. Biomaterials. 2005;26:5999-6008.
[93] Zhang YZ. Electrospinning of gelatin fibers and gelatin/PCL composite fibrous scaffolds. J Biomed Mater Res B. 2005;72B:156-65.
[94] Sisson K, Zhang C, Farach-Carson MC, Chase DB, Rabolt JF. Evaluation of cross-linking methods for electrospun gelatin on cell growth and viability. Biomacromolecules. 2009;10:1675-80.

[95] Soffer L, Wang X, Zhang X, Kluge J, Dorfmann L, Kaplan DL, et al. Silk-based electrospun tubular scaffolds for tissue-engineered vascular grafts. J Biomater Sci Polym Ed. 2008;19:653-64.
[96] Alessandrino A, Marelli B, Arosio C, Fare S, Tanzi MC, Freddi G. Electrospun Silk Fibroin mats for tissue engineering. Eng Life Sci. 2008;8:219-25.
[97] Alsberg E, Jeong SI, Krebs MD, Bonino CA, Khan SA. Electrospun Alginate Nanofibers with Controlled Cell Adhesion for Tissue Engineering. Macromol Biosci. 2010;10:934-43.
[98] Zhang MQ, Bhattarai N. Controlled synthesis and structural stability of alginate-based nanofibers. Nanotechnology. 2007;18.
[99] Kim MS, Kang YM, Lee BN, Ko JH, Kim GH, Kang KN, et al. In Vivo Biocompatibility Study of Electrospun Chitosan Microfiber for Tissue Engineering. Int J Mol Sci. 2010;11:4140-8.
[100] Powell HM, Boyce ST. Engineered Human Skin Fabricated Using Electrospun Collagen-PCL Blends: Morphogenesis and Mechanical Properties. Tissue Eng Pt A. 2009;15:2177-87.
[101] Bonino CA, Krebs MD, Saquing CD, Jeong SI, Shearer KL, Alsberg E, et al. Electrospinning alginate-based nanofibers: From blends to crosslinked low molecular weight alginate-only systems. Carbohyd Polym. 2011;85:111-9.
[102] Yoshimoto H, Shin YM, Terai H, Vacanti JP. A biodegradable nanofiber scaffold by electrospinning and its potential for bone tissue engineering. Biomaterials. 2003;24:2077-82.
[103] Gupta P, Wilkes GL. Some investigations on the fiber formation by utilizing a side-by-side bicomponent electrospinning approach. Polymer. 2003;44:6353-9.
[104] Zhang YZ, Wang X, Feng Y, Li J, Lim CT, Ramakrishna S. Coaxial electrospinning of (fluorescein isothiocyanate-conjugated bovine serum albumin)-encapsulated poly(epsilon-caprolactone) nanofibers for sustained release. Biomacromolecules. 2006;7:1049-57.
[105] Jiang HL, Hu YQ, Zhao PC, Li Y, Zhu KJ. Modulation of protein release from biodegradable core-shell structured fibers prepared by coaxial electrospinning. J Biomed Mater Res B. 2006;79B:50-7.
[106] Badami AS, Kreke MR, Thompson MS, Riffle JS, Goldstein AS. Effect of fiber diameter on spreading, proliferation, and differentiation of osteoblastic cells on electrospun poly(lactic acid) substrates. Biomaterials. 2006;27:596-606.
[107] Li D, Wang YL, Xia YN. Electrospinning of polymeric and ceramic nanofibers as uniaxially aligned arrays. Nano Lett. 2003;3:1167-71.
[108] Kumbar SG, James R, Nukavarapu SP, Laurencin CT. Electrospun nanofiber scaffolds: engineering soft tissues. Biomed Mater. 2008;3.
[109] Li M, Mondrinos MJ, Chen X, Gandhi MR, Ko FK, Lelkes PI. Co-electrospun poly(lactide-co-glycolide), gelatin, and elastin blends for tissue engineering scaffolds. J Biomed Mater Res A. 2006;79A:963-73.
[110] Ge ZG, Goh JCH, Lee EH. Selection of cell source for ligament tissue engineering. Cell Transplant. 2005;14:573-83.
[111] Koh CJ, Atala A. Tissue engineering, stem cells, and cloning: Opportunities for regenerative medicine. J Am Soc Nephrol. 2004;15:1113-25.
[112] Caplan AI. Adult mesenchymal stem cells for tissue engineering versus regenerative medicine. J Cell Physiol. 2007;213:341-7.
[113] Bianco P, Riminucci M, Gronthos S, Robey PG. Bone marrow stromal stem cells: Nature, biology, and potential applications. Stem Cells. 2001;19:180-92.

[114] Van Eijk F, Saris DBF, Riesle J, Willems WJ, Van Blitterswijk CA, Verbout AJ, et al. Tissue engineering of ligaments: A comparison of bone marrow stromal cells, anterior cruciate ligament, and skin fibroblasts as cell source. Tissue Engineering. 2004;10:893-903.
[115] Liu H, Fan H, Toh SL, Goh JC. A comparison of rabbit mesenchymal stem cells and anterior cruciate ligament fibroblasts responses on combined silk scaffolds. Biomaterials. 2008;29:1443-53.
[116] Mooney DJ, Lee K, Silva EA. Growth factor delivery-based tissue engineering: general approaches and a review of recent developments. J R Soc Interface. 2011;8:153-70.
[117] Cohen GB, Ren RB, Baltimore D. Modular Binding Domains in Signal-Transduction Proteins. Cell. 1995;80:237-48.
[118] Molloy T, Wang Y, Murrell GAC. The roles of growth factors in tendon and ligament healing. Sports Med. 2003;33:381-94.
[119] Jenner JM, van Eijk F, Saris DB, Willems WJ, Dhert WJ, Creemers LB. Effect of transforming growth factor-beta and growth differentiation factor-5 on proliferation and matrix production by human bone marrow stromal cells cultured on braided poly lactic-co-glycolic acid scaffolds for ligament tissue engineering. Tissue Eng. 2007;13:1573-82.
[120] Moreau JE, Chen J, Bramono DS, Volloch V, Chernoff H, Vunjak-Novakovic G, et al. Growth factor induced fibroblast differentiation from human bone marrow stromal cells in vitro. Journal of orthopaedic research : official publication of the Orthopaedic Research Society. 2005;23:164-74.
[121] Moreau J, Chen J, Kaplan D, Altman G. Sequential growth factor stimulation of bone marrow stromal cells in extended culture. Tissue Eng. 2006;12:2905-12.
[122] Seidi A, Ramalingam M, Elloumi-Hannachi I, Ostrovidov S, Khademhosseini A. Gradient biomaterials for soft-to-hard interface tissue engineering. Acta Biomaterialia. 2011;7:1441-51.
[123] Lu HH, Subramony SD, Boushell MK, Zhang X. Tissue Engineering Strategies for the Regeneration of Orthopedic Interfaces. Ann Biomed Eng. 2010.
[124] Barrere F, van Blitterswijk CA, de Groot K. Bone regeneration: molecular and cellular interactions with calcium phosphate ceramics. Int J Nanomed. 2006;1:317-32.
[125] Lee KY, Park M, Kim HM, Lim YJ, Chun HJ, Kim H, et al. Ceramic bioactivity: progresses, challenges and perspectives. Biomed Mater. 2006;1:R31-R7.
[126] Fabbri P, Bondioli F, Messori M, Bartoli C, Dinucci D, Chiellini F. Porous scaffolds of polycaprolactone reinforced with in situ generated hydroxyapatite for bone tissue engineering. J Mater Sci Mater Med. 2010;21:343-51.
[127] Wutticharoenmongkol P, Pavasant P, Supaphol P. Osteoblastic phenotype expression of MC3T3-E1 cultured on electrospun polycaprolactone fiber mats filled with hydroxyapatite nanoparticles. Biomacromolecules. 2007;8:2602-10.
[128] Venugopal J, Low S, Choon AT, Kumar AB, Ramakrishna S. Electrospun-modified nanofibrous scaffolds for the mineralization of osteoblast cells. J Biomed Mater Res A. 2008;85:408-17.
[129] Erisken C, Kalyon DM, Wang HJ. Functionally graded electrospun polycaprolactone and beta-tricalcium phosphate nanocomposites for tissue engineering applications. Biomaterials. 2008;29:4065-73.
[130] Ozkan S, Kalyon DM, Yu X. Functionally graded beta-TCP/PCL nanocomposite scaffolds: in vitro evaluation with human fetal osteoblast cells for bone tissue engineering. J Biomed Mater Res A. 2010;92:1007-18.

[131] Singh M, Dormer N, Salash JR, Christian JM, Moore DS, Berkland C, et al. Three-dimensional macroscopic scaffolds with a gradient in stiffness for functional regeneration of interfacial tissues. J Biomed Mater Res A. 2010;94:870-6.
[132] Li XR, Xie JW, Lipner J, Yuan XY, Thomopoulos S, Xia YN. Nanofiber scaffolds with gradations in mineral content for mimicking the tendon-to-bone insertion site. Nano Lett. 2009;9:2763-8.
[133] Spalazzi JP, Doty SB, Moffat KL, Levine WN, Lu HH. Development of controlled matrix heterogeneity on a triphasic scaffold for orthopedic interface tissue engineering. Tissue Eng. 2006;12:3497-508.
[134] Spalazzi JP, Dagher E, Doty SB, Guo XE, Rodeo SA, Lu HH. In vivo evaluation of a tri-phasic composite scaffold for anterior cruciate ligament-to-bone integration. Conf Proc IEEE Eng Med Biol Soc. 2006;1:525-8.
[135] Xie JW, Ma B, Michael PL, Shuler FD. Fabrication of Nanofiber Scaffolds With Gradations in Fiber Organization and Their Potential Applications. Macromol Biosci. 2012;12:1336-41.
[136] Detamore MS, Dormer NH, Busaidy K, Berkland CJ. Osteochondral Interface Regeneration of Rabbit Mandibular Condyle With Bioactive Signal Gradients. J Oral Maxil Surg. 2011;69:E50-E7.
[137] Mohan N, Dormer NH, Caldwell KL, Key VH, Berkland CJ, Detamore MS. Continuous gradients of material composition and growth factors for effective regeneration of the osteochondral interface. Tissue Eng Part A. 2011;17:2845-55.
[138] Kaplan DL, Wang XQ, Wenk E, Zhang XH, Meinel L, Vunjak-Novakovic G. Growth factor gradients via microsphere delivery in biopolymer scaffolds for osteochondral tissue engineering. J Control Release. 2009;134:81-90.
[139] Phillips JE, Burns KL, Le Doux JM, Guldberg RE, Garcia AJ. Engineering graded tissue interfaces. Proc Natl Acad Sci U S A. 2008;105:12170-5.
[140] Kokubo T, Takadama H. How useful is SBF in predicting in vivo bone bioactivity? Biomaterials. 2006;27:2907-15.
[141] Jayasuriya AC, Shah C, Ebraheim NA, Jayatissa AH. Acceleration of biomimetic mineralization to apply in bone regeneration. Biomed Mater. 2008;3.
[142] Yang F, Wolke JGC, Jansen JA. Biomimetic calcium phosphate coating on electrospun poly (epsilon-caprolactone) scaffolds for bone tissue engineering. Chem Eng J. 2008;137:154-61.
[143] Jalota S, Bhaduri SB, Tas AC. Effect of carbonate content and buffer type on calcium phosphate formation in SBF solutions. J Mater Sci Mater Med. 2006;17:697-707.
[144] Jayasuriya AC, Kibbe S. Rapid biomineralization of chitosan microparticles to apply in bone regeneration. J Mater Sci Mater Med. 2010;21:393-8.
[145] Kweon H, Yoo MK, Park IK, Kim TH, Lee HC, Lee HS, et al. A novel degradable polycaprolactone networks for tissue engineering. Biomaterials. 2003;24:801-8.
[146] Guelcher SA, Gallagher KM, Didier JE, Klinedinst DB, Doctor JS, Goldstein AS, et al. Synthesis of biocompatible segmented polyurethanes from aliphatic diisocyanates and diurea diol chain extenders. Acta Biomater. 2005;1:471-84.
[147] Yang F, Both SK, Yang XC, Walboomers XF, Jansen JA. Development of an electrospun nano-apatite/PCL composite membrane for GTR/GBR application. Acta Biomater. 2009;5:3295-304.

[148] Kretlow JD, Mikos AG. Review: mineralization of synthetic polymer scaffolds for bone tissue engineering. Tissue Eng. 2007;13:927-38.
[149] Tas AC, Bhaduri SB. Rapid coating of Ti6A14V at room temperature with a calcium phosphate solution similar to 10x simulated body fluid. Journal of Materials Research. 2004;19:2742-9.
[150] Madurantakam PA, Rodriguez IA, Cost CP, Viswanathan R, Simpson DG, Beckman MJ, et al. Multiple factor interactions in biomimetic mineralization of electrospun scaffolds. Biomaterials. 2009;30:5456-64.
[151] Tanahashi M, Matsuda T. Surface functional group dependence on apatite formation on self-assembled monolayers in a simulated body fluid. J Biomed Mater Res. 1997;34:305-15.
[152] Goldstein SA, Wilson DL, Sonstegard DA, Matthews LS. The Mechanical-Properties of Human Tibial Trabecular Bone as a Function of Metaphyseal Location. Journal of Biomechanics. 1983;16:965-9.
[153] Engelberg I, Kohn J. Physicomechanical Properties of Degradable Polymers Used in Medical Applications - a Comparative-Study. Biomaterials. 1991;12:292-304.
[154] Katti KS, Turlapati P, Verma D, Bhowmik R, Gujjala PK, Katti DR. Static and dynamic mechanical behavior of hydroxyapatite-polyacrylic acid composites under simulated body fluid. American Journal of Biochemistry and Biotechnology. 2006;2:73-9.
[155] Du FY, Wang H, Zhao W, Li D, Kong DL, Yang J, et al. Gradient nanofibrous chitosan/poly epsilon-caprolactone scaffolds as extracellular microenvironments for vascular tissue engineering. Biomaterials. 2012;33:762-70.
[156] Samavedi S, Olsen Horton C, Guelcher SA, Goldstein AS, Whittington AR. Fabrication of a model continuously graded co-electrospun mesh for regeneration of the ligament-bone interface. Acta Biomater. 2011;7:4131-8.
[157] Lee JH, Rim NG, Jung HS, Shin H. Control of Osteogenic Differentiation and Mineralization of Human Mesenchymal Stem Cells on Composite Nanofibers Containing Poly [lactic-co-(glycolic acid)] and Hydroxyapatite. Macromol Biosci. 2010;10:173-82.
[158] Bernhardt A, Despang F, Lode A, Demmler A, Hanke T, Gelinsky M. Proliferation and osteogenic differentiation of human bone marrow stromal cells on alginate-gelatine-hydroxyapatite scaffolds with anisotropic pore structure. J Tissue Eng Regen Med. 2009;3:54-62.
[159] Haimi S, Suuriniemi N, Haaparanta AM, Ella V, Lindroos B, Huhtala H, et al. Growth and osteogenic differentiation of adipose stem cells on PLA/bioactive glass and PLA/beta-TCP scaffolds. Tissue Eng Part A. 2009;15:1473-80.
[160] Takahashi Y, Yamamoto M, Tabata Y. Osteogenic differentiation of mesenchymal stem cells in biodegradable sponges composed of gelatin and beta-tricalcium phosphate. Biomaterials. 2005;26:3587-96.
[161] Popp JR, Laflin KE, Love BJ, Goldstein AS. In vitro evaluation of osteoblastic differentiation on amorphous calcium phosphate-decorated poly(lactic-co-glycolic acid) scaffolds. J Tissue Eng Regen Med. 2011;5:780-9.
[162] Frank O, Heim M, Jakob M, Barbero A, Schafer D, Bendik I, et al. Real-time quantitative RT-PCR analysis of human bone marrow stromal cells during osteogenic differentiation in vitro. J Cell Biochem. 2002;85:737-46.
[163] Wei GB, Ma PX. Structure and properties of nano-hydroxyapatite/polymer composite scaffolds for bone tissue engineering. Biomaterials. 2004;25:4749-57.

[164] Kavlock KD, Pechar TW, Hollinger JO, Guelcher SA, Goldstein AS. Synthesis and characterization of segmented poly(esterurethane urea) elastomers for bone tissue engineering. Acta Biomater. 2007;3:475-84.
[165] Livak KJ, Schmittgen TD. Analysis of relative gene expression data using real-time quantitative PCR and the 2(T)(-Delta Delta C) method. Methods. 2001;25:402-8.
[166] Wutticharoenmongkol P, Sanchavanakit N, Pavasant P, Supaphol P. Preparation and characterization of novel bone scaffolds based on electrospun polycaprolactone fibers filled with nanoparticles. Macromol Biosci. 2006;6:70-7.
[167] Thomas V, Dean DR, Jose MV, Mathew B, Chowdhury S, Vohra YK. Nanostructured biocomposite scaffolds based on collagen coelectrospun with nanohydroxyapatite. Biomacromolecules. 2007;8:631-7.
[168] Wang KF, Zhou CC, Hong YL, Zhang XD. A review of protein adsorption on bioceramics. Interface Focus. 2012;2:259-77.
[169] Zhou GS, Su ZY, Cai YR, Liu YK, Dai LC, Tang RK, et al. Different effects of nanophase and conventional hydroxyapatite thin films on attachment, proliferation and osteogenic differentiation of bone marrow derived mesenchymal stem cells. Bio-Med Mater Eng. 2007;17:387-95.
[170] Hu QH, Tan Z, Liu YK, Tao JH, Cai YR, Zhang M, et al. Effect of crystallinity of calcium phosphate nanoparticles on adhesion, proliferation, and differentiation of bone marrow mesenchymal stem cells. J Mater Chem. 2007;17:4690-8.
[171] Okada S, Ito H, Nagai A, Komotori J, Imai H. Adhesion of osteoblast-like cells on nanostructured hydroxyapatite. Acta Biomater. 2010;6:591-7.
[172] Liu Y, Shelton RM, Gbureck U, Barralet JE. Influence of calcium phosphate crystal morphology on the adhesion, spreading, and growth of bone derived cells. Journal of Biomedical Materials Research Part A. 2009;90A:972-80.
[173] Kim K, Dean D, Lu AQ, Mikos AG, Fisher JP. Early osteogenic signal expression of rat bone marrow stromal cells is influenced by both hydroxyapatite nanoparticle content and initial cell seeding density in biodegradable nanocomposite scaffolds. Acta Biomater. 2011;7:1249-64.
[174] Liu Y, Cooper PR, Barralet JE, Shelton RM. Influence of calcium phosphate crystal assemblies on the proliferation and osteogenic gene expression of rat bone marrow stromal cells. Biomaterials. 2007;28:1393-403.
[175] Fang B, Wan YZ, Tang TT, Gao C, Dai KR. Proliferation and Osteoblastic Differentiation of Human Bone Marrow Stromal Cells on Hydroxyapatite/Bacterial Cellulose Nanocomposite Scaffolds. Tissue Eng Pt A. 2009;15:1091-8.
[176] Whited BM, Skrtic D, Love BJ, Goldstein AS. Osteoblast response to zirconia-hybridized pyrophosphate-stabilized amorphous calcium phosphate. J Biomed Mater Res A. 2006;76:596-604.
[177] Jaiswal N, Haynesworth SE, Caplan AI, Bruder SP. Osteogenic differentiation of purified, culture-expanded human mesenchymal stem cells in vitro. J Cell Biochem. 1997;64:295-312.
[178] Jung GY, Park YJ, Han JS. Effects of HA released calcium ion on osteoblast differentiation. J Mater Sci-Mater M. 2010;21:1649-54.
[179] Khoshniat S, Bourgine A, Julien M, Petit M, Pilet P, Rouillon T, et al. Phosphate-dependent stimulation of MGP and OPN expression in osteoblasts via the ERK1/2 pathway is modulated by calcium. Bone. 2011;48:894-902.
[180] Nishikawa M, Myoui A, Ohgushi H, Ikeuchi M, Tamai N, Yoshikawa H. Bone tissue engineering using novel interconnected porous hydroxyapatite ceramics combined with marrow

mesenchymal cells: Quantitative and three-dimensional image analysis. Cell Transplantation. 2004;13:367-76.
[181] Ogata K, Imazato S, Ehara A, Ebisu S, Kinomoto Y, Nakano T, et al. Comparison of osteoblast responses to hydroxyapatite and hydroxyapatite/soluble calcium phosphate composites. Journal of Biomedical Materials Research Part A. 2005;72A:127-35.
[182] Muller P, Bulnheim U, Diener A, Luthen F, Teller M, Klinkenberg ED, et al. Calcium phosphate surfaces promote osteogenic differentiation of mesenchymal stem cells. J Cell Mol Med. 2008;12:281-91.
[183] Genin GM, Kent A, Birman V, Wopenka B, Pasteris JD, Marquez PJ, et al. Functional grading of mineral and collagen in the attachment of tendon to bone. Biophys J. 2009;97:976-85.
[184] Bashur CA, Dahlgren LA, Goldstein AS. Effect of fiber diameter and orientation on fibroblast morphology and proliferation on electrospun poly(D,L-lactic-co-glycolic acid) meshes. Biomaterials. 2006;27:5681-8.
[185] Katta P, Alessandro M, Ramsier RD, Chase GG. Continuous electrospinning of aligned polymer nanofibers onto a wire drum collector. Nano Lett. 2004;4:2215-8.
[186] Xie JW, MacEwan MR, Ray WZ, Liu WY, Siewe DY, Xia YN. Radially Aligned, Electrospun Nanofibers as Dural Substitutes for Wound Closure and Tissue Regeneration Applications. Acs Nano. 2010;4:5027-36.
[187] Dalton PD, Klee D, Moller M. Electrospinning with dual collection rings. Polymer. 2005;46:611-4.
[188] Li WJ, Mauck RL, Cooper JA, Yuan XN, Tuan RS. Engineering controllable anisotropy in electrospun biodegradable nanofibrous scaffolds for musculoskeletal tissue engineering. Journal of Biomechanics. 2007;40:1686-93.
[189] Cardwell RD, Dahlgren LA, Goldstein AS. Electrospun fibre diameter, not alignment, affects mesenchymal stem cell differentiation into the tendon/ligament lineage. J Tissue Eng Regen Med. 2012.
[190] Lyu S, Huang C, Yang H, Zhang X. Electrospun Fibers as a Scaffolding Platform for Bone Tissue Repair. Journal of orthopaedic research : official publication of the Orthopaedic Research Society. 2013.
[191] Nathan AS, Baker BM, Nerurkar NL, Mauck RL. Mechano-topographic modulation of stem cell nuclear shape on nanofibrous scaffolds. Acta Biomater. 2011;7:57-66.
[192] Liu Y, Ji Y, Ghosh K, Clark RAF, Huang L, Rafailovichz MH. Effects of fiber orientation and diameter on the behavior of human dermal fibroblasts on electrospun PMMA scaffolds. J Biomed Mater Res A. 2009;90A:1092-106.
[193] Dhandayuthapani B, Yoshida Y, Maekawa T, Kumar DS. Polymeric Scaffolds in Tissue Engineering Application: A Review. Int J Polym Sci. 2011.
[194] James R, Toti US, Laurencin CT, Kumbar SG. Electrospun nanofibrous scaffolds for engineering soft connective tissues. Methods in molecular biology. 2011;726:243-58.
[195] Goh YF, Shakir I, Hussain R. Electrospun fibers for tissue engineering, drug delivery, and wound dressing. J Mater Sci. 2013;48:3027-54.
[196] Zhang YZ, Su B, Venugopal J, Ramakrishna S, Lim CT. Biomimetic and bioactive nanofibrous scaffolds from electrospun composite nanofibers. Int J Nanomedicine. 2007;2:623-38.
[197] Hankemeier S, Keus M, Zeichen J, Jagodzinski M, Barkhausen T, Bosch U, et al. Modulation of proliferation and differentiation of human bone marrow stromal cells by fibroblast

growth factor 2: potential implications for tissue engineering of tendons and ligaments. Tissue Eng. 2005;11:41-9.
[198] Petrigliano FA, English CS, Barba D, Esmende S, Wu BM, McAllister DR. The effects of local bFGF release and uniaxial strain on cellular adaptation and gene expression in a 3D environment: implications for ligament tissue engineering. Tissue Eng. 2007;13:2721-31.
[199] Sahoo S, Ang LT, Goh JCH, Toh SL. Growth factor delivery through electrospun nanofibers in scaffolds for tissue engineering applications. J Biomed Mater Res A. 2010;93A:1539-50.
[200] Tabata Y, Hijikata S, Muniruzzaman M, Ikada Y. Neovascularization effect of biodegradable gelatin microspheres incorporating basic fibroblast growth factor. J Biomat Sci-Polym E. 1999;10:79-94.
[201] Holland TA, Tabata Y, Mikos AG. In vitro release of transforming growth factor-beta 1 from gelatin microparticles encapsulated in biodegradable, injectable oligo(poly(ethylene glycol) fumarate) hydrogels. J Control Release. 2003;91:299-313.
[202] Li Y, Jiang HL, Zhu KJ. Encapsulation and controlled release of lysozyme from electrospun poly(epsilon-caprolactone)/poly(ethylene glycol) non-woven membranes by formation of lysozyme-oleate complexes. J Mater Sci-Mater M. 2008;19:827-32.
[203] Hiwale P, Lampis S, Conti G, Caddeo C, Murgia S, Fadda AM, et al. In Vitro Release of Lysozyme from Gelatin Microspheres: Effect of Cross-linking Agents and Thermoreversible Gel as Suspending Medium. Biomacromolecules. 2011;12:3186-93.
[204] Dinarvand R, Mahmoodi S, Farboud E, Salehi M, Atyabi F. Preparation of gelatin microspheres containing lactic acid--effect of cross-linking on drug release. Acta Pharm. 2005;55:57-67.
[205] Choi JS, Leong KW, Yoo HS. In vivo wound healing of diabetic ulcers using electrospun nanofibers immobilized with human epidermal growth factor (EGF). Biomaterials. 2008;29:587-96.
[206] Li C, Vepari C, Jin HJ, Kim HJ, Kaplan DL. Electrospun silk-BMP-2 scaffolds for bone tissue engineering. Biomaterials. 2006;27:3115-24.
[207] Liu JJ, Wang CY, Wang JG, Ruan HJ, Fan CY. Peripheral nerve regeneration using composite poly(lactic acid-caprolactone)/nerve growth factor conduits prepared by coaxial electrospinning. J Biomed Mater Res A. 2011;96A:13-20.
[208] Ji W, Yang F, van den Beucken JJ, Bian Z, Fan M, Chen Z, et al. Fibrous scaffolds loaded with protein prepared by blend or coaxial electrospinning. Acta Biomater. 2010;6:4199-207.
[209] Ionescu LC, Lee GC, Sennett BJ, Burdick JA, Mauck RL. An anisotropic nanofiber/microsphere composite with controlled release of biomolecules for fibrous tissue engineering. Biomaterials. 2010;31:4113-20.
[210] Dong B, Smith ME, Wnek GE. Encapsulation of Multiple Biological Compounds Within a Single Electrospun Fiber. Small. 2009;5:1508-12.
[211] Muller P, Bulnheim U, Diener A, Luthen F, Teller M, Klinkenberg ED, et al. Calcium phosphate surfaces promote osteogenic differentiation of mesenchymal stem cells. J Cell Mol Med. 2008;12:281-91.
[212] Zhu XD, Fan HS, Xiao YM, Li DX, Zhang HJ, Luxbacher T, et al. Effect of surface structure on protein adsorption to biphasic calcium-phosphate ceramics in vitro and in vivo. Acta Biomater. 2009;5:1311-8.
[213] Li X, van Blitterswijk CA, Feng Q, Cui F, Watari F. The effect of calcium phosphate microstructure on bone-related cells in vitro. Biomaterials. 2008;29:3306-16.

[214] Song G, Habibovic P, Bao C, Hu J, van Blitterswijk CA, Yuan H, et al. The homing of bone marrow MSCs to non-osseous sites for ectopic bone formation induced by osteoinductive calcium phosphate. Biomaterials. 2013;34:2167-76.
[215] Tutak W, Sarkar S, Lin-Gibson S, Farooque TM, Jyotsnendu G, Wang D, et al. The support of bone marrow stromal cell differentiation by airbrushed nanofiber scaffolds. Biomaterials. 2013;34:2389-98.

Appendix A

Calcium phosphate ceramics in bone tissue engineering:

A review of properties and their influence on cell behavior

Satyavrata Samavedi[a], Abby R. Whittington[a,b,c], Aaron S. Goldstein[a,c]

[a] Department of Chemical Engineering, Virginia Tech, Blacksburg, VA

[b] Department of Materials Science and Engineering, Virginia Tech, Blacksburg, VA

[c] School of Biomedical Engineering and Sciences, Virginia Tech, Blacksburg, VA

A1. Abstract

Calcium phosphate ceramics (CPCs) have been widely used as biomaterials for the regeneration of bone tissue because of their ability to induce osteoblastic differentiation in progenitor cells. Despite the progress made towards fabricating CPCs possessing a range of surface features and chemistries, the influence of material properties in orchestrating cellular events such as adhesion and differentiation is still poorly understood. Specifically, questions such as why certain CPCs may be more osteoinductive than others, and how material properties contribute to osteoinductivity/osteoconductivity still remain unanswered. Therefore, this review article systematically discusses the effects of the physical (e.g., surface roughness) and chemical properties (e.g., solubility) of CPCs on protein adsorption, cell adhesion and osteoblastic differentiation *in vitro*. The review also provides a summary of possible signaling pathways involved in osteoblastic differentiation in the presence of CPCs. In summary, these insights on the contribution of material properties towards osteoinductivity and the role of signaling

molecules involved in osteoblastic differentiation can potentially aid the design of CPC-based biomaterials that support bone regeneration without the need for additional biochemical supplements.

Keywords: calcium phosphate, ceramics, osteoinduction, protein adsorption, cell adhesion, osteoblastic differentiation, bone tissue engineering

A2. Introduction

Calcium phosphate ceramics (CPCs) are a class of tunable bioactive materials that have been widely used for bone tissue repair and augmentation [1]. They possess surface properties that support osteoblast adhesion/proliferation (i.e., osteoconduction) and stimulate new bone formation (i.e., osteoinduction) [2, 3]. More significantly, CPCs have been shown to promote bone growth *in vivo* [4], and recruit bone marrow stromal cells (BMSCs) to ectopic sites to induce bone formation [5]. However, not all types of CPCs have the same biological effect *in vivo* [6-8]; while most are osteoconductive, only certain types are osteoinductive [9]. Such differences in their ability to induce osteoblastic differentiation are related to subtle differences in the physical and chemical properties of CPCs. For example, chemical properties such as surface chemistry and charge can influence biological phenomena like protein adsorption [10], which can subsequently drive osteoblastic differentiation via cell-extra cellular matrix (ECM) interactions [11, 12]. Likewise, physical properties such as surface roughness can also aid cell differentiation by influencing cell adhesion [13]. Furthermore, certain surface features can facilitate the adsorption of cell-adhesive proteins and thus provide conditions conducive to the formation of stable focal adhesive complexes. Thus, understanding the roles of specific material properties in modulating cell behavior is critical towards designing osteoinductive CPCs.

This review discusses the influence of the physical and chemical properties of CPCs on the adhesion and osteoblastic differentiation of cells in the context of bone tissue engineering (BTE). In particular, it seeks to explain how the differences in CPC properties such as surface roughness, chemistry, solubility and crystallinity correlate to differences in osteoconductivity and osteoinductivity (**Figure A1**). The review begins by highlighting the osteoinductive effects

of CPCs *in vitro* (**Section A3**), and then summarizes important chemical properties of four types of CPCs commonly used in BTE, namely hydroxyapatite (HAP), tricalcium phosphate (TCP), amorphous calcium phosphates (ACPs) and biphasic calcium phosphates (BCPs) (**Section A4**). Since osteoblastic differentiation is also regulated via other biological phenomena, **Section 5** provides an analysis of how CPC properties affect two key precursor events: protein adsorption and cell adhesion. Here, the review does not describe data from *in vivo* experiments because of intrinsic ambiguities associated with animal studies. **Section 6** provides a summary of possible signaling pathways involved in osteoblastic differentiation in the presence of CPCs, with special focus on the roles of ions and focal-adhesion mediated changes. Finally, **Section 7** offers concluding remarks concerning the present and future roles of CPCs in BTE.

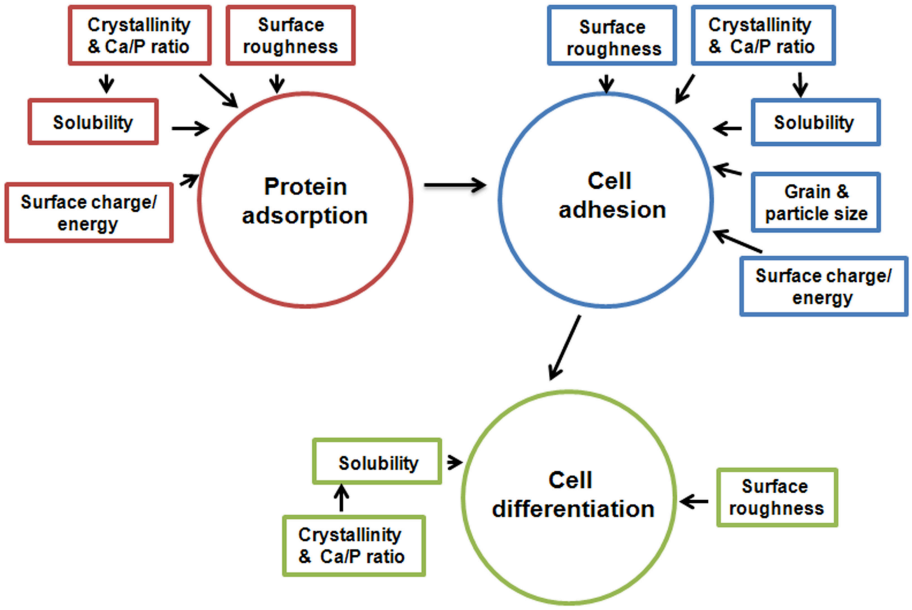

Figure A1: Schematic of key CPC properties that affect a cascade of biological processes including protein adsorption, cell adhesion and cell differentiation.

A3. Osteoinductivity of CPCs

Generally, osteoinductivity is the ability of a material to recruit and induce progenitor or undifferentiated cells to differentiate towards the osteoblastic lineage [3]. Common markers of the osteoblastic phenotype include type I collagen, alkaline phosphatase (ALP), bone morphogenetic protein-2 (BMP-2), osteopontin (OPN), osteocalcin (OCN), and bone sialoprotein (BSP); the roles of these and other proteins involved in osteoblastic differentiation are

summarized in **Table A1** [14-23]. The osteoinductivity of CPCs in particular varies significantly depending on material properties. In addition, cell type and the presence of osteogenic supplements also influence the degree of osteoinduction. Typically, undifferentiated mesenchymal stem cells (MSCs) such as BMSCs and adipose derived stem cells (ADSCs) offer a more rigorous test of osteoinductivity than osteoblastic cell lines such as MC3T3-E1 and MG63. However, MSCs are also commonly cultured in the presence of osteogenic supplements to direct their differentiation towards the osteoblastic lineage. While the use of osteogenic supplements can potentially marginalize the contribution of CPCs, a considerable number of studies have reported the osteoinductive effect of CPCs in their presence. Therefore, the following sections summarize the effect of CPCs on cell differentiation both in the presence and absence of osteogenic supplements.

Name	**Type**	**Primary function during differentiation**
Runx2	Transcription factor	Helps in the differentiation of mesenchymal stem cells into immature osteoblasts
Osterix (OSX)	Transcription factor	Acts down-stream of Runx2 and promotes osteogenesis, while inhibiting chondrogenesis
Alkaline phosphatase (ALP)	Enzyme	Increases local concentration of phosphate ions that in turn initiate mineral growth
Type I collagen	ECM protein	Mineral nucleation begins at the junction between two collagen fiber bundles
Osteopontin (OPN)	ECM protein	Acts as an inhibitor towards irregular formation of mineral crystals
Bone sialoprotein (BSP)	ECM protein	Binds to Ca^{2+} via free hydroxyl groups and promotes nucleation of mineral
Osteocalcin (OCN)	ECM protein	Regulates mineral growth, direction, size and quantity during late stages of differentiation
Osteonectin (ONN)	ECM protein	Similar role to that played by osteocalcin
Bone morphogenic protein 2 (BMP2)	Growth factor	Secreted by immature osteoblasts and may trigger a variety of autocrine/paracrine pathways
Bone morphogenic protein 7 (BMP7)	Growth factor	Similar role to that played by BMP2

Table A1: Markers of osteoblastic differentiation [14-20].

A3.1. Osteoinduction in the presence of osteogenic supplements

In vitro studies of osteoblastic maturation conducted in the presence of osteogenic supplements (e.g., dexamethasone, ascorbic acid and β-glycerolphosphate [24]) show that CPCs generally have a positive osteoinductive effect. For example, Lee et al – who examined the differentiation of human MSCs on electrospun scaffolds with and without HAP – showed elevated expression of ALP, OCN and BSP mRNA at days 14 and 21 on scaffolds loaded with HAP [25]. Further, the authors found that the expression of ALP, BSP and OCN mRNA increased with increasing HAP content, indicating a positive osteoinductive effect of HAP loading concentration. In another study, Eslaminejad et al showed an increase in the expression of OCN and OPN mRNA from day 1 to day 21 by rat BMSCs cultured on alginate-gelatin-βTCP scaffolds in the presence of osteogenic supplements [26]. While the studies by Lee et al and Eslaminejad et al indicate that the incorporation of a CPC phase into a scaffold can promote osteoblastic differentiation, comparison of the osteoinductivity of CPCs with different stoichiometries and crystallinities reveals diverse trends. In a study comparing ACP and HAP of similar particle sizes, Hu et al showed that HAP induced higher expression of OCN, OPN and type I collagen mRNA by rabbit BMSCs than ACP at day 14 [27]. Similarly, ter Brugge et al reported that amorphous CPC surfaces inhibit mineralization in rat BMSCs, as compared to amorphous-crystalline CPC surfaces of comparable surface roughness [28]. The authors also suggested that the higher solubility of the amorphous CPCs than the amorphous-crystalline CPCs might result in cell apoptosis. Lastly, Yuan et al – who compared TCP, HAP, and BCP minerals – found a significantly higher expression of OCN and BSP mRNA by human BMSCs cultured on TCP, as compared to HAP or BCP [29]. Together, these studies reveal that while all CPCs facilitate cell differentiation in the presence of osteogenic supplements, a range of osteoinductive potentials exists: TCP > BCP ≈ HAP > ACP.

Such differences in the osteoinductivities across CPC types may stem from a number of factors including chemical properties (e.g., stoichiometry, solubility) and topographical features (e.g., microporosity, roughness). Although these factors will be discussed in more detail in subsequent sections, the better performance of HAP over ACP in the presence of supplements

may be a result of the higher crystallinity [27], while the better performance of TCP over HAP and BCP in the presence of supplements may stem from the higher solubility of TCP [29]. At the same time, the better performance of TCP reported in the study by Yuan et al may be related to higher microporosity relative to HAP and BCP, which can facilitate protein adsorption [29].

A3.2. Osteoinduction in the absence of osteogenic supplements

Although osteogenic supplements are commonly used while studying the influence of CPCs on MSCs, a few studies have suggested that certain CPCs are osteoinductive in the absence of supplements. Moreover, this osteoinductive capacity has been found to vary with the type and properties of the CPCs. For example, Muller et al showed elevated expression of OCN and BSP mRNA by human BMSCs cultured on BONIT Matrix (BCP with the major component being 60/40 HAP/TCP) [11]. Side-by-side comparison of different CPCs reveals further differences in their osteoinductive potentials. Polini et al showed that human BMSCs, in the absence of osteogenic supplements, expressed higher levels of Runx-2 and BSP mRNA on PCL nanofibers loaded with TCP particles, compared to nanofibers loaded with HAP particles [30]. In another study, Guha et al showed that BMSCs cultured on HAP/TCP biphasic substrates produced more OCN than cells cultured on HAP [31]. Concurrently, Arinzeh et al showed that a 20/80 HAP/TCP scaffold – but neither a 60/40 HAP/TCP nor a pure TCP scaffold – was able to induce production of ALP and OCN in human MSCs in the absence of dexamethasone [32].

Together, these results suggest that a range of osteoinductive potentials exist for CPCs in the absence of osteogenic supplements: BCP > TCP > HAP. Although this trend is not identical to that described for CPCs in the presence of supplements, it indicates that CPC properties can significantly influence osteoinduction. It also suggests that BCPs, which combine the attractive properties of both HAP and TCP, may possess higher osteoinductivities than either HAP or TCP.

A4. Chemical properties of CPCs

Differences in the osteoinductive capacities of CPCs are likely linked to the inherent differences in properties such as solubility, crystallinity and stoichiometry (e.g., calcium to phosphate (Ca/P) ratio). This section provides a brief description of these properties for four

types of CPCs **(Table A2)**. Additional information describing the syntheses and properties of these CPCs can be found elsewhere [33-36].

A4.1. HAP

HAP is widely used in bone regeneration because its composition is closest to that of bone mineral [37]. Among the various monophasic CPCs, HAP is the most stable and least soluble phase [38, 39], possessing a Ksp value of around 2.9×10^{-58} over a pH range of ~ 3.5 to ~ 9.7 [40]. Moreover, stoichiometric HAP ($Ca_5(PO_4)_3)OH$) has a Ca/P ratio of 1.67 and is considered to be osteoconductive but not osteoinductive [41]. However, these properties can be tuned via ionic substitutions. For example, anionic substitution of carbonate for phosphate has been shown to increase HAP solubility (and bioactivity [42]), while substitution of fluoride for hydroxide increases stability. Similarly, cationic substitutions such as magnesium in place of calcium can potentially have favorable biological effects by providing trace ions.

A4.2. TCP

Stoichiometric TCP ($Ca_3(PO_4)_2$) possesses a Ca/P ratio of 1.5 and occurs in two phases, α and β; these phases possess identical chemistries but different crystal structures [10]. Both phases are less stable than HAP and hence more soluble in aqueous environments [39]: Ksp values of $10^{-25.5}$ for α-TCP and $10^{-28.9}$ for β-TCP at 25 °C have been reported [43]. However, β-TCP is considered to be both osteoconductive and osteoinductive, and has been used more extensively in bone regeneration than α-TCP. Therefore, α-TCP is not discussed further.

CPC	Solubility (~ Ksp)	Ca/P ratio	Osteoinductivity
HAP	Poor (10^{-58})	1.67	+
TCP	Fair (10^{-25} to 10^{-29})	1.5	++
ACP	High (10^{-23} to 10^{-25})	1.15- 1.67	+++
BCP	Variable (dependent on TCP/HAP ratio)	1.5- 1.67	++++

Table A2: Summary of key CPC properties that influence osteoblastic differentiation.

A4.3. ACP

ACPs are a family of CPCs characterized by a lack of long-range order [28]. They can be produced by rapid precipitation of calcium and phosphate ions from aqueous solutions. Consequently, they lack a well-defined stoichiometry and are marked by the presence of impurities (e.g., Na^+, Cl^-) [44]. ACPs typically exhibit a broad range of Ca/P ratios (usually between 1.15 and 1.67) depending on synthesis conditions such as pH and starting ratio of ions in solution [45]. An amorphous nature, low Ca/P ratio and high concentration of ionic substitutions (e.g., Na^+, K^+, Mg^{2+}, Cl^-, CO_3^{2-}) confer a high degree of solubility on ACPs: Ksp values of $10^{-24.8}$ for ACPs possessing a Ca/P ratio of 1.5, and $10^{-23.9}$ for ACPs that incorporate small amounts of carbonate have been reported [36]. Upon exposure to aqueous environments, ACPs typically release a host of ions that re-precipitate in a more stable form, such as poorly-crystalline apatite [22]. More importantly, their ability to release calcium, phosphate, and other ions in aqueous environments is thought to contribute towards their osteoinductivity [23, 44, 46]. However, the inclusion of divalent cations such as Zn and ZrO can lower their dissolution rates and the incorporation of Zn and Cu can impede their conversion to HAP [47-49].

A4.4. BCP

Biphasic calcium phosphates (BCPs) are a family of two-phase ceramics that combine the low solubility and osteoconductivity of apatite, with the osteoinductivity of a more soluble phase such as TCP [50]. BCPs may be produced physically by mixing HAP and TCP, or chemically by sintering calcium deficient apatites at high temperatures to result in a mixture of two different phases [33]. Specific chemical properties of BCPs such as solubility depend heavily upon the characteristics of the individual phases and their relative amounts. The Ca/P ratios of BCPs typically fall between those for pure TCP and HAP.

A5. Effect of CPC properties on protein adsorption and cell adhesion

A5.1. Protein adsorption

Adsorption of cell-adhesive ECM proteins (e.g., fibronectin) plays an important role in cell adhesion and subsequent tissue formation on biomaterial surfaces [51]. Protein adsorption is

a complex process, driven by thermodynamic and kinetic considerations that depend upon the properties of the biomaterial surface, the ionic environment and the structural/chemical properties of the protein [52, 53]. In this section, the effect of surface roughness, microporosity, surface charge and solubility of CPCs on protein adsorption is discussed. A summary of this analysis is presented in **Table A3**.

A5.1.1. Effect of surface roughness

As a quantitative measure of surface texture, roughness is usually measured in terms of a root mean square value, R_a that describes the distance between peaks (or troughs) along an arbitrary line. Roughness is chiefly influenced by the grain size of CPC crystallites and CPC particle size. In a study that investigated the effect of CPC topography on protein adsorption, dos Santos showed higher adsorption of bovine serum albumin (BSA) onto lower R_a gold-coated nano-HAP substrates (R_a ~ 32 nm) than onto higher R_a gold-coated nano-TCP substrates (R_a ~ 142 nm) [54]. (Here, gold films were used to prevent the effects of mineral chemistry from influencing protein adsoprtion). In another study, Webster et al showed greater adsorption of serum proteins onto HAP possessing a grain size of 67 nm and R_a value of 17 nm, as compared to HAP possessing a grain size of 179 nm and R_a value of 10 nm [55]. In this study, the increase in protein adsorption was attributed to an increase in nano-scale roughness for the HAP samples possessing grain sizes of 67 nm, over the samples possessing grain sizes of 179 nm. Recently, Li et al reported greater adsorption of BSA and lysozyme on BCP samples possessing a grain size of ~ 86 nm, compared to BCP samples with grain sizes of ~ 167 nm and ~ 768 nm [56]. Together, these studies indicate that surfaces with feature sizes (i.e., R_a and grain size) less than 100 nm may promote protein adsorption better than surfaces that exhibit feature sizes larger than 100 nm.

A5.1.2. Effect of microporosity

High microporosity of CPCs can significantly enhance protein adsorption because the presence of micropores increases the specific surface area available for adsorption. Zhu et al showed that BCP surfaces with higher microsporosity adsorbed more TGF β_1 than BCP surfaces with lower microporosity [57]. In addition, larger number of micropores was also shown to

enhance the adsorption of proteins like fibrinogen and insulin, but not type I collagen. (This result also indicates that protein structure and chemistry play important roles in influencing adsorption.) In a study that investigated the role of physico-chemical properties of HAP on protein adsorption, Rouahi attributed the higher protein adsorption on one type of HAP powder over another to higher microporosity [58]. Similarly, Zhu et al showed that HAP and BCP particles with higher microporosities and/or more micropores greater than 20 nm in size adsorbed more fibrinogen and insulin than particles with lower microporosities [59]. Finally, Li et al reported higher protein adsorption on BCP discs with higher specific surface areas than on discs possessing considerably lower specific surface areas [60]. In summary, these studies strongly indicate that high microporosity of CPCs favors protein adsorption.

Property	**Effect on protein adsorption**	**References**
Surface roughness	Size-dependent effect: features (i.e. R_a and grain size) smaller than 100 nm appear to promote protein adsorption better than features larger than 100 nm.	[54-56]
Microporosity	High microprosity favors protein adsorption due to high specific surface area of the CPCs.	[57-60]
Surface charge, ionic environment & solubility	Adsorption influenced by electrostatic interactions between protein and surface, as well as by the charge and structural stability of individual proteins. Crystalline and stable CPCs appear to influence adsorption via charged sites and structural rearrangement of proteins, while amorphous and soluble CPCs influence adsorption by causing changes in local pH and ion concentration.	[25, 59, 61-65]

Table A3: Effect of CPC properties on protein adsorption.

A5.1.3. Effect of surface charge, ionic environment and solubility

In addition to physical properties such as roughness and microporosity, protein adsorption depends on chemical factors such as surface charge and solubility. For example, incorporation of small amounts of nano-phase CPCs into hydrophobic polymer scaffolds (e.g., poly-propylene fumarate [61] and poly(lactic-co-glycolic acid) [25]) is an attractive and effective means to facilitate protein adsorption. Model studies using self-assembled monolayers have demonstrated that hydrophobic surfaces (such as those found in conventional degradable polyesters) can strongly denature adsorbed proteins like fibronectin [51]. In contrast, surfaces

that present charged groups such as carboxyl and hydroxyl frequently exhibit higher adsorption of proteins in conformations that preserve protein structure and function [66].

Protein adsorption on CPCs may be mediated via electrostatic interactions with both cationic calcium sites and anionic phosphate sites; however, adsorption also depends upon the structure and chemistry of the proteins. In a study that investigated protein adsorption on HAP, Kandori et al proposed that adsorption of anionic BSA at neutral pH on more crystalline HAP surfaces was primarily mediated via positively charged sites (exposed calcium), despite the overall surface charge of HAP being negative [63]. In another study, Kandori et al – who compared the adsorption of multiple proteins on various CPC particles – demonstrated that the rate of adsorption depends on the nature, charge and structural stability of the individual proteins [62]. In particular, the authors attributed differences in the initial rates of adsorption of lysozyme, BSA, immunoglobulin G and myoglobin to differences in the molecular weights of the proteins, and their ability to undergo structural rearrangement upon adsorption. Although proteins such as BSA and lysozyme are not directly involved in cell adhesion, the studies by Kandori et al suggest that flexible cell-adhesive proteins (e.g., fibronectin and vitronectin) can undergo structural rearrangement and adsorb on CPC surfaces, while fibrillar proteins (e.g., collagens) may not [57]. In summary, the presence of cationic groups (e.g., calcium) and the capacity of proteins to conform to the surface appear to facilitate adsorption on poorly soluble CPCs such as HAP.

In addition to surface charge, the nature of the ionic environment also affects protein adsorption. For example, Zhu et al showed that protein adsorption depends on pH and ionic strength of the aqueous medium [64]. Specifically, the authors reported a decrease in BSA adsorption on BCP particles with either an increase in the pH of the medium or in the concentration of phosphate ions. In contrast, adsorption was enhanced upon increasing the concentration of NaCl in solution. In another study, Boix et al demonstrated that calcium ions in solution promoted adsorption of BMP-2 to HAP surfaces, while phosphate ions appeared to inhibit BMP-2 adsorption [65]. The solubility of CPCs (ACP>TCP>BCP>HAP: **Table 1**) may also influence protein adsorption by affecting the equilibrium ion concentration near the material surface. In support of this hypothesis, Zhu et al showed higher adsorption of fibrinogen, insulin and type I collagen on BCP than on HAP surfaces [59]. Here, the authors speculated that the

more soluble β-TCP phase in BCP may have undergone dissolution, causing local increases in ion concentration, surface charge and pH. Indeed, Whited et al showed a transient increase in the pH of medium over 24 hours after the addition of more soluble Zr-stabilized-ACP, but not upon the addition of HAP [22]. Overall, these studies suggest that increases in ion concentration and changes in pH near the surface of soluble CPCs (e.g., ACP) can promote protein adsorption. Furthermore, these studies may explain why BCPs, which possess a mixture of highly soluble and poorly soluble phases, may perform better than either HAP or TCP in promoting osteoblastic differentiation.

A5.2. Cell adhesion

As robust cell adhesion is mediated via integrin binding to ECM proteins (e.g., collagens, fibronectin, vitronectin), it is dependent on the density, conformation and type of adsorbed proteins, as well as the topography of the underlying biomaterial surface. Integrin binding initiates the clustering of adhesion receptors, formation of focal adhesion contacts, cell spreading, re-organization of the actin cytoskeleton and the exertion of contractile forces. In turn, these phenomena permit a broad array of normal cell functions including migration, proliferation and differentiation. In this section, the effect of topography, surface roughness, charge, solubility and crystallinity of CPCs on cell adhesion is discussed. A summary of this analysis is presented in **Table A4**.

A5.2.1. Effect of topography and surface roughness

Surface topography of CPCs – marked by contours and surface features – appears to have a direct effect on cell adhesion. In an elaborate analysis of cell morphology on CPC surfaces with different nano-scale topographies, Okada et al reported that partially differentiated rat BMSCs were well-spread with many membrane extensions on wide nano-sheets and dense HAP surfaces [67]. In contrast, very few membrane extensions were observed on HAP nano-fibers (40-50 nm diameter), nano-needles (particles of size 20-40 nm) and flakes (10 nm thickness). The authors suggested that the nano-sheets and dense HAP surfaces appeared smoother to the cells at the nano-scale than the nano-fibers, nano-needles and flakes. In general, surface topographies that exhibit nano- and sub-micron roughness are thought to disrupt integrin

binding and clustering, resulting in smaller focal adhesions than those observed for cells on smooth surfaces [68]. Moreover, the specific types of integrins within the focal adhesions depend on surface topography and cell type. Siebers et al provide a list of specific integrin subunits that are activated in various osteoblastic cell types in response to different surface topographies [69]. For example, $\alpha 3$ and $\alpha 6$ subunits were shown to be expressed by human osteoblasts on polished titanium surfaces compared to rough surfaces in a study by Sinha et al [70], while the expression of $\alpha 5$ and $\alpha 6$ subunits by rat BMSCs was found to be elevated on rough titanium surfaces compared to smooth surfaces in a study by ter Brugge et al [71]. (These results may also be related to the differences across species). Thus, topographical features influence cell spreading, shape and phenotype by affecting the size of focal adhesions and the integrin receptor composition therein.

In contrast to surface topography, surface roughness does not appear to have a consistent effect on cell adhesion. At the micron length scale, Deligianni et al found that human BMSCs attach better on HAP discs with larger features ($R_a \sim 4$ μm compared to ~ 0.7 μm) [72]. In contrast, Li et al observed that MC3T3-E1, BMSCs and C2C12 cells attached to similar extents on BCP surfaces with different feature sizes (i.e. $R_a \sim 3.12$ μm and 0.67 μm), despite differences in adsorbed protein between the surfaces [60]. Moreover, Zhou et al showed that rabbit BMSCs adhered better on HAP surfaces with an R_a value of 11.9 nm compared to surfaces possessing an R_a value of 54.2 nm, although the particle sizes of the two substrates were also different in this study [73]. However, Dulgar-Tulloch et al reported the opposite trend: grain sizes of 50-100 nm reduced the adhesion of human BMSCs, relative to grain sizes above 200 nm [74]. In addition, the authors found no effect of grain size larger than 200 nm on cell adhesion. Thus, the effect of surface roughness and grain size on cell adhesion is inconclusive due to contradicting data in the literature.

Property	Effect on cell adhesion	Reference
Surface topography & roughness	Cell adhesion is poor on rough surfaces such as nano-needles and nano-flakes, as compared to smooth surfaces such as dense sheets of CPC that can promote integrin clustering. In contrast, the effect of roughness on cell adhesion is inconclusive due to contradicting data in the literature.	[60, 67-69, 72-74]
Surface charge, solubility & crystallinity	High crystallinity and low solubility appears to favor cell adhesion. Moreover, cell adhesion seems to be facilitated by the direct adsorption of negatively charged cell-adhesive proteins on positively charged surfaces (e.g., cationic calcium sites on CPCs).	[27, 75-77]

Table A4: Effect of CPC properties on cell adhesion.

A5.2.2. Effect of solubility, crystallinity and surface charge

As mechanically robust cell adhesion is mediated via interactions between integrins and ECM proteins, solubility, crystallinity and surface charge of CPCs may affect adhesion by influencing protein adsorption (i.e., both protein concentration and conformation). For example, Hu et al showed that rabbit BMSCs adhered better on HAP (higher crystallinity) than ACP (lower crystallinity) of comparable sizes [27]. Similarly, Berube et al also demonstrated that rat calvarial osteoblasts attached better on HAP surfaces with higher crystallinity than on HAP surfaces with lower crystallinity or on various ACPs [77]. These two studies indicate that more crystalline and less soluble CPCs may present more stable surfaces (i.e. less ion exchange between the CPC and the aqueous phase) for cell adhesion.

Concurrently, surface charge may affect cell adhesion by affecting the concentration and conformation of adsorbed proteins. In particular, cationic surfaces appear to promote cell adhesion. For example, Feng et al showed that titanium implants coated with calcium improved the adhesion of osteoblasts compared to phosphate-coated implants [75]. The authors also reported better adhesion on apatite-coated implants compared to the calcium-coated samples. Here, the authors suggested that calcium provided positively charged sites that potentially facilitated adsorption of negatively charged cell-adhesive glycoproteins (e.g., fibronectin, vitronectin). As the apaptite-coated surface performed the best in terms of cell adhesion, this study also suggests that phosphate ions may synergistically aid calcium ions in facilitating protein adsorption and cell adhesion. In contrast, Bodhak et al showed that human fetal

osteoblasts adhered and spread better on HAP surfaces that were negatively polarized, as compared to positively polarized HAP [76]. (Here, the surfaces were polarized prior to cell adhesion studies by the application of a DC potential across HAP surfaces at either 300 or 400 °C using platinum electrodes). The authors suggested that the negatively polarized HAP allowed for the adsorption of Ca^{2+} ions first, followed by the adsorption of cell-adhesive proteins (e.g., fibronectin).

A6. Cell signaling in CPC-mediated osteogenesis

Although the osteoinductive effect of certain CPCs has been demonstrated in the literature, the mechanisms of CPC-mediated osteoblastic differentiation are not clearly understood. Differentiation seems to be influenced by the release of ions from CPCs, as well as focal-adhesion mediated changes that arise from protein adsorption and cell adhesion. Based on insights from the literature, a diagram of possible signaling pathways can be constructed (**Figure A2)**. In the following sub-sections, the specific roles of ions and focal-adhesion mediated changes are discussed.

A6.1. Role of calcium (Ca^{2+}) and phosphate ions

Ca^{2+} ions – released from or in equilibrium with the CPC surfaces – appear to play a major role in influencing osteoblastic differentiation. For example, the involvement of L-type and non L-type calcium channels and calcium sensing receptors (CaSR) in Ca^{2+}-mediated osteogenesis of MC3T3-E1 cells has been proposed by Jung et al [78]. Specifically, the authors suggested that extracellular calcium, derived from slight dissolution of HAP, might be internalized via ion channels and activate the CaMK2α/CAM pathway. In turn, the CaMK2α/CAM pathway may modulate osteoblastic differentiation via the CREB and/or the extracellular signal-regulated kinase 1/2 (ERK1/2) pathway [79] (green pathway in **Figure A2**). In an independent study, Barradas et al showed that increasing the Ca^{2+} levels in medium enhanced the expression of BMP-2 mRNA by human BMSCs in the absence of osteogenic supplements [80]. The authors proposed a mechanism by which Ca^{2+} ions, possibly internalized through ion channels, could activate protein kinase C (PKC)- and ERK1/2-dependent pathways. They also suggested that this activation may result in a signal transduction pathway, where a c-

FOS (whose up-regulation was demonstrated in the study)-c-JUN dimer could bind to the AP- 1 domain in the promoter region of the BMP-2 gene (red and blue pathways in **Figure A2**). Although this study was not conducted on a CPC surface, it lends support to the theory proposed by Jung et al that dissolved Ca^{2+} from CPC surfaces can promote osteoblastic differentiation via the ERK1/2 pathway.

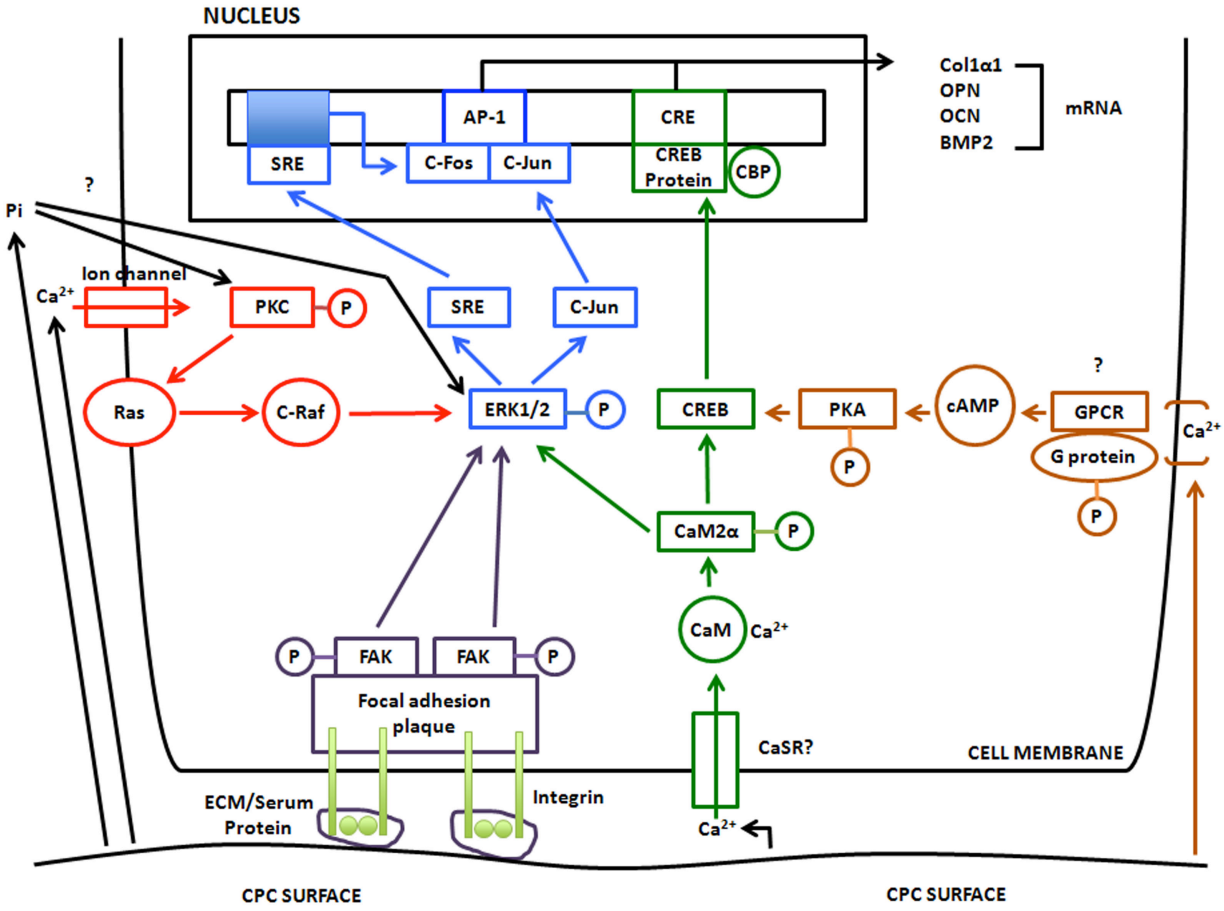

Figure A2: Mechanisms of osteoinduction by CPCs, based on [11, 12, 78-88].

In contrast to the role played by Ca^{2+}, phosphate appears to play only a secondary role in aiding osteoblastic differentiation. Beck et al showed specific induction of OPN in MC3T3-E1 cells in direct response to increased phosphate levels via the activity of ALP [84]. In a follow-up study, phosphate-induced elevation of OPN was found to proceed via the activation of ERK1/2- and PKC- dependent pathways (black pathways in **Figure A2**), but not the p38-dependent pathway [83]. In another study, Chai et al demonstrated a dose-dependent up-regulation of

BMP-2 in human periosteum-derived cells, in response to treatment with phosphate ions alone or in combination with calcium [82]. The authors suggested the involvement of these ions towards activating autocrine/paracrine signaling mechanisms that eventually result in cell differentiation. However, Khoshniat et al recently indicated that Ca^{2+} is required for phosphate to activate the ERK1/2-dependent pathway via the formation of a calcium phosphate precipitate (CaPp) outside the cell [85]. (The precipitates were not found to be endocytosed within the first 30 min, suggesting extracellular mediation of osteoblastic differentiation). Although CaSRs were not found to be involved in the CaPp-mediated phosphorylation of ERK1/2, the authors suggested that CaPp-mediated signaling is dependent on the integrity of caveolae-containing lipid rafts. Thus, while phosphate appears to enhance the osteoinductive effect of Ca^{2+}, its independent role in promoting osteoblastic differentiation is not clear.

In summary, Ca^{2+} activates the ERK1/2- and PKC-pathways and promotes the subsequent expression of osteoblastic genes such as BMP-2. These genes can in turn lead to the activation of autocrine/paracrine signaling mechanisms that eventually result in osteoblastic differentiation and maturation. In contrast, the role of phosphate appears to be less important than Ca^{2+} in promoting osteoblastic differentiation.

A6.2. Focal-adhesion mediated changes

Cell-ECM interactions have a potent effect on osteoblastic differentiation. As described previously, the topography and surface features of CPCs strongly affect protein adsorption. In turn, protein adsorption is known to influence cell behavior by inducing changes in integrin binding. For example, the aggregation of $\alpha 2\beta 1$ and $\alpha v\beta 3$ integrins has been shown to occur specifically during osteogenesis [87, 89]. Matsuura et al have suggested that the RGD domains of fibronectin and vitronectin have major roles to play in the spreading of osteoblasts on HAP surfaces, thus contributing to the osteoconductivity of the surfaces [86]. In support of this theory, Stephansson et al have shown that integrin ($\alpha 5\beta 1$) -fibronectin interactions may be a vital event to the matrix mineralization of MC3T3-E1 cells [88], while the disruption of these interactions can significantly inhibit osteoblastic differentiation and mineralization. Specifically, integrin binding can result in the phosphorylation of focal adhesion kinase (FAK), which in turn can lead to the activation of the ERK1/2-dependent pathway (purple pathway in Figure A2). In

support of this theory, Salasznyk et al have shown that osteoblastic differentiation in human BMSCs may proceed via the phosphorylation of FAK in response to type I collagen- and vitronectin-coated surfaces [12]. Although this study was not conducted on a CPC surface, the authors showed that FAK phosphorylation can result in the activation of Runx2 via the ERK1/2-pathway. **T**he presence of phosphorylated-FAK and evidence of differentiation in the absence of supplements in the study by Marino et al (conducted with human ADSCs on TCP surfaces) strongly supports this mechanism [81]. Thus, CPC properties such as roughness and surface topography can modulate osteoblastic differentiation by influencing the adsorption of cell-adhesive proteins, subsequent phosphorylation of FAK and activation of the ERK1/2-pathway.

A7. Summary and future outlook

CPCs represent a class of tunable bioactive materials that possess unique properties such as osteoconductivity and osteoinductivity, making them suitable candidates for the regeneration of bone. The osteoinductive capacity of CPCs *in vivo* appears to be driven by solubility and resorption capacity of CPCs. From this perspective, β-TCP and ACP appear to be osteoinductive and promote bone in-growth faster than a slowly dissolving CPC such as HAP. However, for greater *in vivo* longevities and sustained osteoconduction, HAP may be preferable. Osteoconductivity and osteoinductivity depend strongly on the physical and chemical properties of CPCs. In particular, solubility and surface topography appear to be the most significant factors that influence cell differentiation. In addition, CPC properties such as surface roughness, surface charge and crystallinity influence several key pre-cursor events such as protein adsorption and cell adhesion, which ultimately influence osteoblastic differentiation. Therefore, designing CPCs with appropriate physical and chemical properties and ascertaining the contribution of these properties towards their osteoinductive potential may provide vital clues to improving their bioactivity *in vivo*.

Despite the progress made towards understanding the role of CPC properties in influencing cell behavior, much work remains to be done in fabricating materials with inherent osteoinductivity. First, varying the physical properties of CPCs independent of their chemistry and vice-versa is critical to elucidating the role of specific properties. Second, mesenchymal stem cells behave differently in the presence and absence of osteogenic supplements, with the

CPCs appearing to play only a secondary role in the presence of supplements. Thus, testing the *in vitro* osteoinductive capacity of CPCs in the absence of supplements provides a rigorous method of analysis and may thus aid *in vivo* translation. Third, investigating the role of CPC properties towards influencing protein adsorption and cell adhesion is critical towards understanding their osteoinductive capacity in the larger context of the biological milieu. In this regard, much work remains to be done in studying the adsorption of cell-adhesive proteins such as fibronectin onto CPC surfaces. Finally, studying the activation of specific signaling molecules in response to CPCs and cross-talk between various pathways can provide cues to understanding the mechanisms of CPC-mediated osteogenesis. Further work in one or more of these areas can help towards the design of osteoinductive CPCs that support the attachment, growth and differentiation of stem cells without the need for osteogenic supplements or growth factors.

A8. Acknowledgments

The authors thank the Institute for Critical Technologies and Applied Sciences (Virginia Tech) and the National Science Foundation for funding, Dr. Carl Simon Jr., (Biosystems & Biomaterials Division, National Institute of Standards and Technology, Gaithersburg, MD) for a critical review of the manuscript and for providing valuable suggestions to widen its scope, and Cynthia Keister (School of Biomedical Engineering and Sciences, Virginia Tech) for help with artwork. S Samavedi is currently supported by the David & Lillian Francis dissertation scholarship from the graduate school at Virginia Tech.

References

[1] Dorozhkin SV, Epple M. Biological and medical significance of calcium phosphates. Angew Chem Int Edit. 2002;41:3130-46.
[2] Lee KY, Park M, Kim HM, Lim YJ, Chun HJ, Kim H, et al. Ceramic bioactivity: progresses, challenges and perspectives. Biomedical Materials. 2006;1:R31-7.
[3] Albrektsson T, Johansson C. Osteoinduction, osteoconduction and osseointegration. European Spine Journal. 2001;10:S96-S101.
[4] Krebsbach PH, Kuznetsov SA, Satomura K, Emmons RV, Rowe DW, Robey PG. Bone formation in vivo: comparison of osteogenesis by transplanted mouse and human marrow stromal fibroblasts. Transplantation. 1997;63:1059-69.
[5] Song G, Habibovic P, Bao C, Hu J, van Blitterswijk CA, Yuan H, et al. The homing of bone marrow MSCs to non-osseous sites for ectopic bone formation induced by osteoinductive calcium phosphate. Biomaterials. 2013;34:2167-76.
[6] Nagano M, Nakamura T, Kokubo T, Tanahashi M, Ogawa M. Differences of bone bonding ability and degradation behaviour in vivo between amorphous calcium phosphate and highly crystalline hydroxyapatite coating. Biomaterials. 1996;17:1771-7.
[7] Apelt D, Theiss F, El-Warrak AO, Zlinszky K, Bettschart-Wolfisberger R, Bohner M, et al. In vivo behavior of three different injectable hydraulic calcium phosphate cements. Biomaterials. 2004;25:1439-51.
[8] Ghosh SK, Nandi SK, Kundu B, Datta S, De DK, Roy SK, et al. In vivo response of porous hydroxyapatite and beta-tricalcium phosphate prepared by aqueous solution combustion method and comparison with bioglass scaffolds. J Biomed Mater Res B Appl Biomater. 2008;86:217-27.
[9] LeGeros RZ. Calcium Phosphate-Based Osteoinductive Materials. Chemical Reviews. 2008;108:4742-53.
[10] Barrere F, van Blitterswijk CA, de Groot K. Bone regeneration: molecular and cellular interactions with calcium phosphate ceramics. Int J Nanomedicine. 2006;1:317-32.
[11] Muller P, Bulnheim U, Diener A, Luthen F, Teller M, Klinkenberg ED, et al. Calcium phosphate surfaces promote osteogenic differentiation of mesenchymal stem cells. J Cell Mol Med. 2008;12:281-91.
[12] Salasznyk RM, Klees RF, Williams WA, Boskey A, Plopper GE. Focal adhesion kinase signaling pathways regulate the osteogenic differentiation of human mesenchymal stem cells. Experimental Cell Research. 2007;313:22-37.
[13] Lee WK, Lee SM, Kim HM. Effect of surface morphology of calcium phosphate on osteoblast-like HOS cell responses. Journal of Industrial and Engineering Chemistry. 2009;15:677-82.
[14] Nakashima K, Zhou X, Kunkel G, Zhang ZP, Deng JM, Behringer RR, et al. The novel zinc finger-containing transcription factor Osterix is required for osteoblast differentiation and bone formation. Cell. 2002;108:17-29.
[15] Boccaccini AR, Gough J. Tissue engineering using ceramics and polymers. Florida, USA: CRC ;Woodhead Pub.; 2007.
[16] Roach HI. Why Does Bone-Matrix Contain Noncollagenous Proteins - the Possible Roles of Osteocalcin, Osteonectin, Osteopontin and Bone Sialoprotein in Bone Mineralization and Resorption. Cell Biol Int. 1994;18:617-28.
[17] Orimo H. The mechanism of mineralization and the role of alkaline phosphatase in health and disease. J Nihon Med Sch. 2010;77:4-12.

[18] Shea JE, Miller SC. Skeletal function and structure: Implications for tissue-targeted therapeutics. Adv Drug Deliver Rev. 2005;57:945-57.
[19] Brown WE, Chow LC. Chemical Properties of Bone-Mineral. Annu Rev Mater Sci. 1976;6:213-36.
[20] Komori T. Regulation of Osteoblast Differentiation by Runx2. Osteoimmunology: Interactions of the Immune and Skeletal Systems Ii. 2010;658:43-9.
[21] Frank O, Heim M, Jakob M, Barbero A, Schafer D, Bendik I, et al. Real-time quantitative RT-PCR analysis of human bone marrow stromal cells during osteogenic differentiation in vitro. Journal of Cellular Biochemistry. 2002;85:737-46.
[22] Whited BM, Skrtic D, Love BJ, Goldstein AS. Osteoblast response to zirconia-hybridized pyrophosphate-stabilized amorphous calcium phosphate. J Biomed Mater Res A. 2006;76:596-604.
[23] Popp JR, Laflin KE, Love BJ, Goldstein AS. In vitro evaluation of osteoblastic differentiation on amorphous calcium phosphate-decorated poly(lactic-co-glycolic acid) scaffolds. J Tissue Eng Regen Med. 2010.
[24] Shin H, Zygourakis K, Farach-Carson MC, Yaszemski MJ, Mikos AG. Modulation of differentiation and mineralization of marrow stromal cells cultured on biomimetic hydrogels modified with Arg-Gly-Asp containing peptides. Journal of biomedical materials research Part A. 2004;69:535-43.
[25] Lee JH, Rim NG, Jung HS, Shin H. Control of osteogenic differentiation and mineralization of human mesenchymal stem cells on composite nanofibers containing poly[lactic-co-(glycolic acid)] and hydroxyapatite. Macromol Biosci. 2010;10:173-82.
[26] Eslaminejad MB, Mirzadeh H, Mohamadi Y, Nickmahzar A. Bone differentiation of marrow-derived mesenchymal stem cells using beta-tricalcium phosphate-alginate-gelatin hybrid scaffolds. J Tissue Eng Regen Med. 2007;1:417-24.
[27] Hu QH, Tan Z, Liu YK, Tao JH, Cai YR, Zhang M, et al. Effect of crystallinity of calcium phosphate nanoparticles on adhesion, proliferation, and differentiation of bone marrow mesenchymal stem cells. Journal of Materials Chemistry. 2007;17:4690-8.
[28] ter Brugge PJ, Wolke JG, Jansen JA. Effect of calcium phosphate coating composition and crystallinity on the response of osteogenic cells in vitro. Clin Oral Implants Res. 2003;14:472-80.
[29] Yuan HP, Fernandes H, Habibovic P, de Boer J, Barradas AMC, de Ruiter A, et al. Osteoinductive ceramics as a synthetic alternative to autologous bone grafting. P Natl Acad Sci USA. 2010;107:13614-9.
[30] Polini A, Pisignano D, Parodi M, Quarto R, Scaglione S. Osteoinduction of Human Mesenchymal Stem Cells by Bioactive Composite Scaffolds without Supplemental Osteogenic Growth Factors. Plos One. 2011;6.
[31] Guha AK, Singh S, Kumaresan R, Nayar S, Sinha A. Mesenchymal cell response to nanosized biphasic calcium phosphate composites. Colloids and Surfaces B-Biointerfaces. 2009;73:146-51.
[32] Arinzeh TL, Tran T, Mcalary J, Daculsi G. A comparative study of biphasic calcium phosphate ceramics for human mesenchymal stem-cell-induced bone formation. Biomaterials. 2005;26:3631-8.
[33] Vallet-Regi M, Gonzalez-Calbet JM. Calcium phosphates as substitution of bone tissues. Progress in Solid State Chemistry. 2004;32:1-31.
[34] Carrodeguas RG, De Aza S. alpha-Tricalcium phosphate: synthesis, properties and biomedical applications. Acta biomaterialia. 2011;7:3536-46.

[35] Legeros RZ, Lin S, Rohanizadeh R, Mijares D, Legeros JP. Biphasic calcium phosphate bioceramics: preparation, properties and applications. Journal of Materials Science-Materials in Medicine. 2003;14:201-9.
[36] Combes C, Rey C. Amorphous calcium phosphates: Synthesis, properties and uses in biomaterials. Acta Biomaterialia. 2010;6:3362-78.
[37] Yoshikawa H, Myoui A. Bone tissue engineering with porous hydroxyapatite ceramics. J Artif Organs. 2005;8:131-6.
[38] Klein CP, de Blieck-Hogervorst JM, Wolke JG, de Groot K. Studies of the solubility of different calcium phosphate ceramic particles in vitro. Biomaterials. 1990;11:509-12.
[39] Ducheyne P, Radin S, King L. The effect of calcium phosphate ceramic composition and structure on in vitro behavior. I. Dissolution. J Biomed Mater Res. 1993;27:25-34.
[40] Bell LC, Mika H, Kruger BJ. Synthetic Hydroxyapatite-Solubility Product and Stoichiometry of Dissolution. Archives of Oral Biology. 1978;23:329-36.
[41] Ogata K, Imazato S, Ehara A, Ebisu S, Kinomoto Y, Nakano T, et al. Comparison of osteoblast responses to hydroxyapatite and hydroxyapatite/soluble calcium phosphate composites. J Biomed Mater Res A. 2005;72:127-35.
[42] Huang J, Best SM, Brooks RA, Rushton N, Bonfield W. In vitro evaluation of nanosized carbonate-substituted hydroxyapatite and its polyhydroxyethylmethacrylate nanocomposite. J Biomed Mater Res A. 2008;87:598-607.
[43] Fernandez E, Gil FJ, Ginebra MP, Driessens FCM, Planell JA, Best SM. Calcium phosphate bone cements for clinical applications - Part I: Solution chemistry. Journal of Materials Science-Materials in Medicine. 1999;10:169-76.
[44] Popp JR, Laflin KE, Love BJ, Goldstein AS. Fabrication and characterization of poly(lactic-co-glycolic acid) microsphere/amorphous calcium phosphate scaffolds. J Tissue Eng Regen Med. 2011.
[45] Zhao J, Liu Y, Sun WB, Zhang H. Amorphous calcium phosphate and its application in dentistry. Chemistry Central Journal. 2011;5.
[46] Eanes ED. Amorphous calcium phosphate. Monogr Oral Sci. 2001;18:130-47.
[47] Skrtic D, Antonucci JM, Eanes ED, Eldelman N. Dental composites based on hybrid and surface-modified amorphous calcium phosphates. Biomaterials. 2004;25:1141-50.
[48] Skrtic D, Antonucci JM, Eanes ED, Brunworth RT. Silica- and zirconia-hybridized amorphous calcium phosphate: Effect on transformation to hydroxyapatite. Journal of Biomedical Materials Research. 2002;59:597-604.
[49] Okamoto Y, Hidaka S. Studies on Calcium-Phosphate Precipitation - Effects of Metal-Ions Used in Dental Materials. Journal of Biomedical Materials Research. 1994;28:1403-10.
[50] Bansal S, Chauhan V, Sharma S, Maheshwari R, Juyal A, Raghuvanshi S. Evaluation of hydroxyapatite and beta-tricalcium phosphate mixed with bone marrow aspirate as a bone graft substitute for posterolateral spinal fusion. Indian Journal of Orthopaedics. 2009;43:234-9.
[51] Keselowsky BG, Collard DM, Garcia AJ. Surface chemistry modulates fibronectin conformation and directs integrin binding and specificity to control cell adhesion. Journal of Biomedical Materials Research Part A. 2003;66A:247-59.
[52] Tsapikouni TS, Missirlis YF. Protein-material interactions: From micro-to-nano scale. Mater Sci Eng B-Adv. 2008;152:2-7.
[53] Fujii E, Ohkubo M, Tsuru K, Hayakawa S, Osaka A, Kawabata K, et al. Selective protein adsorption property and characterization of nano-crystalline zinc-containing hydroxyapatite. Acta Biomaterialia. 2006;2:69-74.

[54] dos Santos EA, Farina M, Soares GA, Anselme K. Surface energy of hydroxyapatite and beta-tricalcium phosphate ceramics driving serum protein adsorption and osteoblast adhesion. J Mater Sci Mater Med. 2008;19:2307-16.
[55] Webster TJ, Ergun C, Doremus RH, Siegel RW, Bizios R. Specific proteins mediate enhanced osteoblast adhesion on nanophase ceramics. J Biomed Mater Res. 2000;51:475-83.
[56] Li B, Liao XL, Zheng L, Zhu XD, Wang Z, Fan HS, et al. Effect of nanostructure on osteoinduction of porous biphasic calcium phosphate ceramics. Acta Biomaterialia. 2012;8:3794-804.
[57] Zhu XD, Fan HS, Xiao YM, Li DX, Zhang HJ, Luxbacher T, et al. Effect of surface structure on protein adsorption to biphasic calcium-phosphate ceramics in vitro and in vivo. Acta Biomater. 2009;5:1311-8.
[58] Rouahi M, Champion E, Gallet O, Jada A, Anselme K. Physico-chemical characteristics and protein adsorption potential of hydroxyapatite particles: influence on in vitro biocompatibility of ceramics after sintering. Colloids Surf B Biointerfaces. 2006;47:10-9.
[59] Zhu XD, Zhang HJ, Fan HS, Li W, Zhang XD. Effect of phase composition and microstructure of calcium phosphate ceramic particles on protein adsorption. Acta Biomater. 2010;6:1536-41.
[60] Li X, van Blitterswijk CA, Feng Q, Cui F, Watari F. The effect of calcium phosphate microstructure on bone-related cells in vitro. Biomaterials. 2008;29:3306-16.
[61] Lee KW, Wang S, Yaszemski MJ, Lu L. Physical properties and cellular responses to crosslinkable poly(propylene fumarate)/hydroxyapatite nanocomposites. Biomaterials. 2008;29:2839-48.
[62] Kandori K, Miyagawa K, Ishikawa T. Adsorption of immunogamma globulin onto various synthetic calcium hydroxyapatite particles. Journal of Colloid and Interface Science. 2004;273:406-13.
[63] Kandori K, Murata K, Ishikawa T. Microcalorimetric study of protein adsorption onto calcium hydroxyapatites. Langmuir. 2007;23:2064-70.
[64] Zhu XD, Fan HS, Li DX, Xiao YM, Zhang XD. Protein adsorption and zeta potentials of a biphasic calcium phosphate ceramic under various conditions. Journal of Biomedical Materials Research Part B-Applied Biomaterials. 2007;82B:65-73.
[65] Boix T, Gomez-Morales J, Torrent-Burgues J, Monfort A, Pulgdomenech P, Rodriguez-Clemente R. Adsorption of recombinant human bone morphogenetic protein rhBMP-2m onto hydroxyapatite. Journal of Inorganic Biochemistry. 2005;99:1043-50.
[66] Keselowsky BG, Collard DM, Garcia AJ. Surface chemistry modulates focal adhesion composition and signaling through changes in integrin binding. Biomaterials. 2004;25:5947-54.
[67] Okada S, Ito H, Nagai A, Komotori J, Imai H. Adhesion of osteoblast-like cells on nanostructured hydroxyapatite. Acta Biomater. 2010;6:591-7.
[68] Erisken C, Kalyon DM, Wang HJ. Functionally graded electrospun polycaprolactone and beta-tricalcium phosphate nanocomposites for tissue engineering applications. Biomaterials. 2008;29:4065-73.
[69] Siebers MC, ter Brugge PJ, Walboomers XF, Jansen JA. Integrins as linker proteins between osteoblasts and bone replacing materials. A critical review. Biomaterials. 2005;26:137-46.
[70] Sinha RK, Tuan RS. Regulation of human osteoblast integrin expression by orthopedic implant materials. Bone. 1996;18:451-7.

[71] ter Brugge PJ, Torensma R, De Ruijter JE, Figdor CG, Jansen JA. Modulation of integrin expression on rat bone marrow cells by substrates with different surface characteristics. Tissue engineering. 2002;8:615-26.
[72] Deligianni DD, Katsala ND, Koutsoukos PG, Missirlis YF. Effect of surface roughness of hydroxyapatite on human bone marrow cell adhesion, proliferation, differentiation and detachment strength. Biomaterials. 2001;22:87-96.
[73] Zhou GS, Su ZY, Cai YR, Liu YK, Dai LC, Tang RK, et al. Different effects of nanophase and conventional hydroxyapatite thin films on attachment, proliferation and osteogenic differentiation of bone marrow derived mesenchymal stem cells. Biomed Mater Eng. 2007;17:387-95.
[74] Dulgar-Tulloch AJ, Bizios R, Siegel RW. Human mesenchymal stem cell adhesion and proliferation in response to ceramic chemistry and nanoscale topography. J Biomed Mater Res A. 2009;90:586-94.
[75] Feng B, Weng J, Yang BC, Qu SX, Zhang XD. Characterization of titanium surfaces with calcium and phosphate and osteoblast adhesion. Biomaterials. 2004;25:3421-8.
[76] Bodhak S, Bose S, Bandyopadhyay A. Role of surface charge and wettability on early stage mineralization and bone cell-materials interactions of polarized hydroxyapatite. Acta Biomaterialia. 2009;5:2178-88.
[77] Berube P, Yang Y, Carnes DL, Stover RE, Boland EJ, Ong JL. The effect of sputtered calcium phosphate coatings of different crystallinity on osteoblast differentiation. J Periodontol. 2005;76:1697-709.
[78] Jung GY, Park YJ, Han JS. Effects of HA released calcium ion on osteoblast differentiation. J Mater Sci Mater Med. 2010;21:1649-54.
[79] Zayzafoon M, Fulzele K, McDonald JM. Calmodulin and calmodulin-dependent kinase IIalpha regulate osteoblast differentiation by controlling c-fos expression. J Biol Chem. 2005;280:7049-59.
[80] Barradas AM, Fernandes HA, Groen N, Chai YC, Schrooten J, van de Peppel J, et al. A calcium-induced signaling cascade leading to osteogenic differentiation of human bone marrow-derived mesenchymal stromal cells. Biomaterials. 2012.
[81] Marino G, Rosso F, Cafiero G, Tortora C, Moraci M, Barbarisi M, et al. Beta-tricalcium phosphate 3D scaffold promote alone osteogenic differentiation of human adipose stem cells: in vitro study. J Mater Sci Mater Med. 2010;21:353-63.
[82] Chai YC, Roberts SJ, Schrooten J, Luyten FP. Probing the Osteoinductive Effect of Calcium Phosphate by Using an In Vitro Biomimetic Model. Tissue Engineering Part A. 2011;17:1083-97.
[83] Beck GR, Knecht N. Osteopontin regulation by inorganic phosphate is ERK1/2-, protein kinase C-, and proteasome-dependent. Journal of Biological Chemistry. 2003;278:41921-9.
[84] Beck GR, Zerler B, Moran E. Phosphate is a specific signal for induction of osteopontin gene expression. Proceedings of the National Academy of Sciences of the United States of America. 2000;97:8352-7.
[85] Khoshniat S, Bourgine A, Julien M, Petit M, Pilet P, Rouillon T, et al. Phosphate-dependent stimulation of MGP and OPN expression in osteoblasts via the ERK1/2 pathway is modulated by calcium. Bone. 2011;48:894-902.
[86] Matsuura T, Hosokawa R, Okamoto K, Kimoto T, Akagawa Y. Diverse mechanisms of osteoblast spreading on hydroxyapatite and titanium. Biomaterials. 2000;21:1121-7.

[87] Schneider GB, Zaharias R, Stanford C. Osteoblast integrin adhesion and signaling regulate mineralization. Journal of Dental Research. 2001;80:1540-4.
[88] Stephansson SN, Byers BA, Garcia AJ. Enhanced expression of the osteoblastic phenotype on substrates that modulate fibronectin conformation and integrin receptor binding. Biomaterials. 2002;23:2527-34.
[89] Mizuno M, Kuboki Y. Osteoblast-related gene expression of bone marrow cells during the osteoblastic differentiation induced by type I collagen. Journal of Biochemistry. 2001;129:133-8.

Appendix B

Indirect fabrication of three-dimensional bone tissue scaffolds by fused-filament fabrication and mineralization

Satyavrata Samavedi[a#], Jesse R. Bernardo[b#], Aaron S. Goldstein[a,c], Abby R. Whittington[a,c,d], Christopher B. Williams[b,e]

[a] Department of Chemical Engineering, Virginia Polytechnic Institute and State University, Blacksburg, VA

[b] Department of Mechanical Engineering, Virginia Polytechnic Institute and State University, Blacksburg, VA

[c] School of Biomedical Engineering and Sciences, Virginia Polytechnic Institute and State University, Blacksburg, VA

[d] Department of Materials Science and Engineering, Virginia Polytechnic Institute and State University, Blacksburg, VA

[e] Department of Engineering Education, Virginia Polytechnic Institute and State University, Blacksburg, VA

[#]Both authors contributed equally: J. Bernardo was responsible for figures A2.1 – A2.4, while S. Samavedi was responsible for figures A2.5 – A2.7. S. Samavedi and J. Bernardo were equally responsible for writing this manuscript.

B1. Abstract

Although additive manufacturing (AM) approaches have been widely used for manufacturing bone tissue scaffolds, they are restricted by the use of a limited set of compatible materials and poor feature resolution of scaffolds. To overcome these limitations, an indirect AM fabrication method based on a four-step process was developed in this study. In the first and

second steps, a template pattern was created using fused filament fabrication, followed by treatment with a simulated body fluid (SBF) to deposit a mineral coating. Mineralized patterns were heat-treated to pyrolyze the pattern material in the third step, and the mineral coating sintered in the fourth step. To demonstrate that the use of an aqueous solution for mineralization can produce scaffolds with fine feature sizes, three-dimensional scaffolds with wall thicknesses of 150 μm and internal channel diameters of 280-340 μm were created. X-ray diffraction revealed the presence of a mixture of β-tricalcium phosphate and hydroxyapatite phases in the mineral layer, while a cell metabolic activity assay using MC3T3-E1 cells confirmed mineral biocompatibility. The results from this study demonstrate that an indirect fabrication process, and mineralization with an aqueous SBF solution may be used to create scaffolds with very fine architectures and precise geometries.

Key terms: Additive Manufacturing, Indirect scaffold fabrication, Simulated Body Fluid, Mineralization, Bone tissue Engineering

B2. Introduction

The mesostructure of bone tissue scaffolds play vital roles in influencing cell behavior and the eventual formation of mineralized tissue. In particular, scaffold architecture, porosity, pore size and pore orientation can directly influence cell growth and infiltration [1, 2]. While pore sizes in the range of 200-400 μm are generally considered appropriate for proliferation of bone cells [3-5], micro-scale topography (microporosity [1] and surface roughness [6]) can also significantly affect cell attachment, migration and signaling [7]. Thus, precisely controlling the mesostructure of scaffolds is important towards determining the ultimate fate of engineered bone tissue.

Additive manufacturing (AM) technologies (e.g., 3-D printing, fused-filament fabrication (FFF), laser sintering) offer a designer-precise control of scaffold geometry, pore size, pore distribution and interconnectivity [8]. Although AM approaches enable the realization of scaffold mesostructures that are tailored for specific tissue responses, they also suffer from several disadvantages such as weak mechanical properties, limited resolution and the availability

of relatively few biocompatible materials that can be processed. To circumvent the inherent limitations of AM fabrication techniques, indirect AM-based scaffold fabrication techniques have been employed. Specifically, a variety of materials including hydroxyapatite (HA), collagen and poly (lactic acid) have been used to indirectly create 3-D scaffolds [9-14]. However, the use of viscous ceramic slurries in indirect AM approaches constrains the geometries and feature sizes that can be realized. Specifically, viscous materials such as high loaded ceramic suspensions may trap air bubbles within the mold and cause defects in the scaffold architecture [15]. To mitigate both material and scaffold feature-size limitations found in AM-based processes, the present study uses an aqueous salt solution for coating polymeric template patterns with a mineral phase to indirectly create 3-D porous scaffolds.

Functionalization of scaffolds using a mineral phase is a commonly used strategy for improving scaffold osteoconductivity [16, 17]. One powerful method to incorporate a mineral layer is the use of a simulated body fluid (SBF) [18]. SBF is an aqueous supersaturated salt solution, in which the concentrations of ions (e.g., carbonate) influence the nature of mineral precipitates [19]. SBF has been used for the deposition of bone-like apatite, which is essential for material to bond to living bone [20]. In addition, SBF coatings have been shown to affect osteoblast viability, proliferation and gene expression *in vitro* [21].

The objective of this study was to indirectly create a 3-D scaffold for bone tissue engineering by fabricating a template pattern using FFF, mineralizing the pattern using an SBF solution, burning the pattern material and finally, sintering the mineral layer. Using this general strategy of FFF-mineralization-pyrolysis-sintering, three sets of experiments were conducted in this study. In the first set of experiments, template patterns were fabricated by FFF, and ideal mineralization parameters were determined using a three-factor analysis of variance (ANOVA). In the second set, patterns were mineralized using the parameters from the first set of experiments, followed by pyrolysis and sintering to indirectly create 3-D scaffolds. Percent shrinkage (post-sintering) and scaffold architecture were characterized using optical microscopy. Lastly, 3-D scaffolds with very fine architectures were fabricated to demonstrate that mineralization via an aqueous SBF solution (as compared to viscous ceramic slurries) can produce finer scaffold features than existing indirect processes. The chemistry of the mineral

was characterized using X-Ray diffraction (XRD) and energy dispersive spectroscopy (EDS), and mineral biocompatibility was confirmed using a cell metabolic activity assay.

B3. Methods

B3.1. Fabrication of template patterns and determination of ideal mineralization parameters

The first set of experiments involved the fabrication of FFF template patterns and a systematic study that sought to optimize mineralization parameters.

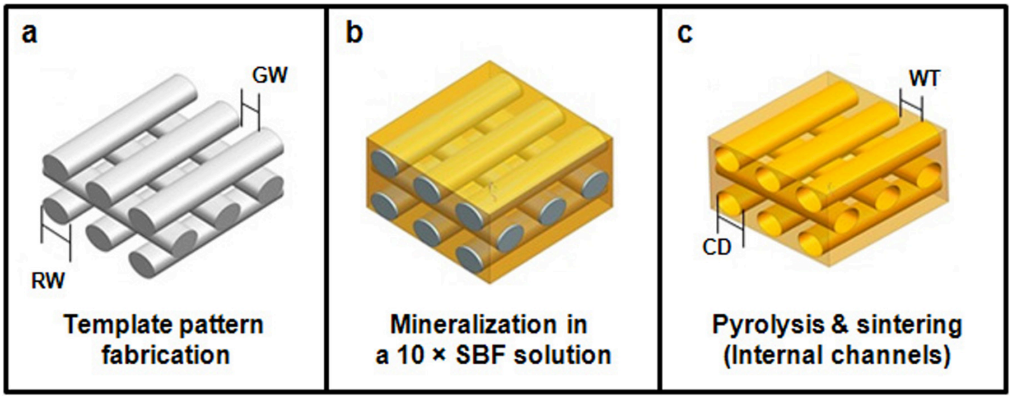

Figure B1: Schematic of indirect scaffold fabrication process a) template pattern fabricated by AM, b) template pattern coated with mineral phase following treatment with simulated body fluid, c) indirect scaffold formed after pyrolyzing template pattern material and sintering the mineral phase. GW and RW refer to the gap width and road width of template patterns, which become the wall thickness (WT) and channel diameter (CD) of the 3-D scaffolds, respectively.

B3.1.1. Manufacture of template patterns using fused-filament fabrication

Template patterns with pre-specified pore geometries were fabricated by an FFF technique (**Figure B1a**). Briefly, two materials, acrylonitrile butadiene (ABS) and investment casting wax (ICW) - both purchased from Stratasys Inc., Eden Praire, MN- were used for the creation of template patterns. A custom MATLAB code was created to automatically generate the tool-path code for depositing materials as "log-cabin" template patterns. Pore geometry and size were controlled by varying the diameter of the deposited filament roads ("road width" – RW), the offset space between the roads ("gap width" – GW), the thickness of each deposited layer and the layer offset angle. ABS patterns were fabricated using a Stratasys FDM 1500 and a

0.305 mm diameter T12 nozzle. These patterns were manufactured with open-ends to increase their porosity and aid the flow of liquids. Printing ICW patterns with open-ends resulted in the ICW continuing to extrude even though filament feed to the nozzle had been stopped, thus creating defects in the scaffold pattern. As a result, ICW patterns were printed using a Stratasys FDM 1600 and a 0.305 mm diameter T12 nozzle via a serpentine extrusion path, resulting in patterns possessing closed-ends. A summary of general fabrication parameters including GW, RW, road orientation, and temperatures is presented in **Table B1**.

Material	**Processing Temperature (Model/Support/Envelope)**	**Gap Width GW (µm)**	**Road Width GW (µm)**	**Road Orientation**	**Printing Pattern**
ABS	270/ 265 / 270 °C	500	300	0-90°	Open-ends
ICW	70 / 71 / 28 °C	500	400	0-90°	Closed-ends

Table B1: Template pattern fabrication: processing parameters (theoretical).

B3.1.2. Surface treatment and mineralization of template patterns

Following their fabrication, template patterns were chemically treated to activate their surfaces for subsequent mineralization. Two types of treatments were tested in this study: plasma etching and a chemical treatment. For plasma etching, samples were incubated in an oxygen environment for 15 min at 50 mA within an SPI Plasma Prep II. For the chemical treatment, samples were immersed in a 0.1M sodium hydroxide (Sigma-Aldrich, St. Louis, MO) solution for 15 min. After treatment with sodium hydroxide, samples were rinsed thrice in deionized water. Following the treatment step, template patterns were immersed in a 10 × SBF solution to promote the growth of mineral crystals on their surfaces (**Figure B1b**). The ion concentrations of the 10 × SBF solution used in this study were adopted from a previously published report [22]. For preparing 2 L of the 10 × SBF solution, two aqueous solutions were made: 1.6 L of a stock solution consisting of all of the ions excluding bicarbonate, and 0.4 L of an aqueous solution of sodium bicarbonate. (Salts were purchased from Fisher Scientific, Pittsburgh, PA.) These solutions were stored at 4 °C until further use. Just prior to mineralization, the stock and bicarbonate solutions were mixed in a ratio of 4:1 by volume to generate a 10 × SBF solution. ABS and ICW pattern templates were anchored to the center of a

P150 petri-dish containing the 10 × SBF solution. For the mineralization process, two flow conditions (static or dynamic) were tested. For the dynamic flow condition, the petri-dish was placed on an orbital shaker (~70 Hz) at 37 °C. For both flow conditions, SBF solution was replaced with freshly prepared solution every 2 h to ensure that ion concentration remained at a level appropriate for mineralization.

B3.1.3. Determination of ideal mineralization parameters: Three-factor ANOVA

The effect of three different variables on the mineralization process was examined: template pattern chemistry (ABS or ICW), treatment (plasma or sodium hydroxide) and flow condition during mineralization (static or dynamic). ABS or ICW scaffolds with GW values of 500 μm were either plasma-treated or subject to treatment with sodium hydroxide and subsequently mineralized in a 10 × SBF solution for 8 h under either static or dynamic conditions, with solution replaced every 2 h. In each case, template patterns were weighed before and after mineralization to determine the mass of mineral deposited. A three-factor ANOVA was performed on the mineral mass data thus obtained to determine the individual and combined effects of the three variables. The combination of variables that gave the highest mass of mineral was used for the rest of the study.

B3.2. Indirect fabrication of scaffolds via mineralization and sintering

In the second set of experiments, indirect scaffolds were fabricated via mineralization of FFF patterns using optimized parameters, followed by pyrolysis and sintering.

B3.2.1. Fused-filament fabrication and mineralization

ABS and ICW samples with GW values of 500 μm were fabricated as described in **Section B3.1**. From the first set of experiments, plasma treatment and dynamic flow condition for mineralization were found to result in the highest mass of mineral. Hence, ABS and ICW template patterns were plasma-treated in 5 min steps for a total of 15 min, with 5 min cooling stages between each treatment step. Samples were subsequently treated with a 10 × SBF solution for 48 h under dynamic conditions, with freshly prepared solution replaced at 2 h intervals.

B3.2.2. Pyrolysis and sintering

The mineralized template patterns were pyrolyzed to remove the pattern material and sinter the deposited mineral crystals, thus resulting in a 3-D bioceramic scaffold (**Figure B1c**). Briefly, scaffold templates with mineral were placed in a furnace to burnout the pattern material (ABS or ICW). A slow heating rate of 0.5 °C /min was used to prevent cracking and distortion of the scaffold. After removal of either ABS or ICW template patterns, the heating rate of 0.5 °C/min was continued until the sintering temperature of 800 °C was reached. Samples were maintained at 800 °C for 1 h to sinter the mineral crystals. Once pyrolyzed and sintered, the GW and RW values for the template pattern became the wall thickness (WT) and channel diameter (CD) of the scaffold (**Figure A2.1c**).

B3.2.3. Evaluation of scaffold architecture

To analyze scaffold architecture, all samples were imaged using a Dino-Lite Pro digital microscope (Dino-lite, Torrance, CA) prior to and post mineralization. The accompanying software (DinoCapture) was used to capture photographs of samples to measure the GW, RW and outside diameter of template patterns. The WT and CD were recorded pre- and post-sintering so as to calculate percent shrinkage due to the sintering process. A "%Shrinkage" value was used to quantify the maximum and minimum linear shrinkage of the WT and CD dimensions using the formula:

$$\%\text{Shrinkage} = \frac{\text{D presint} - \text{D postsint}}{\text{D presint}}$$

where D presint = Maximum or minimum measured scaffold dimension (WT or CD) before sintering and D postsint = Scaffold dimension (WT or CD) after sintering.

B3.3. Fabrication of scaffolds with fine architectures

The third and final set of experiments was conducted to test the hypothesis that mineralization via an aqueous SBF solution would be able to create finer scaffold features than existing indirect processes which typically use viscous ceramic slurries.

B3.3.1. Scaffold fabrication

ICW samples with low GW values of 150 μm and 300 μm were fabricated by the FFF-mineralization-pyrolysis-sintering process, as described in **Section B3.2**. These scaffolds were designated ICW150 and ICW300.

B3.3.2. Scanning electron microscopy (SEM) of ICW150 scaffolds

SEM was used to determine the internal architecture and WT of the 3-D scaffolds. Briefly, samples were secured to conductive carbon tape and sputter-coated with a layer of gold-palladium (Model 208 HR, Cressington Scientific Instruments, Cranberry, PA). Samples were subsequently imaged at an operating voltage of 5 kV using an SEM instrument (LEO1550, Oxford Instruments, Oxfordshire, UK), fitted with InLens and SE2 detectors. Measurements were made on the SEM micrographs using ImageJ software (National Institutes of Health, Bethesda, MD).

B3.3.3. Evaluation of mineral composition

The composition of mineral in the ICW150 and ICW300 scaffolds was evaluated using XRD and EDS. For these measurements, scaffolds were crushed into powder and XRD spectra were acquired using an X-ray diffractometer (D8 Discover, Bruker AXS Inc., Madison, WI) fitted with a Cu K_α radiation source, operating at 40 kV and 40 mA. Spectra were obtained in the 2θ range 15 ° to 60 ° at a scan speed of 0.1 sec/step and a step size of 0.01 °. EDS of the mineral powder (3 whole-screen scan regions for the ICW150 samples and 5 whole-screen scan regions for the ICW300 samples) was performed in conjunction with SEM, using an INCAx-act EDS instrument (Carl Zeiss SMT, Thornwood, NY), fitted with a silicon drift detector at an operating voltage of 20 kV.

B3.3.4. Evaluation of mineral cytotoxicity

Cell metabolic activity, in the presence of mineral particles (obtained from ICW150 and ICW300 3-D scaffolds), was investigated using MC3T3-E1 osteoprogenitor cells (ATCC, Manassas, VA) and an Alamar Blue (AB) colorimetric assay (Sigma-Aldrich, St. Louis, MO).

Cells were maintained in growth medium (minimal essential medium α modification supplemented with 10% fetal bovine serum (Gemini, Calabasas, CA) and 1% antibiotic/antimycotic) in a 37 °C, 5% CO_2 incubator. For testing mineral cytotoxicity, cells were lifted with trypsin/EDTA (Sigma-Aldrich, St. Louis, MO), seeded onto the bottom of a 24-well plate at 25,000 cells per well and allowed to attach overnight. The following day, designated day 0, mineral particles (sterilized by UV-radiation overnight) were added to cells growing in culture at a concentration of 5 mg/ml. Control wells were not exposed to mineral particles and were designated tissue culture polystyrene (TCPS). Cells were maintained in growth medium for 5 days, with medium replaced every 3 days. Two days (day 2) and five days (day 5) after the addition of mineral, an AB assay was performed on all the samples. Briefly, 100 μL of AB reagent was added aseptically to cells and allowed to incubate for 4 h. AB reagent incubated with growth medium served as a negative control. After 4 h, fluorescence of 200 μL aliquots was read at excitation and emission wavelengths of 550 nm and 590 nm respectively using a micro-plate reader (Molecular Devices, Sunnyvale, CA. Fluorescence values from the samples were corrected for the fluorescence from the negative control, and reported as mean ± standard deviation for n = 4 samples per group. To determine statistical significance, a one-way ANOVA and a Tukey-Kramer *post-hoc* test were performed using JMP 9.0 (SAS Institute Inc., Cary, NC). A p-value less than 0.05 was considered statistically significant.

B4. Results

B4.1. Fused-filament fabrication of ABS and ICW materials

Template patterns fabricated via FFF were designed to have a theoretical GW value of 500 μm (measured at the smallest pore gap); this value corresponds to a WT value of 500 μm for the scaffold after mineralization and sintering. A summary of actual template pattern parameters (obtained experimentally) is presented in **Table B2.**

Template material	Printed template patterns		Mineralized and sintered scaffolds	
	Gap width GW (μm)	Road width RW (μm)	Wall thickness WT (μm)	Channel diameter CD (μm)
ABS	510	290- 310	530	280
ICW	430	360- 410	470	340

Table B2: Actual gap width (GW), road width (RW), wall thickness (WT) and channel diameter (CD) values for printed template patterns and mineralized scaffolds.

Specifically, RW values were found to be 290 – 310 μm and 360 – 410 μm for the ABS and ICW patterns respectively. While the ABS template patterns were reproducibly fabricated with open-ends and consistent RW values, the RW values for the ICW template patterns (printed with closed-ends) were not as constant (**Figure B2**). Both the ABS and ICW printed patterns were 1200 μm in diameter (gross) and consisted of five printed layers, with each layer being 300 μm thick.

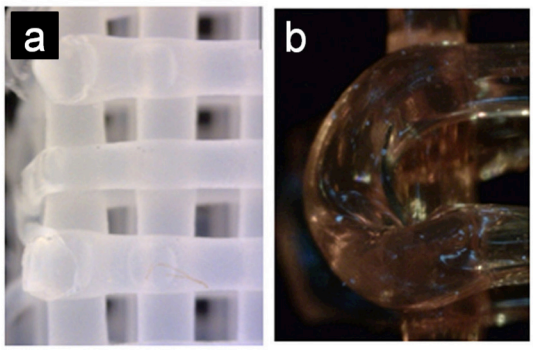

Figure B2: a) ABS and b) ICW template patterns, depicting open- and closed- ends respectively.

B4.2. Determination of ideal mineralization parameters

A three-factor ANOVA was performed on the mineral mass data following the mineralization step. The analysis indicated that flow condition and surface treatment were the two most significant factors in this experiment (F-ratios of 170 and 10 respectively), while the pattern material had only a small effect (F-ratio of 1.9). Template patterns that were plasma-treated mineralized more than those treated with sodium hydroxide (**Table B3**). Also, dynamic conditions resulted in a higher amount of mineral deposition than static conditions (a 77 - 96 % increase). *p*-values were 0.049 and 0.19 for the flow condition and surface treatment parameters

respectively. These results indicate a strong relation between the experimental factors and amount of mineral deposited. All further experiments were conducted using plasma treatment and dynamic flow.

Mineralization condition	**ABS**	**ICW**	**Surface Treatment**
Dynamic	0.0153	0.0141	Plasma
	0.0108	0.0109	NaOH
Static	0.0033	0.0026	Plasma
	0.0030	0.0004	NaOH

Table B3: Mass of mineral deposited (grams).

B4.3. Analysis of scaffold architecture fabricated using ideal mineralization conditions

ABS and ICW template patterns were plasma-treated, mineralized in a 10 × SBF solution for 48 h under dynamic flow conditions, pyrolyzed and sintered. Fracture surfaces of mineralized ABS and ICW samples prior to sintering are presented in **Figure B3**, while fracture surfaces of sintered samples are presented in **Figure B4**. The patterns' pores (now the scaffold walls) were filled with mineral. Post-sintering, WT and CD values of the scaffolds were measured (**Table B2**). Shrinkage during the burnout and sintering process was also noted, which caused the CD to decrease slightly. Specifically, CD shrank between 6.7 – 15 % and 5.6 – 17 % for ABS and ICW scaffolds respectively. The scaffolds fabricated with the ICW pattern had a WT percent shrinkage of 6.0 – 15 %. The WT of the ABS pattern was the only feature that did not reduce during sintering; on the contrary, WT increased by 6.0 %.

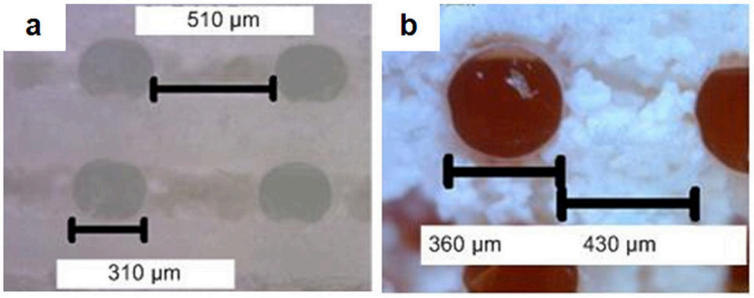

Figure B3: Digital microscopy images of the fracture surface of pre-sintered (a) ABS and (b) ICW template patterns, fabricated with a theoretical GW value of 500 µm.

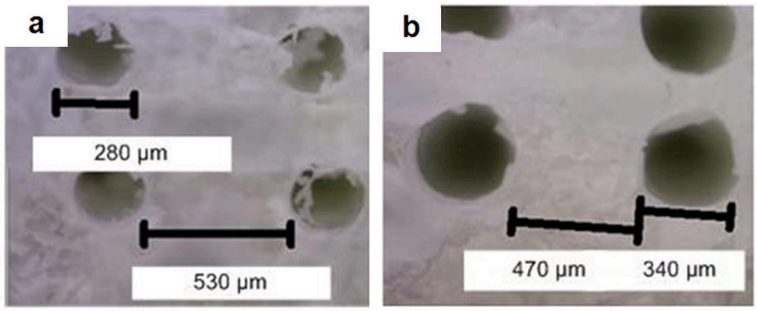

Figure B4: Digital microscopy images of the fracture surface of sintered (a) ABS and (b) ICW template patterns, fabricated with a theoretical GW value of 500 μm.

B4.4. Analysis of scaffolds with fine architectures

To validate the hypothesis that mineralization via an aqueous SBF solution would be able to create finer scaffold features than existing indirect processes, ICW samples with GW values of 150 μm and 300 μm were fabricated. SEM images of the fracture surfaces of the 3-D scaffolds indicate that the SBF mineralization approach was able to deposit mineral crystals in gaps as small as 150 μm (**Figure B5**). The resulting WT value from these scaffolds was 158 ± 33.4 μm.

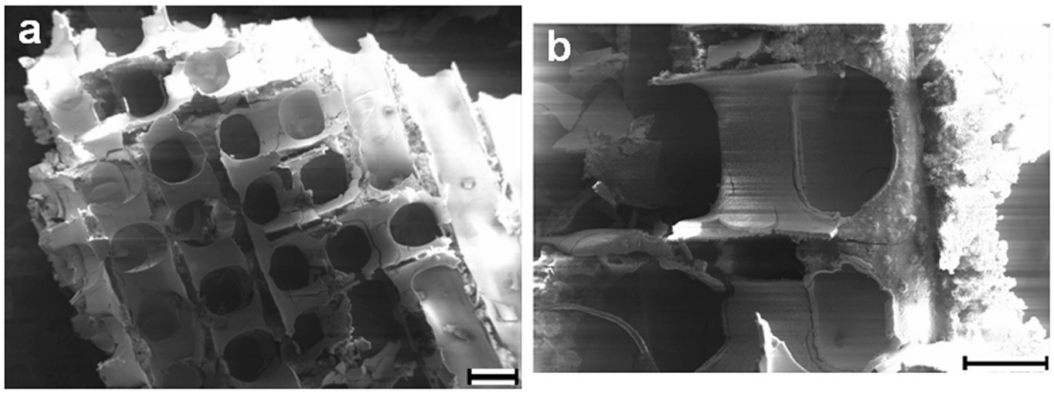

Figure B5: SEM micrographs of 3-D scaffolds obtained via the four-step process, possessing a theoretical WT value of 150 μm. Scale bars represent 300 μm in (a) and 200 μm in (b).

B4.5. Mineral composition

To characterize the mineral in the 3-D scaffolds, XRD and EDS were performed on the powdered ICW150 and ICW300 scaffolds. XRD spectra (**Figure B6**) are indicative of predominantly β-tricalcium phosphate (27.6, 29.5, 31, 34.2) and hydroxyapatite (25.7, 32.5, 40, 47, 53) mineral phases in both samples. The sharpness of peaks in both spectra indicates a

crystalline mineral phase. EDS performed on the powdered ICW150 and ICW300 samples revealed the presence of large amounts of calcium, phosphorous and oxygen, and smaller amounts of sodium and chlorine. The average Ca/P ratios for the ICW150 and ICW300 samples were found to be 1.60 ± 0.08 and 1.68 ± 0.16 respectively.

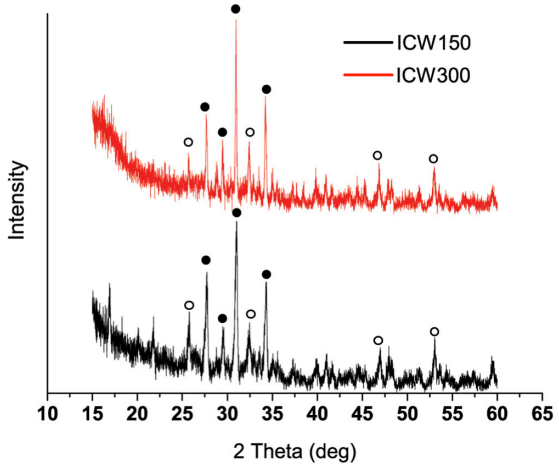

Figure B6: X-ray diffraction spectra of powdered ICW150 and ICW300 scaffolds. Closed circles indicate β-tricalcium phosphate peaks, while open circles indicate hydroxyapatite peaks.

B4.6. Mineral cytotoxicity

To evaluate cytotoxicity, mineral particles from the 3-D scaffolds were added to MC3T3-E1 osteoprogenitor cells growing in culture. Two days after the addition of mineral, metabolic activity of cells (**Figure B7**) in the presence of the ICW150 and ICW300 samples was found to be lower than the TCPS samples, with activity in the presence of ICW300 samples being significantly lower ($p = 0.007$). However, metabolic activity was comparable at day 5 for cells cultured in the presence of the TCPS, ICW150 and ICW300 samples. The increase in metabolic activity in the presence of ICW150 and ICW300 samples from day 2 to day 5 was statistically significant ($p = 0.002$ and $p = 0.034$ respectively).

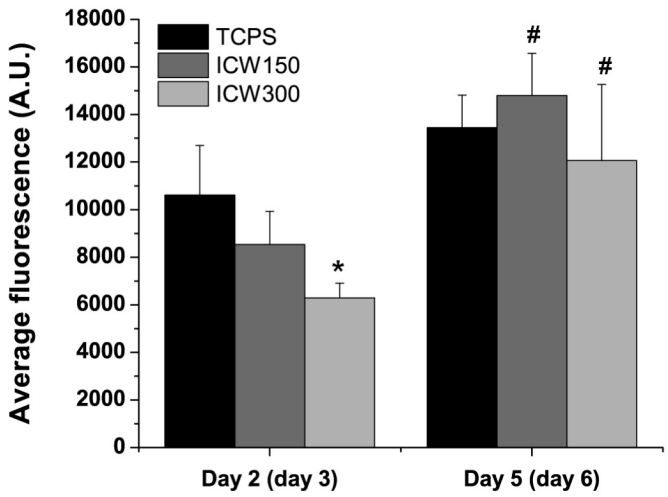

Figure B7: Viability of MC3T3-E1 cells (as assessed by an Alamar Blue assay) after 2 and 5 days following the addition of mineral (obtained from ICW150 and ICW300 3-D scaffolds) to cells growing in culture. Time points within parenthesis indicate total number of days in culture. Bars correspond to mean ± standard deviation for n = 4 samples per group. An asterisk indicates statistical significance ($p < 0.05$) compared to TCPS samples within the same point and a pound symbol indicates statistical significance ($p < 0.05$) compared to respective samples at day 2.

B5. Discussion

The overall objective of this study was to indirectly fabricate a 3-D scaffold by means of an FFF method, followed by mineralization, pyrolysis and sintering. Towards this end, three sets of experiments were performed. In the first set of experiments, template patterns with theoretical GW values of 500 μm were fabricated from ABS and ICW materials. These patterns were mineralized using a 10 × SBF solution and a variety of processing parameters. A three-factor ANOVA revealed that treatment of template patterns with plasma, and dynamic flow conditions during mineralization yielded the highest mass of mineral, while template pattern chemistry was found to have little effect. In the second set of experiments, ABS- and ICW-based 3-D scaffolds were fabricated by an FFF-mineralization-pyrolysis-sintering process, using the idealized set of parameters for mineralization. Post-sintering, the ABS- and ICW-based scaffolds were found to possess WT values of ~ 280 μm and ~ 340 μm respectively. In the final set of experiments, 3-D scaffolds with very fine architectures (WT values of 150 μm and 300 μm) were fabricated. The mineral was found to consist of a mixture of β-tricalcium phosphate and hydroxyapatite phases.

Finally, MC3T3-E1 cells cultured in the presence of mineral particles (obtained from the 3-D scaffolds) were found to be metabolically active over a period of 5 days.

In this study, ABS and ICW were chosen for the fabrication of template patterns because these two materials have been shown to span small gaps and have been used successfully in other burnout processes [23, 24]. Although ICW has been designed for casting and burnout processes, it is not as flexible as ABS when designing geometry; its lower viscosity compared to ABS resulted in closed ends of the printed template patterns (**Figure B2**). Moreover, the low viscosity of the extruded wax caused the roads to sag when spanning gaps. Nevertheless, both the ABS and ICW materials used in this study are sufficient to provide proof-of-concept for the fabrication and mineralization processes.

SBF solutions have been routinely used for mineralizing scaffold surfaces meant for bone tissue engineering applications. In particular, SBF has been previously used to mineralize several different scaffold materials: PLLA and PLGA [25], Ti6A14V [26], Bioglass® [27]. A 10 × SBF was used in this study to accelerate the formation of mineral crystallites compared to lower SBF concentrations [19, 28]. Since mineralization using SBF solutions does not typically result in cohesive coatings without a preliminary surface treatment of the substrate [29], the patterns underwent either plasma or a sodium hydroxide treatment prior to mineralization. Plasma-treatment activates surface groups for mineralization and decreases the contact angle, thus allowing for aqueous solutions to easily penetrate the template pattern [17]. Plasma-treatment has been successfully used in stochastic scaffold processes including PCL- [22] and PCL-HA- [17] based scaffolds. In contrast, sodium hydroxide etching creates negatively charged groups on surfaces, and has been shown to increase mineralization of treated surfaces when compared to identical, non-treated surfaces [18]. In the present study, plasma-treatment was found to result in more mineral deposition than sodium hydroxide, indicating that the reduced hydrophobicity of the template pattern (resulting from plasma-treatment) was a key factor in promoting wetting and mineralization of template patterns by the 10 × SBF solution. During the mineralization process, dynamic flow conditions were found to yield higher amounts of mineral than static because the dynamic flow probably allowed for better distribution of SBF solution within the pores of the template patterns [30]. Pattern chemistry had no significant

effect on mass of mineral deposited, as both the ABS and ICW materials were inert and hydrophobic.

Following mineralization, the burnout and sintering steps caused a small shrinkage of scaffold features, probably due to the loosely packed crystals sintering together and filling voids. Providing a higher density of mineral coating during the SBF treatment may reduce the amount of shrinkage during sintering. Reducing the concentration of the 10 × SBF solution to 5 × and concurrently increasing the treatment time may result in slower but more controlled nucleation of mineral crystallites, in turn leading to tighter packing and higher density.

The low-viscosity SBF solution used in this study was expected to penetrate complex scaffold geometries with relative ease, thus eliminating the geometry and feature-size limitations associated with existing indirect techniques. Specifically, the WT (~ 158 μm for ICW-based and ~ 530 μm for ABS-based scaffolds) and CD (~340 μm for ICW-based and ~ 280 μm for ABS-based scaffolds) values in the present study met or exceeded the resolution of other indirect methods of scaffold fabrication that have used viscous ceramic slurries. For example, Chu et al used a laser sintering technique to fabricate HA scaffolds from Cibatool S5170-based molds and HA suspensions [9]. They reported WT and CD values of 560-755 μm and 366-968 μm respectively. Taboas et al used a inkjet printing technique to fabricate PGA, PLA and HA indirect scaffolds from wax-based molds [10]. They reported WT and CD values of ~ 500 μm and 500-800 μm respectively. To date, Detsch et al have reported the lowest WT (~ 500 μm) and CD (~ 300 μm) values for HA scaffolds fabricated from wax-based molds and HA-slurries [13]. In comparison, the WT value of ~ 158 μm demonstrated in this study is the smallest reported thus far in the literature to the best of the authors' knowledge (**Figure B5**).

The chemistry of the mineral in both scaffolds suggests that the mineral may be osteoconductive and may promote the regeneration of bone tissue [31]. Ca/P ratios between 1.60 and 1.68 obtained from EDS analysis is consistent with the presence of β-tricalcium phosphate (theoretical Ca/P ratio = 1.5) and hydroxyapatite (theoretical Ca/P ratio = 1.67) as determined by XRD (**Figure B6**). However, osteoconductivity of the scaffolds could not be tested directly because the presence of channels weakened the mechanical integrity of the scaffolds. Nevertheless, a cell cytotoxicity assay was performed to demonstrate the compatibility of

mineral with cells. Although the presence of mineral particles had an initial effect of lowering the metabolic activity of MC3T3-E1 cells, viability was comparable to a TCPS control at a later time point (**Figure B7**). These results are consistent with the onset of rapid proliferation [32] and demonstrate that the mineral is not cytotoxic.

In summary, this study demonstrates that an indirect process may be used to fabricate scaffolds with controlled geometries and fine feature sizes. The study also suggests that these scaffolds may be an attractive alternative to traditional scaffolds for regeneration of bone tissue. Future studies will seek to fabricate mechanically robust scaffolds by increasing the density of mineral deposition, and examine the effects of scaffold architecture in promoting cell proliferation and infiltration.

B6. Acknowledgements

The authors thank Stephen McCartney (Nanoscale Characterization and Fabrication Laboratory, Virginia Tech) for help with SEM imaging and EDS, Rick Caudill (Department of Sustainable Biomaterials, Virginia Tech) for help with obtaining XRD spectra, Dr. Carlos Suchicital (Department of Materials Science and Engineering, Virginia Tech) for the use of the furnace and Dr. Richey Davis (Department of Chemical Engineering, Virginia Tech) for the use of the SPI Plasma Prep II instrument.

References

[1] van Tienen TG, Heijkants RG, Buma P, de Groot JH, Pennings AJ, Veth RP. Tissue ingrowth and degradation of two biodegradable porous polymers with different porosities and pore sizes. Biomaterials. 2002;23:1731-8.
[2] Karande TS, Ong JL, Agrawal CM. Diffusion in musculoskeletal tissue engineering scaffolds: design issues related to porosity, permeability, architecture, and nutrient mixing. Ann Biomed Eng. 2004;32:1728-43.
[3] Hutmacher DW. Scaffolds in tissue engineering bone and cartilage. Biomaterials. 2000;21:2529-43.
[4] Burg KJ, Porter S, Kellam JF. Biomaterial developments for bone tissue engineering. Biomaterials. 2000;21:2347-59.
[5] Hollinger J. Factors for osseous repair and delivery: Part II. J Craniofac Surg. 1993;4:135-41.
[6] Salgado AJ, Coutinho OP, Reis RL. Bone tissue engineering: state of the art and future trends. Macromol Biosci. 2004;4:743-65.
[7] Leong KF, Cheah CM, Chua CK. Solid freeform fabrication of three-dimensional scaffolds for engineering replacement tissues and organs. Biomaterials. 2003;24:2363-78.
[8] Yeong WY, Chua CK, Leong KF, Chandrasekaran M. Rapid prototyping in tissue engineering: challenges and potential. Trends Biotechnol. 2004;22:643-52.
[9] Chu TM, Halloran JW, Hollister SJ, Feinberg SE. Hydroxyapatite implants with designed internal architecture. J Mater Sci - Mater Med. 2001;12:471-8.
[10] Taboas JM, Maddox RD, Krebsbach PH, Hollister SJ. Indirect solid free form fabrication of local and global porous, biomimetic and composite 3D polymer-ceramic scaffolds. Biomaterials. 2003;24:181-94.
[11] Lee M, Dunn JC, Wu BM. Scaffold fabrication by indirect three-dimensional printing. Biomaterials. 2005;26:4281-9.
[12] Yeong WY, Chua CK, Leong KF, Chandrasekaran M, Lee MW. Indirect fabrication of collagen scaffold based on inkjet printing technique. Rapid Prototyping J. 2006;12:229-37.
[13] Detsch R, Uhl F, Deisinger U, Ziegler G. 3D-Cultivation of bone marrow stromal cells on hydroxyapatite scaffolds fabricated by dispense-plotting and negative mould technique. J Mater Sci - Mater Med. 2008;19:1491-6.
[14] Dellinger JG, Cesarano J, 3rd, Jamison RD. Robotic deposition of model hydroxyapatite scaffolds with multiple architectures and multiscale porosity for bone tissue engineering. J Biomed Mater Res A. 2007;82:383-94.
[15] Chrisey DB. MATERIALS PROCESSING: The Power of Direct Writing. Science. 2000;289:879-81.
[16] Ciapetti G, Granchi D, Devescovi V, Baglio SR, Leonardi E, Martini D, et al. Enhancing Osteoconduction of PLLA-Based Nanocomposite Scaffolds for Bone Regeneration Using Different Biomimetic Signals to MSCs. Int J Mol Sci. 2012;13:2439-58.
[17] Venugopal J, Low S, Choon AT, Kumar AB, Ramakrishna S. Electrospun-modified nanofibrous scaffolds for the mineralization of osteoblast cells. J Biomed Mater Res A. 2008;85A:408-17.
[18] Kretlow JD, Mikos AG. Review: mineralization of synthetic polymer scaffolds for bone tissue engineering. Tissue Eng. 2007;13:927-38.
[19] Muller L, Muller FA. Preparation of SBF with different HCO3- content and its influence on the composition of biomimetic apatites. Acta Biomater. 2006;2:181-9.

[20] Kokubo T, Takadama H. How useful is SBF in predicting in vivo bone bioactivity? Biomaterials. 2006;27:2907-15.
[21] Chou YF, Huang W, Dunn JC, Miller TA, Wu BM. The effect of biomimetic apatite structure on osteoblast viability, proliferation, and gene expression. Biomaterials. 2005;26:285-95.
[22] Yang F, Wolke JGC, Jansen JA. Biomimetic calcium phosphate coating on electrospun poly (epsilon-caprolactone) scaffolds for bone tissue engineering. Chem Eng J. 2008;137:154-61.
[23] Lee CW, Chua CK, Cheah CM, Tan LH, Feng C. Rapid investment casting: direct and indirect approaches via fused deposition modelling. Int J Adv Manuf Tech. 2004;23:93-101.
[24] Bandyopadhyay A, Danforth SC, Safari A. Effects of processing history on thermal debinding. J Mater Sci. 2000;35:3983-8.
[25] Zhang RY, Ma PX. Biomimetic polymer/apatite composite scaffolds for mineralized tissue engineering. Macromol Biosci. 2004;4:100-11.
[26] Tas AC, Bhaduri SB. Rapid coating of Ti6A14V at room temperature with a calcium phosphate solution similar to 10x simulated body fluid. J Mater Res. 2004;19:2742-9.
[27] Kokubo T. Surface-Chemistry of Bioactive Glass-Ceramics. J Non-Cryst Solids. 1990;120:138-51.
[28] Li JS, Beaussart A, Chen Y, Mak AFT. Transfer of apatite coating from porogens to scaffolds: Uniform apatite coating within porous poly(DL-lactic-co-glycolic acid) scaffold in vitro. J Biomed Mater Res A. 2007;80A:226-33.
[29] Qu X, Cui WJ, Yang F, Min CC, Shen H, Bei JZ, et al. The effect of oxygen plasma pretreatment and incubation in modified simulated body fluids on the formation of bone-like apatite on poly(lactide-co-glycolide) (70/30). Biomaterials. 2007;28:9-18.
[30] Chrzanowski W, Yeow WJ, Rohanizadeh R, Dehghani F. Bone bonding ability-how to measure it? Rsc Adv. 2012;2:9214-23.
[31] Rojbani H, Nyan M, Ohya K, Kasugai S. Evaluation of the osteoconductivity of alpha-tricalcium phosphate, beta-tricalcium phosphate, and hydroxyapatite combined with or without simvastatin in rat calvarial defect. J Biomed Mater Res A. 2011;98A:488-98.
[32] Whited BM, Skrtic D, Love BJ, Goldstein AS. Osteoblast response to zirconia-hybridized pyrophosphate-stabilized amorphous calcium phosphate. J Biomed Mater Res A. 2006;76A:596-604.

Appendix C

Synthetic biomaterials for regenerative medicine applications

Satyavrata Samavedi[a], Lauren K. Poindexter[b], Mark Van Dyke[c], Aaron S. Goldstein[a,c]

[a] Department of Chemical Engineering, Virginia Polytechnic Institute and State University, Blacksburg, VA

[b] Virginia Tech Carillion School of Medicine and Research Institute, Roanoke, VA

[c] School of Biomedical Engineering and Sciences, Virginia Polytechnic Institute and State University, Blacksburg, VA

C1. Abstract

Synthetic biomaterials for regenerative medicine (RM) range from non-degradable classic materials such as metals that primarily replace damaged tissues, to degradable polymers that regenerate tissue structure and function. This chapter discusses the properties of several classes of synthetic materials commonly used in RM, including metals, ceramics, non-degradable polymers, degradable polymers and hydrogels. Under each class, the merits and limitations of specific materials are reported. Furthermore, clinical and *in vivo* applications of several of these materials are also discussed.

Key words: metals, ceramics, non-degradable polymers, degradable polyesters, polyorthoesters, polyanhydridres, polyphosphazenes, polyphosphoesters, hydrogels, regenerative medicine

C2. Introduction

Synthetic materials have been used for the reconstruction and regeneration of a variety of tissues and organs for the last 100 years. Beginning with inert implantable materials that primarily provided replacement of mechanical function, the field of regenerative medicine (RM) has become a field unto itself with essential ties to engineering, materials and biology. RM has seen the use of a wide spectrum of materials ranging from metals and ceramics to polymers

whose properties can be appropriately designed for specific applications. Materials in RM applications may be used to augment existing tissue (e.g., engraftment of stem cells), promote the growth of neo-tissue (e.g., engineered blood vessels), or engineering a tissue equivalent for full organ replacement. Thus, a regenerative strategy mandates the use of degradable materials that serve as temporary implants and subsequently degrade once tissue is regenerated or engrafted *in vivo*. In contrast, relatively long-lasting implants may be used in cases where the implants are expected to replace the function of damaged tissue. While RM in its strictest sense encompasses the former strategy- leveraging the human body's intrinsic ability to regenerate damaged tissue- non-degradable materials for tissue replacement will also be discussed in this chapter.

Primary considerations for the use of synthetic biomaterials are biocompatibility, degradation characteristics, mechanical, chemical and increasingly, biological properties. While the first generation of biomaterials was designed to be inert and primarily meant for replacing tissue mechanical function, the second and third generations have incorporated degradability and bioactivity (e.g., cell-responsive cues) respectively. The third generation of materials in particular has utilized polymeric vehicles for the delivery of therapeutics. From the perspective of long-term implants, materials such as metals and ceramics have shown a lot of promise for hard tissue replacement due to their mechanical properties. In contrast, polymers offer much more flexibility in terms of chemical properties (e.g., degradation rates, surface chemistry, glass transition temperature(T_g)) that make them attractive for soft tissue repair and RM. Thus, material properties drive their application and these properties can be suitably designed to elicit a specific host response.

This chapter discusses important classes of synthetic biomaterials used in RM applications. **Section C3** describes biologically relevant properties of synthetic biomaterials such as biocompatibility, degradation and mechanical properties that influence their use in specific applications. This section also provides a brief overview of design criteria for implants and scaffolds based on synthetic biomaterials. **Section C4** briefly discusses classes of non-degradable materials that have traditionally been used for replacement of tissue and organs. While **Section C5** forms the bulk of this chapter and addresses a whole array of degradable polymers that have been used for in RM applications, **Section C6** describes hydrogels. Both **Sections C5** and C**6** include a description of key material properties, their merits and limitations,

and a summary of applications in which materials have been employed. (Here, discussions are limited to clinical trials and animal models.) Finally, **Section 7** provides insights on current and future directions for the use of synthetic biomaterials in RM applications.

C3. Biologically relevant properties of polymeric biomaterials

Materials used in RM applications possess certain essential properties such as biocompatibility and appropriate mechanical/chemical properties (1). In cases where biomaterials are used as temporary implants or as delivery systems, the materials are degradable and the products of degradation non-toxic. In addition to these generic properties, materials used in specialized applications possess other specific properties. For example, in the case of ocular applications, implants possess suitable optical properties (2). In several other applications such as wound healing or controlling cell fate *in situ*, biologically inert biomaterials can be functionalized via chemical treatments, coatings and surface grafting (1). Herein, some significant properties of these materials relevant to RM applications are discussed.

C3.1. Biocompatibility

The definition of the term "biocompatibility" has undergone several changes over the years (3). In its most general sense, biocompatibility may be defined as the ability of a material, device or system to perform without a clinically significant host response in a specific application (4). While this definition extends the concept of biocompatibility to mean more than mere biological safety to the patient, it is still broad and general. For example, this generality does not account for interactions of the biomaterial with the body or vice versa in applications where the biomaterial is intended to elicit a specific biological response as in the case of wound healing. To overcome such ambiguities, the use of the phrase "biological performance" to describe the concept of biocompatibility has been suggested (5). Biological performance is in turn divided into two sub-categories, namely host response and material response. While host response refers to the local and systemic response of the biological system to the implanted material, material response refers to the effect of the material on the biological system. In light of these ideas, biocompatibility may be re-defined as the ability of a material, device or system to perform appropriately in an intended application and elicit a host response suitable to that application. This umbrella definition of biocompatibility includes physical/chemical properties

of the biomaterial, its bioactivity, degradability and products of degradation, all of which are critical in determining the appropriateness of material performance as well as the host response.

C3.2. Mechanical properties

Typically, the design of biomaterials is inspired by the nature of the tissue to be regenerated. The biomaterial implant is expected to match the mechanical properties of target tissue and confer a certain degree of functionality until complete regeneration occurs (6). For example, biomaterials used in the regeneration of ligaments are visco-elastic and thus promote joint stability, allowing for joint flexibility. In RM applications such as the regeneration of load-bearing stiff tissues, mechanical properties such as stiffness and compressive moduli of the biomaterials play a major role in influencing the eventual success of the implant (7). In other applications such as engineering blood vessels, the biomaterial is robust enough to flex under cyclic hydrostatic pressure as well as hydrodynamic shear stress. In the regeneration of cartilage tissue, hydrogels are typically used because they mimic the mechanical properties of cartilage and allow for effective load transfer (8). In the reconstruction of complex organs such as the bladder, the mechanical properties of biomaterials must be carefully chosen, keeping in mind the various mechanical deformations and forces the organ undergoes under normal physiological conditions (9). In addition, the mechanical properties of the biomaterial will change as the material degrades and new tissue replaces it; moreover, mechanical demands on the biomaterial may change on a short-term scale (i.e., hours to days) as physiologic loading occurs. All of these considerations must be kept in mind when selecting materials for a particular application.

C3.3. Degradability

In cases where biomaterials are used as replacements (such as in total hip replacement), degradability can be detrimental to the functionality of the biomaterial. In contrast, degradability is a desired property in most RM applications where tissue regeneration is the ultimate goal (6). Degradation rate is typically chosen to match with the regeneration rate of neo-tissue (10) (**Figure C1**). In this context, polymers have assumed great importance in RM due to an ability to tune their degradation rates based on the application. The degradation rate of the biomaterial depends on the backbone chemistry of the polymer as well as the side groups attached to the backbone. Properties of biomaterials such as hydrophobicity, molecular weight and crystallinity

strongly affect degradation (**Figure C2**). The degradability of polymeric biomaterials can be exploited to load and deliver therapeutics such as drugs, vaccines and proteins to host tissue (6). In other words, the polymeric biomaterial can aid the controlled release of therapeutics as it degrades. While degradable polymers are very useful in RM applications, a vital requirement is that the products of degradation be non-toxic and non immunogenic (11). Products should be readily cleared by the excretory system and not accumulate in the liver, kidney and spleen.

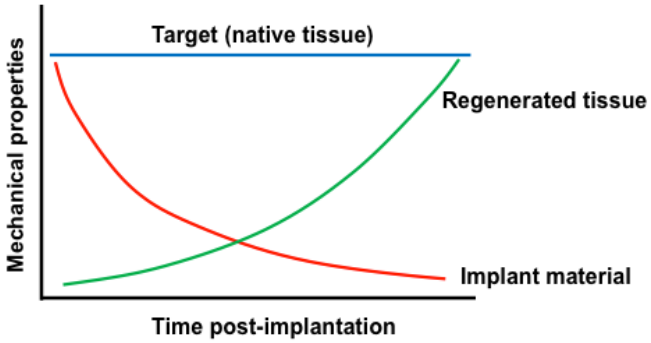

Figure C1: Immediately following implantation, the mechanical properties of the implant material matches the properties of the target tissue. As the material degrades with time, the mechanical properties of the regenerated tissue slowly increase due to tissue maturation within the implant. This process leaves behind biologically functional neo-tissue.

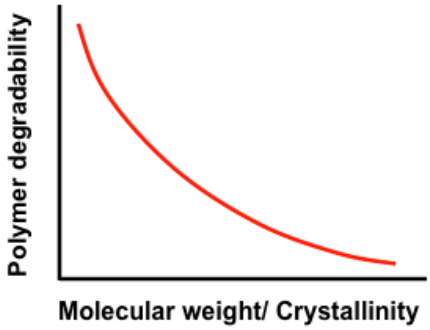

Figure C2: The degradability of polymeric materials decreases with an increase in molecular weight and crystallinity. Polymers possessing high molecular weights and crystallinity degrade slowly *in vivo*.

C3.4. Bioactivity

Bio-chemical properties of materials play a crucial role in guiding tissue regeneration *in vivo*. Here, two distinct strategies have been employed. In a cell-free approach, biomaterial scaffolds are used to enhance the intrinsic ability of the tissue for regeneration via release of a biochemical agent that directs homing and recruitment of progenitor cells. In a tissue-engineering approach, biomaterial scaffolds are seeded with cells, scaffolds are subsequently conditioned in a bioreactor before implantation into a patient (12). In both the approaches, the

biomaterials used for the fabrication of scaffolds can be appropriately "bio-activated" (13). For example, biomaterials used for wound healing applications can be designed to incorporate chemo-attractants to promote cell migration and subsequent healing of injured tissue. Certain other applications require non-fouling surfaces, for which biomaterials can be coated with poly (ethylene glycol) (14). In applications such as bone tissue implants, inert titanium plates are often coated with a layer of calcium phosphate mineral in order to promote osseointegration with host tissue (15). Thus, biomaterials can be suitably designed to promote specific cell responses in various applications.

C4. Classic materials

C4.1. Metals

Metals have been traditionally used in surgical procedures since the 17th century. Due to their superior mechanical properties as compared to other biomaterials, metals have been extensively used in load-bearing applications such as the reconstruction of knees and hips. Conventional metals used for these applications include stainless steel, cobalt-chromium- (Co-Cr) based alloys and titanium (and its alloys) (16). The properties of these metals are briefly discussed in the following paragraphs.

C4.1.1. Stainless steel (SS)

SS materials are cost-effective and exhibit mechanical strength sufficient for orthopedic applications (17). They possess moduli close to 200 GPa and ultimate tensile strengths in excess of 500 MPa depending on their processing method. They are also resistant to corrosion due to the presence of small amount of molybdenum and a high percentage of chromium. Other elements, when present in trace amounts, confer various types of functionalities. For example, low phosphorous content is usually tied to improved ductility, while carbon – usually restricted to very low amounts – improves corrosion resistance (17). The presence of nickel in SS materials can be a cause for concern because nickel is a known allergen and its release from SS implants can cause severe allergies in patients with a known history of nickel allergy (17, 18). Therefore, nickel-free SS materials with the inclusion of nitrogen have been developed (19). These materials exhibit the excellent mechanical and corrosion-resistance properties of SS in addition to being nickel-free. SS materials suffer from poor wear resistance, leading to severe

wear and debris formation especially in prostheses where excessive contact between two metallic implants occurs (20). As a result, SS is usually used in devices such as fracture plates and hip nails, and much less in applications such as joint prosthesis.

C4.1.2. Co-Cr-based alloys

Co-Cr-based alloy implants help overcome the limitations encountered with SS implants. In addition to exhibiting corrosion-resistance like SS materials, these alloys also resist wear better than SS implants (16). Co-Cr-based alloys also possess a high elastic modulus similar to that of SS and have higher fatigue strength (in excess of 600 MPa) in air compared to SS (less than 400 MPa) (21). They also possess higher resistance to corrosion even in alkaline environments. As with SS materials, the presence of nickel is a concern due to its potential as an allergen. Therefore, Ni-free and low-C Co-Cr-based alloys have been more recently investigated (18). Due to their high ultimate tensile strength and fatigue strength, these alloys may cause stress-shielding, a phenomenon by which the absence of mechanical loading on bone results in a local resorption of the tissue (22). Moreover, ions from these alloys can leach out of implantation and accumulate in tissue over a period of time (23). Nevertheless, Co-Cr-based alloys have been used in joint prosthesis, hip prosthesis and in artificial disc replacement systems.

C4.1.3. Titanium (Ti)

Ti based implants have been explored for orthopedic applications primarily due to their moderately high elastic modulus of around 110 GPa and low density compared to the metals previously described (16). As compared to SS-based and Co-Cr-based materials, Ti-based alloys exhibit lower cyclic fatigue (21). Ti-based implants are also favored because of their superior corrosion-resistant properties compared to SS-based and Co-Cr-based materials and a relatively lower amount of ions released from the implant (24). Ti derives its corrosion resistance from the ability to form an inert oxide layer on its surface, which allows for passivation. Ti-based implants can readily ossointegrate, allowing them to function better in the long-term than traditional SS implants. Ti alloys such as Ti-6Al-4V, which incorporate varying amounts of other metals such as aluminum (Al) and vanadium (V), have been manufactured to help improve

the properties of the base metal. However, V and Al ions released from the alloys have been found to be cytotoxic and detrimental to the long-term health of patients (25). Moreover, Ti suffers from poor wear resistance and is not easily amenable to processing. To overcome these limitations, alloys such as Ti-6Al-7Nb and Ti-5Al-2.5Fe, which include the niobium (Nb) and iron (Fe) instead of V, have been synthesized (18). Ti alloys have also been fabricated with Young's moduli closer to that of bone (25). Ti-Ni-based alloys (Nitinol) have been studied for application in orthopedics due to their shape-memory properties (superelasticity) (26). Despite possessing attractive properties, the use of Nitinol has been restricted due to the allergy and toxicity associated with Ni. Therefore, Ni-free alternatives such as Ti-Nb-Al and Ti-Mo-Al have also been explored. Several studies have investigated the role of surface properties such as roughness, charge and ceramic/biochemical coating towards improving their osseointegration with host tissue (16).

C4.2. Ceramics

Ceramics are biocompatible materials typically used in orthopedics and dentistry, particularly as components in joint prostheses and bone fillers. Due to their popular use, they have evolved considerably over the years: first generation materials were designed to replace bone, second generation materials were intended to repair bone, and third generation materials aim to regenerate bone (27). Common ceramic materials include calcium phosphates, as well as silica-based (eg. Bioglass 45S5®) and alumina-based compounds.

C4.2.1. Calcium phosphate (CaP)

CaP materials are biocompatible, osteoconductive and can be engineered to possess a wide variety of physical and chemical properties (28, 29). Specific formulations of synthetic CaP include hydroxyapatite (HAP), β-tri calcium phosphate (TCP) and biphasic calcium phosphate (varying ratios of HAP and TCP). Some forms of CaP readily osseointegrate (achieve intimate biological fixation) with natural bone due to their chemical and physical similarities with carbonated hydroxyapatite crystals. However, CaP biomaterials are brittle, and therefore perform best *in vivo* in a limited array of forms or in conjunction with stronger materials as a nano-scale coating on titanium rods, screws, and plates, among others (27, 30, 31).

Commercially-available FDA-cleared CaP products range from moldable putties to pre-sized wedges. Moreover, injectable CaP cements are widely employed in surgery because of their high compressive strength and ease of defect-filling, despite inconclusive documentation of their slow resorption rates *in vivo* (29, 32).

C4.2.2. Bioglass

Melt-derived bioactive silicate glass (Bioglass 45S5®) is an inorganic, modified silica network comprised of 45% SiO_2, 24.5% Na_2O, 24.5% CaO, and 6% P_2O_5 (33). Due its ability to bond chemically with surrounding native tissue, this material promotes excellent repair of bony defects (27, 33), and does not stimulate an immune-derived fibrous capsule around the implant. However, histological evaluation of long-term indwelling Bioglass® prostheses reveals partial degradation, fragmentation, and connective tissue invasion of the implant and implant site (34). An alternative sol-gel process for glass formation results in a bioactive glass that, unlike melt-derived Bioglass 45S5®, is able to degrade *in vivo* (35, 36). In particular, a $70SiO_2/30CaO$ (mol %) composition with or without additional compounds such as P_2O_5, is now a popular material for third generation tissue regeneration applications (33). Recently, the sol-gel process has been applied to Bioglass 45S5® (37, 38). To date, sol-gel silica glasses have been manufactured in a large spectrum of sizes and shapes (scaffolds, foams, powders, nanoparticles, etc.) for a vast array of orthopedic and dental applications. While the bioglass foam structure approximates that of cancellous bone, few studies demonstrate adequate strength (relative to cancellous bone) of bioglass scaffolds pre- and post-implantation for tissue engineering (39).

C4.2.3. Alumina

Alumina (Al_2O_3) has been widely used in the manufacture of artificial prostheses for total hip arthroplasty (THA) since the 1970's. Although these inert oxide ceramic components (first generation) performed marginally well initially, improvements in manufacturing, design, and surgical technique have significantly improved their success rate as hip prostheses (40). Fine-grain alumina is a desirable material for orthopedic applications because a nearly perfect spherical alumina surface, well-lubricated with joint fluid, exhibits minimal friction and dramatically reduced metallic wear, as compared to other joint prosthesis materials (41). One

example of an FDA-approved alumina-on-alumina model (Al-Al) is the Stryker® Trident® Ceramic System. This prosthesis is composed of a titanium acetabular component and an alumina insert that articulates with an alumina ball. Two separate follow-up studies on Al-Al THAs show mid-term (5 to 9 years) prosthetic survival rates above 90% for patients (42, 43). Despite its wide use in orthopedic applications, alumina-based biomaterials can suffer from squeaking, component wear from edge-loading, chipping and fracture (40).

C4.3. Non-degradable polymers

C4.3.1. Polymethylmethacrylate (PMMA)

PMMA is a strong but lightweight polymer possessing a compressive strength between 85 and 110 MPa and the tensile strength between 30 and 50 MPa (44). PMMA possesses a relatively high coefficient of thermal expansion, and during polymerization *in situ,* temperatures can reach values as high as 40 and 56 °C (45, 46). Consequently, the curing process *in vivo* can result in a shrinkage of around 6-7 % (45) and cause tissue necrosis. The mechanical properties of PMMA can be tuned by varying the mixing ratios of monomer and initiator during polymerization. PMMA can absorb water over several weeks at body temperature (45) and properties such as tensile strength and fatigue strength decrease upon water absorption. Despite this seemingly poor stability, PMMA degrades very little in aqueous environments. In addition to strength and stability in aqueous environments, PMMA possesses excellent optical properties (47).

Due to its biocompatible nature and tunable mechanical and optical properties, PMMA has been widely used in bone cements, as intraocular lenses and as screw in bone fixation (48). Although PMMA's use as bone cement has certain disadvantages such as causing thermally-induced necrosis, chemically-induced necrosis due to the release of unreacted monomer, shrinkage after setting and inflammation due to particles released from the cement, bone cement continues to enjoy popularity in orthopedic surgery and is used under six commercial formulations in the United States (48). Concurrently, bone cements have also been used extensively in percutaneous vertebroplasty (49). Since PMMA does not play a role in inducing new bone formation, recent work has investigated the addition of small quantities bioactive

glass, ceramics and osteogenic growth factors to PMMA resulting in the formation of "bioactive" bone cements (49). Apart from use as bone cement, PMMA has also found wide-spread application as hard contact lenses due to its excellent optical properties (2). However, PMMA's use as long-term lenses is limited due to its low oxygen permeability. This limitation can be overcome by co-polymerizing methyl methacrylate with methacrylate-functionalized siloxanes. PMMA has also been used in intraocular implants and as intrastromal corneal rings due to its superior mechanical and optical properties, and biocompatibility (50, 51).

C4.3.2. Poly(ethylene terephthalate) (PET)

PET is a thermoplastic semi-crystalline polymer, first commercialized under the trade name Dacron (52). Its T_g is generally accepted to be 70 °C, while its melting point (T_m) is ~ 250 °C. Although it is light-weight, PET possesses a yield strength of around 40 MPa (53) and a tensile strength of around 170 MPa. In addition, it is extremely resistant to wear and has a high flexural modulus. PET is quite impermeable to most gases and liquids, and this property can be improved by either increasing its crystallinity or by co-polymerizing it with other monomers (54). Once molded and set, PET does not absorb water easily due to its crystalline nature, and is also resistant to dissolution by common solvents.

PET is biocompatible and is FDA-approved for the repair of large blood vessels and other soft tissues. It has been widely used in procedures such as axillofemoral bypass (55), rhinoplasty (56) and ligament reconstruction (57), particularly in the form of woven/knitted structures. Although Dacron has been used successfully in reconstruction surgery for a number of decades, it has several limitations. For example, it is known to elongate, creep and undergo permanent deformation under sustained loads; this behavior can be detrimental to reconstructed blood vessels or ligaments where the shape of the device is critical for its proper function. Arterial procedures based on Dacron have been found to result in graft dilation (58) and multiple aneurysms, while carotid patching procedures have been reported in a small number of instances to result in pseudoaneurysms and infection (59).

C4.3.3. Poly(tetrafluoroethylene) (PTFE)

PTFE, more commonly known by its trade name Teflon, is yet another thermoplastic crystalline polymer that is highly resistant to thermal treatment (52). It possesses a T_g value

between -110 and -97 °C, while its T_m value is 330 °C. Teflon is highly hydrophobic and is also resistant to attack from most commonly used chemicals and solvents. Its inert properties stem the strong carbon-fluoride bonds and the absence of virtually any branching. Teflon is generally thought to possess a Young's modulus of around 500 MPa, while its tensile strength is between 14 and 23 MPa. Although strong and highly resistant to wear, Teflon can also undergo creep, which can pose a problem when used in medical applications.

Similar to PET, Teflon has been used in a number of reconstructive procedures due to its biocompatibility, inertness and mechanical properties. Specifically, woven/knitted Teflon-based materials have been used for small artery replacement (60), as synthetic ligament prostheses (under the name Gore-tex) (61) and as prosthetic patches for congenital diaphragmatic hernia repair (62). Teflon, in its injectable form, has also been used for vocal-fold augmentation (63) and in the treatment of vesicoureteric reflux in young adults and children (64). However, the performance of Teflon has been shown to deteriorate over time when used in the reconstruction of ligaments (61). In addition, in certain cases, it has been reported to migrate away from site of injection (65) and has been reported to result in Teflon granulomas and subglottic overfilling when used in vocal fold augmentation (63).

C4.3.4. Silicones

Silicones, or polysiloxanes, are a class of polymers that exhibit a wide variety of properties that range from being liquids to gels and elastomers. The specific properties of silicones depend upon the side chains and the extent of cross-linking. Liquid silicones are biocompatible and non-degradable (66). They possess very low surface tension values and have the ability to repel water. In fact, they are considered to possess the highest surface tension values for biocompatible elastomers. Silicones have low thermal conductivity and are almost non-reactive chemically. They are very stable and resistant to degradation by heat or ultraviolet radiation. Due to a large free volume, silicones demonstrate high permeability to gases such as oxygen and nitrogen. They are considered non-degradable and are non-toxic. Silicones are also biocompatible and do not support the growth of microbes. Given their broad properties, silicones have been used for a wide variety of applications including intraocular lenses, bandages, scar treatment sheets and breast implants (liquid silicone).

C4.3.5. Polyurethanes (PUs)

PUs are a class of elastomers that are typically produced by the reaction between a diol (soft segment) diisocyanate and a chain extender (hard segments) (67). The wide variety of choices available for each of these monomers allows for the fabrication of PUs possessing a range of mechanical and chemical properties. PUs are usually very flexible and elastic, displaying minimal hysteresis over repeated cycles of cyclic strain. For example, an ether-based PU has been shown to possess Young's moduli between 4.7 and 7.4 MPa (depending on the humidity and temperature), and to exhibit rate-dependent viscoelastic behavior (12% viscoelasticity) (68). Also, PUs possess better tear and abrasion resistance than silicones. Although classic PUs, synthesized from aromatic diisocyanates, are considered non-degradable, materials synthesized from degradable monomers such as polylactide and polycaprolactone can undergo hydrolysis. Moreover, the use of non-aromatic diisocyanates such as lysine ethyl ester diisocyanate and 1,4 diisocyanatobutane has resulted in the fabrication of degradable PUs that can be used for regeneration of tissues (69, 70). Finally, the use of non-aromatic diisocyanates mitigates toxicity issues typically encountered with the degradation of aromatic-diisocyanate-based PUs. Due to their elastomeric nature and blood compatibility, PUs have been used for the reconstruction of blood vessels (vascular grafts), as breast implants, as wound healing materials and in facial reconstruction (71, 72).

C5. Degradable polymers

Degradable polymers comprise several different families of polymers possessing a wide variety of properties that eventually determine their specific application. The following section discusses clinically important properties of some of these polymers and examines their applications in RM. **Table C1** provides a list of these polymers, along with their applications.

C5.1. Polyesters

Polyesters are a class of polymers that have been used widely in RM applications due to their biocompatibility and biodegradability. These polymers derive their biodegradability from an ability of the ester bonds to undergo hydrolysis in aqueous environments. Among the various

types of polyesters, poly(lactic acid), poly(glycolic acid) and polycaprolactone have widely used. The properties and potential applications of these polymers are discussed in detail below.

Polymer class	Applications	References
Polyesters	• Bone fixation • Absorbable sutures • Long-term contraception device	(80, 97, 98)
Polyorthoesters	Drug delivery for: • Opthalmic applications • Periodontitis • Pain management (analgesics)	(107-111)
Polyanhydrides	Drug delivery: • To treat gliobalstoma • For osteomyelitis (antibiotics) • Anesthetics • For prevention of restenosis (heparin) • In ophthalmic surgery (5-fluorouracil)	(120-128)
Polyphosphazenes	Drug delivery for: • Periodontal diseases • Bone regeneration • Nerve regeneration • Inflammation • Diabetes	(136-141)
Polyphosphoesters	Drug delivery for: • Tumor treatment (paclitaxel) • Nerve regeneration	(142, 149-151)

Table C1: Degradable polymers used in RM applications.

C5.1.1. Poly(lactic) acid (PLA): properties

PLA exists in several isoforms given the inherent chirality of the pendant methyl groups. The L-isoform (PLLA) and the racemic DL-isoform (PDLLA) in particular have been routinely used in RM applications. PLLA is a semi-crystalline polymer with a T_g value of 60-65 °C, while PDLLA is an amorphous polymer possessing a T_g value of 55-60 °C. Enantiomerically pure PLA possesses a T_m value of around 180 °C (73). In general, properties such as crystallinity and T_m depend on the molecular weight of the polymer as well as its thermal history (74, 75). However, these properties can be varied by co-polymerization with other monomers such as

glycolide and caprolactone. PLA and its isoforms are hydrophobic and typically soluble in chlorinated and fluorinated organic solvents. Moreover, the racemic mixture is soluble in solvents such as acetone, tetrahydrofuran, xylene and dimethylsulfoxide. However, PLA and its isoforms are not soluble in water and alcohols. PLA possesses a high tensile modulus (~ 3 GPa) and strength (~ 50-70 MPa), and as a result, it is commonly used as a fixative in anchoring bone implants (73, 76). Mechanical properties such as tensile modulus and elongation at break depend upon molecular weight and crystallinity. For example, increasing the molecular weight of PLLA has been shown to result in superior mechanical properties; however, this effect appears to plateau at very high molecular weights (77). In aqueous environments, pure PLA has a slow degradation rate i.e., over months to years) due to its high crystallinity, which hinders water penetration. However, crystallinity can be reduced by the addition of small amounts of D-lactide resulting in amorphous PDLLA that can degrades faster (78). Degradation rate can also depends on molecular weight, with low molecular weight polymers degrading more quickly. The mechanism of degradation occurs essentially via the hydrolysis of ester bonds, resulting in progressive loss of molecular weight. However, the acidic degradation products can cause damage to surrounding tissue when used in RM applications. Moreover, when used as scaffolds in traditional tissue engineering applications, acidic by-products can be detrimental to seeded cells.

C5.1.2. Poly(glycolic) acid (PGA): properties

In contrast, PGA is a crystalline polymer with a T_g value between 35 and 40 °C, and a T_m value between 224 and 227 °C. PGA can be up to 55% crystalline (76). Using a variety of synthesis routes, a range of molecular weights can be obtained for PGA (79). Due to its high crystallinity, PGA is insoluble in common organic solvents such as chloroform, tetrahydrofuran and acetone, but soluble in highly fluorinated solvents such as hexafluoroisopropanol (80). PGA is more hydrophilic than PLA and thus more easily degraded in aqueous environments. However, PGA has a higher tensile modulus (~7 MPa) than PLA, although its mechanical properties can decrease considerably over time due to bulk degradation (80). As with PLA, high molecular weights and crystallinity of PGA can result in higher mechanical properties, while also reducing degradation rates. This property can potentially be useful depending on the nature of the applications. PGA is very unstable in aqueous environments and can typically degrade over

a period of a few weeks. Due to its hydrolytic instability, it is typically used in temporary sutures. The products of degradation are biocompatible and can enter the acetic acid cycle within the body, and be metabolized to carbon dioxide and water. However, major concerns with PGA include the sudden drop in mechanical properties upon absorption of water, subsequent degradation, and the accumulation of acidic degradation products. Moreover, foreign body responses have been noted when PGA has been used in animal studies (81, 82).

C5.1.3. Poly(lactic-co-glycolic acid) (PLGA): properties

PLGA is a random co-polymer of lactic and glycolic aid groups that combines the attractive properties of PLA and PGA (83). Physical and chemical properties (e.g., crystallinity, Young's modulus, degradation rate) can be tuned by varying the ratio of monomer units. However, copolymer properties are not linearly related to monomer properties (84, 85). Rather, copolymers generally degrade more rapidly than corresponding homopolymers (86, 87), are completely amorphous unlike either homopolymer, and possesses T_g values of around 40-60 °C. Finally, PLGA is also soluble in a wide range of organic solvents including acetone, tetrahydrofuran, choloroform and other chlorinated/fluorinated organic solvents (88).

C5.1.4. Polycaprolactone (PCL): properties

PCL is another semi-crystalline polyester that has been widely used for a variety of applications. It has a T_g value of –60 °C and a T_m value of 55-60 °C (89, 90). As with other polyesters, the mechanical and physical properties of the polymer depend upon its molecular weight and degree of crystallinity. Like PLGA, PCL is soluble in a wide variety of chlorinated/fluorinated organic solvents, as well as partially soluble in acetone and dimethylformamide; however, it is insoluble in alcohols and water (91). The polymer possesses a tensile strength of around 16-500 MPa and a Young's modulus of around 400 MPa (77, 89, 90). Due to its semi-crystalline nature, PCL possesses relatively low degradability in aqueous environments and can degrade over a period of two to four years depending on its molecular weight and degree of crystallinity (92). It is easily amenable to polymerization with a variety of other polymers resulting in co-polymers with a host of tunable characteristics. Co-polymer blends may be useful in drug delivery applications where degradation and subsequent release of

drug is critical. PCL has also been co-polymerized with poly ethylene oxide (PEO) to yield polymers with both hydrophobic and hydrophilic micro-domains (93).

C5.1.5. Poly(propylene fumarate) (PPF): properties

PPF is an unsaturated linear polyester that can be chemically modified and/or cross-linked to polymers with a wide variety of degradation characteristics. As with other polyesters, degradation occurs by the hydrolysis of ester bonds, and the products of degradation (fumaric acid and propylene glycol) are non-toxic and easily processed by the human body (94). Subcutaneous implantation studies in rats indicate that PPF induces a mild initial inflammatory response, but no any long-term negative effects (95). Degradation and mechanical properties heavily depend on the molecular weight, cross-linking duration, and cross-linking chemistry (96).

C5.1.6. Applications of polyesters

The different types of degradable polyesters have been employed in a wide variety of RM applications. Since the products of degradation from PLA, PGA and PLGA are non-toxic and readily processed in the human body (80), these polymers are approved by the FDA for application in bone fixation and sutures. For example, PLA has been used extensively as a bone fixative, while PGA is commonly used for the preparation of absorbable sutures (e.g., DEXON (97)) and fixatives (e.g., Biox) possessing degradation periods less than three months. Like its monomers, PLGA has also been used extensively as bone fixation screws and absorbable sutures. In contrast, PCL is often used in applications such as long-term drug delivery and in slow-degrading sutures due to its much slower rate of degradation as compared to PLGA. PCL has also been used in a long-term contraception device Capronor for the release of levonorgestrel over extended periods of time (98).

C5.2. Poly ortho-esters (POE)

POEs are a class of surface-eroding polymers that can be processed into materials that exhibit near zero-order release of drugs and therapeutics (99). Their surface-eroding properties stem from the presence of a hydrolytically degradable backbone within a hydrophobic polymer.

These polymers can be formed into dense hydrophobic matrices that subsequently degrade into smaller water-soluble polymers (100). Four families of POEs, namely POE I, POE II, POE III and POE IV have been synthesized and used for various applications.

C5.2.1. POE I, II & III: properties

Although POE I, II and III have been developed with a wide range of properties, they suffer from inherent limitations (97, 100). For example, POE I was initially used in several applications such as the treatment of burns (101), for drug delivery (102) and in bone regeneration (103). Later, its usage was discontinued due to a rather low T_g value and the acidic degradation products that also promoted auto-catalytic degradation. In the case of POE II, the polymer's hydrophobicity hinders its degradation under normal physiological conditions. Although POE III, possessing a flexible backbone, was developed as an improvement over the first two families of POEs, its use has been limited due to long synthesis periods and a lack of reproducibility (97).

C5.2.2. POE IV: properties

In contrast, POE IV has shown promise for commercialization primarily as a result of the presence of latent acidic chain segments (based on lactic and glycolic acids) within the backbone of the polymer, which allows for controlled degradation rates from few weeks to a few months (104). The polymer degrades with a linear decrease in weight loss over time, primarily driven by surface erosion and to a smaller extent by bulk degradation (105). Moreover, the products of degradation are neither toxic nor acidic. The thermal and mechanical properties of POE IV can be controlled independent of erosion rates by appropriate choice of diols during synthesis (104). These polymers show excellent stability at room temperature and are also relatively stable upon irradiation (106).

C5.2.3. Applications of POE II, III & IV

POEs have been shown to be useful for the controlled delivery of drugs and other therapeutics. For example, POE III has been routinely used in ophthalmic applications (107). In particular, it has been shown to be biocompatible in rabbit ophthalmic models and has been used

(in a semisolid form) in intravitreal injections for the delivery of the anti-inflammatory/anti-scarring agent 5-fluorouracil (108). The biocompatibility of viscous semisolid POE IV has been demonstrated in rabbits during subconjunctival, intracameral, intravitreal and suprachoiroidal injections (109). Importantly, the lifetime of POE IV was found to be much higher *in vivo* than POE III. Inflammatory reactions were found to be none to minimal. POEs have also been used for the delivery of bupivacaine for the management of post-surgical pain (110) and for the delivery of tetracycline into periodontal pockets in humans (111). In the latter case, patients suffering from periodontitis tolerated the POE formulations with no observable signs of irritation or discomfort. Furthermore, an improved clinical procedure ensured the longer retention of the formulations in the periodontal pockets, which allowed for the release of therapeutic doses of tetracycline over a period of 11 days.

C5.3. Polyanhydrides (PAH)

C5.3.1. Properties

PAHs have been investigated extensively as biomaterials for the delivery of drugs and other therapeutics (112). These polymers are biocompatible and degrade to release their respective diacids, which are non-toxic and non-mutagenic (113). Due to a hydrophobic backbone, these polymers degrade via surface erosion, thus allowing for close-to zero-order release kinetics over a period of weeks (112). While aliphatic anhydrides are prone to degradation (and require storage under moisture-free conditions), aromatic anhydrides are very stable in hydrolytic environments (97). Aliphatic PAHs usually possess T_m values less than 100 °C, while the aromatic PAHs possess T_m values over 100 °C. The properties of PAHs can be tuned by adjusting polymer composition. For example, the inclusion of poly-ethylene glycol improves their hydrophilicity (114), while co-polymerization of sebacic acid with fatty acid dimers results in hydrophobic polymers with lower rates of degradation (112). PAHs are generally crystalline, but their crystallinity can be tuned based on the choice of monomers (112). PAHs suffer from poor mechanical properties. For example, poly 1,6 carboxy-phenoxy hexane has a Young's modulus of about 1.3 MPa (115). However, copolymers such as poly anhydrides-co-imides have been shown to possess improved mechanical properties (116). In particular, compressive strengths in the range of 50 to 60 MPa have been reported for poly anhydrides-co-

imides (117). Mechanical properties and degradation rates can also be varied by the use of cross-linkable polyanhydrides. Polymers based on dimethacrylated anhydride have been synthesized (118), and the mechanical properties of these polymers can potentially be tuned based on monomer-cross-linker ratios and the choice of monomers and cross-linkers (80). Specifically, such cross-linked anhydrides have been shown to posses compressive strengths of 30-40 MPa and tensile strengths of 15-27 MPa (119).

C5.3.2. Applications

Like POEs, PAHs have traditionally been used for the localized delivery of drugs and therapeutics in RM applications (120). Poly carboxy phenoxy propane sebacic acid (PCPP-SA), a type of PAH, has been shown to be biocompatible (121) and has also been approved by the FDA for the delivery of a therapeutic for treating brain cancer (glioblastoma) under the commercial name Gliadel. This system has been used for the delivery of the drug carmustine (BCNU) to residual tumor cells after surgical removal of the tumor (122). Studies of delivery in a monkey brain model revealed a local reaction at the site of implantation, including subacute inflammation and local edema; however, no negative effects were observed after 72 days (123). In another study with a rat malignant glioma model, paclitaxel delivery from a PAH-based delivery system was found to significantly increase the survival rates of rats compared to controls (124). PAH-based systems have also been used for the delivery of carboplatin (125) and methotrexate (122), and have been shown to increase median survival times in rat glioma models. In addition, poly(fatty acid dimer-sebacic acid) has been used for the delivery of cisplatin to treat human squamous cell carcinoma xenografts in an animal model (126). Apart from the delivery of drugs to treat cancer, a PAH-based system, under the commercial name Septacin, has been used for the delivery of antibiotics to treat osteomyelitis, for the delivery of local anesthetics (120), for the delivery of heparin to prevent restenosis in an animal model (127) and for the delivery of 5-FU in prolonging the success of glaucoma filtering surgery in a rabbit model (128).

C5.4. Polyphosphazenes (PNE)

C5.4.1. Properties

PNEs are high molecular-weight linear polymers that possess alternating nitrogen and phosphorous in their backbone (129). Most PNEs are soluble in commonly used organic solvents, which allows for easy processing (97). The properties of PNEs can vary very widely depending on the nature of their organic side chains. For example, the use of glycine side groups results in PNEs with a T_g value of -40 °C, while phenylalanine results in a T_g value of 41.6 °C (130), consistent with the hypothesis that a bulkier side-chain results in a higher T_g value. The mechanical properties and crystallinity of these polymers can be varied based on the nature of the side groups as well. While methoxy and ethoxy side groups result in thermoplastics, fluoroalkoxy and chloroalkoxy side chains result in the formation of elastomers (129). Elastomeric PNEs possessing T_g values as low as -60 °C have been manufactured and used in a wide variety of applications. By appropriate choice of side groups, PNE-based hydrogels with pH- and temperature-dependent properties have been synthesized (131, 132). Side groups such as amines and imidazoles can confer hydrolytic instability, making these polymers degrade more quickly. In contrast, the substitution of hydrophobic side groups has the opposite effect on degradation rates. In fact, the degradation of PNEs can be tuned from weeks to months depending on the molecular weight, nature of the side groups and degree of substitution (133, 134). Products of degradation include phosphate, ammonia and side groups, which are non-toxic (135). Finally, the pentavalent phosphorous atom in the polymer backbone facilitates drug complexation and delivery.

C5.4.2. Applications

PNEs have been used for the controlled delivery of drugs and therapeutics for a wide variety of applications (136). Initial studies revealed that these polymers could be used to release progesterone in Sprague-Dawley rats at a very sustained rate (137). PNE-based polymeric vehicles have also been used for the delivery of naproxen and the sustained therapeutic efficacy in a rat model of acute inflammation and chronic arthritis has been demonstrated (138). PNE-based microspheres prepared by a double-emulsion method were found to release insulin over a

sustained period of time and kept glucose levels low in a diabetic mouse model for over 1000 h (139). PNE membranes and microspheres have also been investigated as delivery vehicles in the treatment of periodontal diseases and in bone regeneration (140). The release of trimethoprim and succinlysulfathiazole was tested in a rat model and the results indicated that the PNE-membranes were able to release these drugs locally to surrounding gingival tissue over a period at least 110 h. The release of Naproxen, an anti-inflammatory drug, from PNE-based membranes and microspheres was also tested in the same model and the blood concentration levels of the drug were found to be therapeutically satisfactory. In the same study, significant bone healing was noted after one month in a rabbit tibial bone defect model, when the defects were implanted with PNE-based membranes. Moreover, no signs of inflammation were detected. Poly organo phosphazenes have also been used for the regeneration of neural tissue (141). Specifically, PNE-based nerve guides were found to promote the formation of tissue cable bridging a rat sciatic nerve defect, 45 days post-implantation.

C5.5. Polyphosphoesters (PPE)

C5.5.1. Properties

PPEs are nucleic acid/techoic acid analogs that possess phosphorous atoms in the backbone attached to an oxygen atom and a side group. Based on the nature of the side group, these polymers are further classified as polyphosphites, polyphosphonates and polyphosphates (97, 142). PPEs possess a hydrolytically degradable phosphoester backbone, resulting in the formation of phosphate, alcohols and diols upon degradation. Like PNEs, the degradation of PPEs can be tuned by changing the molecular weight, crystallinity, backbone chemistry, as well as the chemistry of the side groups. The presence of amino pendant groups has been shown to result in PPEs that can degrade within a period of days to weeks (143). PPEs can also undergo enzymatic degradation via the action of intracellular enzymes such as phosphodiesterase I (144). The side groups and the organic moieties within the backbone can be varied to also tune the mechanical properties of PPEs including the production of crystalline or amorphous solids, liquids and elastomers (142). Co-polymers of PPEs have been investigated widely for the production of polymers possessing an interesting and useful blend of properties. For example, blending PPE with PDLA to result in poly (lactide-co-ethyl phosphate) has been shown to alter

T_g, degradation rates and degradation mechanism of the co-polymer based on the relative amounts of the monomers (145). The synthesis of photo-polymerizable hydrogels based on phosphoester-poly ethylene glycol co-polymers has been investigated for alkaline phosphatase-mediated degradation (146). More recently, the production of thermosensitive PPEs has been reported. In particular, block co-polymers based on PEG and PPE or PCL and PPE have been shown to confer thermosensitive properties such as tunable lower critical solution temperatures (LCST) (147, 148). The LCST values depend on the molecular weights of the blocks, their hydrophobicity and ratios of the blocks.

C5.5.2. Applications

PPEs have been used for a variety of applications including controlled delivery of drugs as well as in tissue engineering due to their biocompatible nature and degradation properties (142). Co-polymers of PLA and PPE have been used a drug delivery system under the name PACLIMER (149). Specifically, the release of paclitaxel from the polymeric system was found to reduce tumor volume as well as significantly increase in tumor doubling time as compared to intra-tumoral administration of paclitaxel in nude mice possessing human NSCLC cell lines. The release of paclitaxel from PACLIMER microspheres, when injected intra-peritoneally into dogs, was found to reach a much lower peak plasma concentration as compared to bolus injections of paclitaxel (142). The microspheres also helped maintain therapeutic levels of paclitaxel in the plasma over extended periods of time. In a similar manner, PACLIMER microspheres were found to be more active against OVCAR-3, a relevant animal model for ovarian cancer, compared to Taxol injections. Finally, a phase I clinical trial involving PACLIMER microspheres to treat ovarian cancer, demonstrated that the PACLIMER system was able to maintain therapeutic levels of paclitaxel (below toxic threshold levels) in the plasma over a two month period (150). PPE-based systems also have been used for the regeneration of neural tissues. In a study by Wang et al., two PPE-based nerve conduits were found to result in the formation of a thin fibrous capsule upon implantation in the sciatic nerve of rats (151). Although tube breakage was observed five days post-implantation, regeneration of a gap defect in the rat sciatic nerve model was observed. Moreover, the conduits demonstrated negligible swelling and no crystallization upon implantation

C6. Hydrogels

Hydrogels differ from other degradable polymeric biomaterials in their hydrophilicity and capacity to absorb many times their weight in water. Consequently, most hydrogel materials are chemically cross-linked to prevent their dissolution in aqueous environments. Although several hydrogel materials have been tested for RM applications, the following polymers have been extensively used clinically. **Table C2** provides a list of these hydrogels, along with their applications.

Hydrogel	Applications	References
Polyacrylamide	• Tissue bulking procedures • Subcutaneous injections for aesthetic purposes • Muscle regeneration	(153, 154, 156, 160, 161)
Poly(2-hydroxyethyl methacrylate)	• Opthalmic applications: corneal prosthesis • Controlled release of proteins • Cardiac tissue regeneration • Axonal regeneration in spinal cord injury • Replacement of intervertebral discs	(163, 165, 167, 169, 171, 172)
Polyvinyl alcohol	• Surgical sponges • Wound dressings • Hyaline cartilage reconstructions • Meniscal implant • Injectable intravascular emboli	(175, 185-189)
Polyethyelene glycol	• Antimicrobial/ low-fouling coatings • Wound dressings • Osmotic laxatives • Reducing the formation of fibrin bands between adjacent tissues	(191, 195-199)

Table C2: Hydrogels used in RM applications.

C6.1. Polyacrylamide (PAAM)

C6.1.1. Properties

PAAM forms soft, cationic non-degradable hydrogels consisting of entangled polymer chains tethered to one another via cross-linkers (152). Its hydrophilic nature results in a high

capacity for swelling and tendency for cell (bacterial and mammalian) adhesion and migration, granuloma formation, and fibrosis *in vivo* (153-155). The extent of swelling is inversely related to the extent of cross-linking. However, lightly cross-linked PAAM gels – composed of up to 99% water by weight – still maintain their physical, chemical, and mechanical stability (156). Alterations in the physical properties of PAAM have been achieved primarily by varying the degree of cross-linking and by co-polymerization with other monomers: these modifications change hydrogel swelling capacity and stiffness respectively (155). Specifically, copolymerization – with synthetic or biologic monomers – allows the modulation of material properties, including stiffness, charge, and the densities of amide and ester side groups for surface modification (155, 157). Although PAAM is a versatile hydrogel, it requires purification prior to clinical use, as acrylamide monomers *in vivo* degrade to glycidamide, a genotoxic compound (158, 159).

C6.1.2. Applications

Popular surgical applications of PAAM hydrogels include tissue bulking procedures and subcutaneous injections for aesthetic purposes (153, 160, 161). As a bulking agent, Bulkamid® has been injected into urethral submucosa for the creation of artificial urethral cushions to treat stress urinary incontinence (or mixed urinary incontinence) (160). Furthermore, Aquamid® is an alternative to silicone oil for soft tissue augmentation (e.g., face, breasts) with few reports of severe adverse reactions (154, 161). Additionally, the cationic nature of PAAM allows it to deform under electric fields, allowing its potential use in muscle regeneration (156). However, PAAM has not been approved for use in the US, despite its use in plastic surgery in Europe and Asia for over 10 years. At present Aquamid® and Bulkamid® are undergoing FDA clinical trial and premarket approval, respectively.

C6.2. Poly(2-hydroxyethyl methacrylate) (pHEMA)

C6.2.1. Properties

pHEMA is an inert, water-stable, non-degradable hydrogel (162) with high transparency. The physical properties of pHEMA (e.g., swelling, stiffness, rheology) can be tuned by varying crosslinking density, incorporating different chemistries through copolymerization, and

introducing mesoscopic pores. Specifically, a reduction in crosslinking density results in a softer, more malleable hydrogel (163) that may be better suited for soft tissue regeneration. Moreover, copolymerization with acetic acid, methyl methacrylate, or dextran can adjust the permanence, hydrophilicity and cellular adhesion *in vivo* (164-166). Finally, the introduction of mesoscopic porogens can facilitate vascular in-growth, improve cellular attachment, and overcome limited permeability (167, 168). Although pHEMA is considered non-degradable (which makes it ideally suited for long-term applications *in vivo*), degradable pHEMA copolymers have been fabricated by the integration of enzymatically-susceptible monomers (e.g., dextran) or cross-linking agents (165). These degradable materials show promise for controlled release of pharmaceuticals and proteins (165, 169, 170).

C6.2.2. Applications

Due to its excellent optical properties, pHEMA has primarily been used in ophthalmic applications (163) under the generic names etafilcon A and vifilcon A. In addition, it has been examined for controlled release of proteins and drugs (165, 171), engineering of cardiac tissue (167), axonal regeneration in spinal cord injury (169), and replacement of intervertebral discs (172). However, two limitations of pHEMA are its propensity for calcification and the toxicity of the 2-hydroxyethyl methacrylate monomers. Phase I testing of pHEMA for corneal prostheses (keratoprosthesis) revealed calcium salt deposition within 2.5 years after implantation (162, 164). At the same time, residual HEMA monomer can compromise the mechanical properties of the hydrogel, and leach into surrounding tissue with toxic effects (173, 174).

C6.3. Polyvinyl alcohol (PVA)

C6.3.1. Properties

PVA is a biodegradable, biocompatible and protein-resistant polymer that gels spontaneously in aqueous media. Improved stability has been achieved by freeze-thawing (175, 176) and covalent cross-linking (e.g., glutaraldehyde (177), gamma irradiation (162, 175, 178)). Both physically and chemically cross-linked PVA can be processed into a wide range of forms including solutions, pellets, sheets, sponges, foams, coatings, meshes, and microspheres (176, 179). The degradation rate of PVA hydrogels can be controlled by varying polymer molecular

weight, polymer concentration, and the combination of physical and chemical cross-links (179). By copolymerization and blending with natural and synthetic polymers, PVA has been used to create a vast array of hydrogels with diverse characteristics (180-184). These blends allow for a greater diversity of behaviors and applications than PVA alone.

C6.3.2. Applications

PVA's resistance to cell adhesion and protein absorption prevents bacterial infection, granuloma formation, and post-operative adhesions. Therefore, PVA-based hydrogels have been extensively used in a wide variety of RM applications. Such FDA-approved applications include contact lenses (185), eye wetting drops, surgical sponges, wound dressings (186), catheter coatings, barrier films and injectable intravascular emboli. Cartiva™ (not FDA-approved as on date) is a PVA-based implant to replace degraded hyaline cartilage in osteoarthritis. Additionally, research is under way to develop a PVA meniscal implant (187-189).

C6.4. Polyethylene glycol (PEG)

C6.4.1. Properties

Cross-linked PEG materials are widely considered biocompatible and biodegradable, suitable to be used in a vast array of medical applications (162). PEG hydrogels biodegrade *in situ* via hydrolysis and low molecular weight PEG oligomers excreted in the urine. Due to the scarcity of side chains and overall hydrophilicity, PEG hydrogels are considered to be "stealth materials". Specifically, they are surrounded by an impenetrable water layer *in vivo* that permits diffusion, but prevents protein adsorption and cell adhesion (190). This property reduces both the formation of biofilms on PEG-coated devices and the metabolism/degradation of PEG-encapsulated drug particles *in vivo* (191, 192). When taken orally, PEG is toxic only at high doses (193), and very limited immunological reaction to indwelling PEG devices has been reported (194).

C6.4.2. Applications

Currently, PEG is employed in several applications, including osmotic laxatives (e.g., MiraLAX®, GoLYTELY®) (195), as antimicrobial coatings/low-fouling coatings on medical

devices (191), and as surgical sealants, adhesion barriers, and wound dressings. PEG-based liquid sealants (e.g., ProGEL™, CoSeal™, and DuraSeal™) have shown positive results as adjuncts to tissue closure for pulmonary, vascular, and neurological surgeries. Moreover, PEG's use as an adhesion barrier in cardiothoracic (e.g., REPEL-CV®), abdominal, and gynecologic surgery has demonstrated reduced formation of fibrin bands between adjacent tissues (196-198). Lastly, PEG hydrogels are well suited as wound dressings as they provide a moist environment and a barrier to bacterial infiltration. Amerigel® Hydrogel Saturated Gauze, which contains a PEG400/3350 mix and proprietary oak-extract compound (Oakin®; an antimicrobial agent) imbedded in a blended polyester-rayon gauze is an FDA-approved product for wound dressings. The PEG-Oakin® mix is highly absorbent, pliable, and inexpensive compared to equally-efficacious silver-impregnated dressings (199).

C7. Summary and future directions

Past generations of biomaterials typically arose from industrial materials and were predominantly used to perform mechanical functions as medical implants. Such devices have been enormously relevant to reconstructive surgery, but not necessarily transplant surgery because the level of sophistication of these devices was not physiologic in nature. More recently, as the technology of biomaterials has evolved, new "smart" materials have appeared, taking on a higher level of sophistication by indirectly or directly performing organ-like function. Innovations that now allow greater cell interaction, and even control over cell behavior, have taken inspiration from nature and in the case of regenerative medicine, developmental biology. New biomaterials are in advanced stages of preclinical development that can support, facilitate, and even direct cell adhesion, migration, assembly, and growth. Technologies that mimic organoid function such as pancreas, liver and kidney are being developed through tissue engineering approaches. Cell delivery using novel biomaterial carriers to augment organ function and rescue diseased organs is beginning to enter clinical trials and small trials of tissue-engineered organs are becoming less sporadic events. These technologies, envisioned decades ago and only now starting to come to fruition are on the horizon of transplant surgery and have great potential to provide the next generation of treatment modalities.

References

1. Roach P, Eglin D, Rohde K, Perry CC. Modern biomaterials: a review-bulk properties and implications of surface modifications. Journal of Materials Science-Materials in Medicine. 2007 Jul;18(7):1263-77.
2. Lloyd AW, Faragher RGA, Denyer SP. Ocular biomaterials and implants. Biomaterials. 2001 Apr;22(8):769-85.
3. Williams DF. On the mechanisms of biocompatibility. Biomaterials. 2008 Jul;29(20):2941-53.
4. Consensus conference on biocompatibility. Nephrol Dial Transplant. [Consensus Development Conference]. 1994;9 Suppl 2:1-186.
5. Black J. Biological performance of materials : fundamentals of biocompatibility. 4th ed. ed. Boca Raton ; London: CRC Taylor & Francis; 2006.
6. Kohane DS, Langer R. Polymeric biomaterials in tissue engineering. Pediatric Research. 2008 May;63(5):487-91.
7. Hutmacher DW. Scaffolds in tissue engineering bone and cartilage. Biomaterials. 2000 Dec;21(24):2529-43.
8. Spiller KL, Maher SA, Lowman AM. Hydrogels for the Repair of Articular Cartilage Defects. Tissue Engineering Part B-Reviews. 2011 Aug;17(4):281-99.
9. Atala A. Tissue engineering of human bladder. British Medical Bulletin. 2011 Mar;97(1):81-104.
10. Dhandayuthapani B, Yoshida Y, Maekawa T, Kumar DS. Polymeric Scaffolds in Tissue Engineering Application: A Review. International Journal of Polymer Science. 2011.
11. Griffith LG. Emerging design principles in Biomaterials and scaffolds for tissue engineering. Reparative Medicine: Growing Tissues and Organs. 2002;961:83-95.
12. Guilak F. Homing in on a biological joint replacement. Stem Cell Research & Therapy. 2010 Dec 14;1.
13. Shin H, Jo S, Mikos AG. Biomimetic materials for tissue engineering. Biomaterials. 2003 Nov;24(24):4353-64.
14. Kingshott P, Griesser HJ. Surfaces that resist bioadhesion. Curr Opin Solid St M. 1999 Aug;4(4):403-12.
15. Ripamonti U, Roden LC, Renton LF. Osteoinductive hydroxyapatite-coated titanium implants. Biomaterials. 2012 May;33(15):3813-23.
16. Navarro M, Michiardi A, Castano O, Planell JA. Biomaterials in orthopaedics. Journal of the Royal Society Interface. 2008 Oct 6;5(27):1137-58.
17. Disegi JA, Eschbach L. Stainless steel in bone surgery. Injury-International Journal of the Care of the Injured. 2000 Dec;31:S2-S6.
18. Niinomi M. Metallic biomaterials. Journal of Artificial Organs. 2008 Sep;11(3):105-10.
19. Uggowitzer PJ, Bahre WF, Wohlfromm H, Speidel MO. Nickel-free high nitrogen austenitic stainless steels produced by metal injection moulding. High Nitrogen Steels '98. 1999;318-3:663-71.
20. Case CP, Langkamer VG, James C, Palmer MR, Kemp AJ, Heap PF, Solomon L. Widespread Dissemination of Metal Debris from Implants. J Bone Joint Surg Br. 1994 Sep;76B(5):701-12.
21. Teoh SH. Fatigue of biomaterials: a review. International Journal of Fatigue. 2000 Nov;22(10):825-37.

22. Bauer TW, Schils J. The pathology of total joint arthroplasty - II. Mechanisms of implant failure. Skeletal Radiology. 1999 Sep;28(9):483-97.
23. Gotman I. Characteristics of metals used in implants. Journal of Endourology. 1997 Dec;11(6):383-9.
24. Okazaki Y, Gotoh E. Comparison of metal release from various metallic biomaterials in vitro. Biomaterials. 2005 Jan;26(1):11-21.
25. Geetha M, Singh AK, Asokamani R, Gogia AK. Ti based biomaterials, the ultimate choice for orthopaedic implants - A review. Progress in Materials Science. 2009 May;54(3):397-425.
26. Bansiddhi A, Sargeant TD, Stupp SI, Dunand DC. Porous NiTi for bone implants: A review. Acta Biomater. 2008 Jul;4(4):773-82.
27. Vallet-Regí M, Ruiz-Hernández E. Bioceramics: from bone regeneration to cancer nanomedicine. Advanced Materials (Deerfield Beach, Fla). 2011;23(44):5177-218.
28. LeGeros RZ. Calcium phosphate-based osteoinductive materials. Chemical reviews. 2008;108(11):4742-53.
29. Vallet-Regí M, González-Calbet JM. Calcium phosphates as substitution of bone tissues. Progress in Solid State Chemistry. 2004;32(1):1-31.
30. Jimbo R, Coelho PG, Vandeweghe S, Schwartz-Filho HO, Hayashi M, Ono D, Andersson M, Wennerberg A. Histological and three-dimensional evaluation of osseointegration to nanostructured calcium phosphate-coated implants. Acta Biomater. 2011;7(12):4229-34.
31. Narayanan R, Seshadri SK, Kwon TY, Kim KH. Calcium phosphate-based coatings on titanium and its alloys. Journal of biomedical materials research Part B, Applied biomaterials. 2008;85(1):279-99.
32. De Long WG, Jr., Einhorn TA, Koval K, McKee M, Smith W, Sanders R, Watson T. Bone Grafts and Bone Graft Substitutes in Orthopaedic Trauma Surgery. A Critical Analysis. Journal of Bone and Joint Surgery. 2007;89(3):649-58.
33. Hench LL. The story of Bioglass. Journal of Materials Science: Materials in Medicine. 2006;17(11):967-78.
34. Bahmad JF, Merchant SN. Histopathology of ossicular grafts and implants in chronic otitis media. The Annals of otology, rhinology, and laryngology. 2007;116(3):181-91.
35. Li R, Clark AE, Hench LL. An investigation of bioactive glass powders by sol-gel processing. Journal of Applied Biomaterials. 1991;2(4):231-9.
36. Nandi SK, Kundu B, Datta S, De DK, Basu D. The repair of segmental bone defects with porous bioglass: An experimental study in goat. Research in Veterinary Science. 2009;86(1):162-73.
37. Cacciotti I, Lombardi M, Bianco A, Ravaglioli A, Montanaro L. Sol–gel derived 45S5 bioglass: synthesis, microstructural evolution and thermal behaviour. Journal of Materials Science: Materials in Medicine. 2012;23(8):1849-66.
38. Chen Q-Z, Thouas GA. Fabrication and characterization of sol-gel derived 45S5 Bioglass®-ceramic scaffolds. Acta Biomater. 2011;7(10):3616-26.
39. Chen QZ, Thompson ID, Boccaccini AR. 45S5 Bioglass-derived glass-ceramic scaffolds for bone tissue engineering. Biomaterials. 2006;27(11):2414-25.
40. Jeffers JRT, Walter WL. Ceramic-on-ceramic bearings in hip arthroplasty: state of the art and the future. The Journal of Bone and Joint Surgery British volume. 2012;94(6):735-45.

41. Hannouche D, Zaoui A, Zadegan F, Sedel L, Nizard R. Thirty years of experience with alumina-on-alumina bearings in total hip arthroplasty. International Orthopaedics. 2011;35(2):207-13.
42. Garcia-Rey E, Cruz-Pardos A, Garcia-Cimbrelo E. Alumina-on-alumina total hip arthroplasty in young patients: diagnosis is more important than age. Clinical Orthopaedics and Related Research. 2009;467(9):2281-9.
43. Bizot P, Larrouy M, Witvoet J, Sedel L, Nizard R. Press-fit metal-backed alumina sockets: a minimum 5-year followup study. Clinical orthopaedics and related research. 2000(379):134-42.
44. Jaeblon T. Polymethylmethacrylate: Properties and Contemporary Uses in Orthopaedics. Journal of the American Academy of Orthopaedic Surgeons. 2010 May;18(5):297-305.
45. Kuehn KD, Ege W, Gopp U. Acrylic bone cements: composition and properties. Orthopedic Clinics of North America. 2005 Jan;36(1):17-28.
46. Webb JCJ, Spencer RF. The role of polymethylmethacrylate bone cement in modern orthopaedic surgery. J Bone Joint Surg Br. 2007 Jul;89B(7):851-7.
47. Chehade M, Elder MJ. Intraocular lens materials and styles: A review. Australian and New Zealand Journal of Ophthalmology. 1997 Nov;25(4):255-63.
48. Frazer RQ, Byron RT, Osborne PB, West KP. PMMA: an essential material in medicine and dentistry. J Long Term Eff Med Implants. [Comparative Study Review]. 2005;15(6):629-39.
49. Provenzano MJ, Murphy KPJ, Riley LH. Bone cements: Review of their physiochemical and biochemical properties in percutaneous vertebroplasty. Am J Neuroradiol. 2004 Aug;25(7):1286-90.
50. Hoffmann F, Kruse H, Schuler A. Mechanical Methods in Refractive Corneal Surgery. Curr Opin Ophthalmol. 1993 Aug;4(4):84-90.
51. Nose W, Neves RA, Schanzlin DJ, Belfort Junior R. Intrastromal corneal ring--one-year results of first implants in humans: a preliminary nonfunctional eye study. Refract Corneal Surg. 1993 Nov-Dec;9(6):452-8.
52. Puskas JE, Chen Y. Biomedical application of commercial polymers and novel polyisobutylene-based thermoplastic elastomers for soft tissue replacement. Biomacromolecules. 2004 Jul-Aug;5(4):1141-54.
53. Arefazar A, Biddlestone F, Hay JN, Haward RN. The Effect of Physical Aging on the Properties of Poly(Ethylene-Terephthalate). Polymer. 1983;24(10):1245-51.
54. Polyakova A, Liu RYF, Schiraldi DA, Hiltner A, Baer E. Oxygen-barrier properties of copolymers based on ethylene terephthalate. J Polym Sci Pol Phys. 2001 Aug 15;39(16):1889-99.
55. el-Massry S, Saad E, Sauvage LR, Zammit M, Davis CC, Smith JC, Rittenhouse EA, Fisher LD. Axillofemoral bypass with externally supported, knitted Dacron grafts: a follow-up through twelve years. J Vasc Surg. [Comparative Study]. 1993 Jan;17(1):107-14; discussion 14-5.
56. Fanous N, Samaha M, Yoskovitch A. Dacron implants in rhinoplasty: a review of 136 cases of tip and dorsum implants. Arch Facial Plast Surg. 2002 Jul-Sep;4(3):149-56.
57. Barrett GR, Line LL, Shelton WR, Manning JO, Phelps R. The Dacron Ligament Prosthesis in Anterior Cruciate Ligament Reconstruction - a 4-Year Review. Am J Sport Med. 1993 May-Jun;21(3):367-73.
58. Nunn DB, Freeman MH, Hudgins PC. Postoperative alterations in size of Dacron aortic grafts: an ultrasonic evaluation. Ann Surg. 1979 Jun;189(6):741-5.

59. Borazjani BH, Wilson SE, Fujitani RM, Gordon I, Mueller M, Williams RA. Postoperative complications of carotid patching: pseudoaneurysm and infection. Ann Vasc Surg. [Case Reports Review]. 2003 Mar;17(2):156-61.
60. Massell TB, Heringman EC, Greenstone SM. Woven Dacron and woven Teflon prostheses. Use for small artery replacement. Arch Surg. 1962 Jan;84:73-9.
61. Roolker W, Patt TW, van Dijk CN, Vegter M, Marti RK. The Gore-Tex prosthetic ligament as a salvage procedure in deficient knees. Knee Surg Sport Tr A. 2000 Jan;8(1):20-5.
62. Grethel EJ, Cortes RA, Wagner AJ, Clifton MS, Lee H, Farmer DL, Harrison MR, Keller RL, Nobuhara KK. Prosthetic patches for congenital diaphragmatic hernia repair: Surgisis vs Gore-Tex. J Pediatr Surg. 2006 Jan;41(1):29-32.
63. Nakayama M, Ford CN, Bless DM. Teflon vocal fold augmentation: failures and management in 28 cases. Otolaryngol Head Neck Surg. 1993 Sep;109(3 Pt 1):493-8.
64. O'Donnell B, Puri P. Treatment of vesicoureteric reflux by endoscopic injection of Teflon. Br Med J (Clin Res Ed). 1984 Jul 7;289(6436):7-9.
65. Bhatti HA, Khattak H, Boston VE. Efficacy and causes of failure of endoscopic subureteric injection of Teflon in the treatment of primary vesicoureteric reflux. Br J Urol. 1993 Feb;71(2):221-5.
66. Narins RS, Beer K. Liquid injectable silicone: A review of its history, immunology, technical considerations, complications, and potential. Plastic and reconstructive surgery. 2006 Sep 1;118(3):77S-84S.
67. Lamba NMK, Woodhouse KA, Cooper SL, Lelah MDPim. Polyurethanes in biomedical applications. Boca Raton ; London: CRC; 1998.
68. Kanyanta V, Ivankovic A. Mechanical characterisation of polyurethane elastomer for biomedical applications. J Mech Behav Biomed Mater. 2010 Jan;3(1):51-62.
69. Guelcher SA, Gallagher KM, Didier JE, Klinedinst DB, Doctor JS, Goldstein AS, Wilkes GL, Beckman EJ, Hollinger JO. Synthesis of biocompatible segmented polyurethanes from aliphatic diisocyanates and diurea diol chain extenders. Acta Biomater. 2005 Jul;1(4):471-84.
70. Spaans CJ, De Groot JH, Belgraver VW, Pennings AJ. A new biomedical polyurethane with a high modulus based on 1,4-butanediisocyanate and epsilon-caprolactone. J Mater Sci Mater Med. 1998 Dec;9(12):675-8.
71. Burke A, Hasirci N. Polyurethanes in biomedical applications. Adv Exp Med Biol. 2004;553:83-101.
72. Zdrahala RJ, Zdrahala IJ. Biomedical applications of polyurethanes: a review of past promises, present realities, and a vibrant future. J Biomater Appl. [Review]. 1999 Jul;14(1):67-90.
73. Sodergard A, Stolt M. Properties of lactic acid based polymers and their correlation with composition. Progress in Polymer Science. 2002 Aug;27(6):1123-63.
74. Jamshidi K, Hyon SH, Ikada Y. Thermal Characterization of Polylactides. Polymer. 1988 Dec;29(12):2229-34.
75. Migliaresi C, Cohn D, Delollis A, Fambri L. Dynamic Mechanical and Calorimetric Analysis of Compression-Molded Plla of Different Molecular-Weights - Effect of Thermal Treatments. Journal of Applied Polymer Science. 1991 Jul 5;43(1):83-95.
76. Middleton JC, Tipton AJ. Synthetic biodegradable polymers as orthopedic devices. Biomaterials. 2000 Dec;21(23):2335-46.
77. Engelberg I, Kohn J. Physicomechanical Properties of Degradable Polymers Used in Medical Applications - a Comparative-Study. Biomaterials. 1991 Apr;12(3):292-304.

78. Li SM, Garreau H, Vert M. Structure Property Relationships in the Case of the Degradation of Massive Aliphatic Poly-(Alpha-Hydroxy Acids) in Aqueous-Media .1. Poly(Dl-Lactic Acid). Journal of Materials Science-Materials in Medicine. 1990 Oct;1(3):123-30.
79. Singh V, Tiwari M. Structure-Processing-Property Relationship of Poly(Glycolic Acid) for Drug Delivery Systems 1: Synthesis and Catalysis. International Journal of Polymer Science. 2010.
80. Gunatillake PA, Adhikari R. Biodegradable synthetic polymers for tissue engineering. European cells & materials. [Review]. 2003 May 20;5:1-16.
81. Bostman O, Partio E, Hirvensalo E, Rokkanen P. Foreign-Body Reactions to Polyglycolide Screws - Observations in 24/216 Malleolar Fracture Cases. Acta Orthopaedica Scandinavica. 1992 Apr;63(2):173-6.
82. Bostman O, Paivarinta U, Partio E, Vasenius J, Manninen M, Rokkanen P. Degradation and Tissue Replacement of an Absorbable Polyglycolide Screw in the Fixation of Rabbit Femoral Osteotomies. Journal of Bone and Joint Surgery-American Volume. 1992 Aug;74A(7):1021-31.
83. Griffith LG. Polymeric biomaterials. Acta Materialia. 2000 Jan 1;48(1):263-77.
84. Miller RA, Brady JM, Cutright DE. Degradation Rates of Oral Resorbable Implants (Polylactates and Polyglycolates) - Rate Modification with Changes in Pla-Pga Copolymer Ratios. J Biomed Mater Res. 1977;11(5):711-9.
85. Gilding DK, Reed AM. Biodegradable Polymers for Use in Surgery - Polyglycolic-Poly(Actic Acid) Homopolymers and Copolymers .1. Polymer. 1979;20(12):1459-64.
86. Park TG. Degradation of Poly(Lactic-Co-Glycolic Acid) Microspheres - Effect of Copolymer Composition. Biomaterials. 1995 Oct;16(15):1123-30.
87. Lu L, Peter SJ, Lyman MD, Lai HL, Leite SM, Tamada JA, Uyama S, Vacanti JP, Langer R, Mikos AG. In vitro and in vivo degradation of porous poly(DL-lactic-co-glycolic acid) foams. Biomaterials. 2000 Sep;21(18):1837-45.
88. Wu XS, Wang N. Synthesis, characterization, biodegradation, and drug delivery application of biodegradable lactic/glycolic acid polymers. Part II: Biodegradation. J Biomat Sci-Polym E. 2001;12(1):21-34.
89. Van de Velde K, Kiekens P. Biopolymers: overview of several properties and consequences on their applications. Polymer Testing. 2002 Jun;21(4):433-42.
90. Ikada Y, Tsuji H. Biodegradable polyesters for medical and ecological applications. Macromolecular Rapid Communications. 2000 Feb;21(3):117-32.
91. Sinha VR, Bansal K, Kaushik R, Kumria R, Trehan A. Poly-epsilon-caprolactone microspheres and nanospheres: an overview. Int J Pharm. 2004 Jun 18;278(1):1-23.
92. Woodruff MA, Hutmacher DW. The return of a forgotten polymer-Polycaprolactone in the 21st century. Progress in Polymer Science. 2010 Oct;35(10):1217-56.
93. Li SM, Chen XH, Gross RA, McCarthy SP. Hydrolytic degradation of PCL/PEO copolymers in alkaline media. Journal of Materials Science-Materials in Medicine. 2000 Apr;11(4):227-33.
94. Fisher JP, Holland TA, Dean D, Mikos AG. Photoinitiated cross-linking of the biodegradable polyester poly(propylene fumarate). Part II. In vitro degradation. Biomacromolecules. 2003 Sep-Oct;4(5):1335-42.
95. Peter SJ, Miller ST, Zhu GM, Yasko AW, Mikos AG. In vivo degradation of a poly(propylene fumarate) beta-tricalcium phosphate injectable composite scaffold. J Biomed Mater Res. 1998 Jul;41(1):1-7.

96. Peter SJ, Kim P, Yasko AW, Yaszemski MJ, Mikos AG. Crosslinking characteristics of an injectable poly(propylene fumarate)/beta-tricalcium phosphate paste and mechanical properties of the crosslinked composite for use as a biodegradable bone cement. J Biomed Mater Res. 1999 Mar 5;44(3):314-21.
97. Nair LS, Laurencin CT. Polymers as biomaterials for tissue engineering and controlled drug delivery. Tissue Engineering I: Scaffold Systems for Tissue Engineering. 2006;102:47-90.
98. Ueda H, Tabata Y. Polyhydroxyalkanonate derivatives in current clinical applications and trials. Adv Drug Deliver Rev. 2003 Apr 25;55(4):501-18.
99. Heller J. Poly (Ortho Esters). Advances in Polymer Science. 1993;107:41-92.
100. Heller J, Barr J, Ng SY, Abdellauoi KS, Gurny R. Poly(ortho esters): synthesis, characterization, properties and uses. Adv Drug Deliver Rev. 2002 Oct 16;54(7):1015-39.
101. Vistnes LM, Schmitt EE, Ksander GA, Rose EH, Balkenhol WJ, Coleman CL. Evaluation of a prototype therapeutic system for prolonged, continuous topical delivery of homosulfanilamide in the management of Pseudomonas burn wound sepsis. Surgery. 1976 Jun;79(6):690-6.
102. Benagiano G, Schmitt E, Wise D, Goodman M. Sustained-Release Hormonal Preparations for the Delivery of Fertility-Regulating Agents. Journal of Polymer Science Part C-Polymer Symposium. 1979(66):129-48.
103. Solheim E, Pinholt EM, Andersen R, Bang G, Sudmann E. The Effect of a Composite of Polyorthoester and Demineralized Bone on the Healing of Large Segmental Defects of the Radius in Rats. Journal of Bone and Joint Surgery-American Volume. 1992 Dec;74A(10):1456-63.
104. Heller J, Barr J. Poly(ortho esters) - From concept to reality. Biomacromolecules. 2004 Sep-Oct;5(5):1625-32.
105. Schwach-Abdellaoui K, Heller J, Gurny R. Hydrolysis and erosion studies of autocatalyzed poly(ortho esters) containing lactoyl-lactyl acid dimers. Macromolecules. 1999 Jan 26;32(2):301-7.
106. Ng SY, Shen HR, Lopez E, Zherebin Y, Barr J, Schacht E, Heller J. Development of a poly(ortho ester) prototype with a latent acid in the polymer backbone for 5-fluorouracil delivery. J Control Release. 2000 Apr 3;65(3):367-74.
107. Heller J. Ocular delivery using poly(ortho esters). Adv Drug Deliver Rev. 2005 Dec 13;57(14):2053-62.
108. Bernatchez SF, Merkli A, Minh TL, Tabatabay C, Anderson JM, Gurny R. Biocompatibility of a New Semisolid Bioerodible Poly(Ortho Ester) Intended for the Ocular Delivery of 5-Fluorouracil. J Biomed Mater Res. 1994 Sep;28(9):1037-46.
109. Einmahl S, Ponsart S, Bejjani RA, D'Hermies F, Savoldelli M, Heller J, Tabatabay C, Gurny R, Behar-Cohen F. Ocular biocompatibility of a poly(ortho ester) characterized by autocatalyzed degradation. J Biomed Mater Res A. 2003 Oct 1;67A(1):44-53.
110. Heller J, Barr J, Ng SY, Shen HR, Schwach-Abdellaoui K, Gurny R, Vivien-Castioni N, Loup PJ, Baehni P, Mombelli A. Development and applications of injectable poly(ortho esters) for pain control and periodontal treatment. Biomaterials. 2002 Nov;23(22):4397-404.
111. Schwach-Abdellaoui K, Loup PJ, Vivien-Castioni N, Mombelli A, Baehni P, Barr J, Heller J, Gurny R. Bioerodible injectable poly(ortho ester) for tetracycline controlled delivery to periodontal pockets: Preliminary trial in humans. Aaps Pharmsci. 2002;4(4).
112. Kumar N, Langer RS, Domb AJ. Polyanhydrides: an overview. Adv Drug Deliver Rev. 2002 Oct 16;54(7):889-910.

113. Leong KW, Damore P, Marletta M, Langer R. Bioerodible Polyanhydrides as Drug-Carrier Matrices .2. Biocompatibility and Chemical-Reactivity. J Biomed Mater Res. 1986 Jan;20(1):51-64.
114. Jiang HL, Zhu KJ. Preparation, characterization and degradation characteristics of polyanhydrides containing poly(ethylene glycol). Polymer International. 1999 Jan;48(1):47-52.
115. Uhrich KE, Thomas TT, Laurencin CT, Langer R. In vitro degradation characteristics of poly(anhydride-imides) containing trimellitylimidoglycine. Journal of Applied Polymer Science. 1997 Mar 14;63(11):1401-11.
116. Muggli DS, Burkoth AK, Anseth KS. Crosslinked polyanhydrides for use in orthopedic applications: Degradation behavior and mechanics. J Biomed Mater Res. 1999 Aug;46(2):271-8.
117. Uhrich KE, Gupta A, Thomas TT, Laurencin CT, Langer R. Synthesis and Characterization of Degradable Poly(Anhydride-Co-Imides). Macromolecules. 1995 Mar 27;28(7):2184-93.
118. Muggli DS, Burkoth AK, Keyser SA, Lee HR, Anseth KS. Reaction behavior of biodegradable, photo-cross-linkable polyanhydrides. Macromolecules. 1998 Jun 30;31(13):4120-5.
119. Anseth KS, Svaldi DC, Laurencin CT, Langer R. Photopolymerization of novel degradable networks for orthopedic applications. Photopolymerization. 1997;673:189-202.
120. Jain JP, Modi S, Domb AJ, Kumar N. Role of polyanhydrides as localized drug carriers. J Control Release. 2005 Apr 18;103(3):541-63.
121. Laurencin C, Domb A, Morris C, Brown V, Chasin M, Mcconnell R, Lange N, Langer R. Poly(Anhydride) Administration in High-Doses Invivo - Studies of Biocompatibility and Toxicology. J Biomed Mater Res. 1990 Nov;24(11):1463-81.
122. Wang PP, Frazier J, Brem H. Local drug delivery to the brain. Adv Drug Deliver Rev. 2002 Oct 16;54(7):987-1013.
123. Brem H, Tamargo RJ, Olivi A, Pinn M, Weingart JD, Wharam M, Epstein JI. Biodegradable Polymers for Controlled Delivery of Chemotherapy with and without Radiation-Therapy in the Monkey Brain. J Neurosurg. 1994 Feb;80(2):283-90.
124. Walter KA, Cahan MA, Gur A, Tyler B, Hilton J, Colvin OM, Burger PC, Domb A, Brem H. Interstitial Taxol Delivered from a Biodegradable Polymer Implant against Experimental Malignant Glioma. Cancer Res. 1994 Apr 15;54(8):2207-12.
125. Olivi A, Ewend MG, Utsuki T, Tyler B, Domb AJ, Brat DJ, Brem H. Interstitial delivery of carboplatin via biodegradable polymers is effective against experimental glioma in the rat. Cancer Chemoth Pharm. 1996 Nov-Dec;39(1-2):90-6.
126. Shikani AH, Eisele DW, Domb AJ. Polymer Delivery of Chemotherapy for Squamous-Cell Carcinoma of the Head and Neck. Arch Otolaryngol. 1994 Nov;120(11):1242-7.
127. Orloff LA, Glenn MG, Domb AJ, Esclamado RA. Prevention of Venous Thrombosis in Microvascular Surgery by Transmural Release of Heparin from a Polyanhydride Polymer. Surgery. 1995 May;117(5):554-9.
128. Lee DA, Leong KW, Panek WC, Eng CT, Glasgow BJ. The Use of Bioerodible Polymers and 5-Fluorouracil in Glaucoma Filtration Surgery. Invest Ophth Vis Sci. 1988 Nov;29(11):1692-7.
129. Allcock HR. Polyphosphazene elastomers, gels, and other soft materials. Soft Matter. 2012;8(29):7521-32.

130. Deng M, Kumbar SG, Wan YQ, Toti US, Allcock HR, Laurencin CT. Polyphosphazene polymers for tissue engineering: an analysis of material synthesis, characterization and applications. Soft Matter. 2010;6(14):3119-32.
131. Allcock HR, Ambrosio AM. Synthesis and characterization of pH-sensitive poly(organophosphazene) hydrogels. Biomaterials. 1996 Dec;17(23):2295-302.
132. Allcock HR, Pucher SR, Turner ML, Fitzpatrick RJ. Poly(Organophosphazenes) with Poly(Alkyl Ether) Side Groups - a Study of Their Water Solubility and the Swelling Characteristics of Their Hydrogels. Macromolecules. 1992 Oct 12;25(21):5573-7.
133. Singh A, Krogman NR, Sethuraman S, Nair LS, Sturgeon JL, Brown PW, Laurencin CT, Allcock HR. Effect of side group chemistry on the properties of biodegradable L-alanine cosubstituted polyphosphazenes. Biomacromolecules. 2006 Mar;7(3):914-8.
134. Andrianov AK, Marin A. Degradation of polyaminophosphazenes: effects of hydrolytic environment and polymer processing. Biomacromolecules. 2006 May;7(5):1581-6.
135. Kumbar SG, Bhattacharyya S, Nukavarapu SP, Khan YM, Nair LS, Laurencin CT. In vitro and in vivo characterization of biodegradable poly(organophosphazenes) for biomedical applications. Journal of Inorganic and Organometallic Polymers and Materials. 2006 Dec;16(4):365-85.
136. Lakshmi S, Katti DS, Laurencin CT. Biodegradable polyphosphazenes for drug delivery applications. Adv Drug Deliver Rev. 2003 Apr 25;55(4):467-82.
137. Laurencin CT, Koh HJ, Neenan TX, Allcock HR, Langer R. Controlled Release Using a New Bioerodible Polyphosphazene Matrix System. J Biomed Mater Res. 1987 Oct;21(10):1231-46.
138. Conforti A, Bertani S, Lussignoli S, Grigolini L, Terzi M, Lora S, Caliceti P, Marsilio F, Veronese FM. Anti-inflammatory activity of polyphosphazene-based naproxen slow-release systems. J Pharm Pharmacol. 1996 May;48(5):468-73.
139. Caliceti P, Veronese FM, Lora S. Polyphosphazene microspheres for insulin delivery. Int J Pharm. 2000 Dec 15;211(1-2):57-65.
140. Veronese FM, Marsilio F, Lora S, Caliceti P, Passi P, Orsolini P. Polyphosphazene membranes and microspheres in periodontal diseases and implant surgery. Biomaterials. 1999 Jan;20(1):91-8.
141. Langone F, Lora S, Veronese FM, Caliceti P, Parnigotto PP, Valenti F, Palma G. Peripheral-Nerve Repair Using a Poly(Organo)Phosphazene Tubular Prosthesis. Biomaterials. 1995 Mar;16(5):347-53.
142. Zhao Z, Wang J, Mao HQ, Leong KW. Polyphosphoesters in drug and gene delivery. Adv Drug Deliver Rev. 2003 Apr 25;55(4):483-99.
143. Wang J, Mao HQ, Leong KW. A novel biodegradable gene carrier based on polyphosphoester. Journal of the American Chemical Society. 2001 Sep 26;123(38):9480-1.
144. Wang YC, Yuan YY, Du JZ, Yang XZ, Wang J. Recent progress in polyphosphoesters: from controlled synthesis to biomedical applications. Macromolecular bioscience. 2009 Dec 8;9(12):1154-64.
145. Chaubal MV, Su G, Spicer E, Dang WB, Branham KE, English JP, Zhao Z. In vitro and in vivo degradation studies of a novel linear copolymer of lactide and ethylphosphate. J Biomat Sci-Polym E. 2003;14(1):45-61.
146. Wang DA, Williams CG, Yang F, Cher N, Lee H, Elisseeff JH. Bioresponsive phosphoester hydrogels for bone tissue engineering. Tissue engineering. 2005 Jan;11(1-2):201-13.

147. Wang YC, Li Y, Yang XZ, Yuan YY, Yan LF, Wang J. Tunable Thermosensitivity of Biodegradable Polymer Micelles of Poly (epsilon-caprolactone) and Polyphosphoester Block Copolymers. Macromolecules. 2009 Apr 28;42(8):3026-32.
148. Wang YC, Tang LY, Li Y, Wang J. Thermoresponsive Block Copolymers of Poly(ethylene glycol) and Polyphosphoester: Thermo-Induced Self-Assembly, Biocompatibility, and Hydrolytic Degradation. Biomacromolecules. 2009 Jan;10(1):66-73.
149. Harper E, Dang WB, Lapidus RG, Garver RI. Enhanced efficacy of a novel controlled release paclitaxel formulation (PACLIMER Delivery System) for local-regional therapy of lung cancer tumor nodules in mice. Clin Cancer Res. 1999 Dec;5(12):4242-8.
150. Armstrong DK, Fleming GF, Markman M, Bailey HH. A phase I trial of intraperitoneal sustained-release paclitaxel microspheres (Paclimer((R))) in recurrent ovarian cancer: A Gynecologic Oncology Group study. Gynecol Oncol. 2006 Nov;103(2):391-6.
151. Wang S, Wan ACA, Xu XY, Gao SJ, Mao HQ, Leong KW, Yu H. A new nerve guide conduit material composed of a biodegradable poly(phosphoester). Biomaterials. 2001 May;22(10):1157-69.
152. Lev B, Alexander Yu G, Eriko Sato M, Yasuo S, Toyoichi T. Dependency of swelling on the length of subchain in poly(N,N-dimethylacrylamide)-based gels. The Journal of Chemical Physics. 1997;106(7):2906-10.
153. Lee S, Son Y, Kim C, Lee J, Kim S, Koh Y. Voice Outcomes of Polyacrylamide Hydrogel Injection Laryngoplasty. The Laryngoscope. 2007;117(10):1871-5.
154. Christensen LH, Breiting VB, Aasted A, Jorgensen A, Kebuladze I. Long-term effects of polyacrylamide hydrogel on human breast tissue. Plast Reconstr Surg. 2003 May;111(6):1883-90.
155. Baker BA, Murff RL, Milam VT. Tailoring the mechanical properties of polyacrylamide-based hydrogels. Polymer. 2010;51(10):2207-14.
156. Bassil M, Davenas J, El Tahchi M. Electrochemical properties and actuation mechanisms of polyacrylamide hydrogel for artificial muscle application. Sensors & Actuators: B Chemical. 2008;134(2):496-501.
157. Kulicke WM, Kniewske R, Klein J. Preparation, characterization, solution properties and rheological behaviour of polyacrylamide. Progress in Polymer Science. 1982;8(4):373-468.
158. Rice JM. The carcinogenicity of acrylamide. MutRes-Genetic Toxicology and Environmental Mutagenesis. 2005;580(1):3-20.
159. Xi TF, Fan CX, Feng XM, Wan ZY, Wang CR, Chou LL. Cytotoxicity and altered c-myc gene expression by medical polyacrylamide hydrogel. Journal of biomedical materials research Part A. 2006 Aug;78(2):283-90.
160. Toozs-Hobson P, Al-Singary W, Fynes M, Tegerstedt G, Lose G. Two-year follow-up of an open-label multicenter study of polyacrylamide hydrogel (Bulkamid®) for female stress and stress-predominant mixed incontinence. International urogynecology journal. 2012;23(10):1373-8.
161. Pallua N, Wolter TP. A 5-year assessment of safety and aesthetic results after facial soft-tissue augmentation with polyacrylamide hydrogel (Aquamid): a prospective multicenter study of 251 patients. Plast Reconstr Surg. 2010 Jun;125(6):1797-804.
162. Slaughter BV, Khurshid SS, Fisher OZ, Khademhosseini A, Peppas NA. Hydrogels in regenerative medicine. Advanced materials (Deerfield Beach, Fla). 2009;21(32-33):3307-29.
163. Refojo MF, Yasuda H. Hydrogels from 2-hydroxyethyl methacrylate and propylene glycol monoacrylate. Journal of Applied Polymer Science. 1965;9(7):2425-35.

164. Lai JY, Wang TP, Li YT, Tu IH. Synthesis, characterization and ocular biocompatibility of potential keratoprosthetic hydrogels based on photopolymerized poly(2-hydroxyethyl methacrylate)-co-poly(acrylic acid). Journal of Materials Chemistry. 2012;22(5):1812-23.
165. Meyvis T, De Smedt S, Stubbe B, Hennink W, Demeester J. On the release of proteins from degrading dextran methacrylate hydrogels and the correlation with the rheologic properties of the hydrogels. Pharmaceutical research. 2001;18(11):1593-9.
166. Lahooti S, Sefton MV. Microencapsulation of normal and transfected L929 fibroblasts in a HEMA-MMA copolymer. Tissue engineering. 2000;6(2):139-49.
167. Madden LR, Ratner BD, Mortisen DJ, Sussman EM, Dupras SK, Fugate JA, Cuy JL, Hauch KD, Laflamme MA, Murry CE. Proangiogenic scaffolds as functional templates for cardiac tissue engineering. Proceedings of the National Academy of Sciences of the United States of America. 2010;107(34):15211-6.
168. Bryant SJ, Cuy JL, Hauch KD, Ratner BD. Photo-patterning of porous hydrogels for tissue engineering. Biomaterials. 2007;28(19):2978-86.
169. Hejcl A, Lesny P, Pradny M, Sedy J, Zamecnik J, Jendelova P, Michalek J, Sykova E. Macroporous hydrogels based on 2-hydroxyethyl methacrylate. Part 6: 3D hydrogels with positive and negative surface charges and polyelectrolyte complexes in spinal cord injury repair. Journal of materials science Materials in medicine. 2009;20(7):1571-7.
170. Denizli A, Tuncel A, Olcay M, Sarnatskaya V, Sergeev V, Nikolaev VG, Piskin E. Biologically modified PHEMA beads for hemoperfusion: Preliminary studies. Clinical Materials. 1992;11(1):129-37.
171. Gupta H, Aqil M. Contact lenses in ocular therapeutics. Drug Discov Today. [Review]. 2012 May;17(9-10):522-7.
172. Gloria A, De Santis R, Ambrosio L, Causa F, Tanner KE. A multi-component fiber-reinforced PHEMA-based hydrogel/HAPEX device for customized intervertebral disc prosthesis. J Biomater Appl. 2011 May;25(8):795-810.
173. Saini R, Bajpai J, Bajpai AK. Synthesis of poly (2-hydroxyethyl methacrylate) (PHEMA) based nanoparticles for biomedical and pharmaceutical applications. Methods in molecular biology. 2012;906(Journal Article):321.
174. Pawlowska E, Poplawski T, Ksiazek D, Szczepanska J, Blasiak J. Genotoxicity and cytotoxicity of 2-hydroxyethyl methacrylate. MutRes-Genetic Toxicology and Environmental Mutagenesis. 2010;696(2):122-9.
175. Peppas NA, Hilt JZ, Khademhosseini A, Langer R. Hydrogels in biology and medicine: From molecular principles to bionanotechnology. ADVANCED MATERIALS. 2006;18(11):1345-60.
176. Baker MI, Walsh SP, Schwartz Z, Boyan BD. A review of polyvinyl alcohol and its uses in cartilage and orthopedic applications. Journal of biomedical materials research Part B, Applied biomaterials. 2012;100(5):1451-7.
177. Peppas NA, Wright SL. Drug diffusion and binding in ionizable interpenetrating networks from poly(vinyl alcohol) and poly(acrylic acid). Eur J Pharm Biopharm. 1998 Jul;46(1):15-29.
178. Hassan CM, Peppas NA. Structure and applications of poly(vinyl alcohol) hydrogels produced by conventional crosslinking or by freezing/thawing methods. Berlin: Springer-Verlag Berlin; 2000. p. 37-65.

179. Alves M-H, Jensen BEB, Smith AAA, Zelikin AN. Poly(vinyl alcohol) physical hydrogels: new vista on a long serving biomaterial. Macromolecular bioscience. 2011;11(10):1293-313.
180. Koyano T, Minoura N, Nagura M, Kobayashi K. Attachment and growth of cultured fibroblast cells on PVA/chitosan-blended hydrogels. Journal of biomedical materials research. 1998;39(3):486-90.
181. Wang M, Li Y, Wu J, Xu F, Zuo Y, Jansen JA. In vitro and in vivo study to the biocompatibility and biodegradation of hydroxyapatite/poly(vinyl alcohol)/gelatin composite. Journal of Biomedical Materials Research Part A. 2008;85A(2):418-26.
182. Lang RA, Grüntzig PM, Weisgerber C, Weis C, Odermatt EK, Kirschner MH. Polyvinyl alcohol gel prevents abdominal adhesion formation in a rabbit model. Fertility and sterility. 2007;88(4 Suppl):1180-6.
183. Kokabi M, Sirousazar M, Hassan ZM. PVA-clay nanocomposite hydrogels for wound dressing. European Polymer Journal. 2007;43(3):773-81.
184. Lin W, Yu D, Yang M. Blood compatibility of novel poly(gamma-glutamic acid)/polyvinyl alcohol hydrogels. Colloids and surfaces B, Biointerfaces. 2006;47(1):43-9.
185. Hyon SH, Cha WI, Ikada Y, Kita M, Ogura Y, Honda Y. Poly(Vinyl Alcohol) Hydrogels as Soft Contact-Lens Material. J Biomat Sci-Polym E. 1994;5(5):397-406.
186. Masters KS, Leibovich SJ, Belem P, West JL, Poole-Warren LA. Effects of nitric oxide releasing poly(vinyl alcohol) hydrogel dressings on dermal wound healing in diabetic mice. Wound Repair Regen. 2002 Sep-Oct;10(5):286-94.
187. Kelly BT, Robertson W, Potter HG, Deng X-H, Turner AS, Lyman S, Warren RF, Rodeo SA. Hydrogel Meniscal Replacement in the Sheep Knee. The American Journal of Sports Medicine. 2007;35(1):43.
188. Kobayashi M, Toguchida J, Oka M. Preliminary study of polyvinyl alcohol-hydrogel (PVA-H) artificial meniscus. Biomaterials. 2003 Feb;24(4):639-47.
189. Kobayashi M, Chang Y-S, Oka M. A two year in vivo study of polyvinyl alcohol-hydrogel (PVA-H) artificial meniscus. Biomaterials. 2005;26(16):3243-8.
190. Lee JH, Lee HB, Andrade JD. Blood compatibility of polyethylene oxide surfaces. Progress in Polymer Science. 1995;20(6):1043-79.
191. Saldarriaga Fernandez IC, Mei HCvd, Metzger S, Grainger DW, Engelsman AF, Nejadnik MR, Busscher HJ. In vitro and in vivo comparisons of staphylococcal biofilm formation on a cross-linked poly(ethylene glycol)-based polymer coating. Acta biomaterialia. 2010;6(3):1119-24.
192. Gref R, Domb A, Quellec P, Blunk T, Müller RH, Verbavatz JM, Langer R. The controlled intravenous delivery of drugs using PEG-coated sterically stabilized nanospheres. Advanced Drug Delivery Reviews. 1995;16(2):215-33.
193. Webster R, Elliott V, Park BK, Walker D, Hankin M, Taupin P. PEG and PEG conjugates toxicity: towards an understanding of the toxicity of PEG and its relevance to PEGylated biologicals. Basel: Birkh√§user Basel; 2009. p. 127-46.
194. Thoma DS, Subramani K, Weber FE, Luder HU, Hämmerle CHF, Jung RE. Biodegradation, soft and hard tissue integration of various polyethylene glycol hydrogels: a histomorphometric study in rabbits. Clinical oral implants research. 2011;22(11):1247-54.
195. Guenaga KF, Matos D, Wille-Jorgensen P. Mechanical bowel preparation for elective colorectal surgery. Cochrane Database Syst Rev. 2011(9):CD001544.

196. Haensig M, Mohr FW, Rastan AJ. Bioresorbable adhesion barrier for reducing the severity of postoperative cardiac adhesions: Focus on REPEL-CV((R)). Med Devices (Auckl). 2011;4:17-25.
197. ten Broek RPG, Kok-Krant N, Verhoeve HR, van Goor H, Bakkum EA. Efficacy of polyethylene glycol adhesion barrier after gynecological laparoscopic surgery: Results of a randomized controlled pilot study. Gynecological Surgery. 2012;9(1):29-35.
198. Suzuki S, Ikada Y. Barriers to Prevent Tissue Adhesion. Totowa, NJ: Humana Press; 2012. p. 91-130.
199. Moore J, Perkins A. Evaluating antimicrobial efficacy and cost of 3 dressings containing silver versus a novel antimicrobial hydrogel impregnated gauze dressing containing Oakin, an oak extract. Advances in skin & wound care. 2010;23(12):544-51.